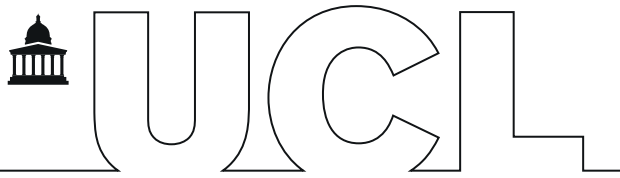

Design of 0D and 1D Magnetic Nanostructures as Magnetic Resonance Imaging Contrast Agents

Aaron Michael King

A thesis submitted for the degree of

Doctor of Philosophy

Department of Chemistry

University College London

London

10th July 2022

Declaration

I, Aaron Michael King confirm that the work presented in this thesis is my own. Where information has been derived from other sources, I confirm that this has been indicated in the thesis.

Abstract

Magnetic resonance imaging (MRI) is a powerful non-invasive clinical imaging technique often combined with contrast agents to increase its diagnostic capabilities. Today, the most widely used contrast agents are based on gadolinium complexes, though these can suffer from toxicity linked to the accumulation of heavy metals in the body. Magnetic nanoparticles (MNPs), in particular iron oxide nanoparticles (IONPs), have demonstrated potential as being a powerful and safe MRI contrast agent alternative. Whilst early examples such as Feridex and Resovist have seen clinical application, issues linked to low efficacy and therefore low uptake by clinicians led to their withdrawal from the market. Therefore, a gap in the market has arisen with a genuine need for a new generation of MNP based contrast agents capable of strong MRI contrast enhancement whilst maintaining good biocompatibility. Recent developments in the field have shown the importance of strong dipolar interactions between neighbouring MNPs and the resulting MRI contrast. However, due to the complexity of these interactions there are still unknowns with how they translate to MRI contrast enhancement and how best they can be used to maximise a contrast agents performance.

The main aim of this thesis is to harness the complex interparticle interactions between magnetic cores in order to produce magnetic nanostructures with exceptional MRI contrast enhancement. This work also seeks to provide new insights on the relationships between these interactions and the resulting MRI behaviour, in order to guide future design of clinical MRI contrast agents.

Chapter 3 describes the work completed on one such approach, where IONPs were prepared via co-precipitation in the presence of the synthetic stabilising polymer, poly(2-acrylamido-2-methylpropane sulfonic acid (P(AMPS)), resulting in particles seeded at the negatively charged sulfonate sites on the polymer backbone. This work details how the colloidal, magnetic, and relaxometric properties of this family of contrast agents can be tuned through changes in reagent

ratio and stabilising polymer molecular weight. In-depth characterisation was carried out using a number of techniques including dynamic light scattering (DLS), transmission electron microscopy (TEM), small angle X-ray scattering (SAXS), vibrating sample magnetometry (VSM), and single field and fast field cycling (FFC) relaxometry. It was revealed that the transverse relaxivity r_2 of these materials was dependent upon both the relative quantity and M_w of P(AMPS) present in the sample. An increase in the seeding density of IONPs along the polymer chain (through lower quantity of polymer or shorter chain length) resulted in an increase in the r_2, with a maximum r_2 of 434.2 ± 59.4 $\mathrm{mM^{-1}s^{-1}}$ being measured. This value far exceeds the clinical examples such as Feridex (120 $^{-1}\mathrm{s^{-1}}$). P(AMPS)-stabilised IONPs also demonstrated unexpected low-field MRI behaviour, as measured by FFC-relaxometry, with exceptionally high low field longitudinal relaxivities (r_1). This was attributed to the clustering of magnetic cores encouraging strong interactions between the IONPs. This clustering behaviour was confirmed by SAXS.

The interparticle interactions that arise when seeding magnetic nanoparticles (MNPs) along a negatively charged polymer backbone were also used to create permanent 1D silica coated magnetic nanostructures. Detailed in Chapter 4, poly(sodium 4-styrenesulfonate) (PSSS) stabilised cobalt ferrite nanoparticles (CFNPs) are used as the precursor for a magnetically triggered trans-phase protocol which results in silica coated chains of MNPs, dubbed nano-necklaces (CFNNs). The trans-phase method was first optimised, with respect to catalyst, precursor, and magnetic trigger strength. The magnetic and MRI properties of the nano-necklaces were then analysed and compared to the parent cobalt ferrite nanoparticles. The CFNN's measured an r_2 of 141.6 $\mathrm{mM^{-1}s^{-1}}$, an increase compared to the PSSS-CFNP precursor ($r_2 = 118.5$ $\mathrm{mM^{-1}s^{-1}}$) resulting from the permanent 1-dimensional alignment of the magnetic cores.

Another potential application for polyelectrolyte stabilised MNPs is described in chapter 5, in which stimuli-responsive polymer microcapsules containing IONPs were prepared by layer-by-layer (LbL) deposition of pH responsive polymers, PSSS and poly(allylamine) hydrochloride (PAH), onto a sacrificial calcium carbonate core. The capsules were characterised using scanning electron microscopy (SEM) and energy dispersive X-ray spectroscopy (EDS) before demonstrating the pH-triggered release of their magnetic cargo which was monitored by MRI analysis. As the capsules become swollen at low pH, greater water access to the IONPs within the capsule core lead to a 95 % increase in r_2 over 24 hours.

The aim of work contained within chapter 5, was to use 'design of experiments' (DoE) for the statistical optimisation of the co-precipitation preparation of bi-magnetic core-shell

nanoparticles, where a CFNP is coated with iron oxide. These materials were characterised using X-ray fluorescence (XRF), energy dispersive X-ray spectroscopy (EDS), powder X-ray diffraction (XRD), as well as TEM, VSM, and DLS.

In summary, this thesis has investigated a wide range of methods for assembling MNPs into more complex nanostructures in order to exploit the strong dipolar interactions between particles. The physical properties of the materials have been characterised using several complementary techniques and their complex behaviours revealed through in-depth analysis.

Impact Statement

Magnetic resonance imaging (MRI) is widely heralded as one of the most important medical developments of the 20^{th} century, and its impact and significance has continued to grow well into to the 21^{st}. Its intrinsic advantages over other imaging modalities, being non-invasive, non-ionising, and inherently quantitative, has led it to become a crucial tool in fields such as oncology and neuroscience. The signal produced by MRI is proportional to the magnetic field strength, therefore since its inception this has motivated a steady trajectory of developing MRI scanners that require stronger and stronger magnetic fields to increase the signal available for imaging, with field strengths of up to 7 T used in cutting-edge clinics.

However, as the strength of MRI scanners has increased so too has their expense, relying on complex superconducting electromagnetic and cryogenic designs, requiring costly infrastructure to install, and leaving clinics with large operational costs. This has resulted in a global issue regarding accessibility, where 90 % of scanners are located in highly developed countries and almost 70 % of the global population have little to no access to MR imaging facilities. A promising modern development in the field is the advance of ultra-low field (ULF) MRI, where imaging is carried out at field strengths a fraction of contemporary scanners (< 0.1 T). Such ULF scanners would cost a fraction of the price and their reduced size would enable point of care use, democratising access to this powerful imaging technique for patients around the world.

For ULF-MRI to become widespread in clinics around the world, its physical limitations must be overcome as the low-field inherently means weaker signals and worse contrast-to-noise ratios. This can be achieved through contrast agents designed to work best at these low field strengths. In this thesis due to their low toxicity, easy preparation, and their behaviour at low fields, contrast agents based on magnetic nanoparticles are investigated. One such study carried out demonstrates how small changes in the preparation of iron oxide nanoparticles can be made to finely tune their low field contrast enhancement. This work can therefore be used

to guide future designs of ULF-MRI contrast agents.

In addition, unique microcapsules containing magnetic nanoparticles were produced with the aim of monitoring drug delivery non-invasively through MRI. This is of great interest to the area of oncology as it allows for the potential of reducing doses and minimizing side effects experience by patients. Within this thesis, the concept of a change in MRI signal induced by an external stimulus illustrates this has a possibility. Also detailed in this thesis are investigations into new approaches for preparing magnetic nanomaterials as potential ULF-MRI contrast agents in as straight-forward and cost-effective manners as possible.

By researching new methods to prepare magnetic nanomaterials and studying their complex behaviours at low magnetic fields this thesis looks to contribute to the development of a new class of ULF-MRI contrast agents that will help bring the technique into common practice for the diagnosis and treatment of disease globally.

Acknowledgements

First, I would like to express my sincerest gratitude to my supervisor, Dr Gemma-Louise Davies, for trusting me with this fantastic opportunity. It has helped me grow more confident both as an academic and individual. Your continuous support during my studies has been invaluable and will always be appreciated. Thank you for all the knowledge, advice, and patience that you have given me over the past 4 years.

I would also like to thank all the UCL staff that have helped me during my PhD, in particular Steve Firth for all the training he gave, Martin Vickers for his knowledge of X-ray diffraction, and Dr Richard Thorogate for his help using the VSM. Also thank you to my collaborators; Dr Lara Bogart for expertise in Mössbauer spectroscopy, Dr Stephen Hall for SAXS measurements and analysis, and Dr Joseph Bear for carrying out ICP-OES measurements.

To the entire Davies group, both past and present, I can not express how grateful I am to have been able to work alongside such fantastic people. My PhD experience would not have been half as enjoyable without such a fun group to share it with. Thank you for keeping me company during the late nights, for the advice and support you gave, for the loud music in the lab, and for the many pints in IoE and Phineas! To Connor, Marwa, Viliyana, Sam, Mark, Alex, Mary, Joe, Craig, Ziwei, Adila, Isabel, and Fuqiang, thank you all for making the Davies group the best research group anyone could ask to be part of, I feel truly lucky to be ending my PhD with new lifelong friends.

I must also thank my family and friends for their support over the past 4 years. Especially thank you to my mum and sister who have always been my number one supporters, and whose examples I have always tried to follow. Finally, I wish to thank my amazing girlfriend, Clarissa. Thank you for being there at the end of long days, for listening to my frustrations, and for supplying me with snacks to fuel my days spent writing. I would not have been able to survive this PhD without all the love and support you have given.

Contents

List of Figures

List of Tables

List of Abbreviations

0D	0-Dimensional
1D	1-Dimensional
APTES	3-aminopropyltriethoxysilane
CFNF	Cobalt Ferrite Nanoflower
CFNN	Cobalt Ferrite Nanonecklace
CFNP	Cobalt Ferrite Nanoparticle
CNT	Carbon Nanotube
CT	Computed Tomography
CTA	Chain Transfer Agent
CTAB	Cetimonium Bromide
DLS	Dynamic Light Scattering
DMSA	Dimercaptosuccinic Acid
DNA	Deoxyribonucleic Acid
DoE	Design of Experiments
DOX	Doxorubicin
EDS	Energy Dispersive X-ray Spectroscopy
EDTA	Ethylenediaminetetraacetic Acid
EG	Ethylene Glycol
ELR	Echo Limiting Regime
FFC	Fast Field Cycling
FTIR	Fourier Transfrom Infrared
ICP-OES	Induced Couple Plasma Optical Emission Spectroscopy
IONP	Iron Oxide Nanoparticle
IR	Infrared

LbL	Layer-by-Layer
MAR	Motion Averaging Regime
MFI	Magnetic Field Induced
Mn	Number Average Molar Mass
MNP	Magnetic Nanoparticle
MRI	Magnetic Resonance Imaging
M_s	Magnetisation Saturation
M_w	Weight Average Molar Mass
NMR	Nuclear Magnetic Resonance
NMRD	Nuclear Magnetic Relaxation Dispersion
NP	Nanoparticle
OFAT	One Factor At A Time
P(AMPS)	Poly(2-acrylamido-2-methylpropane Sulfonic Acid
PAA	Poly(acrylic acid)
PAH	Poly(allylamine) Hydrochloride
PAI	Photoacoustic Imaging
PBS	Phosphate Buffered Saline
PCS	Photon Correlation Spectroscopy
PDI	Polydispersity Index
PEAP	Polyelectrolyte Absorption Procedure
PEG	Polyethylene Glycol
PEI	Polyethylene Imine
PET	Positron Emisson Tomography
PMA	Poly(methacrylic acid)
PMC	Polymeric Capsule
PSSS	Poly(sodium-4-styrene) Sulfonate
PTX	Paclitaxel
PVA	Polyvinyl Alcohol
P-XRD	Powder X-ray Diffraction
QD	Quantum Dot
RES	Reticuloendothelial System
SAXS	Small Angle X-ray Spectroscopy

SDR	Static Dephasing Regime
SEM	Scanning Electron Microscopy
SNC	Superparamagnetic Nanoparticle Cluster
SPION	Superparamagnetic Iron Oxide Nanaparticle
TAC	Tricarboxylic Acid Cylce
Tc	Curie Temperature
TEM	Transmission Electron Microscopy
TEOS	Tetraethyl Orthosilicate
T_N	Neel Temperature
TOPO	Tri-n-octylphosphine Oxide
TREG	Triethylene Glycol
ULF	Ultra Low Frequency
UV	Ultra-violet
VSM	Vibrating Sample Magnetometry
XRD	X-ray Diffraction
XRF	X-ray Fluorescence

Chapter 1

Introduction

1.1 Introduction to Nanomaterials

Nanomaterials are an ever growing sector of materials research, with the global nanomaterials market increasing from an estimated 4.1 billion USD in 2015 to 8.5 billion in 2019, an increase of over 100% in as little as 4 years.[1] Such materials are defined as a "material with any external dimension in the nanoscale or having internal structure or surface structure in the nanoscale", with nanoscale defined as the "length range approximately from 1 nm to 100 nm" (ISO/TS 80004:2015).[2] This includes both nano-objects, which are discrete pieces of material, and nanostructured materials, which have internal or surface structure on the nanoscale; a nanomaterial may be a member of both these categories. These materials have applications in a wide number of industries such as aerospace, bio-technology, energy storage, electronics, construction, agro-chemicals, and consumer goods. Their popularity is due to the unique advantages that are provided when a material's size is in the nanometre range, with properties that are often significantly different from the bulk counterpart. The functional properties of different nanomaterials can be determined by their high surface area-to-volume ratios, their surface functionalisation, and their improved solubility; these can all be tuned to often very fine degrees allowing function specific designs of such materials.

Nanomaterials can be produced in an almost countless number of ways and be formed from a wide array of materials, including silica, metals and metal oxides, fullerenes, metal-organic frameworks, organic polymers, and semi-conductors.[3–9] Each will have its own unique set of mechanical, optical, electronic, magnetic, and biological properties making them suitable for

different applications including, catalysis, printable electronics, gas storage, high performance sports equipment, industrial coatings and lubricants, and many others. In particular, this work is interested in how they can be applied to different biological and clinical uses, such as cell separation and tracking, bio-sensing, drug and gene delivery, and medical imaging.[10–17] One popular example of a nanomaterial with a wide range of applications are carbon nanotubes (CNTs). CNTs can be described as an intermediate between flat graphene and fullerene cages and have a structure consisting of a hexagonal lattice of carbon atoms rolled to form a cylinder with diameters 0.4 – 3 nm and lengths in the micron range. This structure gives them high chemical and thermal stability, high tensile strength, and high surface area. Whilst being popular in nanoelectronic research they have also demonstrated potential for cell tracking and labelling, as well as drug and gene delivery.[18]

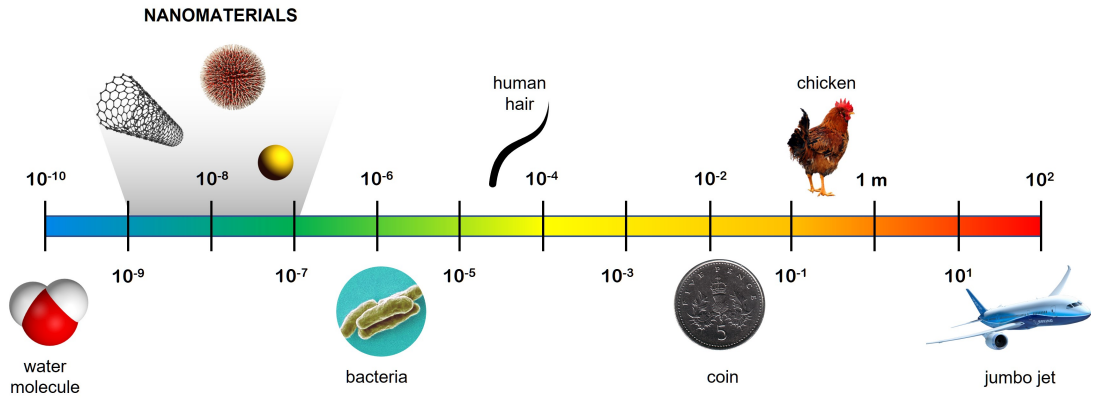

Figure 1.1: Compararitive representation of the relative scale of nanomaterials in metres.

Another class of materials are mesoporous silica nanoparticles, their high surface area-to-volume ratio and tunable porosity provides an excellent platform for the likes of drug delivery, MRI imaging, and biosensing.[19–21] When reducing the size of a material to the nanoscale distinctive optical and electronic behaviour can be observed due to quantum effects. This is true for both nanogold and nanosilver materials which can enhance Raman signals through plasmon resonance on the particles surface. The enhancement is so great that these materials allow for the detection of single molecules making for excellent bio-sensors.[22,23] The tendency for these materials to absorb near-infrared radiation to produce heat also makes them fantastic candidates for photothermal therapy and photoacoustic imaging (PAI).[24,25] Similarly, quantum dots (QDs) which are nanoscale, semiconductors (such as lead sulfide or cadmium telluride) also show different optoelectronic properties as a result of their size. When irradiated with UV light

they will luminesce. The colour of light emitted can be tuned through changing size and shape due to quantum effects. In biomedicine they can therefore be used for cell labelling and tracking, *in vitro* and *in vivo* fluorescent imaging.[26–28]

1.2 Magnetic Nanomaterials

Magnetic nanomaterials are another class of materials whose properties differ considerably compared to their bulk counterparts. As the name suggests they are nanoscale materials that respond to external magnetic fields and are popular with researchers in a wide range of fields; including catalysis, data storage, and environmental remediation due to their unique size/shape dependent magnetic properties.[29–31] They have also demonstrated great potential in biomedicine. For example, magnetic nanoparticles in combination with can efficiently generate heat when exposed to an alternating external magnetic field to induce cancer cell death without the need of an invasive procedure.[32] This form of hyperthermia-based cancer therapy has already been approved in Europe.[33] Magnetic nanoparticles may also be used for targeted drug delivery in which magnetic force is used to guide nanocarriers to a tumour or other diseased tissue.[34,35] Alternatively, a magnetic field can also be used as a trigger for the release of a drug payload once it has reached the desired site.[36,37] Other biomedical uses include cell separation, tissue repair, gene therapy, and magnetic resonance imaging (MRI).[38–40] The latter is expanded on in Section 1.5. Magnetic nanomaterials can even be found in nature and are produced by bacteria, fish, and even birds allowing them to detect the Earth's magnetic field.[41,42]

Among the many types of magnetic nanomaterials, iron oxide nanoparticles (IONPs), have been researched extensively for their biomedical applications. These particles have numerous qualities that make them particularly attractive to researchers, including their small size, strong magnetic properties (high saturation magnetisation in combination with low remanence and coercivity), facile preparation using mild conditions, biocompatibility, and ease of functionalisation. These, as well as, other ferrite based nanomaterials will be the focus of this body of work.

1.2.1 Structure of Ferrite Nanomaterials

Ferrites such as magnetite (Fe_3O_4), cobalt ferrite ($CoFe_2O_4$), and manganese ferrite ($MnFe_2O_4$) are all composed of positively charged metal ions in a lattice with negatively charged oxygen ions. They can be described generally with the formula AB_2O_4 and adopt a spinel crystal

structure with the oxide anions arranged in a cubic close-packed (ccp) lattice and the metal cations A and B will occupy either octahedral (O_h) and tetrahedral (T_h) sites. The charges of metal cations are typically A^{2+} and B^{3+} (exceptions are possible), with the site occupied by the divalent cation used to distinguish between the two possible spinel structures, 'normal' or 'inverse'. If the divalent occupies the tetrahedral sites and none of the octahedral sites, then the structure is described as spinel. However, the divalent ion may instead occupy 1/2 of the octahedral sites with the trivalent occupying the remaining O_h sites. In this example the structure is described as inverse spinel. The spinel structure is illustrated in Figure 1.2.

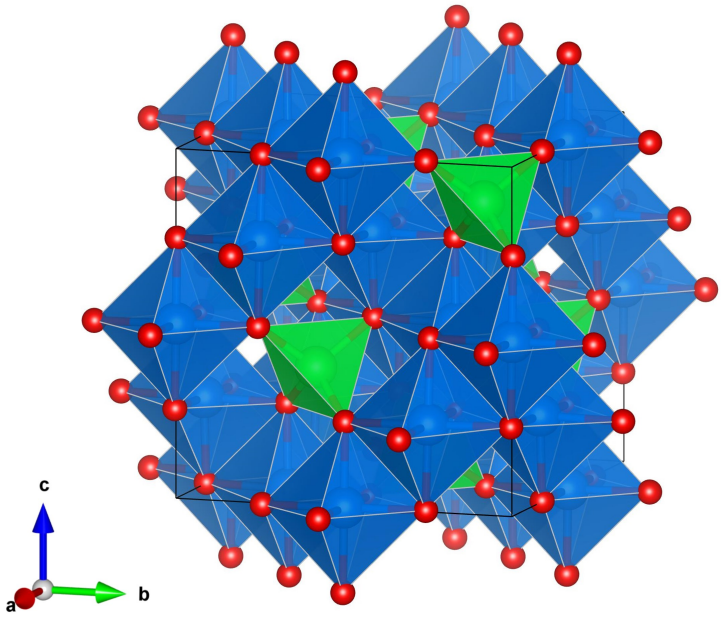

Figure 1.2: Illustration of the cubic inverse spinel structure adopted by Fe_3O_4. The oxygen positions are marked in red, the green polyhedra represent the tetrahedral sites (T_h), and the blue polyhedra represent the octahedral sites (O_h). Image created using structure visualisation software VESTA.[43]

Magnetite (Fe_3O_4) in an example of an inverse spinel material, where the Fe^{2+} ion occupies half of the O_h sites and the Fe^{3+} ion occupies the remaining O_h sites as well as all T_h sites. Similarly, cobalt ferrite also adopts the inverse spinel crystal structure, where the Fe^{2+} of magnetite is replaced by the Co^{2+} ion in the O_h sites. Such structure is adopted for these ferrites due to the divalent cation being larger than the trivalent cation and therefore preferring the larger O_h site. An example of a normal spinel material is zinc ferrite ($ZnFe_2O_4$) where

the divalent zinc cation occupies only the T_h sites, with the trivalent iron cation occupying all O_h sites. This can have a detrimental effect on the magnetic properties on this material due to anti-ferromagnetic coupling. An interesting example where the ferrite is neither spinel nor inverse spinel is manganese ferrite ($MnFe_2O_4$), once disputed, it is now agreed to exist as a mixed spinel structure. As a mixed spinel the Mn^{2+} cation occupies both O_h and T_h sites with a majority being normal spinel (Mn^{2+} in the T_h site) and a small percentage as inverse spinel (Mn^{2+}in the O_h site). This ratio can be affected through synthetic parameters.[44]

1.3 Principles of Magnetism

Magnetite is one of a very few naturally occurring minerals that can be found already magnetized. The propensity of these brownish-black minerals to attract small pieces of iron was how the physical phenomena of magnetism was first discovered in antiquity.[45] These magnetised minerals were named lodestones and would be suspended allowing them to turn freely acting as the first magnetic compasses aiding ancient navigators. The origins of magnetism arise from quantum mechanical effects, though for the sake of the simplicity only a qualitative/semi-quantitative description of the physical principles underlying the phenomenon are described herein. Magnetism ultimately arises because of the movement of an electrically charged particle, this means that all materials display some magnetic properties. Two kinds of electron motion define the magnetic properties exhibited by an element.

Firstly, electrons orbiting the nucleus have an orbital angular momentum, L, such that:

$$L = mvr \tag{1.1}$$

Where m is the mass of the electron, v is the velocity, and r is the radius of the orbit. An orbiting of an electron can be considered equivalent to the flow of current through a loop. This will generate a magnetic field (a magnetic moment of μ).

$$\mu = iA \tag{1.2}$$

Where i is the current and A is the area of the loop. This magnetic moment is quantised in units of μ_B (the Bohr magneton).

Secondly, the electron has a has a quantum spin and a spin angular momentum of S, the axis of said spin can have two possible orientations, either parallel or anti-parallel to an external magnetic field. The spinning charge is what produces an external magnetic field. The

combination of these two forms of electron motion gives rise to the total angular momentum of the atom. Magnetism in solids is dominated by the magnetic moment associated with the electron spin.

The magnetic behaviour of an atom is determined by the arrangement of electrons within its orbitals and according to the Pauli exclusion principle each orbital can contain no more than two electrons, and these must have opposing spins. An atom will posses an overall magnetic moment where there are unpaired electrons in an orbital (the spin moments are not cancelled). Whether a material contains unpaired electrons or not all materials will interact with an external magnetic field due to the aligning of electrons (either parallel or anti-parallel) with the field causing a small degree of rotation and therefore magnetisation. This response is dependent on a material's magnetic susceptibility (χ), this can be considered a measure of how easily a material can be magnetised and is a dimensionless parameter which relates the net magnetic moment of a material (M) with the applied field (H).

$$M = \chi H \tag{1.3}$$

Diamagnetic materials are those with no unpaired electrons and therefore will exhibit no magnetism in the absence of an external field. When a field is applied a small field is induced opposite to the external field. This induced magnetization is linearly dependent on the applied field and will fall back to zero once the field is removed. Examples of diamagnetic materials include water and gold. Other materials will also exhibit diamagnetism but as this effect is much weaker than other forms of magnetism its contribution to magnetic behaviour is negligible. A paramagnetic material possesses unpaired electrons that are randomly distributed throughout the sample. When an external magnetic field is applied an induced magnetization parallel to the external field is observed. This magnetisation is also linearly dependent on the external field and will fall back to zero when the field is removed. This effect however is much stronger than diamagnetism.

The final form of magnetism is observed in transition metals and rare earth elements (and the compounds they form). The d (or f) electrons of these elements occupy highly eccentric orbitals that extend farther from the nucleus allowing for interactions between neighbouring atoms. This can result in the formation of long range order within these materials whereby the orbitals of adjacent atoms overlap (in the case of iron the 3d orbitals) and electrons are effectively shared. As to adhere to the Pauli exclusion principle, this results in strong exchange coupling of electron spin moments through the material and these aligned moments give rise to

strong permanent magnetisation. This is named ferromagnetism. In oxides such as magnetite, the oxygen atom acts as a link between the nearest neighbour Fe cations and causes the atomic dipoles of the Fe atoms to couple anti-parallel. Such coupling results in a net magnetic moment of zero and is referred to as anti-ferromagnetism. However, as ferrites such a magnetite act as ferromagnets there must be a net magnetic moment. In inverse spinel ferrites the O_h and T_h couple anti-parallel to one another but as half of the O_h sites are occupied by a divalent ion the magnetic moment is not fully cancelled out by the trivalent Fe ions at the T_h sites. This difference in valency results in a net magnetic moment meaning the material behaves similar to a ferromagnetic material. These and other similar materials are described as ferrimagnetic.

Unlike paramagnetic materials when a ferro- or ferri-magnetic material is exposed to an external field the induced magnetic field remains after the field is removed and the magnetisation does not exhibit a linear relationship between field and magnetisation. The magnetisation instead increases with increasing field up to a maximum, called the magnetisation saturation (M_s), at this point all moments are aligned parallel to the field and the magnetisation can no longer increase. The M_s will decrease with increasing temperature until it reaches zero, the temperature of this point is known as the Curie temperature (T_c). At the temperature the material undergoes a phase transition and the long range order in the crystal lattice is lost. The T_c for magnetite is approximately 550 °C.[46] The equivalent for anti-ferromagnetic materials is the Néel temperature (T_N) above which the material becomes paramagnetic.

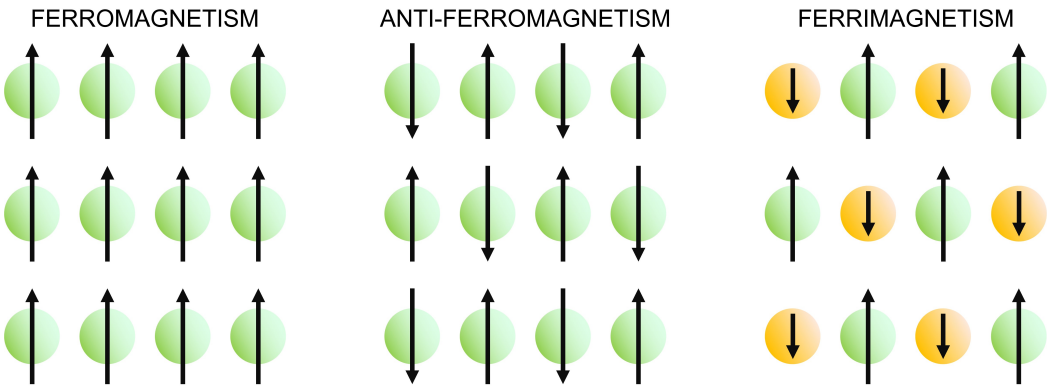

Figure 1.3: Illustration of the 3 forms of magnetic coupling, ferro-, anti-ferro-, and ferrimagnetic coupling. Arrows depict spin orientation with the size of the arrow representing the magnitude of the spin.

For a bulk piece of ferromagnetic material, the long range order that provides it with its

magnetic properties does not extend across the entire material. Instead, the bulk is divided into several magnetic domains inside of which the spins are aligned but are not aligned between different domains. Domains may even cancel one another out reducing the magnetisation of the bulk material. The formation of magnetic domains within ferromagnetic materials is due to the exchange interaction (the coupling between adjacent atoms) only acting over comparatively short ranges. Over longer distances atoms will want to orientate their dipoles in opposing directions to minimise their energy. This can be overcome by reducing the size of the material into the nano-range. For ferrites reducing the size below approx. 20 nm a single domain particle can be formed.[47] At this size all spins within the particle are aligned and the particle can therefore be considered to have a single magnetic moment (the sum of magnetic moments within the particle). The dipole of the particle is able to flip at random, in a manner similar to that of a paramagnetic Fe atom, such that when placed in an external magnetic field a strong internal magnetisation is formed. This phenomenon is called superparamagnetism. The magnetic susceptibility of superparamagnetic IONPs (also referred to as SPIONs) is less than that of ferrimagnetic bulk magnetite but unlike bulk there are no interactions between neighbouring domains which prevent the magnetisation returning to zero once the external field is removed.[48] The phenomena of superparamagnetism is why ferrite MNPs make such an appealing material to be utilised for bio-applications, in particular as biomedical contrast agents. The principles of magnetic resonance imaging (MRI) and how superparamagnetic particles can be exploited as contrast agent are expanded upon in the following section.

1.4 Principles of Magnetic Resonance Imaging

Clinicians today have access to a range of powerful imaging techniques to assist in diagnosing and treating disease. These include X-ray radiography, computed tomography (CT), positron emission tomography (PET), and magnetic resonance imaging (MRI). MRI in particular is widely used due to being non-invasive, high resolution, and unlike others mentioned does not require ionising radiation to produce an image. Its original name of nuclear magnetic resonance (NMR) imaging gives clues on the underlying principles of the technique. The technique exploits the tendency of atomic nuclei (typically ^{1}H) to absorb and emit radio waves when exposed to a strong external magnetic field. The name was switched to MRI due to growing negative connotations associated with word ‘nuclear’ in the 1970’s, despite not exposing patients to any ionising radiation.

To be NMR-active, nuclei must interact with a magnetic field, requiring an intrinsic nuclear magnetic moment and angular momentum. This is true for any isotope that has an odd number of protons and/or neutrons and therefore has a non-zero nuclear spin. For MRI the most important nucleus is ^{1}H due to the high amounts of water and fats in the body. When placed in a magnetic field of strength, B, a particle with a non-zero spin can absorb a photon of frequency, ν (Equation 1.4. The frequency is dependent on the gyromagnetic ratio, γ, which is specific to the nuclei. For ^{1}H $\gamma = 42.58$ MHz/T.

$$\nu = \gamma B \tag{1.4}$$

The spin of a proton when exposed to a magnetic field (B_0) can be considered as if it has its own small magnetic moment, meaning that it behaves as a magnet would. When placed inside the field the proton spin will align itself parallel to the external field (α).[49] In doing so the proton is in the low energy state, it can however also align anti-parallel to the external field in a high energy state (β). It is then possible for the proton to transition between the low and high energy states by absorbing a photon. The frequency of the photon required for this transition is known as the Larmor frequency (ω_0), and will be in the radio frequency (RF) range. When several protons are placed in a magnetic field (B_0) each spin will align in one of the two possible orientations, with the distribution of spins being described by the Boltzmann equation (Equation 1.5)

$$\frac{N_\beta}{N_\alpha} = e^{\frac{-\mu\beta_0}{kT}} \tag{1.5}$$

Where N_α and N_β are the numbers of spin arranged in the low (α) and high (β) energy states respectively, μ is the nuclear magnetic moment, B_0 is the magnetic field strength, k is the Boltzmann constant, and T is the sample temperature. This shows that at room temperature a small majority of spins will be in the low energy state and aligned parallel to B_0. This in turns results in a net magnetisation, M_0 (See Figure 1.4).

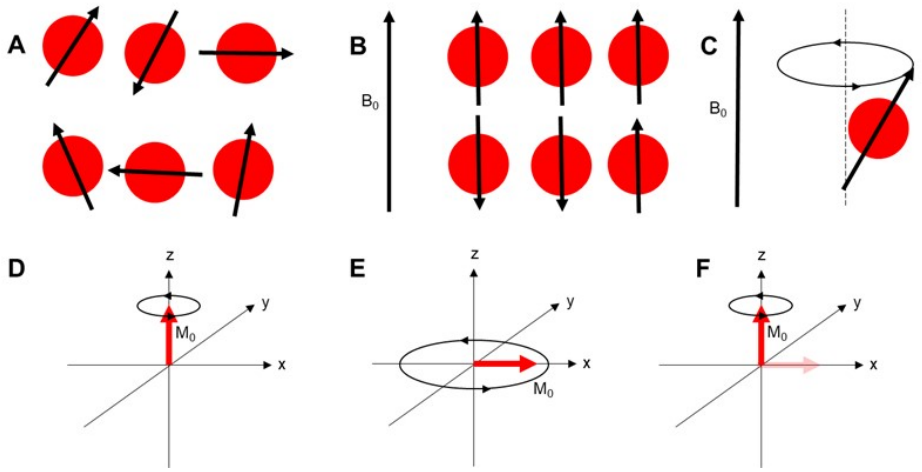

Figure 1.4: (A) Unaligned proton spins. (B) Proton spins align parallel or anti-parallel with external magnetic field, B_0. (C) Precession of proton spins about axis of B_0. (D) Resultant net magnetisation in z-axis, M_0 shown as red arrow. (E) M_0 in xy plane after excitation by a 90 ° RF pulse. (F) M_0 relaxing back to z-axis after removal of RF pulse and energy loss *via* T_1 and T_2 mechanisms.

The proton spins will precess about the axis of B_0, this is called Larmor precession the frequency of which is equal to the Larmor frequency, ω_0 and is proportional to the magnitude of the applied field. The precessing of the proton spins results in the magnetic moments cancelling one another out in all but one direction.[50] A radiofrequency (RF) pulse equal to the Larmor frequency is applied perpendicular to B_0 pushing M_0 parallel to the xy plane. Upon removal to the RF pulse the proton spins relax back to their original orientation, parallel to the external field (Figure 1.4). Relaxation occurs *via* two different mechanisms, longitudinal (T_1) and transverse T_2. T_1 relaxation often referred to as spin-lattice relaxation involves the transfer of energy from the protons to the environment until M_0 returns to its initial maximum value. T_2 relaxation referred to as spin-spin relaxation, occurs as precessing spins fall out of phase with one another.[51] It is the change in energy of the relaxing magnetisation that is detected. By translating the current produced in the detector coils using Fourier transform T_1 and T_2 relaxation times can be obtained. This data can be subsequently spatially resolved electronically, producing the characteristic grey-scale images used by clinicians.

1.5 MRI Contrast Agents

1.5.1 Contrast Agent Mechanisms

Though it is possible to distinguish diseased tissue from healthy tissue using clinical MRI scanners using only the intrinsic differences in relaxation times of the different tissues, contrast agents are regularly applied to improve the technique's potency. MRI contrast agents (CAs) act by predominately decreasing either the T_1 or T_2 relaxation times through dipolar interactions with local water molecules within the body. Contrast agents that are used clinically are most commonly based on paramagnetic gadolinium (Gd^{3+}) complexes, this is due to their seven unpaired electrons, large magnetic moment, and long electronic relaxation times (9-10 seconds).[52] Free Gd^{3+} is toxic however, and can disrupt physiological Ca^{2+} signalling.[53] Therefore kinetically stable chelation is required to prevent leaching using ligands such as tetraazacyclododecane-tetraacetic acid (DOTA). Clinical examples include Magnevist® (Gd-DTPA) and Dotarem® (Gd-DOTA).[54] Such contrast agents are described as 'positive' contrast agents as they cause areas of hyperintense signal in the MR images. They do this by shortening the T_1 relaxation times, the mechanisms of T_1 relaxation by these metal complexes are well established and described by the Solomon, Bloembergen, and Morgan (SBM) equations.[55,56] The efficiency of such CAs is linked to the following key parameters during chemical exchange; the molecular tumbling rate (τ_R), proton residence lifetime (τ_M), and the co-ordinating number (q) of water molecules (represented in Figure 1.5. However, development of nephrogenic systemic fibrosis (NSF) has been described in patients with severe renal impairment.[57–59] There have also been reports concerning the accumulation of gadolinium in various tissues including bone, brain, and kidneys of patients that do not suffer renal impairment.[60–62]

An alternative to the commonly used Gd-based contrast agents are those based on IONPs such as Feridex®, Resovist®, and Lumirem®.[63,64] Due to such contrast agents causing areas of hypointense signal they are referred to as 'negative' contrast agents. Whilst they do have a small effect on the T_1 relaxation times on local molecules they predominately shorten the T_2 relaxation times. The scale of the effect is determined by the translational diffusion of water molecules in the inhomogeneous magnetic field surrounding the IONPs (represented in Figure 1.5. The interaction is described by the quantum mechanical outer-sphere theory which is presented in Equation 1.6.[65,66]

$$\frac{1}{T_2} = \left(\frac{4}{9}\right) \nu \tau_D (\Delta\omega_r)^2 \tag{1.6}$$

Where ν is the volume fraction occupied by the magnetic spheres, τ_D is the diffusional corre-

lation time and is equivalent to $\tau_D = \frac{r^2}{D}$ (r is the radius of the magnetic core and D is the diffusivity of water molecules), and ω_r is the rms angular frequency shift and is proportional to the magnetic moment and magnetisation of the particles.

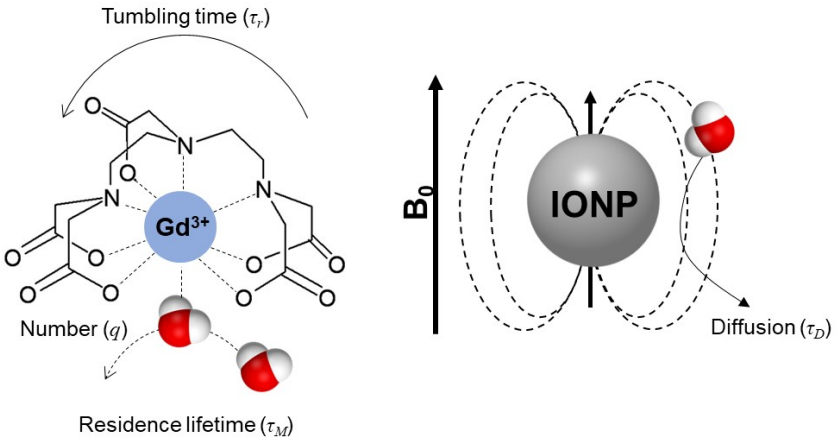

Figure 1.5: Schematic representation of the T_1 and the T_2 relaxation mechanisms for positive and negative contrast agents. (a) Paramagnetic metal complex systems (positive CA) and the key parameters to T_1 relaxation; tumbling time, τ_R, proton residence lifetime, τ_M, and the co-ordinating number of water molecules, q, while the magnetic gradient around the paramagnetic centre is negligible. (b) The interaction of protons with a spherical superparamagnetic particle as water molecule diffuses across the inhomogeneous induced magnetic field, with the chemical exchange between surface and water molecule ignored.

The effectiveness of contrast agents can be quantified by its relaxivity, r_1 or r_2, which is a measure of the proton relaxation rate, R_1 or R_2, with respect to the concentration of the contrast agent (Equation 1.7).[52]

$$r_{1,2} = \frac{R_{1,2obs} - R_{1,2sol}}{[CA]} \tag{1.7}$$

Where $R_{1,2obs}$ is the observed relaxation rate of the agent in an aqueous suspension, $R_{1,2} = 1/T_{1,2}$, where $T_{1,2}$ is the longitudinal or transverse relaxation time of water protons respectively. $R_{1,2sol}$ is the relaxation rate of the unaltered solvent system (*i.e* in the absence of contrast agent) and [CA] is the mM concentration of the contrast agent in suspension.

1.5.2 MRI Contrast Behaviour of Magnetic Nanoparticles

As IONPs and other superparamagnetic/ferromagnetic nanoparticles are predominately negative contrast agents, acting by shortening the T_2 relaxation time, their relaxation behaviour is a result of the inhomogeneous magnetic field that is produced when exposed to an external field. It is therefore desirable for contrast agents to possess large magnetisation m_s values. One of the key advantages of ferrite nanoparticles is the ease at which the magnetic properties can be tuned by controlling certain physicochemical parameters such as size and composition.

From outer-sphere theory (Equation 1.6) we see that the relaxation rate, R_2, is proportional to the square of the particle radius, r^2. The relationship between the two was demonstrated by Cheon *et al.,* using a thermal decomposition method produced Fe_3O_4 nanoparticles with diameter of 4, 6, 9, and 12 nm (all with narrow size distributions).[67] As the size of the magnetic nanoparticle increased so too did the mass magnetisation 25 to 43, 80, and 102 emu g^{-1}, and the measured T_2 value decreased. This result is explained in terms of decreasing surface-to-volume ratios with increasing diameter. As the particle size increases, the proportion of Fe atoms at the surface and the curvature of the particle decreases. The reduces the contribution of surface effects, including spin canting, non-collinear spins, and spin-glass behaviour; all of which can have substantial impact on the particles' magnetic moment and thus its relaxivity.[45].

According to theoretical studies of size effects on T_2 relaxivity, there are three different size regimes; the motional average regime (MAR), the static dephasing regime (SDR), and the echo-limiting regime (ELR).[66] As a particle's radius increases the R_2 increases with the MAR before reaching a plateau (SDR). Any further increase to the particle size results in a decrease in R_2 (ELR). Therefore, according to the theory the nanoparticles in the SDR will have the highest relaxivities, however at this size the nanoparticles will suffer uncontrollable aggregation caused by strong ferromagnetic dipolar interactions. Particles sized within the MAR are therefore preferable for MRI applications.[50]

According to outer-sphere theory, the relaxation rate is also proportional to the magnetisation of a particle which itself increases proportionally with the radius of the magnetic nanoparticle. This relationship is described in Equation 1.8.

$$m_s = M_s[(r-d)/r]^3 \tag{1.8}$$

Where m_s is the saturation magnetisation of the nanoparticle, M_s is the saturation magnetisation of the bulk material, r is the radius of the nanoparticle, and d is the thickness of the disordered surface spin layer.[68] Therefore the relaxivity of a magnetic nanoparticle can be

increased by increasing the radius within the MAR, as demonstrated by Cheon *et al.*[67]

1.5.3 Low-Field MRI of Superparamagnetic Nanoparticles

Most clinical MRI is carried out at either 1.4 or 3.0 Tesla (Larmor frequencies of 60 and 120 MHz respectively) however the relaxivity can be measured over a much wider range of frequencies down to as low as 0.01 MHz. Using the technique of fast field cycling (FFC) NMR relaxometry it is possible to measure the longitudinal relaxation rate of the same sample over a range of frequencies (0.01 – 40 MHz). The resulting relaxation rates (or relaxivities) are then plotted against the magnetic field frequency to provide a graphical representation named a nuclear magnetic resonance dispersion (NMRD) profile. These profiles can then be used a means of studying both the colloidal and magnetic properties of MNP suspensions.[69–72] Conventional NMR and MRI measurements are carried out with a fixed B_0 with RF transmitters and receivers tuned for the corresponding frequency. Measurements would therefore require somehow changing the external field and adjusting the frequency for the RF modules. To overcome these issues, a fast-switching electromagnet is used (hence the term fast field cycling). The experimental principles of these measurements are summarised in Section 2.5.1.

Using FFC for the characterisation of magnetic nanoparticles was first carried out by Roch, Muller, and Gillis in 2002.[73] They analysed the low field behaviour of carboxydextran (SHU 555 and Resovist) and dextran (Endorem) coated iron oxide nanoparticles. In this they were able to successfully apply an earlier devised model for describing the interactions between superparamagnetic colloids and water protons. The model (named SPM theory), conceived by the same group, was derived from the classical theory of paramagnetic relaxation but modified to account for two properties of superparamagnetic particles; a high Curie magnetic component that will be present at low fields and a high value for the anisotropy energy (E_a) of the particle. In this adaptation then the low frequency relaxation is considered to be a result of the random fluctuations of the nanoparticles (Néel relaxation), and not as described in Section 1.4, the result of protons diffusing with the MNPs aligned with B_0 (Brownian relaxation).[74] This model has been shown to hold true for other simple IONP systems such as silica, citrate, and oleate stabilised IONPs.[75–78]. These works demonstrated that low field behaviour was determined by the core size and saturation magnetisation of the particle.

Figure 1.6 shows the model NMRD profile of a superparamagnetic nanoparticles according to this SPM theory. At the higher field strengths (usually > 10 MHz) it is the classical Brownian relaxation that defines the proton relaxation and is related to the strength of the magnetic

moments and water diffusional correlation times around the particle core (correlating to particle size). At lower frequencies Néel relaxation dominates resulting in a plateau (also described as a dispersion), though the presence of this dispersion and relaxation rate at low field is highly dependent on anisotropy. The peak ν_{max} is a result of the re-orientation of magnetic moments with the increasing field strength.[79]

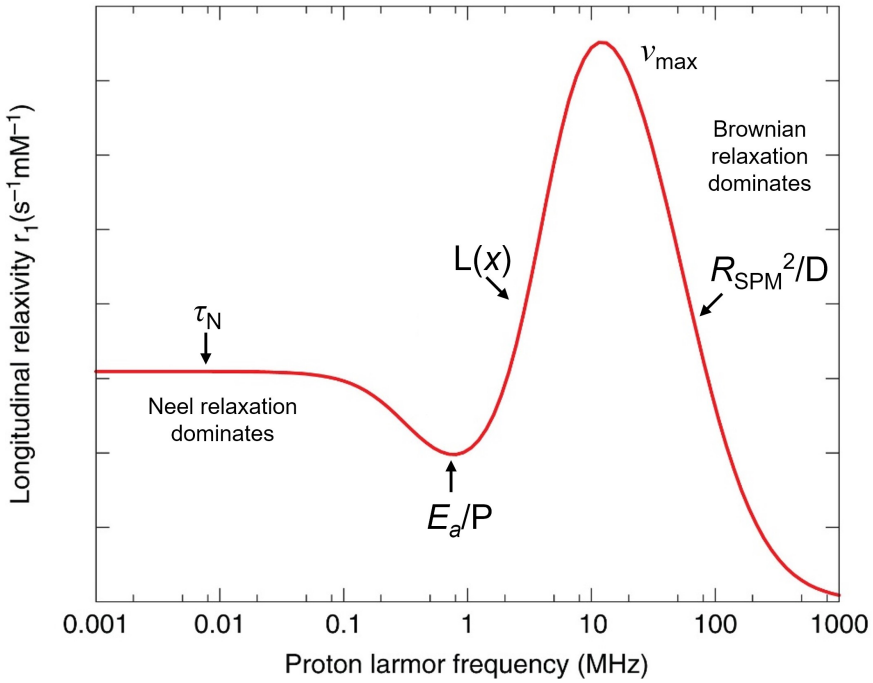

Figure 1.6: Model NMRD profile of superparamagnetic nanoparticles as modelled by SPM theory. Labelled are the parameters that define each of the features. Where R_{SPM} is the radius of the nanoparticle, D is the diffusion coefficient, L(x) is the Langevin function, E_a is the anisotropy energy, P is an empirical parameter that depends on anisotropy, and τ_{N} is the Néel relaxation time. Figure adapted from Vuong *et al.*[79]

It is important to note that this theory requires a number of assumptions such as, all particles must be homogeneously distributed in the sample with zero dispersity in core size, the magnetic moments are distributed according to Boltzmann, and particles will not interact with one another (Néel relaxation time is independent of the magnetic field).[79] In an effort to improve on this model to account for more complex systems the Muller group published an updated model in attempting to account for the agglomeration of MNPs.[80] In this they showed that agglomeration can cause the NMRD profiles to become flatter due to water becoming

trapped and diffusion of the water molecules no longer being equivalent to the bulk. However, this was still shown to be incomplete when measuring iron oxide nanoparticles that had be produced *in situ* in the presence of a sulfonated polymer. These MNPs demonstrated increased low field relaxivities as well as shifted ν_{max}. This was attributed to increased anisotropy of the system arising from strong dipolar interactions between particles. This behaviour has been observed for many other MNP composites such as iron oxide stabilised by DNA, heparin, and fatty acids, as well as similarly stabilised cobalt ferrite nanocomposites.[81–84].

When the anisotropy energy is very high compared to thermal fluctuations, as is the case for dipolar interactions between particles, the magnetic moment of the particle is blocked on its anisotropic axis. To compensate for this Lévy *et al.*, introduced the 'rigid dipole model' which can be applied when the rotational Brownian relaxation is dominant.[85,86] The NMRD curves produced by such a model are absent of any ν_{max} peak. In this work, they put forward that MNPs with slower dynamics should be considered as a new class of MRI contrast agents with exceptionally high low-field relaxivity. Such contrast agents would attractive for the expanding field of ultra-low-field MRI (ULF-MRI) which promises the potential of conventional MRI images without the cost, size, and hazards of much larger MRI machines.[87,88] From the examples discussed in this section there is a growing understanding of the behaviour or more complex magnetic nanocomposites, with the eventual goal of being able to guide the design of contrast agents with unmatched low-field relaxivities. However, there are still gaps to be filled before this is achievable, especially when understanding how behaviour may change when administered *in vivo*.

1.6 Synthesis of Magnetic Nanoparticles

The last decade has seen considerable advances in the synthesis of magnetic nanoparticles (MNPs) for their use in biomedical applications. When designing a synthetic protocol, the final use must be considered with bio-applications in particular facing a number of restrictions due to the unique environment the particles must act in. Most importantly toxicity of any formed MNPs must be considered, though bio-compatibility can be enhanced through the introduction of bio-compatible coatings. These coatings are discussed in Section 1.7.3.

The core size of the particle and the resulting surface area to volume ratio must also be considered due to competing exchange interactions in an incomplete co-ordination shell of surface cations.[89] This in turn can lead to disordered spin configuration at the surface of the particle

and a reduced average net magnetic moment relative to particles with small surface area to volume ratios.[90–93] Dipolar interactions between MNPs also require consideration when preparing MNP aggregates or nanocomposites. See Section 1.8.

The focus of the section is chemical synthetic routes in either aqueous or organic phases though other methods such as gas phase deposition, electron beam lithography, and mechanochemical synthetic methods. All of which have been used to prepare high quality, monodisperse MNPs. However, solution routes are the most used due to control over size and shape being much easier to achieve. The seminal paper published by Lamer and Dinegar on the preparation of monodisperse sulfur hydrosols first established a general mechanism for the formation of monodisperse particles.[94] Since, most solution routes have sought a similar mechanism involving a nucleation in a single event followed by further growth *via* the addition to the nuclei formed. The aggregation of primary nuclei may also play an important role in the morphology.

1.6.1 Aqueous Co-Precipitation

Aqueous co-precipitation is perhaps the most used synthetic route due to its simplicity, cost effectiveness, and use of mild conditions without the need for organic solvents. For this approach, Fe(II) and Fe(III) precursors (usually in the form of metal chlorides, sulfates, or nitrates) are dissolved in a 1:2 ratio followed by the addition of a base catalyst to initiate the precipitation of inverse spinel iron oxide. These reactions can be carried out at room temperature or with mild heating and usually under an inter atmosphere. This methodology was first demonstrated by Massart in 1981.[95]

$$\mathrm{M^{2+}} + 2\,\mathrm{OH^-} \longrightarrow \mathrm{M(OH)_2}$$
$$2\,\mathrm{Fe^{3+}} + 6\,\mathrm{OH^-} \longrightarrow 2\,\mathrm{Fe(OH)_3}$$
$$\mathrm{M(OH)_2} + 2\,\mathrm{Fe(OH)_3} \longrightarrow \mathrm{MFe_2O_4} + 6\,\mathrm{H_2O}$$

Scheme 1.1: Reaction scheme for the co-precipitation preparation of ferrite nanoparticles, M = Fe^{2+}, Mn^{2+}, or Co^{2+}.

Through changing the pH, stirring rate, and the addition of a surfactant, the size of the resulting particles can be manipulated. Vayssieres *et al.*, could tailor the size of magnetite nanoparticles between the range 1.5 – 12.5 nm through controlling the pH and the ionic strength

via a non-complexing salt. It was shown that the greater both the pH and ionic strength the smaller the particles produced.[96] More recently, further control of the size of iron oxide nanoparticles by Salazar *et al.*. They successfully produced iron oxide nanoparticles in the 10 – 40 nm range through altering the aliphatic chain length of the ammonium R_4NOH (R = methyl, ethyl, propyl) base. An inverse relationship between the length of the chain and the size of the nanoparticle produced was observed. This was attributed to an increased adsorption energy on the surface of the particle for larger molecules. Improved control was shown possible with the use of alkanolamines, isopropanolamine and diisopropanolamine as alkaline agents. When compared to the use of NaOH they presented particles up to 6 times smaller as well as having enhanced magnetic properties.[97]

Much work has also been carried out on co-precipitation based synthesis in the presence of various biomolecules. The purpose of which is to act as effective stabilisers whilst ensuring no unwanted side effects when it comes to the MNPs being used clinically. An excellent example of such work was carried out by Byrne *et al.*, in which denatured herring sperm DNA was combined with the co-precipitation of ferric and ferrous chloride salts to form a stable aqueous suspension of superparamagnetic iron oxide NPs.[83] This is also an example of a 1D nanostructure, where the IONPs are ordered in long linear arrays. These are be explored further in a later section. Similarly, the naturally occurring anti-coagulant heparin was used to prepare stabilised Fe_3O_4 nanoparticles using an *in situ* co-precipitation technique.[98] The co-precipitation route has also been demonstrated as adequate to produce elongated rod-like nanostructures. This is achieved through the heating of iron oxyhydroxides such as goethite or akageneite in a reducing atmosphere, appropriate protection of the particles using an inorganic coating is required to prevent sintering. An iron oxyhydroxide is selected as they show a preference for the orientation that they grow, leading to formation of the rod-like shapes.[99,100]

1.6.2 Solvothermal & Thermal Decomposition

There has been a growing shift away from aqueous methods to using organic solvent heated to high temperatures (120 – 350 °C) as this can often result in MNPs with high crystallinity and monodispersity. As the magnetic properties of IONPs are closely linked to the shape and size of the particle the advantages of such control are obvious. As with the aqueous co-precipitation the formation of MNPs occurs through an initial fast nucleation followed by rapid growth associated with the addition of monomers at concentrations well below the critical nucleation concentration. The presence of organic co-ordinating ligands results in the formation

of monodisperse nanosized particles with passivated surfaces.

Thermal decomposition routes are based on the decomposition of organo-iron complexes in organic solvents with surfactants such as oleic acid and hexadecylamine present. By controlling the Fe to surfactant ratio as well as the solvent used it is possible to tune the size and morphology of the nanoparticle. An early example which successfully demonstrated the formation of monodisperse iron oxide nanoparticles using thermal decomposition was carried out by Hyeon *et al.*[101] The group produced highly crystalline monodisperse maghemite nanocrystals with diameters < 14 nm, through high temperature (300 °C) ageing of iron-oleic acid complex followed by a subsequent oxidation step to give γ–Fe_2O_3 nanoparticles. A similar methodology was then utilised for the synthesis of magnetite nanoparticles < 20 nm in diameter, in which $Fe(acac)_3$, oleic acid, oleyamine were reacted at high temperature in the presence of alcohol.[102]

Solvothermal routes using $Fe(acac)_3$ as the precursor and oleic acid, oleyamine, and tri-n-octylphosphine oxide (TOPO) as surfactants to produce monodisperse Fe_3O_4 nanoparticles can provide excellent control over an MNPs size distribution.[103] A range of sizes between 5 – 12 nm can be achieved through adjusting the reaction time, temperature, and surfactants. As a result of using organic solvents and capping agents the final product will be hydrophobic particles that need to be transferred to an aqueous media before use in biomedical applications. This is usually done through a ligand exchange reaction using dimercaptosuccinic acid (DMSA). Interestingly, a hydrothermal route has also been demonstrated for the synthesis of magnetite nanoparticles, using $FeCl_3$ and sucrose as the precursors. The sucrose acted as both the reducing agent and also the source for the coating agents.[104] By adjusting the initial concentration of sucrose, the particle diameter could easily be controlled from 4 – 16 nm.

An adaption of this methodology is carrying out the thermal decomposition of iron precursors in polyol solvent, a high boiling multivalent alcohol such as polyethylene glycol and its derivatives. The polyol acts as the solvent, the surfactant, as well as the reducing agent. An early example of synthesising magnetite nanoparticles *via* the polyol method, was carried out by Wan *et al.* The synthesis was carried out using $Fe(acac)_3$ as the iron precursor in a polyol medium of triethylene glycol (TREG) and produced particles with diameters of approximately 8 nm.[105] The importance of the chosen polyol was investigated by the Gu group, which synthesized magnetic iron oxide nanoparticle (IONP) clusters using two types of polyols with different reductive abilities. Use of ethylene glycol as a solvent resulted in the IONPs forming compact clusters of approximately 300 nm in size, whilst use of 1,2-propylene glycol resulted in smaller clusters of around 50 nm.[106]

1.6.3 Microemulsion & Sol-gel

A microemulsion is defined as a thermodynamically stable, isotropic dispersion of oil, water, and surfactant(s). Within a water-in-oil microemulsion (reverse microemulsion), the aqueous phase is dispersed as microdroplets, encapsulated by a monolayer of surfactant. The surfactant-stabilized microcavities of reverse microemulsions (approximately 10 nm) provide confinement that limits particle nucleation, growth, and agglomeration.[107,108] One of the advantages of using reverse microemulsions for the preparation of MNPs is that the morphology and size can be tuned by changing the surfactant, oil phase, water content and reaction conditions.[109,110]

Sol-gel is a commonly used method for synthesising various metal oxides. It typically requires a colloidal solution that acts as the precursor for a network of particles. The sol is a stable dispersion of colloidal particles in a solvent. For the synthesis of IONPs the precursor used is usually iron alkoxides or iron chlorides, which undergo various hydrolysis and polycondensation reactions, the sol particles subsequently interact through weak intermolecular forces (Van der Waals or hydrogen bonds) and begins to evolve towards the formation of an inorganic continuous network containing a liquid phase, or gel. Following the drying process, a thermal treatment is typically required to achieve the final crystalline state. The final properties of the IONPs are correlated to the structures formed during the initial sol stage of the synthesis. Lemine *et al.* successfully prepared magnetite nanoparticles using a sol-gel method under supercritical conditions of ethyl alcohol, in which the water necessary for hydrolysis was slowly released *via* an esterification reaction. This controlled release of water allowed control over the size of nanoparticles formed, resulting in monodisperse particles with a diameter of approximately 6 nm.[111]

1.7 Tuning MRI Behaviour of Magnetic Nanoparticles

1.7.1 Doping of Iron Oxide Nanoparticles

As described in Section 1.2.1 magnetite and maghemite both adopt an inverse spinel crystal structure. By substituting the non-AF coupled Fe^{2+} cation situated at the O_h with a different 2+ metal cation the magnetic moment can be increased from the 4 μ_B. This in turn can lead to changes in the size and gradient of the inhomogeneous field produced by the particle when exposed to an external magnetic field.

Perhaps the most obvious choice for a dopant is Mn^{2+}, as $MnFe_2O_4$ has an increased mag-

netic moment of 5 μ_B. Therefore, this in theory should result in improved MRI performance. The impact of doping IONPs with other transition metals with respect to MRI performance was first investigated by Cheon *et al.*[112] For this ground-breaking study the metal oxide nanoparticles, $MnFe_2O_4$, $CoFe_2O_4$, $NiFe_2O_4$, and Fe_3O_4 were prepared using a thermal decomposition technique, with the relevant divalent metal chloride used for the respective ferrite. The 4 nanomaterials were initially characterised with a SQUID magnetometer and the mass magnetisation of $MnFe_2O_4$, $CoFe_2O_4$, $NiFe_2O_4$, and Fe_3O_4 nanoparticles were measured to be 110, 99, 85, and 101 emu g^{-1} respectively. The measured M_s of the 4 ferrites also correlated with the r_2 relaxivities, with $MnFe_2O_4$ measuring the highest and $NiFe_2O_4$ measuring the lowest.

The potential of manganese ferrite nanoparticles (MnIONPs) as highly effective MRI contrast agents was further investigated by Yang *et al.*[113] Superparamagnetic manganese ferrite nanoparticles were synthesised *via* a thermal decomposition method. The particles formed were measured to be 7 nm in diameter with a narrow size distribution. The saturated magnetisation was measured to be 39 emu g^{-1} and the transverse relaxivity was measured to be 189 $mM^{-1}s^{-1}$. To compare the r_2 value obtained for the 6 nm MnIONPs produced by Cheon *et al* was 208 $mM^{-1}s^{-1}$. The manganese ferrite particles allowed for the *in vitro* T_2-weighted MR imaging of a mouse liver.

The work mentioned so far in this section only covers MnIONPs containing stoichiometric quantities of Mn. However, more recently novel synthetic techniques have allowed for the production of MnIONPs with non-stoichiometric quantities. Varma *et al.*, successfully demonstrated a novel synthetic method for preparing Mn^{2+} substituted superparamagnetic IONPs via an aqueous co-precipitation route.[114] By varying the molar ratio of Mn^{2+}: Fe^{2+}, nanoparticles of $Mn_xFe_{3-x}O_4$, where $x = 0$, 0.25, 0.50, and 0.75 were synthesised. The transverse relaxivities of the MNIO25, MnIO50, and MnIO75 nanoparticles were measured to be 236.6, 203.9, and 202.1 $mM^{-1}s^{-1}$. Note that the value for MnIO25 is greater than those reported above for stoichiometric manganese ferrite. The diameters of the different MnIONPs were measured to be 8.6, 8.1, and 9.7 nm. No *in vitro* or *in vivo* MR imaging experiments were carried out, but the potential for T2 weighted MR imaging was demonstrated within tissue phantoms.

The mechanism by which the introduction of Mn^{2+} cations in non-stoichiometric quantities to the spinel type structure of magnetite was further investigated the Gao group. The non-stoichiometric MnIONPs were synthesised using a one-pot thermal decomposition method, in which the ratio of iron oleate and manganese oleate was adjusted to control the Mn content ($x = 0$ – 1.06).[115] As with the previous study the T_2 relaxivities for all particles was measured

and compared. The obtained results showed the r_2 values initially rose with increasing Mn content up to $x = 0.43$, which gave a very high value of 904.4 $mM^{-1}s^{-1}$, before sharply decreasing upon any further increase in Mn. The MnIO43 nanoparticles were subsequently selected for *in vivo* imaging a mouse liver, and compared to IONPs and MnIONPs with $x = 1.06$. The signal to noise ratio was enhanced almost 3-fold when compared to the magnetite particles and almost 10-fold when compared to higher Mn content. The reason for this observed trend was posited to be due to the resulting lattice distortion upon doping. This was observed through XRD and showed the change in crystal structure becoming more significant as the Mn doping level rises. These lattice distortions may subsequently interrupt the magnetic dipolar coupling, resulting in lower saturation magnetization.

Like manganese, cobalt cations may also be substituted within the spinel type structure of magnetite. Cobalt ferrite ($CoFe_2O_4$) nanomaterials have already been shown to be promising for different biomedical applications, this is part due to their excellent chemical stability, high magnetocrystalline anisotropy and coercivity. It is important to note however, that the free ion Co^{2+} is acutely toxic in high doses, where it can accumulate in the liver, kidneys, pancreas, and heart.[116] It is therefore of great importance to ensure a biocompatible coating is used in order to prevent leaching (coatings of magnetic nanoparticles is discussed in Section 1.7.3.

One of the first to examine the MRI response of cobalt ferrites was Dravid *et al.* The group synthesised cobalt ferrite magnetic nanostructures using a high temperature solution phase method, to give insight into the effects of shape; spherical nanoparticles were synthesized with the help of seed mediated growth, whilst faceted irregular $CoFe_2O_4$ NPs were synthesized in the presence of a magnetic field.[117] The spherical NPs were produced at sizes of 6, 10, and 15 nm, while the faceted NPs had sizes of 12 and 25 nm. The results showed that both the magnetization and relaxivity was proportional to size. For the spherical particles r_2 increased from 110 $mM^{-1}s^{-1}$ (6 nm) to 301 $mM^{-1}s^{-1}$ (15 nm) and from 155 $mM^{-1}s^{-1}$ to 345 $mM^{-1}s^{-1}$ for the faceted structures. Comparison between the two types of NP showed that though the 25 nm gave the greatest r_2 value it did not give the greatest magnetisation value. The largest being produced by the 15 nm spherical NPs (64.2 emu g^{-1} vs. 59.4 emu g^{-1}). The increased relaxation may be attributed to the faceted NPs having a greater surface-to-volume ratio and a greater number of water hydrogen nuclei in proximity. Therefore, a greater number of nuclei will be simultaneously interacting with the magnetic field, resulting in faster relaxation. For further discussion of the impact of nanoparticle morphology on MRI contrast behaviour see Section 1.7.2.

Bovine serum albumin (BSA) based nanocarriers containing cobalt ferrite nanoparticles were later prepared for MRI diagnosis and hyperthermic therapy. The 6.7 nm $CoFe_2O_4$ NPs were synthesised using a polyol method. The NPs were stabilized by capping the surface with a hydroxamic acid before coating with PLGA and BSA. Following initial relaxometry experiments, MRI experiments on vials at low field (0.2 T) confirmed better negative contrast than the commercial agent Endorem.[118] *In vivo* images of the liver of normal rats, at different times from the injection of BSA-$CoFe_2O_4$ and/or Endorem were collected, with both showing similar efficiency in contrasting images of the liver.

As with manganese ferrites, non-stoichiometric cobalt ferrites have also been produced and examined as potential MRI contrast agents. The Pellegrino group synthesised cobalt ferrite nanocubes with the composition $Co_xFe_{3-x}O_4$, where x = 0.1, 0.4, 0.5, 0.6, 0.8, and 1.0 *via* thermal decomposition.[119] With an average cube edge length of 20 nm, these particles exhibited excellent relaxation properties, the highest r_2 value of 958 $mM^{-1}s^{-1}$ was recorded on nanocubes with x -values of 0.5 (at field strength of 0.5 T). This value far exceeds the values obtained for the other 3 compositions, which were all measured to be around 600 $mM^{-1}s^{-1}$, with a slight increase with increasing x-values. The reason as to why x = 0.5, gave such a dramatically increased r_2 value was due to having a core-shell composition, with a Fe rich centre and Co rich edges, in comparison to a more homogeneous distribution of Fe and Co. It was also posited that as x = 0.5 gave the least concave shaped cubes, the differing shape have contributed to the increase in relaxivity. This work also investigated in great detail the potential for these nanocubes to have use not only as MRI contrast agents but as hyperthermic therapeutic agents. The use of IONPs and their derivatives for localised hyperthermia is not covered in this thesis. However, as mentioned prior, cobalt ferrites have much higher magnetocrystalline anisotropy almost one order of magnitude greater than that of magnetite and is responsible for the large coercivity of cobalt ferrite.[120] Large coercivity is desirable for heating purposes but less so however for MRI contrast, due to the likelihood of increased aggregation.

1.7.2 Morphology Effects on MRI Contrast

As discussed in the previous section, the impact of the shape of the cobalt nanocubes is highlighted as being an important factor in the observed relaxivity trends. The work of Dravid *et al.*, compared the properties of faceted *vs* spherical cobalt ferrite nanoparticles, with the comparably sized 12 nm faceted particles measured to have the greater r_2 value of 345.2 $mM^{-1}s^{-1}$, whilst the 15 nm spherical particles were measured to have an r_2 value of 301 $mM^{-1}s^{-1}$.[117]

The reasoning behind such an observation was attributed to the faceted morphology having a greater number of sharp edges and corners, resulting in pseudo-magnetic charges on the particle surface, this in turn result in a higher gradient of magnetic field in these regions and therefore shortening relaxation times of water protons.

Beyond faceted particles and nanocubes, cobalt ferrite has also been used in the synthesis of so called "nanoflowers" (CFNF's). Synthesised in the presence of the surfactant CTAB which acted to direct the structure, the cobalt ferrite was found to assemble into a cluster, which multiple 'petal' shape gives the flower name.[121] When compared with spherical cobalt ferrite nanoparticles (CFNP's) as a contrast agent for MRI using an aqueous phantom assay, the CFNF's were shown to produce better T_2 weighted contrast than the CFNP's. This is was backed up by the CFNF's having a r_2 value of 101.4 $mM^{-1}s^{-1}$ compared to only 10.4 $mM^{-1}s^{-1}$ for CF spheres. The reasoning for such an improvement was attributed to two factors. The first being the increased surface-to-volume ration of the CFNF's, meaning a better exchange of water between the nanoparticles within the assembly and on the surface. The second is that due to the shape of the CFNF, the tumbling motion is constrained relative to that of the free particle.

It is not only cobalt ferrite that has been used to create nanostructures that adopt differing morphologies, work has been carried out on manipulating the synthesis of iron oxide nanoparticles to create novel shaped nanostructures.[47,122,123] An excellent example of this is the work carried out by Gao *et al.*, who were able to fabricate size-controllable octapod IONPs. These uniquely shaped IONPs were synthesised by introducing chloride anions to a conventional thermal decomposition route. By altering the quantity of NaCl added they were able to produced octapods of 20 and 30 nm in edge length.[124] The octapod IONPs exhibited high transverse relaxivity relative to spherical IONPs. 30 nm octapods (Octapod-30) were measured to have the greatest r_2 value of 679.3 $mM^{-1}s^{-1}$ compared to only 125 $mM^{-1}s^{-1}$ for 16 nm spherical NPs (Spherical-16). To show that this translated into better contrast for MR imaging *in vivo*, T2-weighted MRI of the liver was conducted using a mouse model. Both Octapod-30 and Spherical-16 were injected intravenously at relevant concentrations, Octapod-30 demonstrated a much higher contrast than Spherical-16. This improved performance was attributed to the strong inhomogeneity of local magnetic fields caused by the unique shape of the octapod. This was confirmed using the Landau-Lifshitz-Gilbert equation. Further unique morphologies were successfully synthesised by the Gao group *via* the thermal decomposition of iron oleate (FeOL) in the presence of sodium oleate (NaOL). They found using 1-octadecene as the solvent, NaOL

would preferentially bind to Fe_3O_4 {111} facets resulting in the formation of superparamagnetic magnetite nanoplates with {111} exposed facets, as well as truncated octahedrons, and tetrahedrons. However using a high-boiling temperature tri-n-octylamine (TOA) solvent afforded Fe_3O_4 {100} facet exposed cubes, concaves, multibranches and assembled structures, all by varying the molar ratios of FeOL and NaOL.[125] The anisotropic shape of these novel structures as a whole resulted in stronger T_2 relaxation effects, though it was the more regular shaped nanocube with side length of 21 nm that produced the greatest r_2 value of 298.02 $mM^{-1}s^{-1}$, this was followed by the octahedron and concave which measured values of 239.2 $mM^{-1}s^{-1}$ and 224.37 $mM^{-1}s^{-1}$ respectively. These three best performing nanostructures all out performed IO spheres with a diameter of 16 nm (r_2 = 125.7 $mM^{-1}s^{-1}$). The reasoning for the observed trend was attributed to the increased effective radii when compared to spheres of similar volume.

1.7.3 Surface Functionalisation of Magnetic Nanoparticles

When designing a functional MNP for *in vivo* applications functionalising the surface of the particle is often required to improve its effectiveness. Primarily, a coating is required to enhance the colloidal stability of the MNP. Particles below the superparamagnetic limit will not experience magnetically induced aggregation but will still agglomerate because of the high surface-to-volume ratios yielding high surface energies. Therefore, surface modification will be required to provide a reduction in surface energy, as well as either steric and/or electrostatic repulsion. As mentioned in the previous section particles synthesised in hydrophobic environments required a surface ligand exchange so that they are dispersible in aqueous media.

Preventing aggregation (and maintaining a low hydrodynamic diameter) is one of the most pertinent problems to solve when designing MNPs for bio-applications. In part due to most endothelial barriers being permeable to nanoparticles/aggregates smaller than 150 nm.[126] An MNP must also evade the reticuloendothelial system (RES) upon entering the bloodstream where they will be subject to protein absorption (opsonisation) before eventual clearance from the body. Avoiding RES uptake will increase the blood-half life of the MNP, allowing a greater % of the particles injected to reach their desired site to carry out their designed function. Formation of larger aggregates has been demonstrated to have a negative effect on a MNPs blood half-life.[127] Polyethylene glycol (PEG) in particular has shown to be very effective at preventing this, by creating a 'cloud' of hydrophilic and neutral chains at the particle surface, the blood proteins are then unable to adsorb to the particle surface.[128]

The addition of a coating may also improve the biocompatibility and reduce the cytotoxicity of non-coated MNPs. An example where iron oxide nanoparticles were coated in either PEG or dextran before examining their uptake and cytotoxicity on porcine aortic endothelial cells showed that the uncoated NP's induced a 6 fold increase in cell death at the highest concentration whereas cell viability was constant for the coated particles.[129]

The addition of a functional group onto the surface of an MNP may also provide the particle with increased/extra functionality. This maybe through the addition of certain bioactive molecules or targeting ligands to increase to accumulation of particles within diseased tissues. These strategies are based on the targeting of unique molecular signatures of afflicted cells, such as over-expressed growth factors and nutrient receptors.[130–132] Coatings can also be added to add extra functionalities such as complementary imaging modalities or therapeutic drugs.[133–137] Because of this MNPs make for excellent platforms for the creation of multimodal/theranostic agents. As such a wide range of coatings/functional groups have been demonstrated, in this section they are separated into 3 groups: small molecular stabilisers (carboxylic acids, phosphonates, etc), organic coatings (polymers, biomolecules, lipids, etc), and inorganic shells (metals and metal oxides). Whilst for the purpose of this thesis they have been separated there are often overlaps between the 3 approaches.

Small-Molecule Stabilisers

One of the more facile techniques for the coating of MNPs is the adsorption of organic monomers bearing functional groups like carboxylate, phosphate, or sulfate. The addition of these hydrophilic negatively charged functional groups will increase the hydrophilicity of the MNP as well as provide increased stabilisation through electrostatic repulsion. Therefore, reducing the likelihood of aggregation.

Carboxylates are the most common functional group due to its strong affinity for the Fe(III) ions on the particle, trisodium citrate is particularly popular due to its 3 carboxylate groups. It can be introduced as part of a solvothermal protocol where $FeCl_3$ is reduced at 200 °C with ethylene glycol (EG) and sodium acetate. The EG acts as both the solvent and reductant, and the citrate is then a biocompatible electrostatic stabiliser present on the surface of the resulting particle.[138] The strong affinity of the carboxylate groups means that the surface modification can also be carried out easily post-synthesis by dispersing the particles in citrate solution. A benefit of using trisodium citrate is that is widely used in food and drug industry and citric acid is one of products from the tricarboxylic acid cycle (TAC), a normal metabolic process in

human body.

Other common carboxylates include DMSA and folic acid; as mentioned in the previous section DMSA is commonly used for converting hydrophobic nanoparticles produced by thermal decomposition methods by displacing the surfactant (oleic acid) courtesy of the high coordinative ability of the first acid group whilst the second provides a negatively charged group for electrostatic repulsion and increased hydrophilicity.[139,140]

Organic Coatings

Perhaps one of the most common and effective forms of surface functionalisation for MNPs is the anchoring of polymers to the particles surface. A wide range have already been detailed in the literature including synthetic polymers polyethylene glycol (PEG), polyvinyl alcohol (PVA), poly(NIPAAM), and polyethylene imine (PEI), as well as bio-polymers such as alginate, chitosan, heparin, and DNA.[26,83,98,141–143] The addition of a polymer/biopolymer to the surface of an MNP will provide increased steric repulsion between neighbouring particles and therefore maintain good colloidal stability. The polymers also need to have a hydrophilic exterior (a hydrophobic interior may be beneficial for anchoring to the MNP surface) to provide water solubility. The polymer chains may also be charged conferring extra electrostatic stabilisation of the particle. An MNP may be coated by a polymer through hydrogen bonds, electrostatic forces, or pseudo-covalent interactions.[144]

Of the mentioned polymers, PEG is by far the most used, not only for the coating of MNPs, but for biomedical nanoparticles as a whole. This is due to its biocompatibility and impressive steric stabilisation properties that also supports resistance to protein adsorption and helps the nanoparticles to improve their circulation lifetime and to decrease the reticuloendothelial clearance rate.[145,146] A wide range of approaches for the functionalisation of MNPs with PEG have been described including polymerisation on the particle surface, silane grafting onto oxide surfaces, modification of sol-gel approach, and ligand exchange.[147–151] Biopolymers are also appealing for functionalising MNP surfaces due to their innate biocompatibility, the most common of which is the polysaccharide dextran.[68] An excellent example of how a surface coating can affect the material properties of an MNP was shown by Paul *et al.*, where reducing the terminal sugar had a significant effect on particle size, coating stability, and magnetic properties.[152]

An organic MNP functional group does not only have to be a polymer chain anchored to the surface, alternatively it is possible to form a polymer shell that encases the MNP. These polymeric shells provide functional groups such as terminal amine or carboxylates from which addi-

tional bioactive molecules, targeting ligands, drugs, or fluorophores can be conjugated.[9,153–156]

When choosing a coating for a potential MRI contrast agent it is important to understand the impact it may have on the relaxometric properties of the magnetic nanoparticle.As one of the most popular choice of coatings, work has been carried out to optimise the performance of PEGylated IONPs. Bao *et al.* examined the effect of PEG size on the measured relaxivity.[145] They examined IONPs with two core sizes (5 and 14 nm) and five PEG chain lengths (with molecular weights of 550, 750, 1000, 2000, and 5000 Da). The measured transverse relaxivity of an IONP with core size of 14 nm increased with increasing chain length up to 1000 Da which gave a peak r_2 value of 385 $mM^{-1}s^{-1}$ at 0.47 T. Chains of 2000 and 5000 Da however, resulted in a dramatic decrease in relaxation performance giving r_2 values of approximately 150 $mM^{-1}s^{-1}$. The reasoning for such a trend is that at larger chain lengths, H_2O molecules are kept at a too great distance from the magnetic core to interact with the inhomogeneous magnetic field produced by the core.

Beyond considering chain length it is also important to consider the co-ordination chemistry of any capping ligand(s). Polymers can bind to the iron oxide surface by hydrogen bonds, electrostatic interactions or covalent bonds. It was shown by Daou *et al.* that coupling the chosen coating to the surface *via* carboxylate bonds results in spin canting and thus a decrease of the net magnetization whereas no canting is observed in the case of phosphonates, which preserved the magnetic properties of the IONPs. This could be seen in the measured magnetisation for the carboxylate and phosphonate IONPs which were found to be 72 and 83 emu g^{-1} respectively.[157] A phosphonate anchor was used for the covalent attachment of hydrophilic PEGlyated dendrons to the surface of IONPs by Felder-Felsch *et al.*[158] The choice of dendritic molecules is that as discrete, monodisperse entities their characteristics can be tuned as a function of their generation. Phosphonate coupling agents not only help maintain the magnetic properties of the IONPs but allow for higher grafting rate and stronger binding than carboxylate anchors.[159] The r_2 values for the dendronized IONPs were measured at 1.5 T and were found to be 349 $mM^{-1}s^{-1}$, more than 1.5 times greater than what was measured for Endorem, dextran-coated IONPs (144 $mM^{-1}s^{-1}$). This work was further expanded on by the Felder-Flesch group, as the aforementioned dendronized IONPs formed *via* co-precipitation (NPcop) were compared with dendronized IONPs formed by thermal decomposition (NPtd). The NPcop's demonstrated greater r_2 relaxivity (272 $mM^{-1}s^{-1}$ and 130 $mM^{-1}s^{-1}$ respectively) and improved *in vitro* contrast compared to the NPtd samples. However, the reverse was true for *in vivo* performance with the NPtd's giving the best contrast.[160] This was attributed to greater aggregation of the

dendronized NPcop's.

When considering a coating for IONPs as MRI contrast agents it is important to also note the differences in hydrophilicity as it will determine the levels of hydration around the magnetic core and therefore the proton relaxivity. For example using the hydrophilic molecule polyethyenimine (PEI) as capping ligands rather than the more hydrophobic copolymer poly(maleic acid) and octadecene (PMO) gave an almost 3-fold increase the r_2 values measured for 10 nm IONPs (r_2 = 75.2 and 27.2 $mM^{-1}s^{-1}$ respectively).[161]

Inorganic Shells

Whilst not offering the same enhancements in colloidal stability or RES evasion, inorganic coatings/shells provide platforms for further functionalisation as well as the addition of new properties resulting from the shell material. A hard shell surrounding the MNP will also prevent oxidation of the particle surface which can lead to a change in magnetic behaviour.[14,162] One such coating is SiO_2, which when combined with the surface-reactive groups such as APTES (3-aminopropyltriethoxysilane) allows for colloidal stability as well as a platform for the design of multifunctional nanoparticles.[39,163]The key advantage of a silica shell is its stability in aqueous conditions, biocompatibility (SiO_2 particles are used for a wide-range of biomedical purposes), and ease of functionalisation. Additional functional groups include targeting ligands, fluorophores, and polymers for increased colloidal stability/biocompatibility.[164–166] The use of silica also allows for the formation of a porous shell which can be used for drug delivery.[166] The formation of a silica shell is usually carried out *via* two different methods. The sol-gel whereby hydrophilic particles (often citrate stabilised) are coated through an adapted Stöber synthesis, with the addition of a surfactant such as cetrimonium bromide (CTAB) will result in mesoporous silica.[167,168] The alternative is a reverse microemulsion which usually provides much greater control over the morphology and dispersity of the final product and uses hydrophobic MNPs.[108,169]

In Section 1.1 the unique optical properties of gold nanoparticles have already been discussed. By combining these with the magnetic properties of MNPs, it is possible to create biocompatible multifunctional nanomaterials that may consist of MNPs decorated with Au NPs on the surface or the formation of core-shell structures.[170–172] However due to the chemical inertness of gold some difficulty can be experienced when attempting to form a shell.[173] A gold surface can also be functionalised further due to its strong affinity for thiol groups.[174,175] An example of such a material are the hyaluronic acid-modified Fe_3O_4@Au core/shell nanostars

produced by Li *et al.* Here a star-shaped shell was formed around a magnetite core with the further functionalisation with hyaluronic acid to provide colloidal stability, biocompatibility, and cancer cell targetting.[176] The core shell particles were then demonstrated as nanoprobes for efficient MR and CT imaging as well as showing utility for the photothermal ablation of cancer cells.

Beyond more conventional magnetic nanoparticle (MNP) coatings such as polymers and silica, there is a growing interest in the production of bi-magnetic core-shell particles. Whereby, both the core and shell exhibit some form of magnetic behaviour (antiferromagnetic, ferromagnetic, or ferrimagnetic). In such systems, strong exchange coupling between the core and shell can occur resulting in unique magnetic properties that can be controlled *via* changes in composition and size/thickness of the core and shell.[177] Recently work has been carried out investigating the coupling interactions between 'hard' and 'soft' FM and FiM phases, with research directed towards potential biomedical applications, such as magnetic hyperthermia and MRI contrast. A 'hard' phase is defined as having large magnetic anisotropy (expressed in terms of anisotropy constant, K) and moderate saturation magnetisation (M_S), while 'soft' phases present low K and large M_s. $CoFe_2O_4$, FePt, and CoPt are examples of the former, whilst Fe_3O_4, Fe, $MnFe_2O_4$ are examples of the latter.[178,179]

An example of an exchange coupled hard–soft spinel ferrite-based core–shell nanoparticle was produced by Angotzi *et al.*, where a hard $CoFe_2O_4$ core was coated in soft shells of either γ-Fe_2O_3/Fe_3O_4 or $MnFe_2O_4$.[180] The magnetic properties of the bi-magnetic core-shells were characterised, showing increased M_s and decreased coercivity (H_c) compared to the core alone. This work then demonstrated the potential of the bi-magnetic core-shells for potential magnetic hyperthermia applications, with the spinel iron oxide coated particles showing high heat release that was proportional to the thickness of the shell. The hyperthermia properties of bi-magnetic core-shells have been well documented in the literature with many other examples showing strong heating power.[177,181–183]

Bi-magnetic core-shell particles are typically prepared via a seeded growth method. This is a two step process where pre-made MNPs are used for the subsequent deposition of the magnetic shell.[182,184–186] Most commonly a thermal decomposition or solvothermal procedure is used, which as with the preparation of MNPs affords high crystallinity and control over morphology but does require high temperatures, organic solvents, and post-processing steps for water solubility. Interestingly, high temperatures used can have a detrimental effect on the core particles such as reduced saturation magnetisation (M_s).[181] As nanosized materials

are dynamic entities when in solution, the high temperatures can result in dissolution and recrystallisation by the Otswald ripening process.[187] This dissolution phenomena has been reported for ferrite cores composed of $MnFe_2O_4$ and $ZnFe_2O_4$.[181] Alternatively, fewer examples have been presented where bi-magnetic core-shells have been prepared at much milder conditions using a co-precipitation approach.[188–190] This is due primarily to difficulties in controlling shell growth.

According to outer-sphere theory (see Introduction Section 1.4), the transverse relaxivity of an MNP is proportional to both its M_s and radius (r), both of which increase for bi-magnetic core-shell particles.[65,66] Importantly, this increase does not coincide with an increase in H_c, therefore avoiding possible magnetic aggregation issues and therefore an advantage to merely increasing the core diameter of an MNP. Therefore, bi-magnetic core-shells have potential as strong negative MRI contrast agents. The first example of their capabilities was shown for elemental Fe cores coated in various ferrites (Mn,Co, and Fe), with the bi-magnetic core-shell particles measuring increased r_2 values compared to similarly sized ferrite nanoparticles (as modelled with outer-sphere theory), with $Fe@MnFe_2O_4$ measuring the highest at 430 $s^{-1}mM^{-1}$ (measured at 0.47 T).[191] The increased relaxivity was attributed to the measured increase in M_s for the bi-magnetic samples. Similarly, $Zn_{0.5}Mn_{0.5}Fe_2O_4@Fe_3O_4$ core-shell particles were shown to have increased transverse relaxivities compared to the cores alone (core-shell = 386.6 $s^{-1}mM^{-1}$ and core = 262.6 $s^{-1}mM^{-1}$, at 1.5 T) again as a result of increased M_s values.[188] This increase in r_2 was dependent however on the synthetic approach used, with small changes resulting in the formation of what was described as a 'magnetic dead layer', reducing the M_s and r_2 of the resulting core-shell nanoparticles.

Whilst inorganic coatings are less common than those based on hydro-/amphiphilic polymers, other examples include coating of graphite, gadolinium oxide, and even other ferrites.[192–195]. This difference in popularity is likely due to the relative ease at which polymers can be adhered to the surface as well as hard coatings often requiring further functionalisation for colloidal stability or biocompatibility.

1.8 Multi-Core Assemblies of Magnetic Nanoparticles

When superparamagnetic nanoparticles are brought into proximity to one another they will interact beyond typical forces that are experienced by other colloids (hydrogen bonding, Van der Waals, electrostatic *etc*) due to their magnetic properties. Depending on the distance

between the magnetic cores these interactions will be either dipole-dipole or exchange interactions. Exchange interactions can occur over very short distances and are the coupling of magnetic moments of two neighbouring atoms.[196] This can lead to a continuation of the long range spin order across particles resulting in enhanced magnetic susceptibility whilst superparamagnetic behaviour is maintained.[197] Dipole-dipole interactions however can occur over longer distances, with the strength of the interaction increasing as the interparticle-distance decreases.[198,199] Such interactions can cause the alignment of magnetic moments between cores and thus increase the net magnetic moment.[200] These interactions between particle cores can therefore have considerable effects on the magnetic properties of multi-core assemblies when compared to single core alternatives. In particular, the performance of MNPs for magnetic hyperthermia and MRI contrast enhancement can be much improved.

As discussed earlier Section 1.5.2, though the maximum relaxation rates are achieved in the SDR, due to strong ferromagnetic dipolar interactions contrast agents are sized within the MAR. As a means of overcoming this and to further increase T_2 contrast magnetic nanoparticles have been assembled in to larger clusters. In doing so it is possible to increase m_s through combination of individual magnetic dipoles and as per outer-sphere theory achieve increased R_2. In an attempt to further understand the underlying mechanism of T_2 relaxation for the clustering of magnetic nanoparticles beyond what is described by conventional outer-sphere theory the Gao group used both theoretical simulation and practical experiments to show that magnetic field inhomogeneity (both gradient and symmetry) is the cause of T_2 relaxation enhancement for clusters of magnetic nanoparticles. They proposed that adjacent magnetic nanoparticles may generate higher degrees of local field complexity with reduced symmetry. Two sizes of IONPs were produced, 5.2 nm and 15.1 nm (IO-5 and IO-15). Clusters of only IO-5 (C1), IO-15 only (C2), and a 1:1 mix (C3) were produced using a tandem 'grafting to' and 'grafting from' reaction with PMMA and PEG.[201] The T_2 relaxivities of IONPs and clusters were measured and found that the r_2 increased from the single domain particle compared to the respective particle and that cluster C3 produced the highest r_2. Landau-Lifshitz-Gilbert (LLG) algorithms were used to calculate the stray field and stray field gradient induced by the MNPs and revealed that the coupling of proximal IONPs greatly enhances the local field inhomogeneity. C3 was modelled to possess the strongest stray field gradient, in agreement with the measured relaxivities. This result shows that nanoscopic magnetic field inhomogeneity plays an important role in T_2 relaxation. To further support this, the IO-15 particles in the 1:1 clusters were replaced with anisotropically shaped magnetic nanoparticles (cubes and plates)

giving rise to even larger T_2 enhancements.

When designing a multi-core magnetic assembly, the manner in which the cores are brought together must be finely controlled as there is a distinction between a multi-core assembly and simply uncontrolled aggregation, the latter will often be too large for biomedical purposes. It can be beneficial therefore to use a scaffold/template for the assembly of multiple MNPs. An example of such was demonstrated by Claesson *et al.*, who produced composites consisting of a silica core with many single-domain magnetic particles irreversibly attached using 3-mercaptopropyl(trimethoxy)silane. The size of core could be varied and therefore the dipole-dipole interactions between magnetic cores could be tuned.[202] Similarly, Lee *et al* describe the formation of 'core-satellite' nanoparticles which were fabricated using the conjugation of Rhodamine-dye-doped silica nanoparticles with amine functionalised surfaces with water soluble iron oxide nanoparticles (9 nm) using sulfosuccinimidyl-(4-N-maleimidomethyl)cyclohexane-1-carboxylate (sulfo-SMCC, Pierce) cross-linkers.[203] The hybrid nanoparticles were an approximate 45 nm in diameter and demonstrated a 3.4 fold increase in T_2 relaxivity (116 to 397 $mM^{-1}s^{-1}$) when compared to the free water soluble iron oxide nanoparticles. Also using this approach, a multifunctional MR imaging and drug delivery platform was formed by anchoring multiple iron oxide nanoparticles to the surface of a mesoporous dye-doped silica nanoparticle, the pores of which could be subsequently loaded with the anticancer drug doxorubicin (DOX).

Alternatively, rather than being attached to an internal scaffold, multiple magnetic cores may be encapsulated within a larger structure usually a polymeric micelle or polymersomes. This approach involves the spontaneous self-assembly of a polymer (or block-copolymer) shell around a core of multiple MNPs. For example, the addition of block copolypeptides to an aqueous suspension of maghemite nanoparticles lead to the formation of water soluble clusters. The clustering of the maghemite particles at the centre was believed to be a result of electrostatic interactions between the positively charged MNPs and the negatively charged block of the polypeptide.[204] Assembly of "magnetomicelles" was also demonstrated using the amphiphilic block co-polymer poly(styrene250-block-acrylic acid13) (PS250-*b*-PAA13) copolyolefin. In this work, it was shown that the co-polymer shell would assemble around hydrophobic maghemite nanoparticles and by varying the relative concentrations of magnetic nanoparticles and encapsulating polymer the magnetic properties of these nanocomposites could be controlled.[205] The hydrophobic interior of these micelles also allows for loading with hydrophobic drugs such as doxorubicin (DOX).[206] By selecting certain polymers extra functionality is able to be introduced to "magnetomicelles", this can include pH-sensitivity whereby a loaded drug and magnetic par-

ticles are released at acidic pH or additional cancer targeting functionality through the use of certain ligands and peptides.[207,208]. One such approach demonstrated was by encapsulating multiple magnetic nanoparticles within amphiphilic block-copolymer micelles.[209] Hydrophobic iron oxide nanoparticles (7.3 nm) were combined with the amphiphilic poly(ethylene oxide-b-lactide) copolymer resulting in the hydrophobic particles to cluster with the polylactide core of the copolymer micelle. By controlling the % of iron loading within the micelle a maximum r_2 of 229 $mM^{-1}s^{-1}$ was achieved.

An advantage of encapsulating MNPs within a polymer matrix is that through the use of hydrophilic and hydrophobic polymers, the access of water molecules to the magnetic cores can be controlled. In doing so it is possible to exploit what is commonly referred to as confinement effects, whereby the diffusion of water around the magnetic core is slowed, increasing interaction time and thus increasing relaxation rates. An example of such is the bone cancer targetting hybrid nanoconstruct (HNC) produced by Nguyen *et al.* The HNC was composed of the biocompatible poly(L-lactic-acid-co-glycolic acid) (PLGA) in which 5 nm IONPs were confined.[210] The exterior was then decorated with alendronic acid-conjugated phospholipid to afford bone targetting functionality. By changing the IONP loading density the distance between particles was tuned between 0.5 and 4 nm. By reducing the interparticle distance from 4 nm to 0.5 nm the clusters exhibited a 5-fold increase in T_2 relaxivity producing a maximum r_2 of 641.2 $mM^{-1}s^{-1}$. This large increase in relaxivity is attributed to not only the resulting high magnetic moment of clustered particles but is also a result of the decrease in the diffusion coefficient of water molecules in the gaps between particles. This means that the water molecules interact with the induced magnetic field for an increased period of time, enhancing T_2 relaxation. In this work they propose that the ALE-lipid conjugate on the outer layer trapped water molecules *via* hydrogen bonding and the PLGA polymeric matrix slowed the water diffusion rate and as a result increased interaction times between the water and magnetic nanoparticles.

Of particular interest to the work carried out in this thesis is using a layer-by-layer (LbL) to incorporate MNPs into the core or shell of polymeric capsules (PMCs). This is a well-established method whereby negatively and positively charged polymers are deposited in alternating fashion onto a sacrificial core (ranging in size from 0.1 to 10 μm).[211] After the sequential coating of the template it is dissolved leaving behind a hollow capsule. One of the key advantages of LbL formation of polymer microcapsules are the wide range of templates and polymers that can be combined to offer countless possible functionalities. The functional properties of a PMC are ultimately defined by the physicochemical properties of the polyelectrolytes used

during the LbL deposition process. Common examples include sodium poly(styrenesulfonate) (PSS), poly(acrylic acid) (PAA), poly(methacrylic acid) (PMA), poly(allylamine) hydrochloride (PAH), poly(ethylenimine) (PEI), as well as biopolymers such as, chitosan, alginate, and dextran.[212–217] The choice of core/template can be dependent on the polymers chosen, but may also depend on desired size and on any molecules to be encapsulated. Materials such as calcium carbonate, silica, gold, polystyrene, hydrogel beads and other organic/inorganic hybrid materials have all been demonstrated as possible LbL templates.[218–221] $CaCO_3$ cores are the most commonly used templates as they are easily dissolved with low pH or washing with ethylenediaminetetraacetic acid (EDTA). Due to their porosity they have also been shown to be suitable for pre-loading of drugs such as doxorubicin (DOX).[222]

Through the addition of magnetic nanoparticles, PMCs can become responsive to magnetic fields and offer added MRI contrast functionality.[223–227] One such example was carried out by Ai *et al.* where IONPs were stabilised by the amphiphilic polymer *N*-alkyl-PEI_{25K} and combined with a SiO_2 sacrificial core.[228] The resulting PMC demonstrated increased T_2 relaxivity with an increase of ∼2.5 times compared to the the *N*-alkyl-PEI_{25K} stabilised IONPs alone. This increase was attributed to interactions between the iron oxide cores as seen for other assembled clusters of MNPs.

1.8.1 1-Dimensional Assemblies of Magnetic Nanoparticles

So far in this section all assemblies discussed have had high degrees of symmetry. There is, however, a number of approaches that focus on the formation of 1-D dimensional assemblies with the increased shape anisotropy causing changes to an MNP's magnetic and biological properties. For example, some high aspect ratio nanomaterials (carbon nanotubes and filament-shaped polymer micelles) have been reported to have a considerably longer blood half-life than spherical nanoparticles, which was attributed to the slower uptake of such nanostructures by macrophages.[229–231] Most importantly, 1-dimensional assemblies of magnetic nanoparticles results in unique magnetic behaviour. As with highly symmetrical assemblies strong dipolar interactions are induced as the particles come into close proximity of one another, these interactions lead to the alignment of individual magnetic moments increasing the net magnetisation of the particle assembly as well as increased anisotropic energy due to magnetic blocking.[85] This increase in net magnetic moment means that the assemblies can be manipulated using weaker magnetic fields, making them attractive platforms for magnetic targeted delivery and therapy, as well as for magnetic cell separation.[232] The increased magnetic moments are a result of strong

dipolar interactions which is a result of the uniaxial anisotropy favouring the alignment of MNPs in a specific direction. Nakata *et al.*, compared the magnetic properties of isolated particles, aggregates, and chains. The chains were formed by using a molecular linker on the surface of the MNPs and showed ferromagnetic interactions between the nanoparticles that compose them, this in turn raised the blocking temperature. It was concluded that the chains resulted in more magnetic coupling than the aggregates or isolated MNPs.[233] 1D assemblies of MNPs have been reported to increase magnetic hyperthermia efficiency, improve targeting of tumours, and increase contrast for MRI.[234,235] It has been shown that the non-linear assembling of MNPs may result in particles coupling both ferromagnetically and anti-ferromagnetically resulting in a slight demagnetising effect, preventing any such composites from reaching a theoretical maximum magnetisation (sum of individual magnetic moments).[233,236,237] However, when particles are aligned along a single axis they behave like single elongated particles with strong uniaxial anisotropy and enhanced magnetisation.[233,238] Gao *et al.,* also modelled the inhomogeneous field produced by the increased anisotropy of iron oxide particles of different shapes (spheres, cubes, plates, rhombohedra, tetrahedra, octapods), concluding that an increased 'effective radius', (r_{eff}) that is half the length of a particle's 'easy axis', can also result in strong transverse relaxivity enhancements.[239] These properties have meant 1D assemblies of MNPs have shown strong MRI contrast enhancement.

In an early study demonstrating the MRI capabilities of 1D magnetic nanomaterials, Peiris *et al.* compared the transverse relaxivity of covalently linked 'nanochains' against their constituent spherical particles finding the chains to have a 2.5 fold increase in measured r_2 values.[240] Another excellent example are the 'worm-like' Mn-Zn ferrites produced Sun *et al.* For this in-depth study three different shaped nanocomposites were compared, monodisperse spheres, clusters, and the worm-like high aspect ratio assemblies. The *in vitro* MRI analysis of the 3 samples, revealed the 'worms' to have very strong transverse relaxivities ($r_2 = 474.8$ mM^{-1}s^{-1}), a considerable increase on both the monodisperse spheres and the clustered MNPs ($r_2 = 237.4$ mM^{-1}s^{-1} and 318.9 mM^{-1}s^{-1} respectively, all measured at 1.5 T).[241] This increase in contrast enhancement was attributed to the increased M_s values that were also measured for the worms. The work then went on to compare the 3 nanostructures as drug delivery systems for the anti-cancer drug Paclitaxel (PTX). The *in vivo* results showed that the worms provided good MRI capability alongside longer blood circulation, higher PTX delivery to the tumour, and high efficiency in causing tumour cell death. The improvements were deemed to be a direct result of the high aspect ratio allowing for more contact opportunities with the cell membrane

receptors.[241] This is a phenomenon that has been widely reported for elongated materials such as carbon nanotubes and polymer filaments (filomicelles).[230,231] Due to their increased surface-to-volume ratio, this allows for polyvalent binding and thus increased affinity for cell surface receptors.[242,243]

Other high-aspect ratio magnetic nanostructures to show increased transverse relaxivities compared to spherical MNPs include the worm-like IONP superstructures produced using hyperbranched polyglycerols, iron oxide multi-walled carbon nanotubes hybrids, and magnetic nanowires obtained by protein fibril biotemplating.[244–246] The transverse relaxivities of the 3 examples (r_2 = 650 $mM^{-1}s^{-1}$, 176 $mM^{-1}s^{-1}$ and 161 $mM^{-1}s^{-1}$, measured at 3.0 T, 9.4 T, 3.0 T respectively) were all greater than clinical examples such as Feridex (r_2 = 107 $mM^{-1}s^{-1}$) and Sinerem (r_2 = 53 $mM^{-1}s^{-1}$). The demonstrated superiority of high aspect ratio materials compared to both monodisperse and clustered particles for MRI contrast enhancement, as well as the longer blood half-lives and reduced uptake by the phagocytic system of anisotropic nanomaterials, means there is a real need for a facile, cost-effective approach for the synthesis of these materials.[241,247,248]

The formation of 1D magnetic structures can be divided into two families; 'direct' methods where the high aspect ratio is a result of synthetic parameters or the use of templates. These will in turn form elongated magnetic nanostructures such as nanotubes and nanowires. Templated syntheses will typically use pre-made porous templates composed of materials such as polycarbonates, alumina, and block co-polymers.[249–252] Whilst this route provides good control over the size/morphology of the final product, it can also be expensive, time-consuming, and require extra functionalisation steps for biocompatibility. Direct chemical routes for 1D magnetic materials use various additive to hydrothermal, co-precipitation, and thermal decomposition synthesis. Dextran, for instance, was added after the initial nucleation of iron oxide during a co-precipitation reaction. This step-wise rather than *in situ* approach lead to the formation of elongated magnetic nanorods.[253] Other additives include trioctylphosphine oxide (TOPO), dopamine, sodium sulfate, and polyethyleneimine (PEI), though for these examples a final reduction step is needed as the initial products are either elongated hematite (Fe_2O_3) or akaganéite (β-FeOOH) nanostructures.[102,254–257]

An alternative, and focus of this section, are assembly methods whereby high aspect ratio nanostructures are assembled from individual MNPs. This method results in structures commonly referred to as nanochains or nanoworms. An advantage of assembly over direct methods is that the magnetic and biological properties of the 1D nanostructure can be easily tuned by

adjusting the size, shape, and composition of the magnetic building blocks. The example by Nakata *et al.*, is one such example of an assembly method.[233] The most common assembly routes are *via* magnetic dipole-dipole interactions, self-assembly processes, and covalent chemical linkage.[240,258–260] In examples where the dipole-dipole interactions between individual MNPs are strong enough, they can be used to assemble MNPs into 1D structures. Evidence of this was first produced by Philipse *et al.*, where magnetite chains were imaged using cryo-TEM having been formed from 21 nm particles. The size of the particle was necessary for the formation of strong dipolar interactions with 16 nm particles forming droplet shaped aggregates.[261]

Often magnetic dipole interactions are insufficient for creating 1D magnetic nanostructures, and polymers may be used to assist with alignment. One of the most eminent examples of 1D magnetic assemblies was carried out by Sailor and co-workers. They reported the first preparation of nanoworms formed by an adapted co-precipitation route using higher Fe salt concentrations and 20 kDa molecular weight dextran to induce the linear assembly of 5–10 iron oxide cores.[242] The formation of the nanoworms was thought to be directed by the dextran, with higher or lower weighted dextran resulting in either branched or spherical aggregates. The 1D assemblies were measured to have increase saturation magnetisation and improved MRI performance compared to spherical counterparts. The importance of molecular weight was also demonstrated for iron oxide nanochains produced by thermal decomposition in the presence of polypropylene grafted maleic anhydride (PP-MA). By increasing the molecular weight from 2.5 kDa to 8.0 kDa the M_s of resulting nanochains increased from 46.9 to 51.5 emu g^{-1}.[262]

The most widely exploited route for the fabrication of 1D assemblies of MNPs is through the use of magnetic field induced (MFI) assembly. Such methods will use external fields to align the magnetic 'building blocks', which are either formed prior or *in situ*, and then particles are held together through exterior coatings, electrostatic interactions, or covalent linkages. One popular coating for such purposes are polyelectrolytes such as poly(2-vinyl-N-methyl-pyridinium iodide) (P2VPq), as used by Sheparovych *et al.* In this early example of MFI assembly, 'wire-like' structures of magnetite were formed by placing a reaction vessel containing the P2VPq on top of a permanent magnet to which citrate stabilised Fe_3O_4 NPs were slowly injected. A membrane inside the vessel was used to slow the diffusion of the particles. The MNPs would align parallel to the external magnetic field forming 1D wire-like structures, held together by the P2VPq. The wires were measured to be approximately 1.5 μm (an average of 90 IONPs) in length whilst only a few particles wide. If the reaction was to be carried out in the absence of an external magnetic field, instead of the nanowires random arrays of IONPs would form instead.[263] Alternatively,

the block copolymer poly(trimethylammonium ethylacrylate methylsulfate)-b-poly(acrylamide) was dialysed with polyacrylic acid coated IONPs under a constant magnetic field by Fresnais *et al.* . This resulted in the formation of elongated aggregates with an average length of 12.3 μm (polydispersity, s = 0.50). However, in the absence of any external field only spherical aggregates were formed.[264]

Other than polyelectrolytes, another popular coating used alongside MFI assembly is silica. Hu *et al.,* combined the process of magnetic assembly of Fe_3O_4 nanoparticles with the sol-gel formation of silica to produce individual nanochains. The MNPs were first coated in a thin shell of silica before an external magnetic field was applied to align the particles. This was the followed by coating with an additional layer of silica which resulted in the robust chains of nanoparticles that would remain aligned once the external field was removed.[265] The authors also found that both the interparticle separation and chain length could be controlled by adjusting the timing and duration of applied magnetic field. These small adjustments allowed for fine control of the optical properties of the nanochains with potential use as bio-sensors suggested.

An additional layer of silica was also used by Kralj *et al.* to create the magnetic nanochains and nanobundles. In this example, superparamagnetic nanoparticle clusters (SNCs) with either 5 or 20 nm silica coatings were transferred to a PVP solution and exposed to a homogeneous magnetic field. The PVP was present to temporarily stabilise assembled nanochains in suspension during stirring. The temporary chains were then fixed with an additional deposition of silica through the addition of tetraethyl orthosilicate (TEOS) and ammonia to act as a catalyst. The length of the chains was dependent on the SNC coating thickness, with the 5 nm coating resulting in chains between 6 to 14 SNCs long (0.68 – 1.60 μm) whilst the 20 nm coating producing chains between 10 and 40 SNCs long (1.46 – 5.84 μm). The group also found that by increasing the strength of the magnetic field the nanochains would become much larger in both width and length (1 – 2 μm wide and 5 – 10 μm long) and were named nanobundles as a result.[266] Further work carried out on the nanochains included surface functionalisation with amino and carboxyl groups for improved colloidal stability and characterisation of their magnetic properties. They were able to fit the $M(H)$ data for the nanochains using the Langevin function and show that the magnetic moment of the nanochains was greater than an individual particle.[267,268]

The assembly methods described to this point are multi-step processes, whereby the magnetic cores are first synthesised using common routes (i.e. solvothermal, co-precipitation, see

Section 1.6 for details) before a following step (or steps) are taken to align and fix the MNPs into the final desired nanoworm/nanochain like structure. However, an approach which to date has been utilised to a lesser degree relies upon the *in situ* incorporation of a 'templating' polymer, which acts to both stabilise and also direct the linear alignment of the magnetic cores as they are formed during the co-precipitation synthesis. This one-pot approach therefore being less time-consuming and labour intensive than the previously described methods, whilst the result linear assemblies have demonstrated excellent MRI contrast capabilities. One such example are the iron oxide 'nanoworms' produced by Sailor *et al.,* through an adapted co-precipitation technique where iron salts were precipitated in the presence of the biopolymer dextran. The resulting linear assembly of particles provided stronger contrast enhancement at 4.7 T compared to similar spherical nanoparticles (r_2 values of 116 $mM^{-1}s^{-1}$ and 70 $mM^{-1}s^{-1}$ respectively.) The nanoworms even outperformed the clinical contrast agent Feridex.[269]

Another early example of such *in situ* polyelectrolyte stabilisation was produced by Byrne *et al.*, where denatured herring sperm DNA was used for the *in situ* stabilisation of magnetite nanoparticles.[83] The negatively charged phosphate groups along the biopolymer backbone offered ideal sites at which the iron cations, Fe^{3+}/Fe^{2+}, could electrostatically associate during synthesis, subsequently followed by the precipitation of the iron oxide nanoparticles. After precipitation, the particles remained strongly electrostatically associated to the DNA backbone, the DNA therefore acting as a templating agent for the seeding and growth of the resulting nanoparticles. Transmission electron microscopy (TEM) revealed the nanocomposites to comprise of randomly distributed chains. However, if the nanocomposites were dried in the presence of an external magnetic field before imaging the samples would align in an end-to-end fashion forming ordered 'ropes' several microns in length. Note, this was only observed for the denatured DNA stabilised particles, a magnetic field had little effect on those stabilised by duplex-DNA or those prepared in the absence of any DNA. This difference in behaviour was attributed to the more efficient binding of the nanoparticles to the phosphate backbone of the denatured DNA, these phosphate groups whilst present in duplex-DNA may be less accessible due to the conformational differences compared to the denatured DNA. This was confirmed by IR studies as a band attributable to a Fe–O–P stretch is observed at 1157 cm^{-1}. T The formation of these 'ropes' is as a result of dipole-dipole interactions between neighbouring particles, which are tethered to one another through the biopolymer chain, leading to the alignment of particles parallel to the applied field. The MRI behaviour of these nanocomposites was subsequently described using nuclear magnetic resonance dispersion (NMRD). They found that the profiles produced by the

DNA composite differed dramatically from that expected for a superparamagnetic nanoparticle sample, with extraordinarily high low field longitudinal relaxivities. Unlike the behaviour described by outer-sphere theory,[74,80] the nanocomposites demonstrated an unusual dual power law dependence of T_1 on frequency. In the study it was suggested that the nanocomposites consisted of 'magnetically aggregated' particles, resulting in increased magnetic moments and thus high relaxivity.

Further work on polyelectrolyte stabilised iron oxide particles followed with poly(sodium-4-styrene) sulfonate used as both the stabiliser and template instead of denatured DNA.[71,270] The use of PSSS allowed for greater scope for changing the synthetic conditions and investigating the resulting MR properties of the iron oxide suspensions. By changing the initial ratio of reagents (Fe salts and PSSS), 9 different combinations, divided into 3 groups were produced. As with the previously discussed DNA example, these nanocomposites would also arrange into parallel arrays (dubbed nanowires) when dried in an external magnetic field.[270] Increasing the Fe:PSSS ratio resulted in increased core diameters, deemed a result of reduced nucleation sites along the polymer backbone. NMRD analysis was used to determine the relationship between the initial ratio of reagents and the MR properties.[71] It was evident that the ratio was indeed having an observable effect on the relaxometric properties of these nanocomposites. As the ratio was increased the r_1 maxima (also referred to as the v_{max}) would shift to lower frequencies. Increased r_1 values at low field could also be seen with increased Fe:PSSS resulting in elevated plateaus. Unlike the DNA stabilised iron oxide, these samples conformed with the superparamagnetic model described by outer-sphere theory. However, this conformity would weaken as the ratio increases due to the rising low field plateau. The increased r_1 at low field was attributed to increased magnetic anisotropy energy as a result of the increased density of particles resulting in stronger and/or more numerous interparticle interactions.

The cheap, biocompatible, anti-coagulant heparin has also been used for the *in situ* stabilisation of iron oxide nanoparticles.[98] The reagent ratios were also varied and the relaxometric properties were analysed using NMRD. Again the produced nanocomposites would follow the superparamagnetic model, and again as the ratio of Fe:polymer was increased the v_{max} would shift to lower frequencies and the low field plateau would increase. In concurrence with the PSSS-stabilised nanocomposites, the observed trend correlated with the increased density of particle nucleation. This work further supports the notion that the magnetic anisotropy arising from strong dipole interactions between particles can be mediated and tuned through the availability of nucleation sites on the polymer backbone.

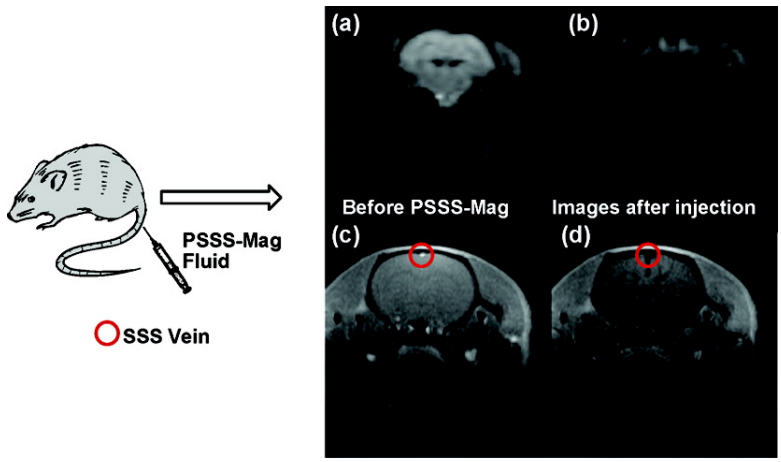

Figure 1.7: Echo planar image (EPI) of mouse brain (a) before and (b) as PSSS-stabilised iron oxide nanoparticles (PSSS-Mag1) passes through; Fast Low Angle Shot (FLASH) image of mouse brain (c) before and (d) as PSSS-Mag1 passes through.[270]

1.9 Aims & Objectives

1.9.1 Research Aims

As described in the earlier sections of this introductory chapter, magnetic nanoparticles are an exciting platform for the development of high-performance MRI contrast agents. With recent developments showing how the assembling of magnetic cores into more complicated multi-core assemblies can result in vast improvements in their relaxation enhancement. However, there are still many unknowns in how this mechanism of contrast enhancement acts and how it may be maximised to produce commercially viable contrast agents.The aim of this research therefore, was to first further the understanding of the complex dipolar interactions that occur between neighbouring magnetic nanoparticles when brought into close proximity within multi-core assemblies. Secondly, this work sought to probe how these interactions can be manipulated through changes in the likes of seeding density and interparticle distance in order to maximise the resulting MRI contrast enhancement. Finally, this work looked to synthesise 4 families of MNP based nanostructures before and analyse their colloidal, magnetic, whilst also evaluating their potential as contrast agents

1.9.2 Objectives

1. Combine the *in situ* approach for preparing linear assemblies, as detailed in Section 1.8.1, with a novel synthetic polyelectrolyte (poly(2-acrylamido-2-methylpropane sulfonic acid), to examine how factors such as particle seeding density and average interparticle distance can influence the MRI properties of the resulting linear assemblies.

2. Optimise a novel MFI assembly method to create 1D silica coated magnetic nanostructures. In which, linear assemblies of MNPs, prepared using the *in situ* method, are used as the precursor. Use FFC-relaxometry to compare their relaxometric properties.

3. Adapt the LbL approach for preparing PMCs to integrate polyelectrolyte stabilised MNPs within the capsule membrane and core. Demonstrate their potential for MRI monitoring of pH-triggered drug release using single field relaxometry.

4. Utilise an statistical approach for experimental design to optimise the co-precipitation preparation of bi-magnetic core-shell nanoparticles (Section 1.7.3).

Chapter 2

Experimental

2.1 Materials & General Procedures

2.1.1 Starting Materials

All chemicals were used as supplied. Acetic acid (99.6 %) was purchased from ACROS organics, heparin sodium salt (from porcine intenstinal mucosa) was sourced from Alfa Aesar. Sodium 2-acrylamido-2-methylpropane sulfonate (AMPS® 2505, 50 wt% in water) was donated by Lubrizol. Thermal initiator, 2,2 -azobis[2-methyl-N-((2- hydroxyethyl)propionamide] (VA-086, 98%) was obtained from Wako Chem. 2-(((butylthio)-carbonothioyl)thio)-2-methylpropanoic acid (BDMAT) was synthesized using previously described literature conditions.[271] Preparation of the polymer poly(2-acrylamido-2-methylpropane), (P(AMPS)) was carried out by Dr. Caroline Bray at the University of Warwick.[271] Ethylene glycol (ReagentPlus®, $\geq$ 99 %), iron(II) chloride tetrahydrate ($\geq$ 99 %), iron(III) chloride hexahydrate (97 %), cobalt (II) nitrate hexahydrate ($\geq$ 98 %), ammonium hydroxide (BioUltra 1M), chitosan (low molecular weight), poly(allylamine hydrochloride) (average $M_w \sim$ 17,500), polyethylenimine, tetraethyl orthosilicate (TEOS, $\geq$ 99 %), tetramethyal ammonium hydroxide (TMAH, 1.0 M), tetraethyl ammonium hydroxide (TEAH, 20 % in H_2O), sodium citrate tribasic dihyrdate (for molecular biology, $\geq$ 99 %), poly(sodium 4-styrenesulfonate) (average M_w ~70 000), polyvinylpyrrolidone (PVP, average M_w ~40 000) hydrochloric acid (37 %), and Xanthan gum (from Xanthomonas campestris) were purchased from Sigma-Aldrich Ltd. Defibrinated sheep's blood, sodium carbonate ($\geq$ 99.5 %), sodium chloride ($\geq$ 99 %), sodium hydroxide, and Triton-X 100 ($\geq$ 90.0 %, molecular biology grade) were purchased from VWR, UK. Ammonia solution (35 % w/w) was purchased

from Fisher Scientific, UK.

2.1.2 Solvents

Dichloromethane (HPLC grade, $\geq$ 99.8 %), methanol (HPLC grade, $\geq$ 99.8 %), and ethanol ((HPLC grade, $\geq$ 99.8 %) were all used as supplied and were sourced from Fisher Scientific, UK. Ultrapure water was either collected from an Elga PureLab system operated at 15.0 MΩ or a Merck Milli-Q Direct water purification system operated at 18.2 MΩ. Degassed solvents were prepared through bubbling with nitrogen gas.

2.1.3 Laboratory Equipment

Centrifugation was carried out using a Sigma 2-16KL, Sigma 2-16P, Sigma 1-14, and SciSpin MICRO centrifuges. Sonication of material was carried out using an Ultrawave U500H ultrasonic cleaning bath. IKA C-MAG HS 7 magnetic stirrers were used for heating of reactions.

2.2 Experimental Procedures

2.2.1 Preparation of P(AMPS)

The preparation of poly(2-acrylamido-2-methylpropane sulfonic acid, P(AMPS), was carried out by Dr. Caroline Bray (University of Warwick), and the work is presented in the paper by Bray *et al.*[271] Briefly, the chain transfer agent (CTA) BDMAT, the initiator VA-086 (from stock solution of 20.0 mg ml^{-1}), and the monomer AMPS, were combined with phosphate buffer tablet solution (0.5 ml), and sodium hydroxide (2.5 mg, 6.3 $\times$ 10^{-2} mmol) in a sealed flask. The relative quantities of CTA, initiator, and monomer were adjusted according to the desired degree of polymerisation (see Table 3.1). The solution was deoxygenated by bubbling with nitrogen for 10 minutes, the flask was subsequently placed in a temperature controlled oil bath at 90 °C, and heated until full conversion was achieved ($\sim$ 2 hours). Once complete, the mixture was allowed to cool to room temperature and then opened to the atmosphere. The number average molar mass as measured by size exclusion chromatography ($M_{n,SEC}$) and dispersity ($Đ$) are tabulated in Table 3.1

Table 2.1: Theoretical and experimental molecular weights of the P(AMPS) used for the synthesis of P(AMPS)-stabilised iron oxide nanoparticles.

Degree of Polymerisation	**[AMPS] : [CTA] : [VA-086] (mol L^{-1})**	$M^{a}_{\mathbf{n,th}}$ **(g mol^{-1})**	$M^{b}_{\mathbf{n,SEC}}$ **(g mol^{-1})**	$\boldsymbol{Đ}^{b}$
20	20 : 1 : 0.033	4,800	8,100	1.10
100	100 : 1 : 0.167	23,000	17,600	1.16
400	400 : 1 : 0.667	91,000	41,300	1.51

[a]Theoretical M_n values were calculated using the following equation; $M_{n,th} = ([\mathrm{M}]_0 * p * M_\mathrm{M})/[\mathrm{CTA}]_0 + M_\mathrm{CTA}$; [b]Experimental M_n and $Đ$ values were determined by size exclusion chromatography in 20 % methanol and 80 % of 0.1 M $NaNO_3$ in milli-Q water eluent using a conventional calibration obtained with PEG/PEO standards. The dispersity, $Đ$, was calculated according to $Đ = M_w/M_n$, where M_w is the weight-average molar mass and M_n is the number-average molar mass.

2.2.2 Preparation of Non-stabilised Iron Oxide Nanoparticles

$FeCl_2 \cdot 4\,H_2O$ (3.3 g, 12.0 mmol) and $FeCl_3 \cdot 6\,H_2O$ (1.2 g, 6.0 mmol) were dissolved in 12.5 ml deoxygenated water (prepared by bubbling with N_2 gas for a minimum of 20 minutes). Separately NaOH (2.5g, 0.0625 mol) was dissolved in 125 ml deoxygenated water and then heated to 40 °C. The $Fe^{2+/3+}$ solution was then added dropwise and the reaction was stirred for 1 hour with the temperature maintained at 40 °C. The resulting brown/black precipitate was washed with ultrapure water using an initial magnetic separation, followed by centrifugation (13,500 rpm, 15,893 g) for 20–30 mins. The pellet was resuspended using sonication before repeating until the pH was measured as neutral. The collected precipitate was then dried in air leaving a black powder.

2.2.3 Preparation of P(AMPS)-stabilised Iron Oxide Nanoparticles

P(AMPS) with different $M_{\mathrm{n,SEC}}$ as prepared in Section 2.2.1 were used to produced stabilised iron oxide nanoparticles using an *in situ* co-precipitation approach adapted from literature.[98] The ratio of the 3 different P(AMPS) to total iron salt were varied as summarised in Table 3.1. P(AMPS) (amount varied) was dissolved in ultrapure water (10 ml), and the solution was subsequently degassed by bubbling with N_2 for 20 minutes. Separately, $FeCl_2 \cdot 4\,H_2O$ and $FeCl_3 \cdot 6\,H_2O$ (number of moles added varied according to Table 3.2) were dissolved in 50 ml deoxygenated ultrapure water. The P(AMPS) solution was added to the $Fe^{2+/3+}$ solution

whilst the N_2 atmosphere was maintained. NH_4OH (1 M) was added in 0.5 ml aliquots until the pH was measured to be in the range 9.0 – 10.0. The reaction was stirred at 40 °C for 2 hours. The resulting brown/black precipitate was washed with ultrapure water using an initial magnetic separation, followed by centrifugation (13,500 rpm, 15,893 g) for 20 – 30 mins. The pellet was resuspended using sonication before repeating until the pH was measured as neutral. The stable aqueous washings were retained for DLS, TEM, and relaxometric analysis, with the final precipitated product being dried to powder to be used for XRD, FTIR, Raman, and VSM analysis.

2.2.4 Preparation of Polyelectrolyte Stabilised Cobalt Ferrite Nanoparticles

$Co(NO_3)_2 \cdot 6\,H_2O$ and $FeCl_2 \cdot 4\,H_2O$ were dissolved in degassed ultrapure H_2O at a molar ratio of 1:2. Poly(sodium-4-styrenesulfonate) (PSSS) (quantity varied dependent on desired metal to polymer ratio) was dissolved in ultrapure water and degassed before being added to the metal salt solution. NH_4OH (35 % w/w) was added in 200 μL aliquots until the pH was measured to be $>$ 11.0. The reaction was stirred at 90 °C for 2 hours, with the black precipitate then washed with ultrapure water using centrifugation until the pH was measured neutral. The collected precipitate was then dried in air. Stable aqueous washings were retained for DLS, TEM, relaxometric analysis.

This protocol was also used for the preparation of P(AMPS)-stabilised CFNPs, with relative quantity of polymer also adjusted as before. The remaining protocol was kept consistent with the PSSS-stabilised CFNPs described above.

2.2.5 Prepartion of Citric Acid Stabilised Magnetic Nanoparticles

Non-stabilised magnetic nanoparticles (cobalt ferrite or iron oxide, 0.11 g) were dispersed in ultrapure water (50 ml) using thorough sonication. Once fully redispersed sodium citrate tribasic dihydrate (1.43 mmol, 0.27 g) was added to the colloidal suspension of nanoparticles and sonicated further (approx. 1 hour). The suspension was neutralised using concentrated ammonium hydroxide solution (8.8 M) whilst mixing vigorously.

2.2.6 Preparation of Silica Coated Cobalt Ferrite Nanonecklaces

Dichloromethane (DCM) (3 ml) and tetraethyl orthosilicate (TEOS) (0.9 ml, 3.6 mmol) were added to a 50 ml beaker placed on top of a permanent neodymium magnet (either 16.3 kg or 45.0 kg pull strength). Separately, 10 ml of aqueous PSSS-stabilised cobalt ferrite nanoparticles or non-stabilised cobalt ferrite nanoparticles (0.05 mg/ml) were combined with methanol (5 ml) and the base catalyst, NH_4OH (8.8 M). The final concentration of base in the aqueous layer is given in Table 4.4. The aqueous layer was carefully transferred *via* pipette to the beaker so that two layers would form. After 24 hours the two layers were removed and the brown precipitate at the bottom of the beaker was washed by centrifugation 3 times with ethanol and then followed by washing by magnetic separation a further 3 times.

2.2.7 Preparation of PVP-stabilised Iron Oxide Nanoparticles

Aqueous suspension of iron oxide nanoparticles (100 ml, 10 mg/ml) was mixed with 2 ml aqueous PVP-40 solution (25.6 g/L, 0.64 mM) and mixed at room temperature for 24 hours. To the suspension, 500 mL of aqueous acetone (H_2O/acetone, 1:10 v/v) and centrifuged at 13 200 rpm for 20 mins. The supernatant was removed and the black precipitate was washed in ethanol before removing solvent *via* rotary evaporation.

2.2.8 Preparation of Calcium Carbonate Microparticles

Aqueous Na_2CO_3 solution (0.33 M, 25 ml) was added rapidly to a flask containing aqueous $CaCl_2$ solution (0.33 M 25 ml) at room temperature with intensive agitation using a magnetic stirrer (time of agitation was varied, see Table 5.1. Once stirring was complete, the white precipitate was collected though filtration under vacuum using 0.1 μm filters. To produce sub-micron spherical particles the solvent was changed from water to ethylene glycol (83 % w/w) and the stirring times were increased to either 15 minutes or 2 hours. The precipitate formed was isolated using centrifugation and washed with ethanol before drying. $CaCO_3$ microparticles doped with iron oxide nanoparticles were prepared as described in this section by the salts were dissolved in aqueous suspensions of iron oxide nanoparticles (5 mg/ml) before combining the salts and filtering.

2.2.9 Layer-by-Layer Preparation of Polyelectrolyte Microcapsules

Polyelectrolyte microcapsules were prepared by alternating incubation of $CaCO_3$ microparticles (1 % w/w in suspension) in positively charged polyelectrolyte solutions (poly(allylamine hydrochloride, PAH, 2 mg/ml) and negatively charged polyelectrolyte solutions (poly(sodium 4-styrenesulfonate), PSSS, 2 mg/ml). Each polyelectrolyte adsorption procedure (PEAP) was carried out as follows, the $CaCO_3$ microparticles (1 % w/w) were incubated with the respective polyelectrolyte solution for 10 minutes (unless stated otherwise) with magnetic stirring. The excess was removed using centrifugation (3.0 mins, 500 ×g) before washing with NaCl solution (0.05 M) a total of 3 times before beginning the next PEAP. The number of PEAPs was dependent on the experiment as described in Section refLbL-chapter, once completed the $CaCO_3$ core was removed by incubating in ethylenediaminetetraacetic acid (EDTA) solution (0.1 M) for 30 minutes. The microcapsules were then centrifuged (5.0 mins, 1500 ×g) before repeating the incubation with EDTA for another 2 washes. The microcapsules were then stored in ultrapure water at 4 °C. When adding polyelectrolyte stabilised iron oxide nanoparticles, the PEAP was carried out in the same manner but with the cores incubated in the colloidal suspension rather than the polymer solution. The point at which the magnetic particles was added varied between experiments (Section 5.3.1).

2.2.10 Stimuli Response Study

Polymer microcapsules (PMCs) containing iron oxide nanoparticles were suspended in aqueous Xanthan gum solution (0.25 % w/w). The pH of the Xanthan gum solution was adjusted using sodium hydroxide (0.05 M) and hydrochloric acid (0.05 M) prior to the addition of the PMCs. The transverse relaxation rate was measured for each sample upon suspension in the pH-adjusted Xanthan solution, with further measurements collected at initial intervals of 15 mins, increasing to 30 mins, 1 hour, and finally measuring after a full 24 hours. The transverse relaxation was then normalised with respect to the concentration of Fe present in the sample, and the resulting r_2 was plotted against time. The study was repeated for pH's 3.0, 7.0 and 10.0.

2.2.11 Preparation of Bi-Magnetic Core-Shell Nanoparticles

The experiments for the formation of bi-magnetic core-shell nanoparticles were determined using a design of experiment approach and JMP software.[272] The experiments were based on

a 2^4 fractional factorial experimental design, in which the 4 variable factors selected were the quantity of non-stabilised cobalt ferrite nanoparticles (range 40 – 200 mg), the quantity of iron salts (0.3 – 3.0 mmol), time of reaction (30 – 120 minutes) and the method of iron salt solution addition. The addition of the iron salts was carried out either 'fast' by which the solution is added at once with rapid stirring to the colloidal suspension of cobalt ferrite nanoparticles, or 'slow' where by the iron salt solution was added dropwise using a syringe pump at a rate of 0.15 ml min^{-1}. The variables that were fixed for this design of experiments was the temperature (40 °C), volume of cobalt ferrite suspension (30 ml) and iron salt solution (3 ml), and the quantity and choice of base (NH_4OH, 35 % w/w, 0.6 ml).

The generalised experimental protocol is as follows; non-stabilised cobalt ferrite nanoparticles were suspended in ultrapure water (30 ml) and subsequently degassed by bubbling N_2 gas for a minimum of 30 minutes. Separately, $FeCl_2 \cdot 4\,H_2O$ and $FeCl_3 \cdot 6\,H_2O$ was dissolved in degassed ultrapure H_2O (3 ml), NH_4OH (35 % w/w, 6.0 ml) was added to the colloidal suspension of cobalt ferrite nanoparticles followed by the addition of the $Fe^{2+/3+}$ salt solution by either the 'fast' or 'slow' method before the reaction was heated to 40 °C for the experiment specific amount of time. The resulting brown/black precipitate was washed with ultrapure water using an initial magnetic separation, followed by centrifugation (13,500 rpm, 15,893 g) for 20 – 30 mins. The pellet was resuspended using sonication before repeating until the pH was measured as neutral. The precipitate was then dried to a powder in a vacuum oven to be used for characterisation.

2.2.12 *In Vitro* Haemolysis Assay

Defibrinated sheep blood (2 ml) was divided between two 1.5 ml Eppendorf tubes (1 ml each) and centrifuged at 4500 g (8200 RPM). The supernatant was removed and replaced with 800 μL phosphate buffered saline (PBS), in which the pellet was resuspended using sonication. This was repeated a minimum of 5 times, until supernatant became colourless. The red blood cell suspension was diluted 1:150 (by volume) in PBS. The samples were diluted in ultrapure water to give concentrations of 0.5, 0.1, 0.05, and 0.01 mg/ml. 20 μL of each suspension was added to 380 μL of diluted red blood cells making final concentrations of 10, 2, 1 and 0.2 μg/ml. Negative controls of 20 μL PBS and ultrapure H_2O, and a 100 % positive control of 1 % Triton-X in PBS was prepared. The diluted red blood cells were incubated at 37 °C for 1 hour. All samples were prepared in triplicate. Particle blood mixtures were separated by centrifugation for 5 minutes before 250 μL of the supernatant was removed and transferred to a 96 well plate and

the absorbance measured across the range 350–700 nm using a Molecular Devices SpectraMax Plus 483 plate reader. The average peak max value for the PBS negative control value was subtracted from the nanoparticles peak max values a divided by the average Triton-X positive control, therefore giving the % haemolysis.

2.3 Contributions

The fitting of Mössbauer spectroscopy was done with the assistance of Dr Lara K. Bogart of the UCL Healthcare Biomagnetics Laboratory, who also provided support and insight for the data collection and interpretation of results. Preparation of the polymer poly(2-acrylamido-2-methylpropane), (P(AMPS)) was carried out by Dr Caroline Bray at the University of Warwick. Small-angle X-ray scattering (SAXS) measurements, analysis, and data interpretation was carried out by Dr Stephen Hall of the University of Warwick. Collection of TEM images and EDS analysis of bi-magnetic core-shell nanoparticles was carried out by Dr Yisong Han (University of Warwick). Collection and analysis of ICP-OES data was performed by Connor Wells of UCL or Dr Joseph Bear of Kingston University.

2.4 Physical & Structural Characterisation

2.4.1 Electron Microscopy

Electron microscopy is a powerful means for the analysis and characterisation of nanomaterials and is utilised across a wide-range of scientific disciplines. The resolution of traditional optical microscopy is limited by the wavelength of visible light, however the de Broglie wavelength of an electron is approximately 100 000 times smaller than a photon. This allows electron microscopy to have a much greater resolving power and can allow for micro- and even nanoscale observations. The two methods of electron microscopy used in this thesis are transmission electron microscopy (TEM) and scanning electron microscopy (SEM).

Transmission Electron Microscopy

Transmission electron microscopy (TEM) operates on very similar principles as conventional optical microscopy, only the sample is “illuminated” using a beam of electrons rather than visible light. There are 3 main components to any TEM microscope. The first is the electron gun (or

source) which produces a high energy electron beam. These typically consist of a tungsten filament or needle connected to a high voltage power source, 100 – 300 kV. The electrons are emitted into a vacuum column in which they are manipulated by magnetic or electrostatic fields. The vacuum is crucial in order to prevent the electrons colliding with molecules in the air.

The second component of a TEM are the lenses. Like in an optical microscope, these allow for the beam to be focused and magnified, producing the image that is used for analysis. As electrons cannot pass through materials such as glass, magnetic lenses are instead needed to focus the electron beam. When an electron enters or exits a magnetic field it will spiral around the curved field as a photon would in a curved optical lens. The magnetic field is therefore acting as a convergent lens. By stacking multiple lenses atop one another, the utility of a TEM can be improved with focusing, magnifying, and/or collimating the beam as it passes through the lenses.

Finally once the electron beam has been focused and magnified, a detector is needed so that an image may be produced for future reference. The projector lens expands the beam onto a phosphorescent screen which is coated in fine particulate zinc sulfide. This generates light from which an image can be produced for direct observation or digital imaging equipment can capture the image, saving it for analysis at a later date. The observed contrast in these images is dependent on the degree of electron scattering, which itself is dependent on the composition of the sample. Factors such as thickness, density, crystal structure, or atomic number of the sample can influence the level of contrast observed in the final image.

Transmission electron microscopy (TEM) images were obtained on a JEOL JEM-1200 microscope, 120 kV, operated with a beam current of 80 mA. Images were captured using a Gatan Orius 11 megapixel camera. Samples were prepared by deposition and drying of nanoparticle samples (20 μL of colloidal magnetic fluid suspensions) onto formvar-coated 300-mesh copper TEM grids (EM Resolutions). Diameters were measured using ImageJ (software version 1.8).[273] Average values were calculated by counting a minimum of 100 particles. Magnetically aligned samples were dried in the presence of a parallel permanent magnetic field (2250 Gauss). Images provided by Dr Yisong Han (University of Wariwick) are noted as such in figure caption

Scanning Electron Microscopy

The key difference between TEM and scanning electron microscopy (SEM) is that images produced by SEM are due to incident electrons being reflected or emitted from a material's surface

and not electrons that have been transmitted through the material. The electron-surface interactions can reveal information on a sample's morphology, topography, chemical composition, and crystalline structure.

The electrons accelerated towards the sample carry high amounts of kinetic energy, this is subsequently dissipated when decelerated by the surface of the sample. This exchange in energy produces secondary electrons (SE's), backscattered electrons (BSE's), diffracted backscattered electrons, photons, and heat. These signals can be detected and used to produce images for analysis. Secondary electrons are the most common signal used for producing images by SEM and can provide information on a samples topography and morphology. They result from inelastic interactions between the electron beam and atoms within the sample and typically have very lower energies. This low energy means that they are only able to travel a few nanometres within a solid, making them highly localised to the point of impact of the electron beam. BSE's are also commonly used for sample analysis, and result from electrons that are reflected from the sample after elastic interactions. BSE's can travel much further through a solid meaning they provide much less resolution but their energies are heavily linked to the atomic number (Z) of a sample. They can therefore be used for illustrating contrasts in compositions of multi-phase samples.

The incident electron beam may also excite an inner shell electron causing it to be ejected. The resulting hole is then filled by a higher energy, outer shell electron which releases the difference in energy in the form of an X-ray photon. The number and energies of these emitted X-ray photons can be measured by an energy-dispersive spectrometer. As the X-ray is the equivalent energy of the difference between the two shells and is characteristic of the emitting element it allows for the elemental composition of the sample to be identified. This technique is named energy-dispersive X-ray spectroscopy (EDS) and is commonly used in tandem with SEM.

The electron beam for SEM is produced and manipulated in a very similar fashion to TEM, using a filament as an electron source and magnetic lenses to condense and focus the electron beam. Additionally, SEM requires scanning coils which deflect the beam in the x and y axes so that it scans in a raster fashion over rectangular area of the sample surface. Different detectors are then required to detect the different signals from the samples. SE's are detected using an Everhart-Thornley detector, which consists of a scintillator inside a Faraday cage, which is positively charged and attracts the SE's. The scintillator then accelerates electrons converting them to light which can be amplified by a photomultiplier. The amplified signal is

then displayed as a 2-D image which can then be saved as a digital image.

SEM images were obtained using JEOL JSM 6701 scanning electron microscope operated an accelerating voltage of 10.0 kV. Samples were prepared using a conductive carbon adhesive tabs which were added to aluminium stubs and coated in gold using an Agar manual sputter coater. Images provided by Dr Yisong Han (University of Wariwick) are noted as such in figure caption.

2.4.2 Dynamic Light Scattering

Dynamic Light Scattering (DLS) or Photon Correlation Spectroscopy (PCS) is a widely used technique for the measuring the size of colloidal particles; typically in the sub-micron region. The key principle behind DLS is the measurement of the Brownian motion of particles and correlating this to the average size, and size distribution of the particles present. As the observed particles are in suspension, they are never stationary and will move randomly due to collisions with one another and solvent molecules. The larger the particles, the slower they will move according to Brownian motion. This relationship between the size of a particle (its hydrodynamic diameter) and the speed at which it diffuses through a medium (the translation diffusion coefficient) is summarised by the Stokes-Einstein equation.

$$d(H) = \frac{kT}{3\pi\eta D} \tag{2.1}$$

Where $d(H)$ is the hydrodynamic diameter, k is the Boltzmann constant, T is the absolute temperature, and η is the solvent viscosity. Note that the diameter refers to how the particle diffuses through a fluid and is not the particle's true diameter but rather the diameter of a sphere that has the same diffusion coefficient. This coefficient is not solely dependent on particle size but also the particle's shape, surface structure, and the concentration and type of ions present in the medium.

To obtain the average size of a sample, laser light is directed at the moving particles and if the particle size is comparatively small with respect to the laser wavelength then the light will be scattered isotropically (in all directions). As the particles are undergoing Brownian motion the observed scattering will fluctuate and the rate of these fluctuations will depend on the particle size. Smaller particles will cause the scattering to fluctuate more rapidly than larger ones.

A digital correlator within the machine measures the degree of similarity between a signal as it evolves over time. The correlation between the intensity at $t = 0$ and the intensity at $t = \delta t$

will reduce as δt increases. How long the correlation persists is dependent on the diffusion coefficient and thus is dependent on the particle size. For a large number of monodisperse particles in Brownian motion, the correlation function is an exponential decaying function of the correlator time delay. This exponential can be mathematically resolved to provide the average hydrodynamic diameter (Z-average) and an estimate of the width of the size distribution (polydispersity index).

Hydrodynamic particle size and zeta-potential measurements were determined by dynamic light scattering (DLS) using a Malvern Zetaszier ZS instrument. A 4 mW He-Ne 633 nm laser module was used and scattered light was measured at 173 ° (back scattering). The attenuator and position was selected automatically by the instrument and particles sizes reported as the average of 4 measurements. All samples were dispersed in ultrapure water unless stated otherwise, and added to either folded capillary zeta cells or disposable plastic cuvettes for measurement.

2.4.3 Zeta Potential

Zeta potential is a physical property that can be measured for any colloidal particle and is the result of a net charge on the surface of the particle. This surface charge affects the distribution of the ions in the surrounding interfacial region and leads to an increased concentration of oppositely charged ions close to the particle surface. The liquid layer surrounding the particles exists as two distinct layers; the inner region is named the Stern layer. The ions here are strongly bound to the surface of the particle due to the electrostatic attraction. Outside of the Stern layer is the diffuse layer where the electrostatic forces are weaker and the ions are less strongly bound. The layers combine to form the electrical double layer. This is represented in the schematic below.

Within the diffuse layer there is a boundary inside of which the particle and surrounding ions form a single stable entity. Therefore, when the particle moves the ions inside the boundary move with the particle. The ions outside of this boundary however will remain in place and not move with the particle. This boundary is referred to as the slipping plane and the potential that exists at this boundary is called the zeta potential. The magnitude of the zeta potential is a strong indicator of the colloidal stability of a sample in suspension. A large negative or positive zeta potential will mean that the particles will repel each other strongly, preventing agglomeration. A smaller or even zero zeta potential will mean that particles are more likely to come together due to the weak electrostatic forces.

The zeta potential of a particle will determine how it behaves when under the influence of

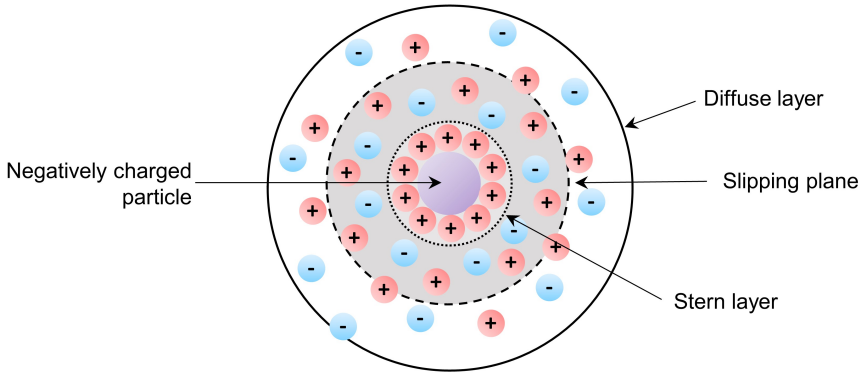

Figure 2.1: Schematic representation of the electrostatic interactions between an negatively charged colloidal particle and surrounding ions resulting in the formation of the electrical double layer.

an applied electrical field will determine how it behaves when under the influence of an applied electrical field. When an electrical field is applied across a medium, the charged particles are attracted to the electrode of opposing charge. The movement of particles is called electrophoresis and the speed at which the particles move at is called the electrophoretic mobility. This is dependent on the strength of the electrical field, the dielectric constant of the medium, the viscosity of the medium, and the zeta potential of the particle. By measuring the electrophoretic mobility, the zeta potential of a sample can be obtained. The two are related by the Henry equation shown in Equation 2.2.

$$U_E = \frac{2\epsilon\zeta}{3\eta} f(Ka) \tag{2.2}$$

Where U_E is the electrophoretic mobility, ζ is the zeta potential, ϵ is the dielectric constant, η is the viscosity, and $f(Ka)$ is Henry's function. For all measurements presented in this work the Smoluchowski approximation is used and therefore $f(Ka)$ is a constant of 1.5.

The electrophoretic mobility of a sample is measured using the technique Laser Doppler Velocimetry (LDV), in which an incident beam of light is scattered at 17 ° angle and combined with a reference beam, this produces a fluctuating signal, the rate of fluctuation is proportional to the speed of the particles. Zeta potential measurements were carried out using a Malvern Zetasizer Nano. The samples were prepared using a folded capillary zeta cell to which approximately 0.7 – 0.8 ml of aqueous sample was added. All measurements were carried out at 25 °C unless stated otherwise.

2.4.4 Small-angle X-ray Scattering

Small-angle X-ray scattering (SAXS) is an analytical technique that measures the intensity of X-rays scattered by a sample as a function of the scattering angle. Typically measurements are made at very small angles, in the range of 0.1 – 5.0 °. SAXS is a versatile technique that can be used for a broad range of materials, such as nanocomposites, polymers, and colloidal suspensions of particles. By evaluating the measured profiles a wide range of properties can be inferred such as nanoparticle size distribution, agglomeration of nanoparticles, and particle structure.

Despite its great utility as a characterisation technique, the SAXS measurements are fairly straight-forward. A solution containing the sample of interest is placed within a capillary and then illuminated with a collimated monochromatic X-ray beam. The intensity of the scattered X-ray photons is then recorded by a detector. The scattering pattern of the pure solvent is also collected and subtracted from the samples, to leave only the scattering pattern of interest. This resulting pattern is determined by the shape and size of the particles being investigated. Due to random orientations of the particles in solution the scattering pattern is isotropic. The patterns are then plotted as one-dimensional curves and used for further analysis.

Small-angle X-ray scattering (SAXS) measurements were carried out by Dr Stephen Hall of the University of Warwick and performed using a Xenocs Xeuss 2.0 equipped with a micro-focus Cu K_α source collimated with scatterless slits providing a 0.8 mm diameter beam. Samples measured were stable aqueous suspensions of particles which were loaded into 1 mm path length borosilicate capillaries. SAXS patterns were recorded using a Pilatus 300K detector with a pixel size of 0.172 mm × 0.172 mm. The sample to detector distance was calibrated using silver behenate ($AgC_{22}H_{43}O_2$) providing a value of 2.481(5) m, providing an effective scattering vector, Q, range of 0.005 – 0.160 $Å^{-1}$ where Q is defined as;

$$Q = \frac{4\pi sin\theta}{\lambda} \tag{2.3}$$

Where 2θ is the scattering angle λ is the X-ray wavelength. Data was collected for 4 hours at 25 °C. A radial integration of the 2D scattering profile was performed using FOXTROT software with the resulting data corrected for the absorption, sample thickness, and background.[274] Finally, the scattering intensity was then rescaled to absolute intensity using glassy carbon as a standard.[275] SAXS data were analysed using model-dependent analysis implemented within SasView software (www.sasview.org).[276] A model describing a fractal aggregate of spherical particles was used, as has been described in detail elsewhere.[277] The scattering length density

(SLD) defining the 'scattering power' of a material is defined as the sum of X-ray scattering lengths, b_i, of N atoms within a given molecular or particular volume, V_m, as given by;

$$SLD = \frac{\sum_{n=1}^{N} b_i}{V_m} \tag{2.4}$$

The SLD of a material can also be calculated using the bulk density, ρ, atomic molar mass, M_i, and Avogadro's constant, N_a, where;

$$SLD = \frac{\rho N_a \sum_{i=1}^{N} b_i}{\sum_{i=1}^{N} M_i} \tag{2.5}$$

Throughout the fitting procedure, the SLD of water and the ferrite nanoparticles were calculated as 9.47 $\times$ 10^{-6} Å^{-2} and 41.1 $\times$ 10^{-6} Å^{-2}, respectively, and held constant. Based on nanoparticles dispersity observed by DLS and TEM, a polydispersity was applied to the nanoparticle radius as a Schultz distribution and held at a value of 0.2. All other parameters were permitted to vary throughout the fitting procedure.

2.4.5 Infrared Spectroscopy

Infrared (IR) spectroscopy is one of the most common and widely used spectroscopic techniques and gives information on the specific functional groups present within a sample. IR data can be compared to existing banks of spectra and be used for both quantitative and qualitative analysis. As the name suggests, IR spectroscopy exploits the absorption of IR radiation by matter. Chemists are particularly interested in the mid-IR range, with radiation of a frequency in the range 3 $\times$ 10^{-4} to 3 $\times$ 10^{-3} cm^{-1}.

Absorption of IR radiation excites rotational and vibrational modes into higher quantised energy levels. As a molecule vibrates there is a fluctuation in its dipole moment, producing a field which interacts with the electric field on any incident radiation. If there is a match in frequency absorption will occur and the molecule will be excited to a higher vibrational energy level. This will also occur for the rotation of asymmetric molecules. For IR radiation to be absorbed there must be a change in dipole moment associated with the vibrational or rotational mode. When measuring IR spectra, the % transmission is plotted against the frequency in wavenumbers (cm^{-1}). Wavenumbers are an easy way to visualise the energies of the vibrational and rotational modes. The higher the wavenumber the higher the energy.

A molecule consisting of n atoms has a total $3n$ degrees of freedom. For a non-linear molecule, 3 of the degrees are rotational and 3 translational, leaving $3n - 6$ vibrational modes. In a linear molecule, where all atoms lie along one axis, there is 1 fewer rotational modes, giving

$3n - 5$ vibrational modes. When two vibrations are equivalent and therefore have the same frequency, they are said to be degenerate. For large polyatomic molecules there will be several vibrational modes, with both stretching and bending vibrations. The stretching frequencies can be approximated using Hooke's Law where the two atoms and connecting bond are treated as a harmonic oscillator.

In this work, all IR spectra were recorded using either a Bruker Alpha FTIR spectrometer or a Shimadzu IRTracer-100 FTIR spectrometer. Both machines were used in attenuated total reflectance (ATR) mode. The spectra were measured in the range 4000 – 400 cm^{-1}, the total number of scans and the resolution was adjusted depending on both the sample and the machine used. All samples were measured as dried solid powders unless stated otherwise.

2.4.6 Raman Spectroscopy

As with other discussed forms of spectroscopy, Raman spectroscopy detects certain interactions between matter and light. Most similar to the previously mentioned IR spectroscopy, it is used to determine the vibrational modes of molecules. However, unlike IR it relies upon the scattering rather than the absorption of light. When an intense light source such as a laser is directed at a material a proportion of that light will be scattered in all directions. The majority of that light will be scattered elastically; the scattered and incident light will have the same wavelength. A tiny fraction however will be scattered inelastically. The incident light will exchange energy with the matter resulting in a shift in frequency of the scattered light. This inelastic scattering is a result of the excitation or de-excitation of vibrational modes. The character of these vibrations will determine the wavelength of the scattered light. This is the main principle of Raman spectroscopy.

There are three scattering processes that are important for Raman spectroscopy, in all, an incident proton of energy $h\nu$ raises the vibration mode to one of an infinite number of short-lived "virtual" states, before relaxing back to a lower energy state. These are visualised in Figure 2.2. The most dominant scattering process is Rayleigh scattering, in which after being excited to the virtual state, the vibrational mode relaxes back to its original state. The photon has thus been scattered elastically, resulting in no change in wavelength meaning that Rayleigh scattering does not provide useful information for Raman spectroscopy.

Stokes scattering is the most exploited scattering process, whereby after excitation to the virtual state, the molecule returns to a higher vibrational energy level. The scattered photon will therefore have an energy equivalent to $h\nu - \Delta E$. ΔE will be equal to the amount of energy

required to excite one of the vibrational modes and can therefore be used to identify the mode. Stokes scattering is however less likely to occur than Rayleigh scattering. The least common scattering process is anti-Stokes scattering in which the molecule begins in a vibrationally excited state and after excitation to the virtual states relaxes to a lower vibrational energy level. The scattered photon will now have an energy of $h\nu + \Delta E$, with ΔE being the amount of energy required to excite a vibrational mode.

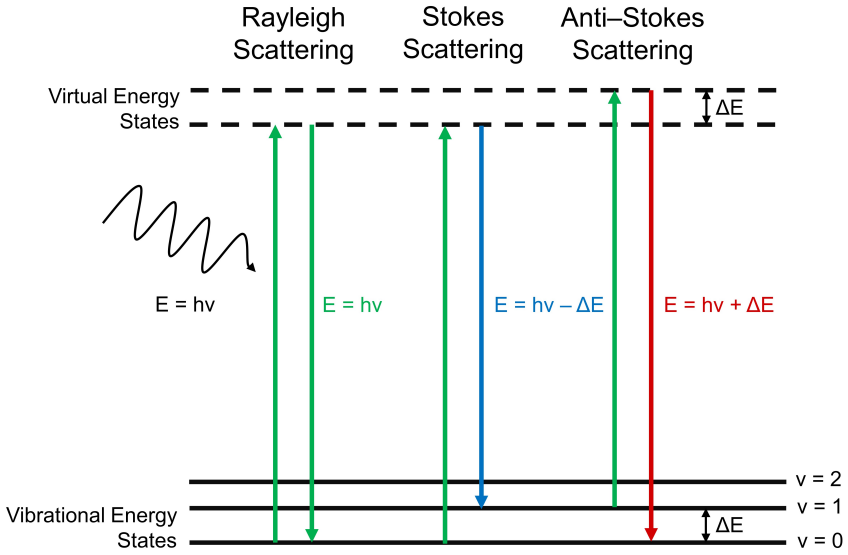

Figure 2.2: Schematic representation of Rayleigh, Stokes, and anti-Stokes scattering.

Raman spectroscopy therefore observes the change in energy of the incident and scattered photons associated with Stokes and anti-Stokes scattering. Like IR, this energy is typically measured in wavenumbers (cm^{-1}). Both IR and Raman are complementary techniques, as vibrations that are inactive by one mechanism may be active for the other. This is because the two techniques operate according to different selection rules. As mentioned in Section 2.4.5, IR spectroscopy requires either a change in the dipole moment or a change in charge distribution associated with a vibrational mode. Raman signals on the other hand, occurs due to a molecules polarizability. When subjected to an electrical field the negatively charged electrons and positively charged nuclei are subject to opposite forces and undergo charge separation. Polarizability is defined as the ratio of the induced dipole moment to the electrical field. Where α is the polarizability, p is the induced dipole moment, and E is the strength of the electrical

field.

$$\alpha = \frac{p}{E} \tag{2.6}$$

A Raman transition between states is only allowed if the polarizability of those vibrational states is different. Where there is a large concentration of loosely held electrons polarizability will be larger, the larger the polarizability the more intense the Raman signal.

All Raman spectroscopy was collected on dried solid powder samples, using a Renishaw Raman inVia microscope with a 785 nm He-Ne laser (operated at 10% equivalent to 0.76 mW).

2.4.7 X-ray Diffraction

X-ray diffraction (XRD) is a rapid analytical technique primarily used for phase identification of crystalline materials. XRD is based on the constructive interference of monochromatic X-rays as they are diffracted by a crystalline sample. The long range orderly arrangements of atoms within a crystal lattice scatter the incident X-ray radiation, resulting in constructive interference at specific angles. The resulting diffraction pattern contains useful information on the atomic arrangement within the crystal.

Parallel planes of atoms intersecting the crystal's unit cell (the basic repeating unit that defines the crystal structure) are used to define directions and distances with that crystal. Each of the plane are assigned a miller index, denoted as (hkl), where hkl is the reciprocal of the axial intercepts. The observed diffractions peaks are related to these planes of atoms; each with its own miller index. The position and intensity of the peaks in a diffraction pattern are determined by the distance between parallel planes of atoms, also known as the d-spacing (d_{hkl}), and therefore the crystal structure. The angle (θ) at which the constructive interference will result in a peak can be calculated using Bragg's law (Equation 2.7). The geometry underpinning Bragg's law is portrayed in Figure 2.3.

$$\lambda = 2d_{hkl} \sin\theta \tag{2.7}$$

Where λ is the wavelength of the incident X-rays. For parallel planes of atoms with a spacing of d_{hkl}, constructive interference only occurs when Bragg's law is satisfied. As every crystal structure will have a unique set of d_{hkl}, diffraction patterns can be used to identify the crystalline material. Typically the diffraction peak positions and intensities are compared against standard references in the Joint Committee on Powder Diffraction Standards (JCPDS) database.

In this body of work powder XRD is utilised. The advantage of this rather than single crystal XRD is that within a powder (or polycrystalline) sample all possible crystal orientations should

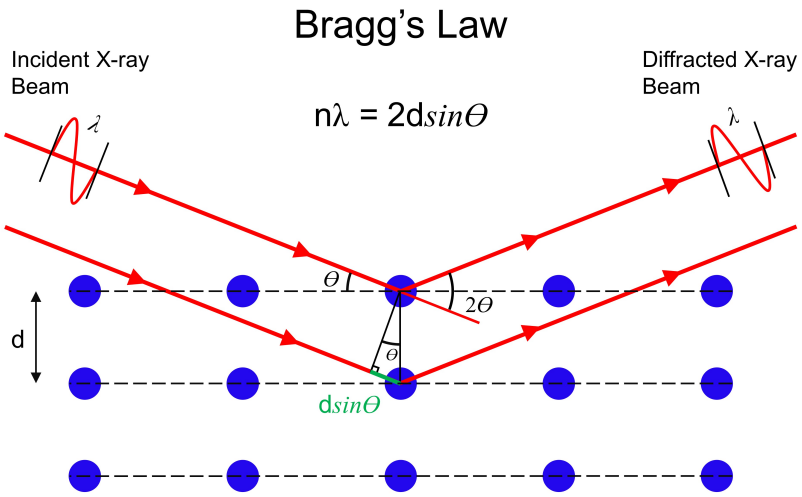

Figure 2.3: Schematic representation of the Bragg diffraction of an X-ray of wavelength, λ by a crystalline material with d-spacing equivalent to d.

be present if the quantity of sample is sufficient. Therefore, assuming that all crystals within a sample are randomly arranged, there will be a statistically significant number of each plane in the correct orientation to diffract the X-rays. This then allows for all possible diffraction peaks to be observed.

The radiation for XRD is produced by bombarding a pure metal anode with a high energy electron beam produced from a tungsten filament. The X-rays are then filtered to produced monochromatic radiation and collimated to concentrate the beam, before being directed toward the sample. The wavelength of the produced X-rays is determined by the metal used for the anode, examples being copper and molybdenum. In this work all powder XRD was performed using a STOE Stadi-P diffractometer with a molybdenum X-ray source (operated at 50 kV and 30 mA), $\lambda = 0.7093$ Å. The 2θ scan range was 2 – 40.115 ° and 5 seconds per step. Samples were prepared using STOE zero scattering foils before being inserted into the transmission sample holder.

The peaks observed in the produced XRD diffraction patterns were analysed using the Scherrer equation (Equation 2.8) which defines the inversely proportional relationship between

the width of a peak and the crystallite size.

$$D = \frac{K\lambda}{Bcos\theta} \tag{2.8}$$

Where D is the crystallite size in nm, K is a dimensionless shape factor and in this instance is set to 0.9, λ is the wavelength of the incident X-rays, and B is the line broadening. The broadening is measured from the peak width at half peak height obtained from the Warren formula (Equation 2.9).

$$B = \sqrt{B_m^2 + B_s^2} \tag{2.9}$$

Where B_m is the measured peak width at half height (obtained from Origin Software peak fitting) and B_s is the standard peak width at half height obtained from a commercial sample.

2.4.8 X-ray Fluorescence

X-ray Fluorescence (XRF) is a non-destructive analytical technique commonly used for elemental and chemical analysis of materials. As with many other techniques detailed in this work, such as SEM, EDS, and XRD, it depends on the fundamental atomic interactions between incident high energy electron beams, primary and secondary X-ray photons, and a samples atoms. As the name suggests this technique uses the phenomenon of X-ray fluorescence whereby the elemental composition of a material can be identify through the characteristic fluorescent X-rays that are produced when a sample is bombarded with high energy X-rays.

The process of X-ray fluorescence is as follows; first a sample is irradiated with high energy X-ray photons. X-rays are generated when electrons at a high voltage are directed towards a metal anode (typically tungsten, rhodium, molybdenum, or chromium). When a photon strikes an atom with sufficient energy (greater than the atoms K or L shell binding) an electron from one of the inner orbital shells is dislodged. This new vacancy in the inner shell is then filled by an electron from a higher energy orbital shell. To do this the high energy electron must release the difference in the form of a fluorescent X-ray. The energy of the emitted photon is therefore equal to the energy difference between the inner and outer shell. This will be characteristic for that specific transition for that element. Fluorescent X-rays emitted by the sample are directed towards a solid state detector where they ionize a number of the atoms in the detector. The amount of charge produced is proportional to the energy of the incoming photon. Charge is collected before the process is repeated by the next incident X-ray. Finally a spectrum is produced by sorting energy spectrum into discrete energy bins.

All XRF analysis was carried out using a Malvern Panalytical Epsilon 4 bench top XRF analyzer. Samples used were dried fine powders prepared using Panalytical plastic sample cups and Chemplex mylar thin film support windows.

2.4.9 Vibrating Sample Magnetometry

Vibrating sample magnetometry (VSM) is a technique used for the characterisation of the magnetic properties of both bulk and nano- materials. The key principle underpinning VSM, is Faraday's Law of Induction, that is where an electromotive force (EMF) can be induced within a conductive coil by a changing magnetic field. This law is described in Equation 2.10. Where ϵ is the induced voltage, N, is the number of loops within the coil, $\Delta\phi$ is the change in the magnetic flux, and Δt is the change in time. By measuring the induced voltage as a sample is vibrated we can gather information on the magnetic field produced and therefore are able to characterise the magnetic material.

$$\epsilon = -N\frac{\Delta\phi}{\Delta t} \tag{2.10}$$

When taking a VSM measurement, the sample is first placed within a constant external magnetic field in order to magnetise the sample, aligning the magnetic domains with the field. The stronger the external field, the larger the magnetisation will be. The induced magnetic dipole moment of the sample will produce its own magnetic stray field. This stray field will change as a function of time as the sample is oscillated, and according to Faraday's Law given above, a detectable EMF is produced. The voltage detected will be proportional to the magnetisation of the sample. For a typical measurement, the strength of the external field is set to 0 and the sample begins to vibrate, the corresponding voltage is translated into a value for the magnetic moment of the sample. The strength of the field is then adjusted and another measurement is recorded. As the field is changed a plot of magnetisation (M) vs magnetic field (H) is generated, and by sweeping from a positive field to a negative and the back, the plot will form a hysteresis loop. An example of such is given in Figure 2.4.

These loops result from the magnetisation of a ferromagnetic material, which when magnetised in one direction will remain magnetised once the external field is removed. From the M vs H plot it is possible to extract particular properties of a material. The magnetisation at which it no longer increases with H is the saturation magnetisation (M_s). The remaining magnetisation when the field strength is returned to zero is the retentivity or remanence (M_r), and the required magnetic force to return the magnetisation back to zero is the coercivity (H_c).

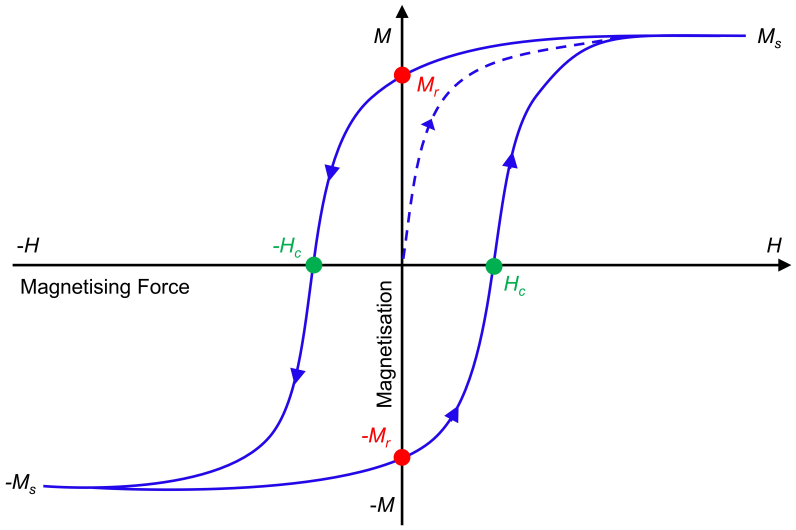

Figure 2.4: An example of a typical magnetisation (M) vs magnetic field (H) plot, with the saturation magnetisation (M_s), remanence (M_r), and coercivity (H_c) labelled. The dashed line represents the initial increase in magnetising force.

Magnetisation measurements were carried out in the range -20.0 kOe to 20.0 kOe using a Quantum Design Physical Property Measurement System Vibrating Sample Magnetometer (VSM). The data is adjusted for the mass of sample measured to give the magnetisation in emu g^{-1}, this is based on the total mass of the solid sample, including the contribution in mass from any possible non-magnetic components.

2.4.10 Mössbauer Spectroscopy

Mössbauer spectroscopy is a powerful analytical technique that can give precise information on the chemical, structural, and magnetic properties of a material, through the absorption and re-emission of gamma-rays. The technique is built on the principles of the Mössbauer effect and Doppler shift, and probes the hyperfine transitions from the ground to an excited state of a nucleus. To be suitable for Mössbauer spectroscopy, a sample must be either solid or crystalline, and be able to absorb gamma radiation in a recoilless manner. The most commonly studied materials are those that contain the ^{57}Fe isotope.

Atomic nuclei frequently undergo various energy level transitions through the emission and

absorption of gamma rays. These energy levels can be split by various factors such as magnetic field and electric charge. Such splitting can give detailed information on the nucleus' local environment. These "hyperfine" interactions are very small however, making them difficult to detect. Typically, as a nucleus absorbs or emits a gamma photon it recoils due to the conservation of momentum, with the energy E_R. For resonant emission and absorption this loss of energy must be overcome. For a nucleus within a solid matrix, there is a probability that the momentum of recoil is delivered to the surrounding crystal lattice rather than the emitting or absorbing nucleus. This results in no energy being lost, and therefore the emitted and absorbed gamma photons will have equivalent energies, and resonant absorption is observed. Resonance will only occur when the transition energy of both the emitter and absorber are exactly matched, meaning it is isotope specific. The Mössbauer effect is only detected in isotopes with very low lying and long lived excited states.

In order to achieve the miniscule variations in emitted gamma ray energy needed to observe nuclei that are in different environments, the Doppler effect is used. The radioactive sources is oscillated at a few mm/s and where the modulated gamma ray energy matches the energy of a transition, a peak is produced from the resonant absorption. For simplicity mm/s is the conventional unit for energy in Mössbauer spectroscopy. The energy levels of an absorbing nuclei can be modified in three ways; isomer shift, quadrupole splitting, and magnetic splitting.

Isomer shift arises from non-identical atoms acting as emitter and absorber. The electron density will differ and therefore the coulombic interactions will affect the ground and excited stated differently. This difference will cause a shift in the resonance energy, and provides information on valency states, ligand bonding states, and electron shielding. For example, Fe^{3+} will have a greater positive isomer shift than Fe^{2+} ions.

Quadrupole splitting occurs for nuclei in states with an angular momentum quantum number $I > \frac{1}{2}$. This is due to the non-spherical charge distribution of such states, resulting in a nuclear quadrupole moment. The energy levels of such states split in the presence of an asymmetrical electrical field. For example, ^{57}Fe has $I = \frac{3}{2}$, where the excited state is split into two substates and is seen as a doublet peak on the spectrum.

Magnetic splitting is seen only when a nucleus is in the presence of an external magnetic field. Inside of which the nuclear spin experiences a dipolar interaction with the magnetic field. This splits the nuclear levels with a spin of l into $(2l + 1)$ substates. For ^{57}Fe this results in the formation of a sextet. The spacing of the peaks is proportional to the strength of the magnetic field acting on the nucleus, the line positions are related to the energy difference between the

split substates, and the relative intensities give information on the moment orientation and magnetic ordering in the sample.

In this work, room temperature ^{57}Fe Mössbauer spectroscopy was performed using a SeeCo W302 spectrometer (SeeCo Inc., USA) operated in constant acceleration mode. Samples were prepared for measurement by mixing the dried powder with sucrose using a pestle and mortar, forming a paste, which was then mounted into a 2.1 cm coin shaped absorber. Samples were mounted in transmission geometry, with a ^{57}Co in Rh foil 14.4 KeV γ-ray source. Velocity calibration was performed by recording a reference spectrum from a 10 μm thick foil of αFe, also at room temperature. For all data analysed, the spectra were folded and the baselines corrected using cubic spline parameters derived from the fitting of the αFe calibration spectrum, following a protocol implemented in the Recoil analysis program.[278] Spectra were least-squares fitted using the 'centre-of-gravity' method, in which Voigtian lineshapes (representing Gaussian distributions of Lorentzian lines) were used in all samples.[279] The running of the measurements as well as the fitting of the produced spectra was carried out by Dr Lara K. Bogart of the UCL Healthcare Biomagnetics Laboratory.

2.5 Characterisation of Relaxometric Behaviour

2.5.1 Fast Field Cycling Relaxometry

Fast field cycling (FFC) NMR relaxometry is a powerful characterisation method for measuring the longitudinal relaxation rate (R_1) as a function of magnetic field strength over a wide range of wide frequencies (a few kHz to 100 MHz). The measured R_1 is linked to the molecular dynamics of a substance or complex material, therefore by measuring R_1 at lower frequencies it is possible to reveal slower molecular dynamics of the material. The technique can be applied to the characterisation of a wide range of complex systems such as porous materials, biomolecules, and polymers. It is also used for the characterisation of MRI contrast agents allowing for the determination of co-ordination numbers, correlation times, and characterising diffusional dynamics and exchange kinetics.

The field dependence of R_1 for a sample is represented in graphical form as a nuclear magnetic resonance dispersion (NMRD) profile. Changes in R_1 are caused by a change in the molecular dynamics of a system, however these changes may not be evident at certain field strengths. Though when measuring over a wide range of frequencies changes become

easier to identify and typically are more visible at lower field strengths. NMRD profiles can be interpreted using available material specific models, thus giving insight into the underlying molecular dynamics.

During FFC measurements the magnetic field strength is rapidly cycled, allowing relaxation to occur at a wide range of fields but always returning to the same field strength for detection of NMR signals. FFC pulse sequences comprise of three distinct periods; polarisation, evolution, and detection. Each are applied at a different magnetic field strength. The first period is for polarisation and increases the amplitude of signal response. The second period is where the spin system is at the field of interest with its corresponding T_1 value. The final period then serves as the field strength for detection of the MRI signal.

Measurement of ^{1}H NMRD profiles were performed on a Stelar Spinmaster FFC2000 1T instrument in the range of 0.01–20 MHz Larmor frequency at two different temperatures (25 and 37 °C). The temperature was controlled using a Stelar VTC-91 airflow heater, equipped with a copper/constantan thermocouple; the temperature calibration in the probe head was done so using a Delta OHM digital thermometer, with an absolute accuracy of 0.5 °C. Fast field cycling (FFC) relaxometry was used to determine the longitudinal relaxation decay over a range of relaxation fields (0.01 – 40 MHz). A set of 24 relaxation interval values (τ) allowed description of the spin-lattice decay curves for each relaxation field. A standard fitting algorithm (mono-exponential relaxation decay curve) allowed for the evaluation of the relative longitudinal relaxation rate ($R_1 = 1/T_1$, s^{-1}, where T_1 is the measured longitudinal relaxation time of water protons in seconds), which was converted to relaxivity using the following equation.

$$r_1 = \frac{R_1}{[CA]} \tag{2.11}$$

Where R_1 the observed relaxation rate of the agent in aqueous suspension) and [CA] is the mM concentration of the contrast agent is suspension, as measured using inductively couple plasma optical emission spectroscopy (ICP-OES).

2.5.2 Single Field Relaxometry

The effectiveness of samples as MRI contrast agents was also assessed using single field relaxometry. This technique allows for the measurement of both the transverse (T_2) and longitudinal (T_1) relaxation rates at a single field strength. Two different pulse sequences are required to measure the two different relaxation rates. To measure the T_1, the inversion-recovery sequence is used. There is an initial 180 degree pulse to invert the net magnetisation followed by a 90

degree radiofrequency (RF) pulse. The time difference between the two pulses is called the inversion time (TI). The purpose of the initial inverting pulse is to flip the M_0 parallel to the external field, B_0, leading to longitudinal relaxation as the magnetisation relaxes back to the positive direction. The 90 degree pulse is needed so that the magnetisation is in the xy plane and can be detected. Therefore by changing the inversion time the magnitude of M_0 as measured in the xy plan will also change. A plot of magnetisation against TI provides a logarithmic growth curve from which the T_1 can be obtained.

To measure the transverse relaxation rate, the Carr-Purcell-Meiboom-Gill (CPMG) pulse sequence is used. Spin echoes are two successive RF pulses, the initial being a 90 degree pulse that is followed by a 180 degree pulse. The net magnetisation is tipped into the transverse phase. The spins then begin to dephase due to differences in local fields acting on the individual spins. The 180 degree pulse flips the spins so that the faster spins catch the slower spins and they are realigned before dephasing again. The CPMG sequence using multiple 180 degree pulses applied after the initial 90 degree pulse, with the interval between each 180 pulse increasing. As the spins are not able to be completely align due to transverse relaxation the measured magnetisation in the xy plane will decay exponentially. The T_2 relaxation can be resolved from the decay curve produced.

Measurements of r_1 and r_2 at a fixed field strength were carried out using an Oxford Instruments MQC+ bench top NMR analyser with a resonant frequency of 23 MHz operated at 25 and 37 °C. A minimum of 6 different concentrations of stable nanoparticle samples were prepared in either ultrapure water or Xanthan gum (specified for measurements) and relaxation time measured for each sample. Relaxivity values, $r_{1,2}$, were calculated from the plotting of the measured relaxation rate $R_{1,2}$ ($1/T_{1,2}$, s^{-1}) vs. [Fe] concentration (mM, as measured by ICP-OES), and subsequently taking the slope from the line of best fit. The values are also normalised with regards to the relaxation resulting from the solvent system. Relaxivity values presented for all samples are the mean of a minimum of 3 samples of the identical composition, with the error being the corresponding standard deviation from the mean. Exceptions to this will be clearly noted as such.

2.5.3 Inductively Coupled Plasma Optical Emission Spectrometry

To calculate the relaxivity of the samples measured by both single field and FFC relaxometry, the metal concentration within a sample must be known. This is measured using inductively coupled plasma optical emission spectroscopy (ICP-OES). This is an emission spectrophoto-

metric technique which is capable of the high accuracy and sensitivity required to determine the concentration of metals in relaxometry samples. A plasma source is used to transform a sample to its constituent ion and excite them to a higher electronic energy level. As they return to their ground state, a photon of a specific wavelength is emitted that is characteristic of their ionic composition. Once compared to standard solutions that concentration of detected ions can be determined.

ICP was carried out using either; an ISA Jobin Yvon Ultima 2C inductively coupled plasma-optical emission simultaneous/sequential spectrometer (ICP-OES) running at 1 KW power with a 40.68 MHz radiofrequency argon plasma; plasma gas flow was 14 L min^{-1}. Nebuliser pressure was 2.6 bar at 1 ml min^{-1} sample flow rate. Or an Agilent Varian 720 ICP-OES running at at 1KW power with a 40 MHz radiofrequency argon plasma; plasma gas flow was 15 L min^{-1} and nebuliser flow rate was 0.75 L min^{-1}. The spectral line for iron was measured at 259.94 nm. Samples were digested for ICP-OES using hot nitric acid (70 %) and diluted in ultrapure water prior to analysis. Samples were then measured against standards provided by QMX Laboratories. Concentrations measured by this technique were used to normalise all relaxation data according to Equation 2.11. ICP measurements were carried out by Connor Wells of University College London (UCL) and Dr Joseph Bear of Kingston University.

Chapter 3

Exploring Precision Polymers to Fine-tune MRI Properties of Iron Oxide Nanoparticles

3.1 Introduction

In the introduction to this thesis, the role of dipolar interactions between neighbouring MNPs in determining the MRI contrast capabilities of a negative contrast agent is highlighted. This has resulted in recent trends towards developing magnetic nanostructures in which such interparticle interactions are encouraged, typically through the formation of more intricate assemblies of multiple magnetic cores. One such method of particular interest is the formation of linear assemblies of magnetic nanoparticles, formed using an *in situ* co-precipitation method, whereby magnetic nanoparticles are precipitated in the presence of a 'templating' polyelectrolyte, such as PSSS and heparin.[71,98]. These examples were able to show that the polymer backbone that was introduced during the co-precipitation of the iron oxide nanoparticles encouraged strong dipolar interactions between particles which subsequently resulted in increased r_2 values.

These two examples also give instances in which attempts are made at tuning these interactions by making adjustments to the ratio of reagents (metal salts to polymer), the effects of which were examined using fast field cycling (FFC) relaxometry (see Section 1.5.3 for further details on this technique). Both showed that it is indeed possible to tune the relaxometric

behaviour of polyelectrolyte stabilised magnetic nanoparticles, as seen by changes in the the low field longitudinal relaxivities dependent upon the ratios of the different reagents. However, whilst demonstrating the potential for controlling interparticle interactions using templating polymers, commercially available polymers generally suffer from high polydispersity and poorly controlled molecular weight distributions. This can detrimentally impact reproducibility, limiting the control over important interactions that we seek and ultimately the MRI contrast performance.

Therefore, the aim of the work detailed within this chapter is to produce a family of polymer-stabilised IONP based negative MRI contrast agents, that exhibit high r_2 values, whilst also showing how the use of a carefully selected polymer affords the possibility of finely tuning the colloidal, magnetic, and relaxometric properties of the contrast agent. For this purpose, the heparin-mimicking polymer poly(2-acrylamido-2-methylpropane sodium sulfonate), herein referred to as P(AMPS) was selected due to having a much narrower molecular weight distribution compared to it's commercial alternative ($Đ_{\text{heparin}} = 1.88$, $Đ_{\text{P(AMPS)}} = 1.14 - 1.49$), this will afford greater control over the number of negative sulfonate seeding sites and thus regulate the templating of iron oxide nanoparticles at these sites, with the possibility of more precise tuning of interparticle interactions and hence MRI contrast behaviour. P(AMPS) has demonstrated excellent biocompatibility and low haemolytic activity, making it an ideal candidate for biomedical application.[271,280].

To achieve the desired aim of this work, 9 compositions of P(AMPS) stabilised IONPs were synthesised through combining 3 different polymer chain lengths with 3 different molar quantities of iron salts. This allowed for the seeding density to be probed. The resulting assemblies of IONPs subsequently had their colloidal, magnetic, and relaxometric properties characterised using a range of techniques in order to determine how their properties differ and to devise a structure-property relationship for the seeding density of IONPs along a polyelectrolyte and their resulting MRI behaviour.

3.2 Preparation of Iron Oxide Nanoparticles

Non-stabilised iron oxide nanoparticles were prepared using a co-precipitation technique in which Fe^{2+} and Fe^{3+} salts are mixed in an oxygen free environment under basic conditions with mild heating, as described in the Experimental chapter, Section 2.2.2.

$$2\,FeCl_3 \cdot 6\,H_2O + FeCl_2 \cdot 4\,H_2O \xrightarrow{NH_4OH} Fe_3O_4 \tag{3.1}$$

Iron oxide nanoparticles stabilised with the synthetic polymer, P(AMPS), were also prepared using the *in situ* co-precipitation method as described in the Experimental chapter, Section 2.2.3. Briefly P(AMPS) of the different number average molecular weights ($M_{n,SEC}$ values of 8,100, 17,600, and 41,300 g mol^{-1} with $Đ$ of 1.10, 1.16 and 1.51 respectively) were initially prepared and characterised by the Perrier group using size exclusion chromatography (See Table 3.1) using a previously published approach.[271] The stabilised iron oxide nanoparticles were produced by the co-precipitation of Fe^{3+} and Fe^{2+} salts (at a molar ration of 2:1) in the presence of the P(AMPS) polymers. With the intention of probing the effect of nanoparticle seeding density on the MRI contrast enhancement, composites were prepared using varied total [P(AMPS)]:[Fe] molar ratios of 1:100, 1:2500, 1:6250, using each of the 3 P(AMPS), resulting in a total of 9 unique compositions of P(AMPS) stabilised iron oxide nanoparticles. Schematic representation is given in Figure 3.1.

Table 3.1: Theoretical and experimental molecular weights of the P(AMPS) used for the synthesis of P(AMPS)-stabilised iron oxide nanoparticles

Degree of Polymerisation	**[AMPS] : [CTA] : [VA-086] (mol L^{-1})**	**$M^a_{n,th}$ (g mol^{-1})**	**$M^b_{n,SEC}$ (g mol^{-1})**	**Đ^b**
20	20 : 1 : 0.033	4,800	8,100	1.10
100	100 : 1 : 0.167	23,000	17,600	1.16
400	400 : 1 : 0.667	91,000	41,300	1.51

[a]Theoretical M_n values were calculated using the following equation; $M_{n,th} = ([M]_0 p M_M)/[CTA]_0 + M_{CTA}$; [b]Experimental M_n and $Đ$ values were determined by size exclusion chromatography in 20 % methanol and 80 % of 0.1 M $NaNO_3$ in mili-Q water eluent using a conventional calibration obtained with PEG/PEO standards. The dispersity, $Đ$ was calculated according to $Đ = M_w/M_n$, where M_w is the weight-average molar mass and M_n is the number-average molar mass.

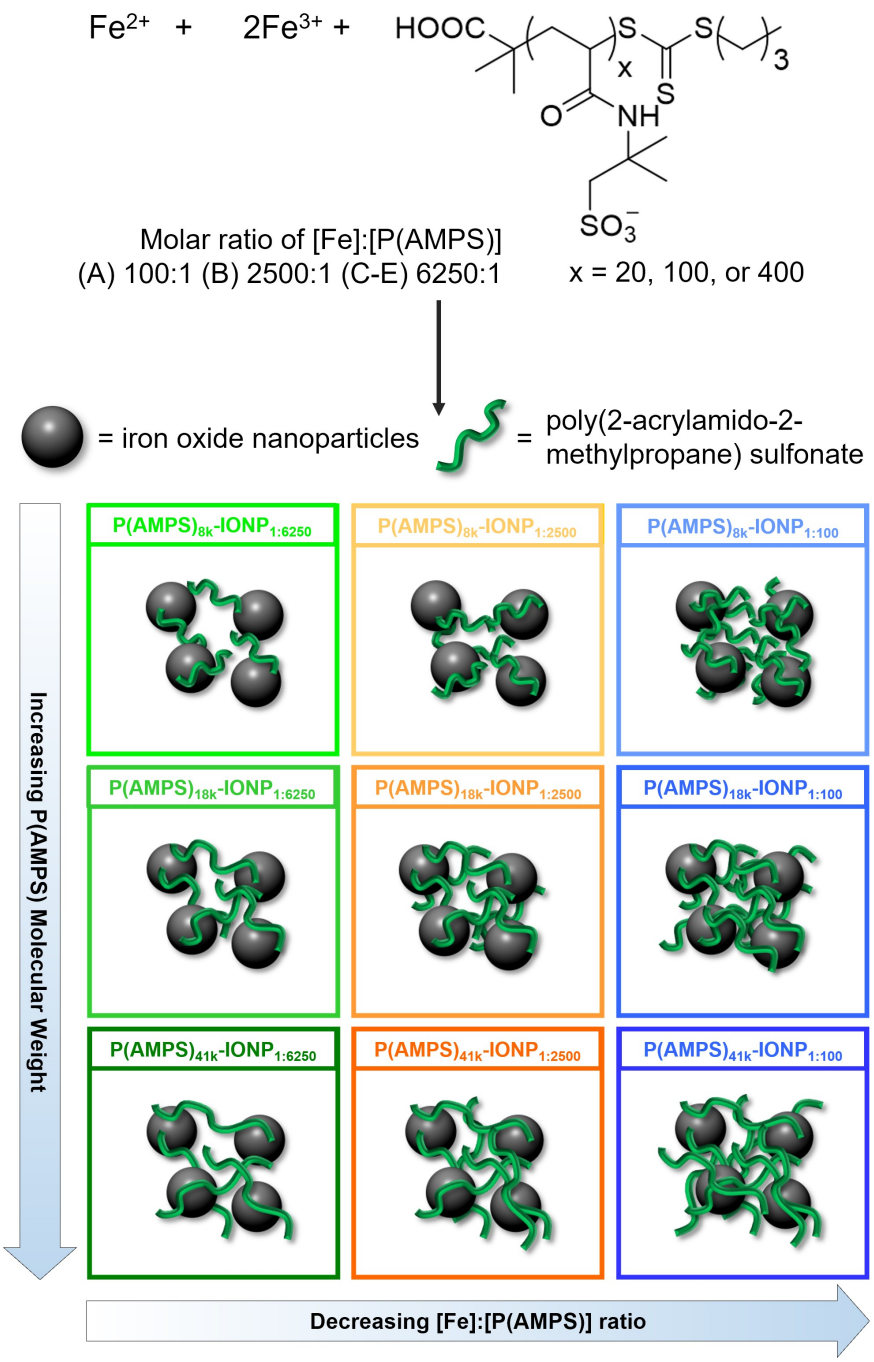

Figure 3.1: Schematic representation of the preparation of poly(2-acrylamido-2-methylpropane) sulfonate (P(AMPS)) stabilised iron oxide nanoparticles, with different polymer molecular weights ($M_{n,SEC}$ = 8,100, 17,600, or 41,300 g mol^{-1}) and molar [P(AMPS)]:[Fe] ratios, as given in Table 3.1.

3.3 Physical & Structural Characterisation

Table 3.2: Molar ratios used during the preparation of poly(2-acrylamido-2-methylpropane) sulfonate (P(AMPS))-stabilised iron oxide nanoparticles and resulting physical characterisation data.

Sample	Total [P(AMPS)]:[Fe] ratio	$M_{n,SEC}$ (g mol^{-1})[a]	d_{hyd} (nm)[b] [PDI]	ζ-pot (mV)[b]	d_{core} (nm)[c]
$P(AMPS)_{8k}$-$IONP_{1:6250}$	1 : 6250	8,100	127.3 ± 5.6 [0.319]	-23.5 ± 1.7	11.0 ± 2.4
$P(AMPS)_{18k}$-$IONP_{1:6250}$	1 : 6250	17,600	167.4 ± 10.4 [0.292]	-20.7 ± 1.7	13.9 ± 5.3
$P(AMPS)_{41k}$-$IONP_{1:6250}$	1 : 6250	41,300	105.2 ± 15.1 [0.298]	-15.3 ± 1.2	12.8 ± 3.2
$P(AMPS)_{8k}$-$IONP_{1:2500}$	1 : 2500	8,100	142.8 ± 33.4 [0.370]	-25.7 ± 7.5	12.9 ± 2.8
$P(AMPS)_{18k}$-$IONP_{1:2500}$	1 : 2500	17,600	118.0 ± 13.6 [0.333]	–	12.6 ± 3.2
$P(AMPS)_{41k}$-$IONP_{1:2500}$	1 : 2500	41,300	159.1 ± 30.4 [0.391]	–	13.5 ± 3.7
$P(AMPS)_{8k}$-$IONP_{1:100}$	1 : 100	8,100	255.7 ± 11.0 [0.347]	-13.2 ± 2.1	12.6 ± 3.2
$P(AMPS)_{18k}$-$IONP_{1:100}$	1 : 100	17,600	175.9 ± 17.5 [0.317]	–	12.5 ± 3.6
$P(AMPS)_{41k}$-$IONP_{1:100}$	1 : 100	41,300	690.4 ± 73.2 [0.250]	–	–

[a] Molecular weight of P(AMPS) as measured by size exclusion chromatography (SEC); [b] hydrodynamic diameter (d_{hyd}), zeta-potential (ζ-pot) and polydispersity index (PDI) measured using dynamic light scattering (DLS); [c] d_{core} is the average particle size calculated by measured > 100 particles as imaged using transmission electron microscopy (TEM).

3.3.1 Size Analysis of Nanocomposites

The size of the produced nanocomposites were characterised through transmission electron microscopy (TEM) and dynamic light scattering (DLS), giving the mean core diameter and the hydrodynamic diameter respectively for each of the 9 samples. The images produced by TEM shows the quasi-spherical morphology of the P(AMPS)-stabilised particles, with all 9 measured to have mean core diameters (d_{core}), in the range of 11.0 – 13.9 nm, with the mean diameters all within error of one another. Most interestingly, when the nanoparticles were dried onto TEM grids in the presence of an external magnetic field they would align parallel to the field (2250 Gauss field applied during sample deposition), as seen in the formation of

long linear 'tracks' of particles running parallel to one another. This behaviour is in keeping with the notion that the sulfonated backbone of the P(AMPS) acts as a template along which the nanoparticles seed. This behaviour is well documented for similar polyelectrolyte stabilised agents employed in the preparation of small magnetic nanoparticles.[71,83,98] The electrostatically driven seeding of the iron oxide nanoparticles at the negatively-charged sulfonate sites resulting in a strong interaction between the particles and polymer. When subjected to an external magnetic field, the polymer subsequently directs the assembly of the nanoparticles into the 1D linear arrays as shown in Figure 3.2, caused by the magnetic dipole interactions between neighbouring superparamagnetic particles.

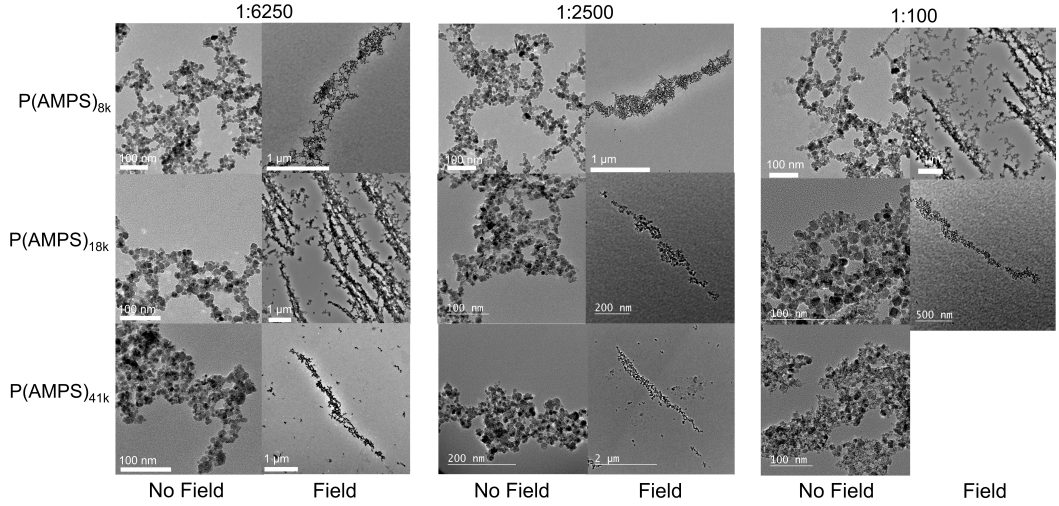

Figure 3.2: Transmission electron microscope (TEM) images collected for P(AMPS) stabilised iron oxide nanoparticles, with samples dried in both the absence of an external magnetic field and in the presence of an external field (denoted by no field and field at the bottom of each column). No image of sample $P(AMPS)_{41k}$-$IONP_{1:100}$ was collected to do non-magnetic very poorly defined particles with weak magnetisation.

Aqueous hydrodynamic diameters (d_{hyd}) of the 9 P(AMPS)-stabilised iron oxide nanoparticle samples, as measured by dynamic light scattering (DLS) (Table 3.2) were found to be in the range 106 – 256 nm. As expected and previously observed, these values were significantly larger than the d_{core} values obtained from TEM, due to the presence of hydrogen bonding and van der Waals forces associated with the polymer stabilisation of the colloids. The d_{hyd} values obtained are larger than similarly prepared iron oxide nanoparticles, for example, heparin-stabilised Fe_3O_4 which demonstrated d_{hyd} of ~40 nm for d_{core} 9.0 nm nanoparticles, indicative

of the presence of larger aqueous clusters of nanocomposites.[98] It is notable that the measured d_{hyd} values do not appear to correlate to the size of the P(AMPS) polymer chains, likely due to the low concentrations of measured samples, and high degree of cross-linking and interactions between neighbouring particles. Measurements were performed on stable suspensions following copious washing procedures resulting in varying concentrations between each of the samples; the d_{hyd} values obtained by DLS therefore cannot be directly compared to one another, and thus no trends can be assigned. Differences in hydrodynamic sizes observed a likely due to the large difference in polymer and particle concentrations leading to difference in cross-linking and Brownian motion behaviour, a well-known phenomenon.[281,282] The impact of the concentration of a suspension of nanoparticles and specifically the observed d_{hyd} is also well documented.[283,284]. The polydispersity index (PDI) quantifies the broadness of distribution of d_{hyd} and is used to estimate the polydispersity and homogeneity of a colloidal sample. Despite the cross-linking that one would expect from the presence of the polymer species in these nanocomposites, PDI values within the range 0.292–0.370 are indicative of their moderate monodispersity. Zeta potential measurements (ζ-pot, Table 3.2) show all samples to have a negatively charged surface as a result of hydroxyl groups adsorbed to the particle surface (confirmed by IR spectroscopy, *vide infra*), as well as the negatively charged P(AMPS) stabiliser.

3.3.2 X-ray Diffraction

Powder X-ray diffraction (P-XRD) was used to confirm the cubic inverse spinel crystal structure of the iron oxide nanoparticles. The reflections observed at 13.8°, 16.2°, 16.9° 19.5°, 23.9°, 25.5°, and 27.8° can be readily indexed to the (220), (311), (222), (400), (422), (511), and (440) planes of the cubic maghemite JCPDS database card number 39-1346.[101]. It is important to note however, that whilst this pattern can be indexed to magnetite, it is also possible to index the pattern to maghemite, which also adopts an inverse spinel crystal structure.[101] Because of the similarities between magnetite and maghemite, XRD is not sufficient in distinguishing between the two. The one sample that does not match this expected pattern is $\mathrm{P(AMPS)_{41k}}$-$\mathrm{IONP_{1:100}}$. This was anticipated however, as during the synthesis of said sample the reaction mixture would reproducibly turn a deep red colour upon the addition of the base, rather than the expected brown/black. This indicates that other iron oxides were being formed (either alongside, or instead of, inverse spinel iron oxide). The very broad and poorly defined peaks in the diffraction pattern make it very difficult to distinguish the phases that are present in the sample due to the overlapping of multiple peaks. The cause of the presence of multiple phases

was attributed to the high concentration of a polymer with a high molecular weight interfering with the seeding of the iron oxide nanoparticles. This is corroborated by the poorly defined particles observed by TEM (Figure 3.2) as well as the low M_s values as measured by vibrating sample magnetometry (*vide infra*, Table 1).

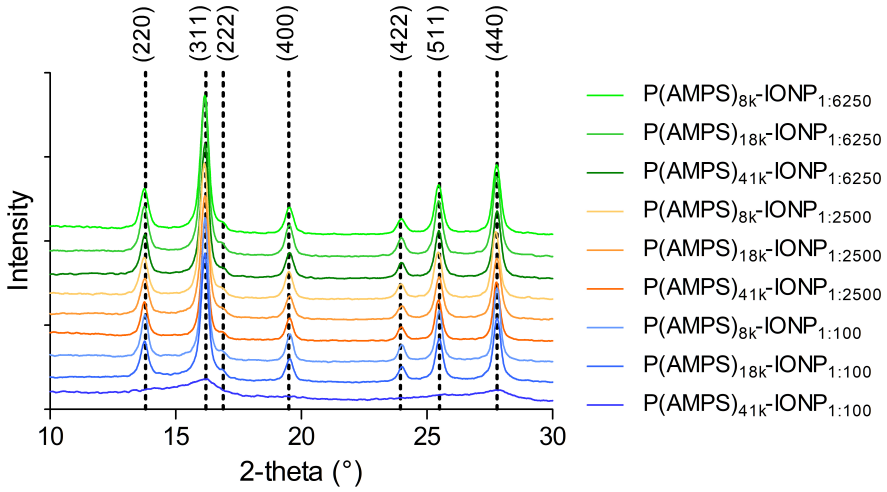

Figure 3.3: XRD patterns of P(AMPS)-stabilised iron oxide nanoparticles ($P(AMPS)_{8,18,41k}$-$IONP_{1:100,2500,6250}$). Dashed lines represent the expected peak positions for cubic inverse spinel type iron oxides according to JCPDS database card number 39-1346. $P(AMPS)_{41k}$-$IONP_{1:100}$ shows much broader peaks due to likely presence of other non-inverse spine type iron oxides as a result of improper seeding of particles.

3.3.3 Raman Spectroscopy

The Raman spectra of P(AMPS)-stabilised iron oxide nanoparticles featured a large peak at 670 cm^{-1} which can be attributed to the the A_{1g} modes of either magnetite and/or maghemite. (Figure 3.4).[285,286] A broad peak at 368 cm^{-1} represents the T_{2g} mode of maghemite, and another at 494 cm^{-1} attributed to the E_g of maghemite.[285,286]. The appearance of peaks that are characteristic of both inverse spinel iron oxides, maghemite and magnetite, demonstrates the likelihood that a mixture of phases is present. The Raman spectra is therefore inconclusive for determining the phase composition of the iron oxide nanoparticles.

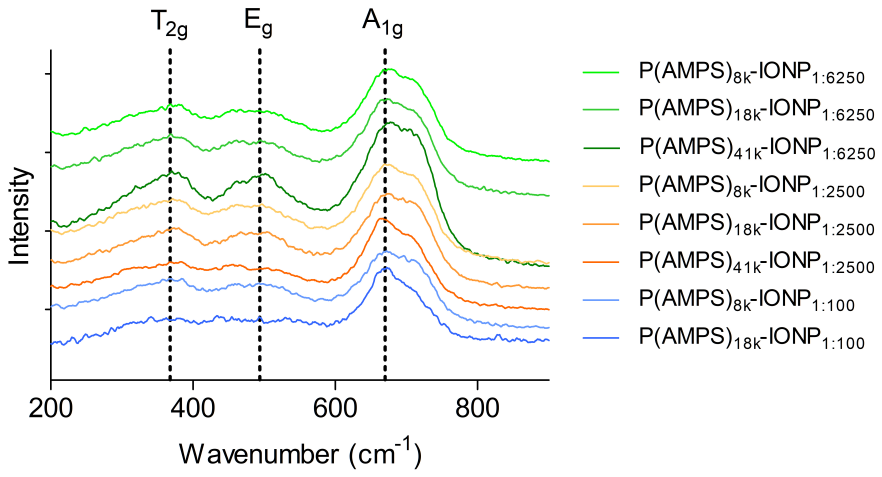

Figure 3.4: Ramam spectra of P(AMPS)-stabilised iron oxide nanoparticles ($P(AMPS)_{8,18,41k}$-$IONP_{1:100,2500,6250}$). The relevant vibrational modes are highlight by the dashed lines and the corresponding modes are labelled. All spectra measured in the range 200 – 900 cm^{-1}

3.3.4 Infrared Spectroscopy

Through the use of infrared spectroscopy it is possible to confirm the presence of P(AMPS) on the iron oxide nanoparticles by identifying stretches unique to the polymer, in particular the O=S=O and C=S stretches. As shown in Figure 3.5, a broad peak can be observed at 3600 – 3000 cm^{-1}, which is representative of the O−H stretch from hydroxy- and physisorbed water molecules on the surface of the nanoparticles. Unsurprisingly, the most intense peak is observed at 650 – 500 cm^{-1} correlating to the Fe−O stretch. It is the region between these two peaks that is the window in which the P(AMPS) stretches should be observed. Sure enough, small peaks can be seen in the regions 1700 – 1500 cm^{-1} and 1100 – 1030 cm^{-1} which correspond to the O=S=O and C=S stretches respectively. The relative low intensity of these peaks is to be expected considering the comparatively low quantities of P(AMPS) required for the stabilisation of the iron oxide nanoparticles. The intensity of the sulfonate stretches increases for samples composed of an increased relative quantity of P(AMPS).

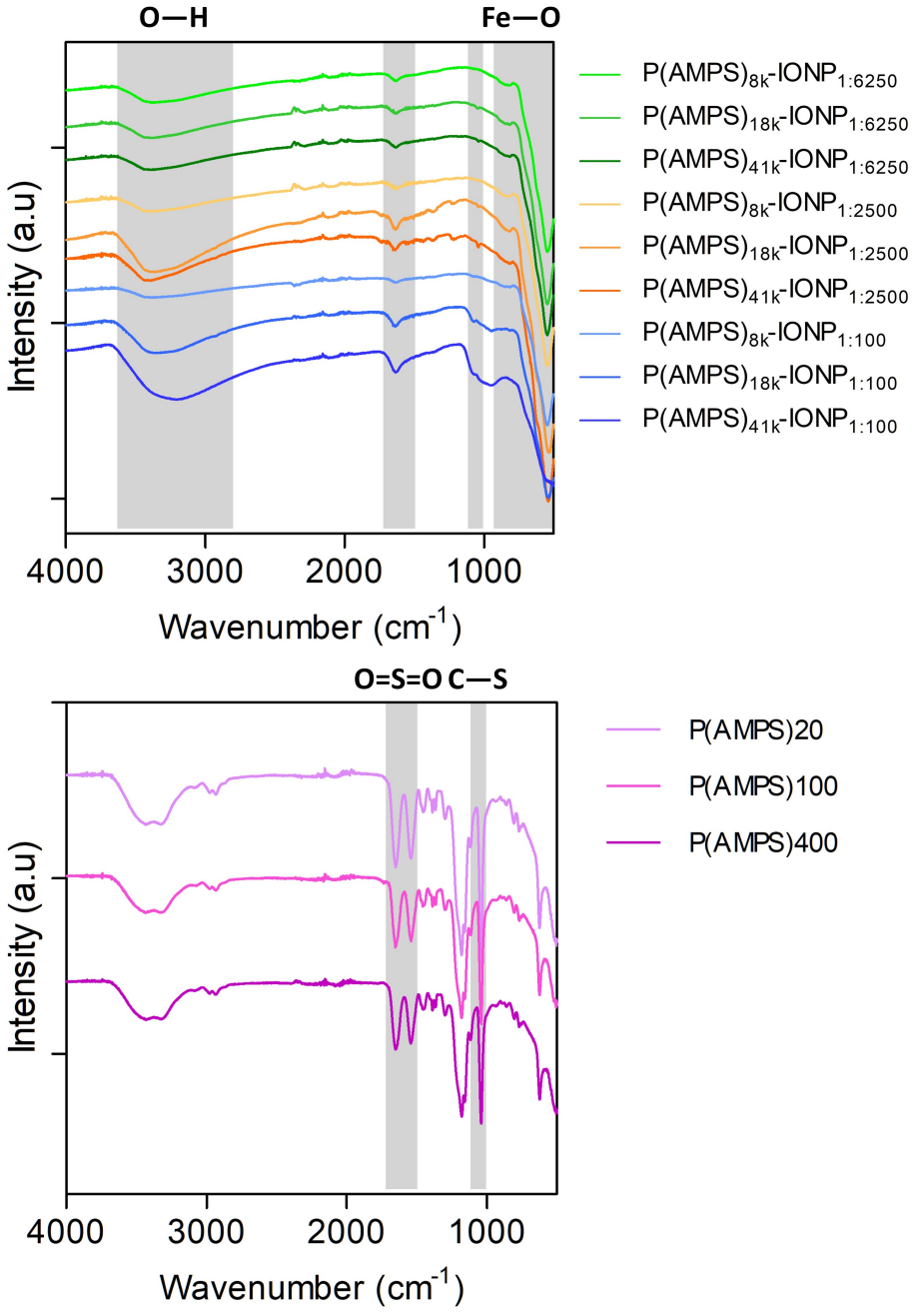

Figure 3.5: Fourier transfrom infrared (FTIR) spectra of left) 9 P(AMPS)-stabilised iron oxide samples ($P(AMPS)_{8,18,41k}$-$IONP_{1:100,2500,6250}$) and right) P(AMPS)20, 100 and 400. All samples are measured in the range 4000 – 500 cm^{-1}.

3.3.5 Vibrating Sample Magnetometry

Vibrating sample magnetometry was measured on the 9 solid powder samples between −15 kOe and 15 kOe. 8 samples exhibited close to superparamagnetic behaviour, with the resulting curve demonstrating little very hysteresis, with coercivity and remanence values of 30.7 – 82.5 Oe and 0.4 – 7.4 emu g^{-1}, (see Figure 3.6 and Table 3.3). The saturation magnetisation (M_s) for the stabilised iron oxide particles were measured to be between 53.5 and 72.8 emu g^{-1}, this is slightly reduced when compared to bulk maghemite (74 – 76 emu g^{-1}) likely due to the presence of the non-magnetic polymer.[287,288] As previously discussed, sample P(AMPS)$_{41k}$-IONP$_{1:100}$ is suspected to contain a much smaller proportion of magnetic maghemite/magnetite, due to the improper seeding of particles. This subsequently results in a much reduced M_s of 12.6 emu g^{-1}. Also included in Table 3.3 are control non-stabilised IONPs, which measured an M_s of 57.5 ± 2.2 emu g^{-1} and coercivity and remanence values of 48.6 Oe and 3.9 emu g^{-1}. These values being lower than the average P(AMPS)-IONP M_s, H_c, M_r values (67.6 ± 6.8 emu g^{-1} , 52.2 ± 15.3 Oe, and 5.1 ± 1.9 emu g^{-1} respectively) is likely due the smaller core size of the non-stabilised particles (d_{core} = 9.4 ± 1.9 nm). A reduction in core size is expected due to the lack of negatively charged seeding sites present to encourage particle growth.

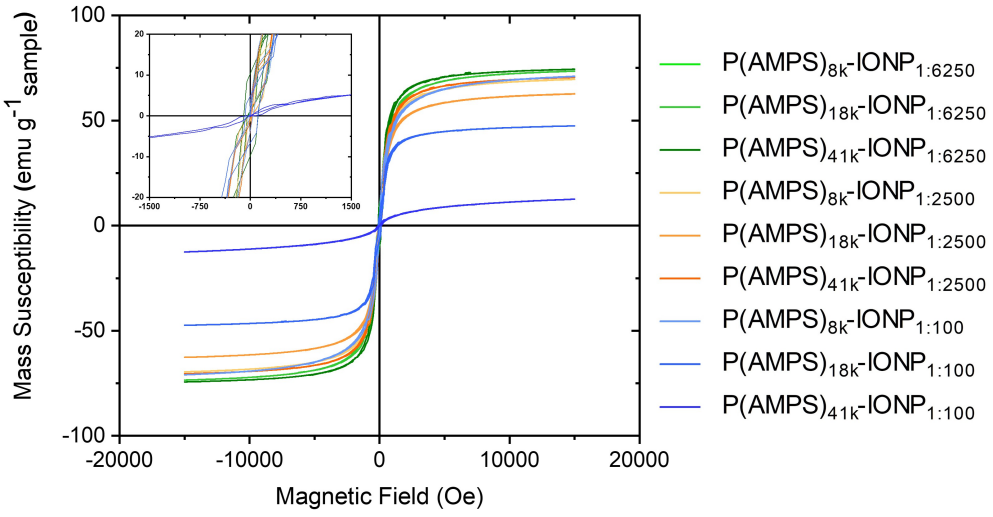

Figure 3.6: Magnetisation (mass susceptibility) of P(AMPS) stabilised iron oxide nanoparticles as measure by vibrating sample magnetometry (VSM) plotted against magnetic field (measured between -15 kOe and 15 kOe). Inset showing very small hysteresis of particles indicating slight ferromagnetic behaviour.

Table 3.3: Saturation magnetisation, remanence, and coercivity of P(AMPS) stabilised iron oxide nanoparticles as measured by VSM across a field range of −15 KOe to 15 KOe

Sample	M_s **(emu g^{-1})**	**Coercivity (Oe)**	**Remanence (emu g^{-1})**
P(AMPS)$_{8k}$-IONP$_{1:6250}$	72.8 ± 3.3	59.2	7.0
P(AMPS)$_{18k}$-IONP$_{1:6250}$	70.9 ± 1.9	46.2	3.3
P(AMPS)$_{41k}$-IONP$_{1:6250}$	71.7 ± 1.9	47.1	4.8
P(AMPS)$_{8k}$-IONP$_{1:2500}$	70.8 ± 3.4	30.7	2.3
P(AMPS)$_{18k}$-IONP$_{1:2500}$	61.0 ± 2.3	50.8	4.3
P(AMPS)$_{41k}$-IONP$_{1:2500}$	67.9 ± 3.6	42.2	7.4
P(AMPS)$_{8k}$-IONP$_{1:100}$	71.9 ± 2.3	59.1	7.0
P(AMPS)$_{18k}$-IONP$_{1:100}$	53.5 ± 8.6	82.5	5.0
P(AMPS)$_{41k}$-IONP$_{1:100}$	12.6 ± 3.7	53.5	0.4
Non-stabilised IONPs	57.5 ± 2.2	48.6	3.9

3.3.6 Single Field Relaxometry

Both the longitudinal (R_1) and transverse relaxation rates (R_2) were measured for all 9 P(AMPS)-stabilised samples at a Larmor frequency of 23 MHz and at temperatures of 25 and 37 °C. The corresponding relaxivities were subsequently calculated using Equation 1.7. The results of which are summarised in Table 3.4. The transverse relaxivity is often used as a means of quantitatively comparing the contrast enhancement of potential negative MRI contrast agents. All samples demonstrated high r_2 values, in the range of 331.5 – 434.2 $mM^{-1}s^{-1}$ at 25 °C. The exception to the excellent relaxivities is sample $P(AMPS)_{41k}$-$IONP_{1:100}$, r_2 = 44.8 $mM^{-1}s^{-1}$. This poor performance is expected when considering the low M_s as measured by VSM, and the XRD revealing that the sample contained very little inverse spinel iron oxide. Therefore the weak magnetic properties of this sample ultimately leads to the poor MRI performance.

This correlates with the data obtained by VSM, XRD, and TEM, indicating that the magnetic cores were not seeded in the same manner as other samples. Resulting in particles with diminished magnetic properties and ultimately poor MRI performance.

Table 3.4: Summary of relaxometric properties of P(AMPS)-stabilised iron oxide nanoparticle samples as measured at a field strength of 23 MHz and at temperatures of 25 and 37 °C.

Sample	r_2 **($mM^{-1}s^{-1}$)**		r_1 **($mM^{-1}s^{-1}$)**		r_2/r_1	
	25 °C	**37 °C**	**25 °C**	**37 °C**	**25 °C**	**37 °C**
$P(AMPS)_{8k}$-$IONP_{1:6250}$	434.2 ± 59.4	386.2 ± 32.2	42.7 ± 1.9	41.2 ± 0.2	10.2	9.4
$P(AMPS)_{18k}$-$IONP_{1:6250}$	431.0 ± 25.4	386.4 ± 17.4	39.9 ± 1.7	39.3 ± 1.5	10.8	9.8
$P(AMPS)_{41k}$-$IONP_{1:6250}$	367.1 ± 18.7	318.5 ± 19.4	40.3 ± 3.3	39.9 ± 3.3	9.2	8.0
$P(AMPS)_{8k}$-$IONP_{1:2500}$	363.4 ± 30.8	318.5 ± 21.9	34.6 ± 1.4	33.1 ± 2.9	10.5	9.6
$P(AMPS)_{18k}$-$IONP_{1:2500}$	232.0 ± 28.4	195.3 ± 26.2	27.0 ± 2.2	27.1 ± 2.2	8.6	7.2
$P(AMPS)_{41k}$-$IONP_{1:2500}$	324.8 ± 49.9	286.4 ± 38.6	30.7 ± 6.4	31.2 ± 6.1	10.6	9.2
$P(AMPS)_{8k}$-$IONP_{1:100}$	331.5 ± 13.3	312.4 ± 31.4	40.1 ± 1.6	41.0 ± 1.5	8.3	7.6
$P(AMPS)_{18k}$-$IONP_{1:100}$	279.1 ± 8.0	246.1 ± 14.4	32.5 ± 0.8	34.2 ± 3.1	8.6	7.2
$P(AMPS)_{41k}$-$IONP_{1:100}$	44.8	35.6	8.0	7.3	5.6	4.9
Heparin-IONPs[98]	264.9	–	34.8	–	7.1	–
Feridex[98]	107.0	–	23.7	–	4.5	–
Lumirem[98]	53.1	–	22.7	–	6.0	–

When comparing the relaxivities (and therefore the MRI performance) between each of the 3 sub-families of samples, as the relative quantity of iron in relation to the stabilising polymer is increased, the measured r_2 value also increases. This trend is better portrayed in Figure 3.7. The reasoning for such a trend can be explained in terms of particle seeding density. During the synthesis of the nanocomposites, an increase in the availability of iron cations will result in a greater proportion of the sulfonate seeding sites becoming occupied as the particles seed and grow. An increase in the seeding density decreases the average distance between each of the magnetic cores, and therefore increasing in a greater number of strong interparticle interaction. The consequence in doing so is seen in by shorter T_2 relaxation times of the water protons and therefore improved MRI contrast.

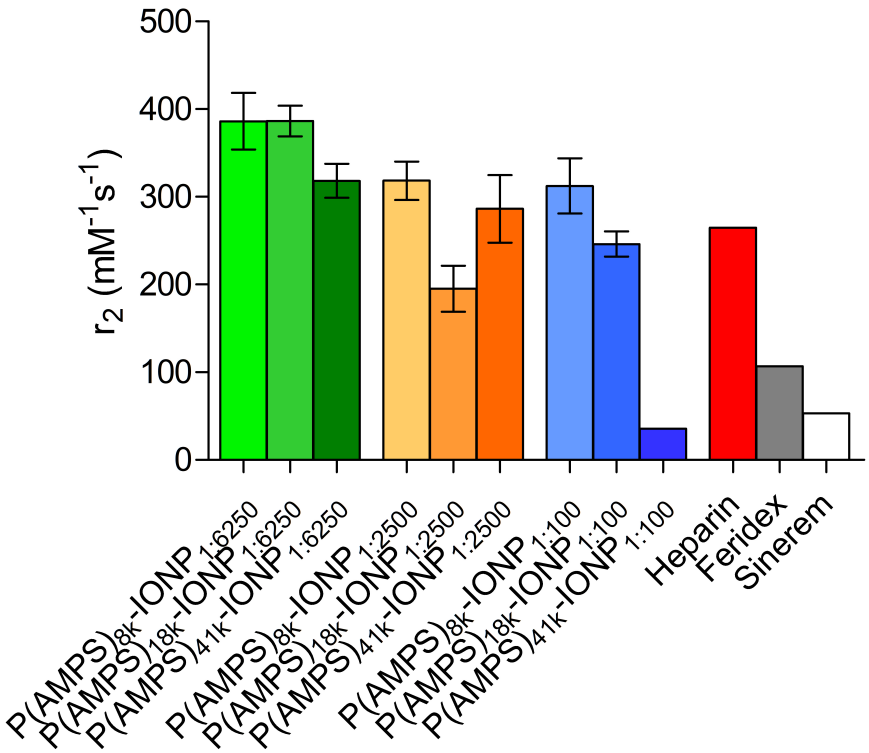

Figure 3.7: Transverse relaxivities (r_2) of the P(AMPS) stabilised iron oxide nanoparticles as measured at 25 °C and at a field strength of 23 MHz.

This behaviour have been well established as a cause of increased r_2 relaxivity.[71,82,83,98] We know from the literature that changes in transverse relaxivity may also be attributed to

differences in the core diameter, the magnetic properties (M_s), and the chemical composition (presence of dopants). The previous analysis using TEM, VSM, XRD, and Raman spectroscopy allows these potential causes to be excluded, with all samples but P(AMPS)$_{41k}$-IONP$_{1:100}$ having comparable results for d_{core}, M_s, XRD patterns, and Raman spectra. We can therefore attribute the differences in relaxation behaviour to differences in the magnitude and number of interparticle interactions. Interactions that are encouraged by the stabilising P(AMPS) result in increased magnetic anisotropy and hence increased relaxivities. The increased negative contrast due to the interactions between magnetic cores is supported by similar studies which show that these interactions between magnetic cores are important for boosting relaxivity.[83,98] The r_1 values obtained for all 9 samples are significantly lower than the respective r_2's, as expected. As discussed in the Introduction Section 1.4, negative MRI contrast agents act *via* the T_2 relaxation mechanism. Using the measured r_1 values, the r_2/r_1 ration can be calculated (Table 3.4), this gives an indication of the samples potential as a negative contrast agent. All samples, except P(AMPS)$_{41k}$-IONP$_{1:100}$, give exceptionally high r_2/r_1 values (> 8.0 at 25 °C) showing that these examples would make strong negative contrast agents. This is highlighted further when comparing to similar polyelectrolyte stabilised iron-oxide nanoparticles. The best performing P(AMPS)-stabilised sample (P(AMPS)$_{8k}$-IONP$_{1:6250}$) outperformed both PSSS-stabilised IONPs (r_2 = 132.4 mM^{-1}s^{-1}, r_2/r_1 = 5.9) and heparin-stabilised IONPs (r_2 = 264.9 mM^{-1}s^{-1}, r_2/r_1 = 7.1). Most importantly, all samples but P(AMPS)$_{41k}$-IONP$_{1:100}$ outperformed clinical examples such as Feridex and Lumirem (107 mM^{-1}s^{-1} and 53 mM^{-1}s^{-1} respectively).[98]

Within each sub-family there appears to be a loose correlation between the length of the polymer chain and the measured r_2, such that as the chain length of P(AMPS) is decreased the relaxivity increases. A shorter polymer chain will have a reduced number of sulfonate seeding sites, which in turn will result in more densely seeded particles. And as described before, with increasing Fe, the number of and strength of dipolar interactions between neighbouring cores increases. This is most evident for samples P(AMPS)$_{8k}$-IONP$_{1:6250}$, P(AMPS)$_{8k}$-IONP$_{1:2500}$, and P(AMPS)$_{8k}$-IONP$_{1:100}$, all of which are composed of the shortest P(AMPS), P(AMPS)20.

All samples demonstrated lower r_1 and r_2 at the higher temperature, 37 °C due to the thermal activation of water molecules and its subsequent impact on the diffusional correlation times around the particle cores.[289]

3.3.7 Discussion

The characterisation techniques detailed in the previous sections of this chapter allow for a number of observations to be made with regards to how the composition, physical properties, and relaxometric behavior is dependent upon the [P(AMPS)]:[Fe] ratio during the co-precipitation synthesis. From the TEM, XRD, Raman spectroscopy, and FTIR spectroscopy data it is evident the composition of 8 of the 9 samples is very consistent regardless of ratio used for preparation. All samples prepared at 1:6250, 1:2500, and 2 of the 3 samples prepared at 1:100 [P(AMPS)]:[Fe] were shown to produce quasi-spherical nanoparticles with core size between 11.0 and 13.9 nm as determined by TEM. XRD and Raman spectroscopy also confirmed that the cores observed consisted of inverse spinel iron oxide (though unable to distinguish between maghemite and magnetite), and the O=S=O and C=S stretches observed by FTIR spectroscopy confirmed the presence of the stabilising sulfonate polymer. Furthermore, VSM revealed the superparamagnetic behaviour with low coercivity and remanence values measured for all. The saturation magnetisation (M_s) of 7 samples was found to be between 61.0 - 72.8, with $P(AMPS)_{18k}$-$IONP_{1:100}$ being an outlier with M_s = 53.5 ± 8.6 emu g^{-1}, though this can be attributed to the high relative quantity of polymer in relation to iron present in this sample.

In contrast, using a ratio of 1:100 in combination with the high polymer M_w, 41,000 (sample $P(AMPS)_{41k}$-$IONP_{1:100}$) resulted in nanoparticles of far lower quality both in terms of homogeneity and magnetic properties. Rather than distinct (quasi-)spherical particles, TEM analysis revealed smaller seed-like particles that were poorly defined and therefore could not measured. This indicates that the high quantity of very large polymer was inhibiting the formation of the inverse spinel iron oxide nanoparticles. This is further supported by the XRD and Raman spectroscopy which made it clear that no single crystal structure was present in this sample, and instead a mix of maghemite/magnetite as well as non-magnetic phases such as hematite and/or akaganeite which may also be produced through co-precipitation of iron salts. One notable observation, is that during synthesis the reaction mixture did not turn brown/black but rather a deep orange red-colour, hinting towards the formation of other iron oxide phases. VSM however did show that small quantities of magnetic iron oxide was present in this sample due to a measured M_s of 12.6 ± 3.7. A hypothesis for the cause of the different composition of this material compared to the other P(AMPS)-stabilised IONPs is that the high quantity of the 41 kDa polymer inhibited the seeding of the iron salts at the negative sulfonate sites. This may be due to the increased viscosity or the excess number of negative sites causing the local

relative concentration of Fe(II) : Fe(III) at each site to not be homogeneous and therefore the necessary 1:2 ratio would not be present at every site.

Finally, comparing the r_2 values measured for the confirmed inverse spinel samples, certain trends were observed with respect to how seeding density (either through change in polymer M_n or [P(AMPS)]:[Fe] ratio) impacted the MRI behaviour of the nanocomposites. When comparing between each of the samples, as the relative quantity of iron in relation to polymer is increased, the measured r_2 value also increases. This is attributed to the increase in seeding density along the polymer chain, reducing the average interparticle distance and thus increasing the strength of the dipolar interactions between neighbouring particles. Interestingly, it appears an maximal seeding is reached for the samples P(AMPS)$_{18k}$-IONP$_{1:6250}$ and P(AMPS)$_{8k}$-IONP$_{1:6250}$ for which at this high concentration of Fe a decrease in polymer M_n does not translate into an increased r_2 value (see Figure 3.7). The trend for increasing polymer chain length is less apparent compared to increasing relative [Fe], whilst at ratios 1:6250 and 1:100 there is a clear decrease in r_2 as M_n increases, this is not observed at ratio 1:2500, with the minimum relaxivity of this group seen for sample P(AMPS)$_{18k}$-IONP$_{1:2500}$. From characterisation carried out to this point it is not apparent the cause for this outlier, however it is important to note that seeding density is not the only factor in determining interparticle distance as particle seeded along different polymer chains will interact with one another as they diffuse through the medium due to Brownian motion. Small differences in the structural confirmation or charge of a polymer will therefore effect how they diffuse and interact with one another in suspension. This is expanded upon in future section, Section 3.4.2.

3.4 Advanced Characterisation

The initial characterisation discussed in Section 3.3 has already illustrated the importance of both the molar ratio of polymer to Fe salts as well as the chain length of polymer, on both the magnetic and relaxometric properties of a negative MRI contrast agent. However, the techniques discussed so far are only capable of providing a small amount of information into explaining why this is the case, and what the cause of the observed trends are. Due to their colloidal, magnetic, and relaxometric properties, samples P(AMPS)$_{8k,18k,41k}$-IONP$_{1:6250}$ and P(AMPS)$_{8k}$-IONP$_{1:2500,1:100}$ were selected for further in-depth characterisation. This selection still allows for the examination of both polymer chain length and [P(AMPS)]:[Fe] on the MRI contrast potential of this family of nanocomposites. The advanced techniques to be discussed

in this section are Mössbauer spectroscopy, small-angle X-ray scattering (SAXS), and fast field cycling (FFC) relaxometry, with the aim of gaining deeper insight into the complex behaviour of these materials.

3.4.1 Mössbauer Spectroscopy

^{57}Fe Mössbauer spectroscopy was carried out to reveal greater detail with regards to the structural composition of the magnetic iron oxide cores. Though X-ray diffraction and Raman spectroscopy are sufficient to confirm the inverse spinel cubic phase of the iron oxide cores, they are unable to differentiate between magnetite and maghemite. The spectra that were produced comprised of magnetically split sextets, characteristic of particles magnetically blocked on the Mössbauer timescale (approx. 1 ns). Best fits to the spectra were obtained using the model independent 'centre of gravity' method to evaluate the numerical proportion of Fe atoms in the magnetite environment (α), with Voigtian line shapes found to obtain the best fit to the spectrum.[279] We see that, within the value of uncertainty for all samples, calculated according to Fock *et al.* 2016, the value of α is ca. 0.11.[290] (Figure 3.8 and Table 3.5). This is indicative of maghemite rich iron oxide cores, with a small amount of magnetite character.

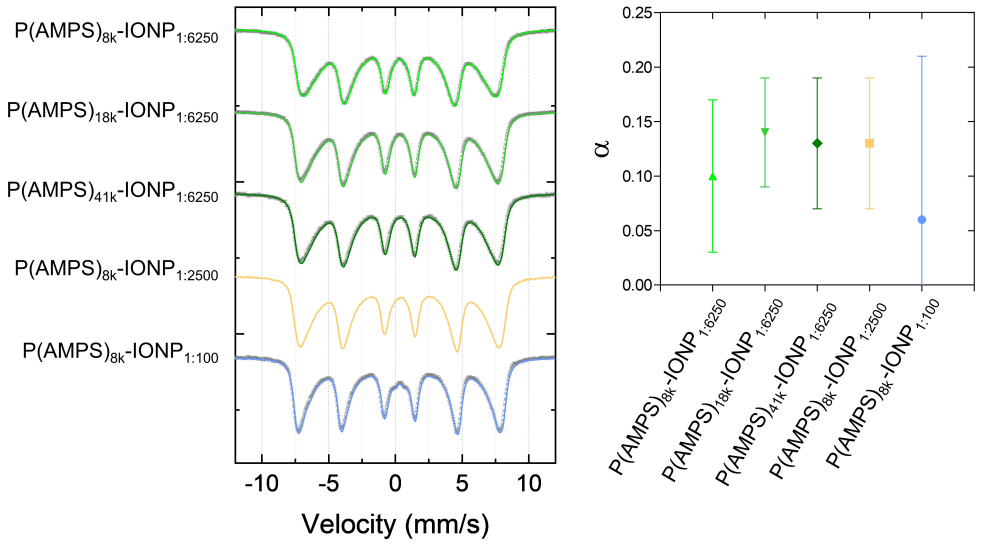

Figure 3.8: Left) Room temperature ^{57}Fe Mössbauer spectra of dried powder samples mixed with sucrose and best fits to the observed spectra (lines) obtained using the 'centre of gravity' method. All best fits were obtained using Voigtian lines (Gaussian distributions of Lorentzian lines). Right) comparison of the best fit values of spectra α, the numerical proportion of Fe atoms in a magnetite environment, for the five samples with corresponding uncertainty values obtained for each spectrum represented by error bars.

Notably, the Mössbauer spectra also demonstrate significant differences in shape correlating to changes in both the amount and length of the P(AMPS) polymer used within each of the syntheses. For samples, P(AMPS)$_{8k}$-IONP$_{1:6250}$, P(AMPS)$_{8k}$-IONP$_{1:2500}$, and P(AMPS)$_{8k}$-IONP$_{1:100}$ - across which the iron to polymer ratio increases (see sample summary Table 3.5) - we see significant changes in both the mean static hyperfine field, $<H>$, as well as in the distribution, P(H). Values obtained for the mean static hyperfine field are summarised in Table 3.5. As the relative quantity of iron increases, $<H>$ decreases from 409 kOe to 375 kOe, which is suggested as being the result of increasing magnetic frustration of the cores as a result of increasing structural confinements associated with the increasing amount of iron within the particle, and is also likely to cause clustering of the cores leading to corresponding alignment along a magnetic easy axis. As the length of the P(AMPS) increases between samples

$P(AMPS)_{8k}$-$IONP_{1:6250}$ to $P(AMPS)_{41k}$-$IONP_{1:6250}$, we see a slight restructuring of the cores with these clusters. This is indicated by the slight increase in the mean hyperfine field, and which we suggest gives the iron oxide cores more freedom to re-orientate, which in turn reduces the overall amount of frustration in the system.

Table 3.5: Room temperature ^{57}Fe Mössbauer parameters as deduced from best fits to the data presented in Figure 3.8, obtained using the "centre of gravity" model, with fitting to spectra performed using Recoil.[279]

Sample	α^a	**Linewidth (mm/s)**	**<H>^{b} (kOe)**	$\sigma_{<H>}{}^b$ **(kOe)**	**FWHM^c (kOe)**
$P(AMPS)_{8k}$-$IONP_{1:6250}$	0.10 ± 0.07	0.34	375.3	20.8	50
$P(AMPS)_{18k}$-$IONP_{1:6250}$	0.14 ± 0.05	0.30	390.8	36.2	60
$P(AMPS)_{41k}$-$IONP_{1:6250}$	0.13 ± 0.06	0.32	392.0	25.6	54
$P(AMPS)_{8k}$-$IONP_{1:2500}$	0.13 ± 0.06	0.31	400.5	28.5	63
$P(AMPS)_{8k}$-$IONP_{1:100}$	0.06 ± 0.15	0.27	408.6	20.1	45

[a] α is the numerical proportion of Fe atoms in the magnetite environment as determined by the 'centre of gravity' method with the corresponding uncertainty given as error bars; [b] <H> is the mean static hyperfine field and $\sigma_{<H>}$ is the standard deviation of the mean. [c] FWHM is the full width at half maximum.

3.4.2 Small-angle X-ray Scattering

To further investigate the colloidal conformation adopted by these complex nanocomposites in suspension, small-angle X-ray scattering (SAXS) was performed by Stephen C. L. Hall of the Perrier group at the University of Warwick. The SAXS patterns obtained for all samples show similar trends; the lack of an observable Guinier region within the achievable Q range indicates the formation of relatively large colloidal suspensions in all cases. In order to extract structural information from these SAXS patterns, parameters of a model describing the aggregation of primary spherical particles into a fractal-like cluster were fit to the experimental data, as has been previously reported for similar systems.[291] A detailed description of this model has also been reported previously.[277] Briefly, the fractal dimension represents the self-similarity of the aggregate. Here, we interpret this as a measure of the degree of clustering of the individual magnetic cores, where the total radius of the clustered aggregate is described by the correlation length.

The parameters obtained from these fitting procedures are displayed in Table 3.6. In all

Table 3.6: Structural parameters obtained through fitting of SAXS data of aqueous suspensions of P(AMPS) stabilised aggregates of maghemite/magnetite nanoparticles to a model describing fractal-like clusters of spherical particles. Quoted errors represent the standard error associated with the fitted parameter. Values marked with * were held as constant throughout the fitting procedure.

Sample	Volume Fraction ($\times 10^{-6}$)	Magnetic Core Radius (Å)	Radial Polydispersity	Fractal Dimension	Correlation Length (Å)
$P(AMPS)_{8k}$-$IONP_{1:6250}$	1.6 ± 0.01	64 ± 1	0.2*	2.98 ± 0.01	170 ± 3
$P(AMPS)_{18k}$-$IONP_{1:6250}$	0.7 ± 0.01	83 ± 1	0.2*	3.30 ± 0.09	101 ± 6
$P(AMPS)_{41k}$-$IONP_{1:6250}$	1.5 ± 0.01	69 ± 1	0.2*	3.32 ± 0.05	80 ± 2
$P(AMPS)_{8k}$-$IONP_{1:2500}$	1.9 ± 0.01	62 ± 1	0.2*	3.47 ± 0.03	85 ± 1
$P(AMPS)_{8k}$-$IONP_{1:100}$	0.8 ± 0.01	70 ± 1	0.2*	2.90 ± 0.01	335 ± 15

cases, the nanoparticle radii are similar to the d_{core} values obtained from TEM (for the fitting of raw data points see Appendix 7.1). Comparing samples $P(AMPS)_{8k}$-$IONP_{1:2500}$ and $P(AMPS)_{8k}$-$IONP_{1:100}$, as the ratio of [P(AMPS)]:[Fe] increased, an initial increase in fractal can be observed accompanying a decrease in the correlation length. This indicates the particles compact into smaller, more highly clustered aggregates. When the [P(AMPS)]:[Fe] ratio is further increased ($P(AMPS)_{8k}$-$IONP_{1:6250}$), a swelling of the aggregate can be observed with a decreased clustering of magnetic cores. This result therefore appears to signal a potential optimal ratio of particles to stabilising polymer, in order to produce the most clustered structures. At low particle to polymer concentrations it is possible that the electrostatic repulsion between the negatively charged polymer chains is not countered by the presence of the particles and therefore leads to swelling of the clusters, as described by the larger correlation length and decreased fractal dimension. Similarly, at the maximum particle to polymer concentration the capacity of P(AMPS) to stabilise the cores has been exceeded, potentially leading to electrostatic repulsion between nanoparticles. As the M_n of P(AMPS) is increased, a decrease in correlation length is observed, suggesting an increase in the stabilising effect on the nanoparticle cores thus leading to the formation of smaller aggregates. Interestingly, the fractal dimension initially increases then appears to stabilise close to the maximum value observed for ($P(AMPS)_{8k}$-$IONP_{1:2500}$). This suggests that magnetic cores partition amongst the available P(AMPS) at an apparently optimal compactness. It is also noteworthy that the trends observed in this section do not align with those seen for the DLS measurements. This is due to SAXS being a far more suitable technique for the assessment of aggregation and clustering behaviour. For SAXS, samples were all prepared to the same dilution and are therefore more comparable

in terms of their clustering behaviour. As such it is not appropriate to compare the SAXS and DLS data.

3.4.3 Fast Field Cycling Relaxometry

Nuclear magnetic dispersion (NMRD) analysis is a variable field relaxometry technique which is particularly useful in the analysis of MRI contrast agents.[82,98,241,292] Through fast field cycling relaxometry, the longitudinal proton relaxation rate enhancement (r_1) of a colloidal system is measured at multiple frequencies, thus providing insight into the relaxation properties and the dynamic local environment of water molecules surrounding a contrast agent species. Such behaviour is influenced by the magnetic properties of a particles, and the coupled magnetic interactions between particles, as well as their surroundings. The r_1 relaxivity is calculated according to Equation 2.11.

NMRD analysis was carried on the five samples ($P(AMPS)_{8k}$-$IONP_{1:6250}$–$P(AMPS)_{41k}$-$IONP_{1:6250}$, $P(AMPS)_{8k}$-$IONP_{1:2500}$, and $P(AMPS)_{8k}$-$IONP_{1:100}$), the profiles that were obtained are displayed in Figure 3.9. At magnetic field strengths of $B_0 > 0.2$ T or (> 10 MHz), relaxation behaviour is dominated by Curie relaxation, a phenomenon resulting from the induction of a local magnetic field through the application of an external magnetic field on the superparamagnetic nanoparticles, and the resultant interactions between water protons and these local magnetic fields.[74] Relaxation at these field strengths is determined primarily by the strength of the magnetic moments and water diffusional correlation times around the magnetic particle cores. Therefore, Curie relaxation tends to correlate to the size of the magnetic core, d_{core}. As d_{core} is comparable for the 5 samples in question (11.0 ± 2.4 – 13.9 ± 5.3 nm), it is therefore expected for all profiles they converge at field strengths > 10 MHz (as seen in Figure 3.9).[74]

At lower frequencies (< 10 MHz), the Curie component of relaxation is lost and Néel relaxation (the random fluctuation of magnetic moments) dominates. The seminal model by Roch, Muller, and Gillis first detailed proton relaxation induced by superparamagnetic nanoparticles, with profiles that featured a low field plateau (also referred to as the dispersion), a mid-field peak (ν_{max}), and a decrease in longitudinal relaxivity at high field strengths.[74] In this model, as the diameter of the magnetic nanoparticles is increased, ν_{max} shifted to lower frequencies and low field r_1 relaxivities (0.01 MHz) increased, indicative of an increase in the magnetocrystalline anisotropy linked to particle size. For the samples that are described in this work, ν_{max} is shifted to lower frequencies, and r_1 is greatly increased at low Larmor frequencies. As the core size of the

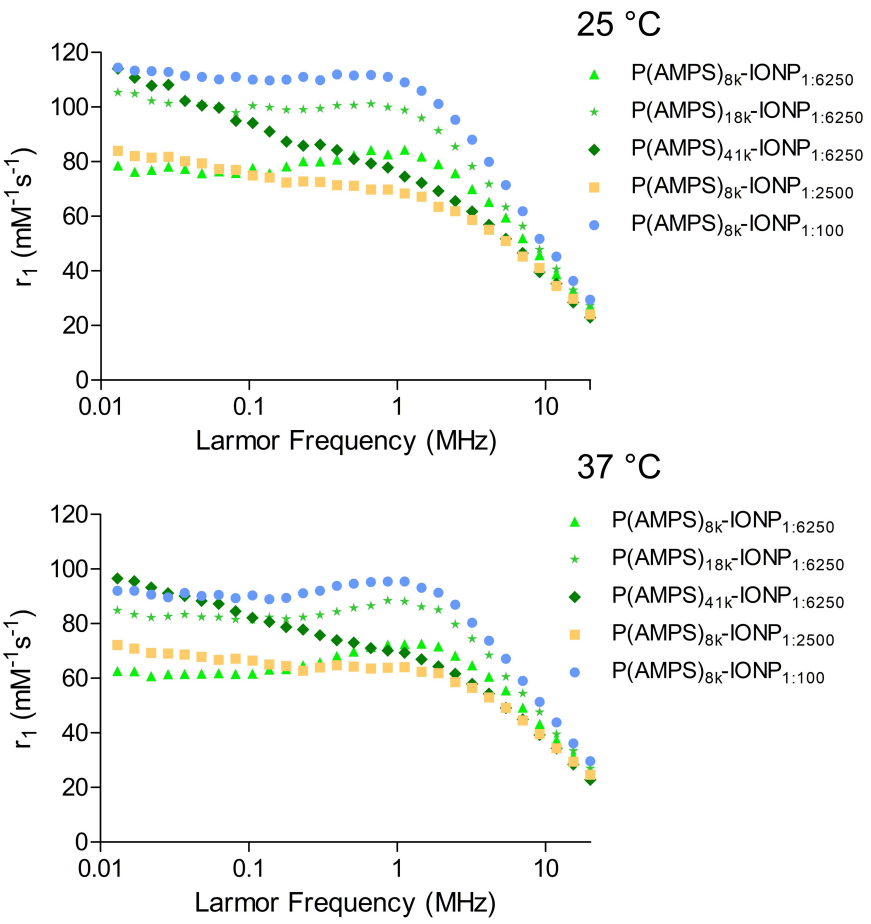

Figure 3.9: ^{1}H NMRD profiles of longitudinal relaxivity (r_1) of P(AMPS) stabilised iron oxide nanoparticles in 0.1 % Xanthan gum, measured at both 25 and 37 °C (top and bottom, respectively) over a frequency range of 0.01 – 20 MHz.

5 samples do not differ significantly (Table 3.2), this observed behaviour is not attributable to this well-modelled size related increase in the magnetocrystalline anisotropy. Such a divergence from the well-accepted superparamagnetic model, as is being observed here, has been previously reported for clustered materials formed from core-shell, multi-core iron oxide nanoparticles, and for superparamagnetic/ferromagnetic nanoparticles seeded along polyelectrolytes, such as denatured DNA strands, poly(sodium-4-styrene) sulfonate, and fatty acids.[71,81,83,84,86]

A model for the effect of agglomeration of superparamagnetic particles r_1 has been developed by Gillis *et al.*, demonstrating aggregation-induced changes in low frequency dispersion

and ν_{max} in NMRD profiles.[80] Through such a model, it was possible to show that agglomeration of magnetic cores results in a decrease longitudinal relaxivity, due to reduced total surface area of particles available for important, diffusive interactions with surrounding water protons. However, this is evidently not the case for samples examined herein, where absolute r_1 values remain extremely high (Figure 3.9). The observed strong enhancement of the longitudinal relaxation rate is attributed to the hydrophilic P(AMPS), facilitating good water access to all the particle surfaces and thus overcoming the previously observed reductions in relaxivity. Similarly, particles stabilised with the hydrophilic biopolymer heparin exhibited enhanced r_1 at low Larmor frequencies (< 0.1 MHz), and was accredited to an increase in anisotropy resulting from interactions between particles seeded along the polymer backbone.[98] An investigation into these interactions between magnetic cores, carried out by Lévy *et al.*, established that the intrinsic magnetic properties of multi-core or clustered nanoparticles results in large relaxivity enhancements at low field strengths due to slowing of the dynamics of the magnetic moments. (*i.e.* progressive blocking of Néel fluctuations due to local magneto-anisotropy).[85,86] This form of clustering enhanced relaxation has also been observed for other multi-core iron oxide nanoparticles, including 'nanoflower' structures (composed of an assembly of magnetic cores).[86,197] Herein, we propose that cross-linking between neighbouring P(AMPS) chains results in the formation of what can be described as 'multi-core like' nanostructures in suspension. The similarities between the multi-core model proposed by Lévy *et al.,* and the observed strong low field relaxivities for the P(AMPS)-stabilised nanoparticles supports this explanation.

This phenomenon observed for this family of contrast agents is likely due to the propensity for colloidal polymers to adopt different energetically favourable conformations (brush, mushroom, coil, *etc.*) when in aqueous suspension.[293,294] This dynamic behaviour is likely to bring the iron oxide cores (electrostatically associated with the negative polyelectrolyte backbone) closer in proximity to one another, therefore resulting in the observed 'multi-core like' behaviour. The hydrophilicity of the polymer prevents the restriction of water access to the cores, as would be seen for typical agglomeration of nanoparticles and therefore maintains high longitudinal relaxivities. Indeed, the templating nature of the polyelectrolyte species and the nanoparticle seeding it encourages may serve to impact the adopted conformation of the polymer chains, with nanoparticles having been shown to have profound effects on the motion and molecular conformation of polymers in polymer-nanoparticle composites.[295,296]

This dynamic impacts the low frequency r_1 of the samples described in this chapter (Figure 3.9). More dynamic and flexible samples, possessing higher amounts and/or longer poly-

mer chain lengths demonstrate the highest r_1 values at 0.01 MHz ($P(AMPS)_{8k}$-$IONP_{1:100}$ and $P(AMPS)_{41k}$-$IONP_{1:6250}$), whereas those with the highest density of iron oxide nanoparticles and smaller polymer chain lengths ($P(AMPS)_{8k}$-$IONP_{1:6250}$) have lower r_1 values at the same frequency, due to their inherently lower dynamic flexibility. Increased flexibility will result in increased hydration and clustering of the iron oxide nanoparticles, giving rise to the observed r_1 enhancements. This behaviour is supported by the the SAXS data discussed in Section 3.4.2, in which the observed fractal-like aggregation of nanoparticles is concurrent with then notion of varying degrees of 'clustering' resulting in differences in the distance between the magnetic cores of these 'multi-core like' structures. The interparticle interactions which are known to boost relaxation will be dependent on this degree of clustering. Similar trends in NMRD relaxation were observed at 25 °C (Figure 3.10).

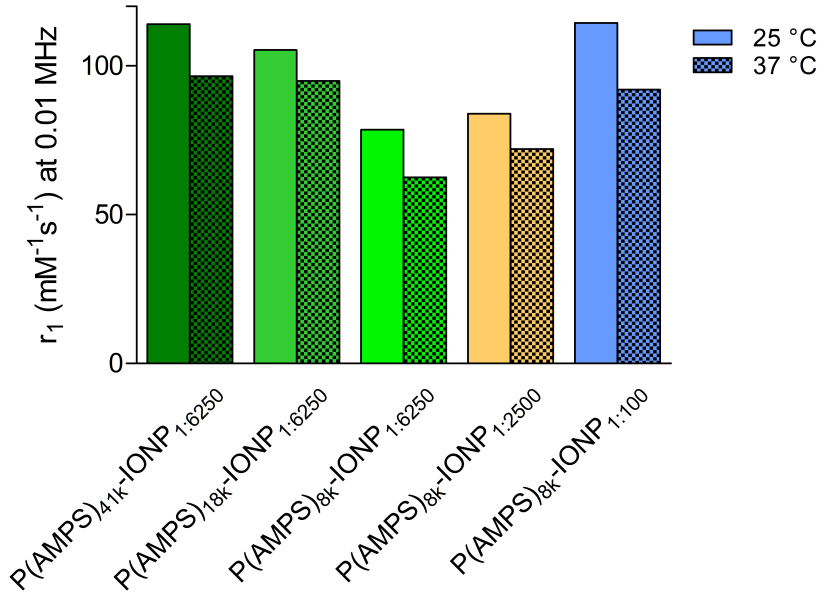

Figure 3.10: Longitudinal relaxivity (r_1) at 0.01 MHz of P(AMPS)-stabilised iron oxide nanoparticles ($P(AMPS)_{8k}$-$IONP_{1:6250}$–$P(AMPS)_{41k}$-$IONP_{1:6250}$, $P(AMPS)_{8k}$-$IONP_{1:2500}$, and $P(AMPS)_{8k}$-$IONP_{1:100}$) in 0.1 % Xanthan gum, measured at 25 and 37 °C)

3.5 *In Vitro* Biological Characterisation

3.5.1 Haemolytic Activity

Haemocompatibility is crucial for *in vivo* bio-applications of nanomaterials, particularly if the nanocomposite is to come into contact with blood through intravenous clinical administration.[26,297] Due to their low colloidal stability uncoated iron oxide nanoparticles have a high tendency for agglomeration under physiological conditions, with such agglomeration having been shown to have a considerable impact on membrane activity and thus levels of haemolysis.[298–300] At certain concentrations it has also been show that uncoated iron oxide nanoparticles can cause significant damage to red blood cells. To quantitatively determine the blood compatibility of the nanocomposites described in this chapter, a widely used haemolysis assay was carried out, adapted from methods detailed in the literature.[280] Briefly, the release of haemoglobin from ovine red blood cells was measured using UV-vis spectroscopy after incubation with the P(AMPS) stabilised γ-Fe_2O_3 nanoparticles (Figure 3.11 and Experimental Section 2.2.12). The percentage haemolysis was calculated for each of the 4 concentrations for each of the 5 samples, with the % haemolysis found to be in the range 8.1 – 24.6 %. These results were found to be statistically insignificant with respect to the negative control (P value > 0.05). Therefore, demonstrating the good haemocompatibility of the P(AMPS) stabilised samples.

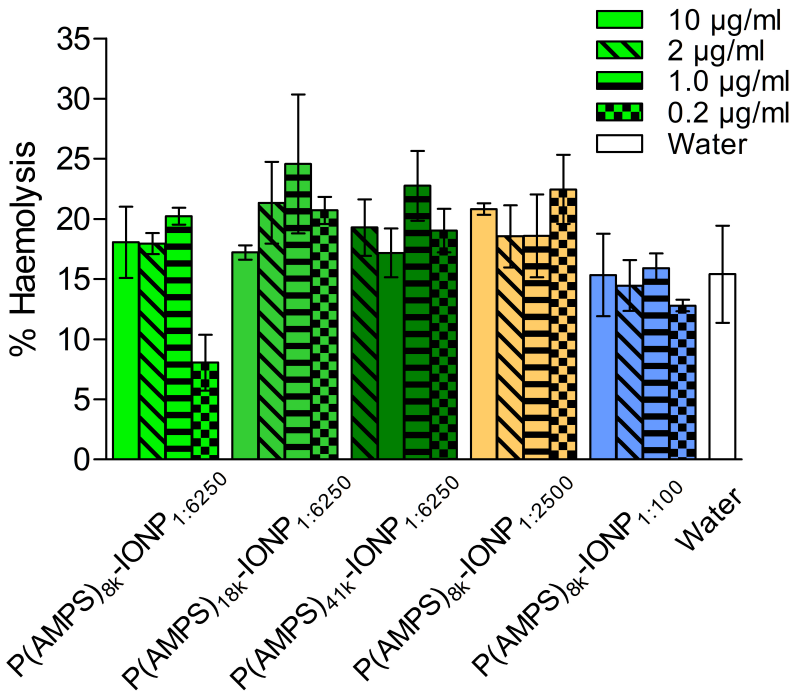

Figure 3.11: Haemocompatibility of P(AMPS) stabilised iron oxide nanoparticles measured as a percentage with 100 % positive control using 1 % Triton-X in PBS, with water and PBS as negative controls. Figure shows the mean ± SEM where n = 3.

The ability of a coating or stabiliser to determine the haemocompatibility of iron oxide nanoparticles has been well documented. For example, a comparison between polyethylenimine (PEI) and polyethylene glycol (PEG) coated IONPs, showed that PEI-coated samples exhibited severe dose-dependent haemolysis whilst the PEG-coated nanoparticles showed almost no haemolytic activity.[301] Likewise, a comparison between polyacrylic acid, hyaluronic acid, and chitosan modified iron oxide nanoparticles, found the chitosan and hyaluronic acid functionalised nanoparticles had superior blood compatibility due to their greater stability under physiological conditions.[298] Whilst providing the samples with the excellent colloidal stability necessary, P(AMPS) has already demonstrated excellent blood compatibility.[280] It is important to note that the concentrations of P(AMPS) present within the nanocomposites are much lower than those that were used to determine the polymers own blood compatibility. Though it is apparent that the quantities used are sufficient in providing both colloidal stability and blood compatibility. The measured haemolysis of the clinically approved anti-coagulant heparin

falls within the range observed for the P(AMPS) stabilised samples, highlighting their excellent blood compatibility and their potential for safe biomedical application.

3.6 Conclusions

The stabilisation of iron oxide nanoparticles using the *in situ* addition of negatively charged polyelectrolytes is well known to aid their application in a biological setting, with the dual stabilising and templating effect of the polymer enhancing MRI properties.[71,82,98] However, the high dispersity of many commercial polymers leads to difficulties in being able to fine-tune key magnetic and colloidal properties of any resulting magnetic colloid. Therefore, when designing possible future MRI contrast agents and attempting to tune their relaxometric properties the use of such polymers will hinder any efforts.

Herein, the work described in this chapter has sought to introduce improved precision of design in the preparation of stabilised iron oxide nanoparticles through the use of the 'designer' poly(2-acrylamido-2-methylpropane sodium sulfonate) (P(AMPS)) polymer. The advantages of using a synthetic polymer such as P(AMPS) is that not only does it allow for the production of colloidal magnetic nanocomposites with strong MRI contrast capabilities but also has allowed for deeper insight into the unique and dynamic behaviour of this family of nanocomposites. After initial physicochemical characterisation using TEM, DLS, and XRD analysis, the impact of both the relative proportion of Fe to P(AMPS) and the M_n of P(AMPS) on the transverse relaxivity was investigated through fixed field relaxometry. After measurements were carried out upon the 9 samples, it became evident that indeed both factors (ratio and M_n) were impacting the relaxometric behaviour of these nanocomposites. It revealed that as the relative quantity of metal was increased so too did the calculated r_2, a result of denser seeding of particles along the polymer chain, in turn leading to increased interparticle interactions between the magnetic cores. When considering the length of the polymer chain, a loose inverse relationship between the length of P(AMPS) and the samples r_2 was revealed, with the reasoning being that a shorter polymer chain will have fewer available seeding sites and therefore encouraging the interparticle interactions.

To gain further insight into complex behaviour of these nanocomposites 5 of the samples were analysed further using more advanced techniques, namely Mössbauer spectroscopy, fast field cycling (FFC) relaxometry, and small-angle X-ray scattering (SAXS). Mössbauer spectroscopy primarily was used to confirm the composition of the nanoparticles in terms of the

% magnetite, which for all 5 was approximately 11 %, the remaining 89 % assumed to be maghemite. The collected spectra also revealed that changes to the polymer M_n lead to variation in the degree of magnetic frustration in the iron oxide cores. Fast field cycling (FFC) relaxometry allowed for the probing and interpretation of these important interactions, revealing unexpected behaviour, in particular at lower frequencies. The loss of a defined ν_{max} and low field dispersion (through increased r_1 values in the range 0.01 – 0.1 MHz range), correlates with similar behaviour previously observed for multi-core magnetic nanoparticles which have been modelled in the literature.[85,86,197] The formation of multi-core clusters when in suspension was confirmed with SAXS, with the degree of clustering influenced by the [P(AMPS)]:[Fe]ratio as well as the P(AMPS) M_n. An increase in chain length resulted in the formation of smaller, more compact clusters, which present increased low field r_1 relaxivities.

This data clearly illustrates the potential for tuning the MRI behaviour by controlling the degree of clustering of a nanocomposite. Transverse relaxivities exceeding 400 $mM^{-1}s^{-1}$, as measured at 23 MHz are far greater than that measured for clinical analogues such as Feridex (r_2 = 120 $mM^{-1}s^{-1}$ at 20 MHz).[156] In addition to excellent MRI performance, the good blood compatibility as quantified through a haemolysis assay further strengthens the potential of this family of nanocomposites to make excellent clinical contrast agents.

In summary, this chapter has shown that judicious choice of polymer based on its dispersity and chain length, as well as carefully selected composite ratios are crucial when tailoring the resulting properties of the nanocomposite. Precision-engineered polymers are therefore ideal for such applications allowing fine control over the interactions between magnetic cores by determining the degree of flexibility and clustering of a composite. By maximising these important interactions in such a fashion, MRI contrast agents with exceptional performance can be produced.

Chapter 4

Magnetically Driven Preparation of 1-Dimensional Nano-necklaces

4.1 Introduction

The previous chapter described how the use of a low dispersity RAFT polymer allowed for the important dipolar interactions to be tuned so that the resulting r_2 value of the nanocomposite could be maximised. One noted property of this nanocomposite is that whilst they align parallel to an external magnetic field, in the absence of such they will coil bringing magnetic cores closer to one another in clusters. In Section 1.8.1, this non-linear assembly of particles is said to result in both ferro- and antiferromagnetic coupling between cores, this slight demagnetising effect may result in reduced magnetic behaviour at lower magnetic fields.[233,237] Therefore, the performance of these nanocomposites may be enhanced further through permanent alignment of the magnetic cores into 1D nanostructures. Such materials with high shape anisotropy have also been detailed to exhibit strong uniaxial anisotropy and increased magnetisation.[233]

One such means for creating permanent 1D nanostructures from polyelectrolyte stabilised MNPs, is the use of magnetically field induced (MFI) assembly. This methodology used by the likes of Sheparovych *et al.*, to produce 'nanowires' by exposing IONPs to an external magnetic field causing them to be aligned parallel to the field before being held in place by the polymer, P2VPq.[263] As demonstrated in Chapter 3, as well as in literature, the likes of P(AMPS)-IONPs and PSSS-CFNPs will align into long linear arrays in the presence of an external magnetic field and thus make for excellent precursor candidates for the formation of

permanent 1D nanostructures.[82,270]

The aim of the work detailed within this chapter was to demonstrate polyelectrolyte stabilised MNPs as precursors for the formation of permanent 1D nanostructures and to compare the relaxometric properties of the two materials at a range of magnetic field strengths. To achieve this, a trans-phase MFI approach that was first devised by Gun'ko and Davies was used[302]. In short, this technique uses an external magnetic field to both align the MNPs and to also trigger the transfer of aligned MNPs from an aqueous to an organic phase containing a reactive silica precursor. This results in the formation of a silica shell encasing the MNPs and fixing them in their 1D alignment. To optimise this technique the influence of chosen precursor (choice of polymer and ferrite), concentration of base catalyst, and strength of external magnetic trigger were assessed. The resulting chains of silica-coated particles, named nano-necklaces had their magnetic and relaxometric properties analysed and compared to the parent polyelectrolyte-stabilised MNPs.

4.2 Cobalt Ferrite Nanoparticles

When considering a suitable precursor for the formation of the desired 1-dimensional nanostructures, it is important that they have a strong magnetic saturation (M_s), are sufficiently colloidally stable, and crucially they align parallel to magnetic field lines when exposed to an external magnetic field. Initial screening experiments were carried out by undergraduate student Teresa Insinna, in which cobalt ferrite nanoparticles (CFNPs) stabilised by P(AMPS) were prepared using the same *in situ* co-precipitation protocol used in the previous chapter only rather than Fe(II) and Fe(III) salts, Co(II) and Fe(II) salts are used (1:2 ratio is maintained). CFNPs were chosen rather than IONPs due to their larger core size (50 – 100 nm) which in turn results in an increased M_s.[71,270] Therefore, the magnetic force experienced by the CFNPs when exposed to the external magnetic trigger will be greater improving both the yield and reaction time of the trans-phase methodology. Importantly, polyelectrolyte stabilised CFNPs have also been shown to align parallel to an external magnetic field as observed for the P(AMPS)-IONPs.[82] P(AMPS)-CFNPs were prepared at [P(AMPS)]:[Metal salt] ratios of 1:100 and 1:2500 for all three polymer M_w's (8 000, 18 000, and 41 000 Da) and their magnetic and colloidal properties were characterised using VSM and DLS (data is provided in the Appendix Table 7.1). Subsequently, attempts at the formation of nano-necklaces using the trans-phase approach were carried out using the six P(AMPS)-CFNP samples were subsequently made.

However, it very quickly became apparent that this material would not make for a suitable precursor due to the rapid formation of large aggregates when exposed to the external magnetic field. This then prevented the particles from traversing the interface between the aqueous and organic phases. No further work was carried out on the P(AMPS)-CFNPs and no results are included within this chapter. This is also the reason as to why the ratio of 1:6250 was not investigated as increased relative quantity of metal salts in preparation would have exasperated. As an alternative this chapter instead focuses on cobalt ferrite nanoparticles stabilised by the commercially available polyelectrolyte, poly(sodium 4-styrenesulfonate) (PSSS). These materials have shown in the literature to have the desired properties mentioned above, with the presence of the PSSS already shown to cause the CFNPs to align parallel to an external magnetic field.

4.2.1 Preparation of Cobalt Ferrite Nanoparticles

The PSSS stabilised cobalt ferrite nanoparticles (PSSS-CFNPs) were prepared using an *in situ* co-precipitation approach. To assess the impact of the relative quantity of templating polymer and how it affects the alignment of magnetic particles in a magnetic field, two different composites were prepared. A schematic representation of the preparation of these nanoparticles is given in Figure 4.1. As demonstrated in Chapter 3, the amount of polymer stabiliser/template present impacts the colloidal properties of the particles, as such it is expected to play a role in the alignment behaviour in a magnetic field and hence production of 1D nanowires. Therefore, the molar ratio of polymer to metal salts was either 1:1000 or 1:100, representing a high and low PSSS component. Cobalt ferrite particles were also prepared *via* co-precipitation without PSSS present. The non-stabilised particles were used as controls for the trans-phase preparation of the magnetic nano-necklaces. The composition, colloidal properties, and magnetic properties of the two PSSS-CFNP nanocomposites and the non-stabilised CFNPs are presented in Table 4.1.

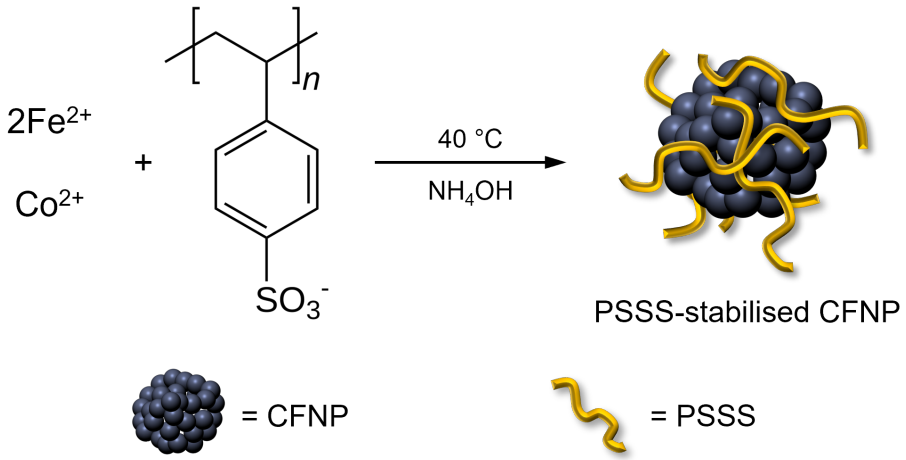

Figure 4.1: Schematic representation of the *in situ* co-precipitation preparation of poly(sodium-4-styrene) sulfonate (PSSS) stabilised cobalt ferrite nanoparticles (CFNPs). Non-stabilised particles were prepared using the same protocol but in the absence of PSSS.

Table 4.1: Description of the composition of cobalt ferrite nanoparticles (CFNPs) used as precursors for the synthesis of cobalt ferrite nano-necklaces. The material and magnetic properties of the CFNPs are also given.

Cobalt Ferrite Nanoparticle	**Stabilising Polymer**	**[Metal] : [PSSS]**	$d_{\mathbf{core}}$ **(nm)**[a]	$d_{\mathbf{hyd}}$ **(nm)**[b]	**PDI** [b]	M_s **(emu g^{-1})**[c]
CFNP	None	N/A	61.0 ± 31.9	394.1 ± 15.6	0.388 ± 0.023	53.4
PSSS-CFNP$_{1:1000}$	PSSS	1:1000	82.4 ± 30.5	217.7 ± 9.5	0.294 ± 0.014	66.2
PSSS-CFNP$_{1:100}$	PSSS	1:100	65.6 ± 21.2	234.7 ± 3.0	0.234 ± 0.066	52.7

[a]The average particle diameter (d_{core}) is calculated by measuring > 100 particles as imaged using transmission electron microscopy (TEM); [b]hydrodynamic diameter (d_{hyd}), and polydispersity index (PDI) as measured using dynamic light scattering (DLS); [c]M_s is the saturation magnetisation measured using vibrating sample magnetometry (VSM) at a field strength of 20 kOe.

4.2.2 Transmission Electron Microscopy

TEM images of the cobalt ferrite nanoparticles (CFNPs) (see Figure 4.2 demonstrates the quasi-spherical shapes of the particles with mean core diameters in the range of 61.0 – 82.4 nm. By comparing the d_{core} values we see that whilst the average diameter may increase with increasing relative metal concentration (PSSS-CFNP$_{1:100}$ = 65.6 nm ± 21.2, PSSS-CFNP$_{1:1000}$ = 82.4 ± 30.5 nm) both are within error of one another. The same is true for the d_{core} of non-stabilised CFNP, the large standard deviations are a result of the high polydispersity which is commonly seen for co-precipitation preparation routes. Upon closer examination of the particles, the structure is revealed to consist of several smaller cores (approx. 1-5 nm) clustered together to form the single cobalt ferrite nanoparticle. This has been documented previously for similar cobalt ferrite nanoparticles.[71,270] For the rest of this section, d_{core} refers to the entire particle and not to the diameter of the smaller component cores. In Figure 4.2, the propensity for the magnetic particles to align in the important 1D linear arrays when exposed to an external magnetic field can be observed, in a similar fashion to the P(AMPS)-stabilised iron oxide particles discussed in the previous chapter. The alignment is a result of strong interaction between the CFNPs and the sulfonate groups along the PSSS backbone. In the presence of an external field the polymer chains guide this linear alignment, acting as a template.[71,82,83]. Also shown in Figure 4.2 are the control non-stabilised particles, here it can be the seen that without the PSSS to act as a template the nanoparticles do not form linear arrays when exposed to an external magnetic field.

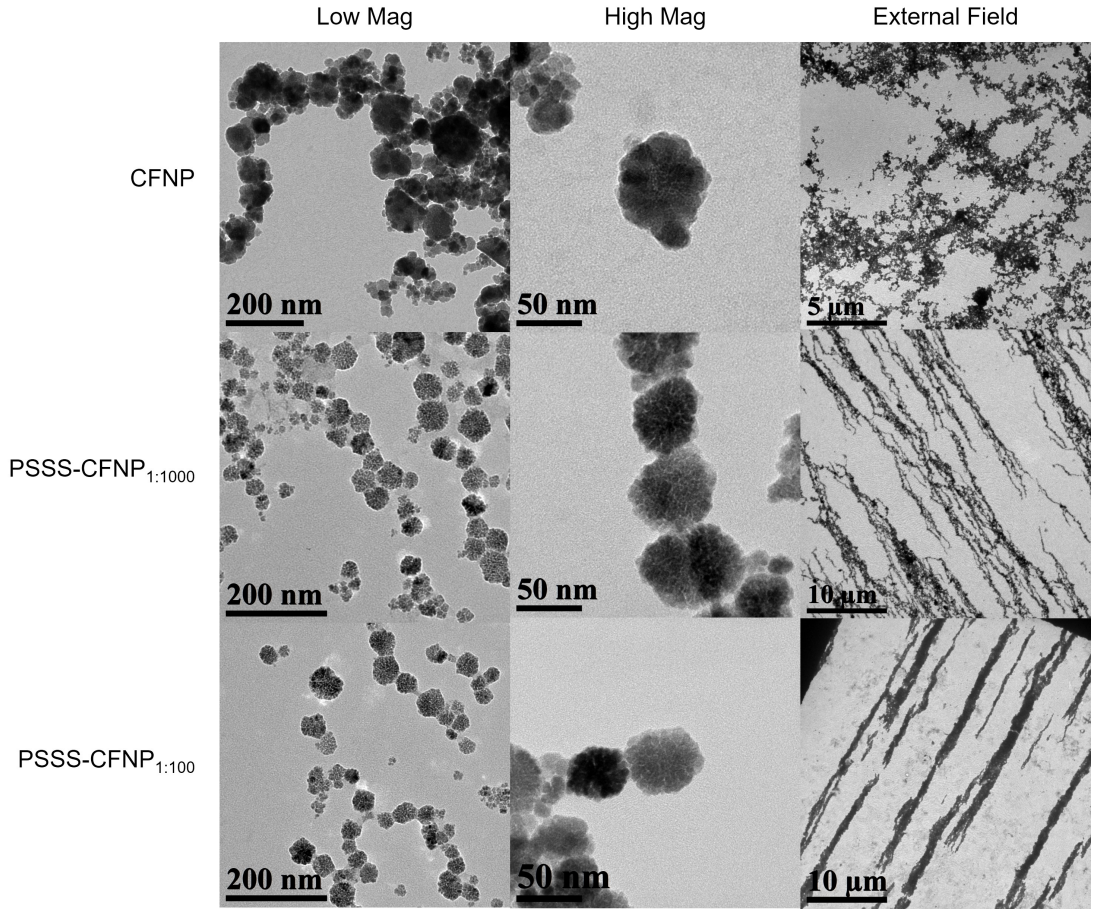

Figure 4.2: Transmission electron microscope (TEM) images of the non-stabilised cobalt ferrite nanoparticles (CFNP) and PSSS-stabilised cobalt ferrite nanoparticles (PSSS-$CFNP_{1:1000}$ and PSSS-$CFNP_{1:100}$). Images taken at low and high magnifications. Images in right hand column show the alignment of PSSS-stabilised CFNPs when TEM samples dried in the presence of an external magnetic field (approx. 0.1 T).

4.2.3 Dynamic Light Scattering & Zeta Potential

To quantify the colloidal stability of the PSSS-CFNPs, the hydrodynamic diameter (d_{hyd}) of the three samples was measured *via* DLS. The average d_{hyd} values are given in Table 4.1, and can be seen that for the stabilised samples, d_{hyd} falls within the range 217.7 – 234.7 nm. These values are larger than those measured for the core size by TEM; as with the iron oxide particles in the previous chapter, this is due to the presence of hydrogen bonding and Van der Waals forces acting upon the particles whilst in suspension. Also, with larger remanence than their

iron oxide counterparts, there will be small magnetic forces acting on each particle resulting in some aggregation. The PDI's for the stabilised CFNPs were both 0.234 – 0.294, evidence of good monodispersity. For the non-stabilised CFNP sample, the d_{hyd} is greater than either PSSS-CFNP$_{1:100}$ or PSSS-CFNP$_{1:1000}$, measured to be 394.1 ± 15.6 nm. The PDI is also larger than PSSS-CFNP$_{1:100}$ at 0.388 ± 0.023 compared to 0.234 ± 0.066 and 294 ± 0.014. Without the presence of the PSSS, there is little to overcome the attraction between particles (both Van der Waals and magnetic) and larger aggregates form in suspension as a result. The formation of aggregates will therefore skew the d_{hyd} and PDI as seen for the non-stabilised samples.

The presence of the negatively charged polymer was made apparent when measuring the zeta potential of the 3 samples. PSSS-CFNP$_{1:10000}$ and PSSS-CFNP$_{1:100}$ measured zeta potentials of -7.95 ± 0.29 mV and -6.97 ± 0.24 mV respectively, whereas the non-stabilised CFNPs were less negative at -2.81 ± 0.29 mV. This small negative charge results from the presence of physisorbed OH^- groups on the particle surface. Interestingly, the increased PSSS concentration of PSSS-CFNP$_{1:100}$ did not result in a more negative particle surface charge. This may explain why the d_{hyd} values did not decrease with increasing PSSS.

4.2.4 X-ray Diffraction

The cubic inverse spinel crystal structure of the cobalt ferrite nanoparticles was validated using powder X-ray diffraction (P-XRD). The P-XRD patterns were measured for all 3 samples and compared to database standards. The acquired patterns are presented in Figure 4.3. For all, reflection peaks were observed at 13.7° , 16.1°, 16.8° 19.4°, 23.8°, 25.3°, and 27.6°. These can be readily indexed to the (220), (311), (222), (400), (422), (511), and (440) crystal planes, respectively, as per JCPDS pattern no. 22-1086 for $CoFe_2O_4$.[121,303]

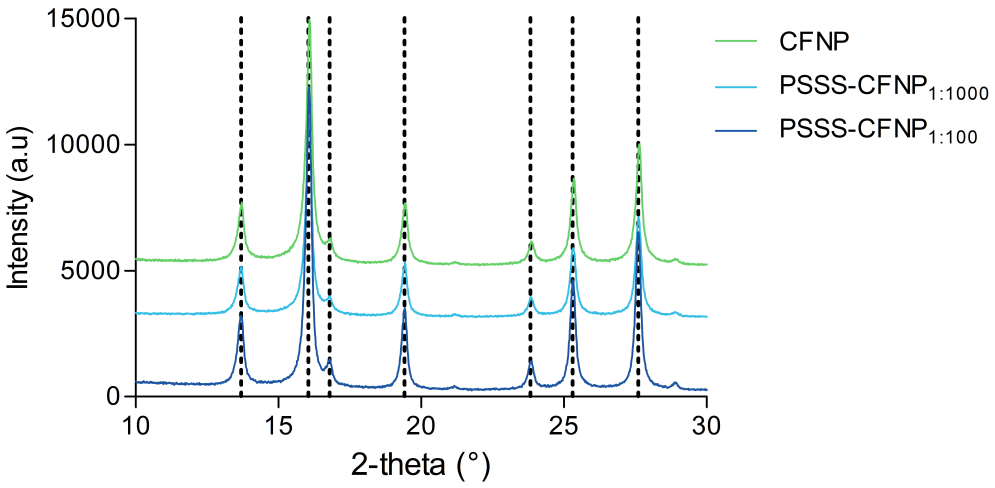

Figure 4.3: X-ray diffraction patterns of cobalt ferrite PSSS-stabilised nanoparticles (PSSS-CFNP$_{1:100}$ or PSSS-CFNP$_{1:1000}$) and non-stabilised cobalt ferrite (CFNP) plotted between $2\theta = 10° - 30°$. Dotted lines represent the expected peak positions for inverse spinel cobalt ferrite according to literature standards (JCPDS No: 22-1086).[121]

4.2.5 Vibrating Sample Magnetometry

As discussed in Section 4.2, the magnetic properties of these PSSS-CFNPs were key when determining what material would make a suitable precursor for this synthetic approach. These properties were investigated using vibrating sample magnetometry (VSM), with the magnetisation (M_s) of dried powder samples measured in an external field ranging from -20 KOe to 20 KOe. The M_s values for the stabilised, as well as the non-stabilised particles, were measured to be in the range 52.7 – 66.2 emu g^{-1}. When compared to the M_s of bulk cobalt ferrite (80.8 emu g^{-1}), these results appear to be much lower.[304] This is a result of both the presence of non-magnetic material in the form of the PSSS (M_s is normalised with respect to total mass of sample), and size associated effects such as spin canting.[45]

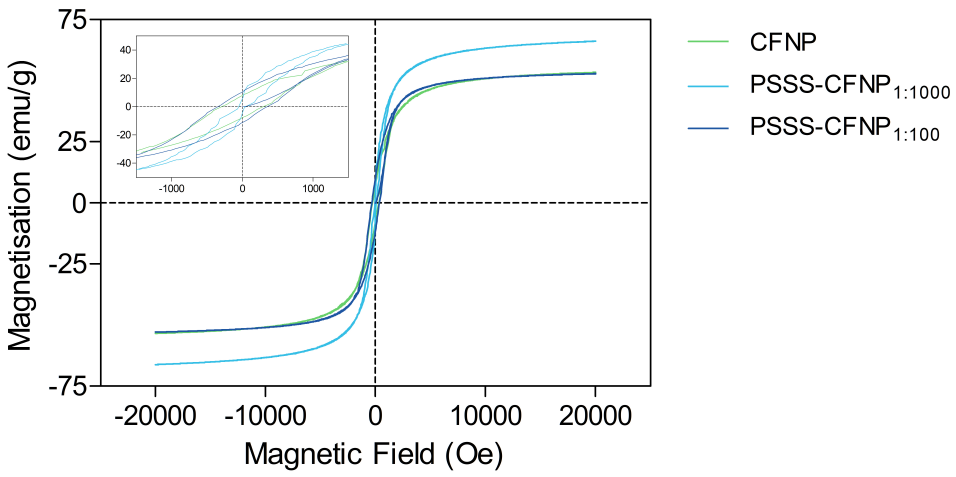

Figure 4.4: Magnetisation (mass susceptibility) of cobalt ferrite nanoparticles (CFNP, PSSS-CFNP$_{1:1000}$, PSSS-CFNP$_{1:100}$) as measured by vibrating sample magnetometry (VSM) plotted against magnetic field strength (measured between 20 000 and – 20 000 Oe). Inset shows the presence of small hysteresis loop indicative of slight ferromagnetic behaviour.

The magnetic remanence (M_r) and the coercivity (H_c) for the samples were also measured from the hysteresis plots shown in Figure 4.4. The remanence for all 3 fell within 5.1 – 8.2 emu g^{-1} and the coercivities were in the range 53.3 – 296.0 Oe. This shows the particles to be slightly ferromagnetic. As the d_{core} for the CFNPs were all measured to be above the theoretical superparamagnetic limit (> 10 nm) this is to be expected.[305,306] Note, the superparamagnetic limit for cobalt ferrite is smaller than for magnetite/maghemite due to its increased magneto-crystalline anisotropy. This degree of hysteresis is relatively small however and it is anticipated that this will be enough to drive strong particle alignment in an applied external magnetic field and be pulled through the two phases but still result in nano-necklaces that are not permanently magnetised. This is desirable as permanent magnetisation would result in reduced MRI performance due to magnetic aggregation *etc.*

4.2.6 Infrared Spectroscopy

To confirm the presence of the PSSS on the two stabilised CFNP samples, the FTIR spectra were recorded and compared against the spectra of the non-stabilised sample (CFNP). The three spectra are reproduced in Figure 4.5. All three samples display a strong stretch between

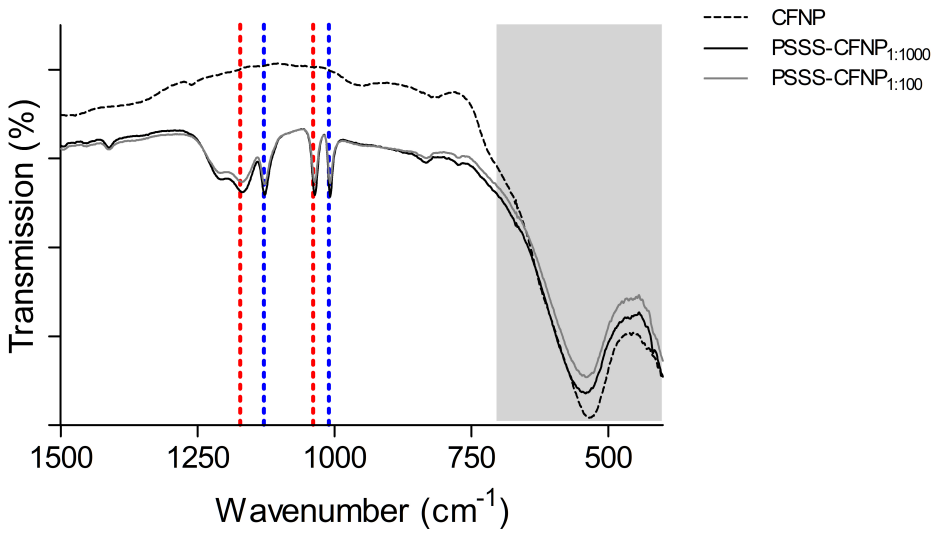

Figure 4.5: Fourier transform infrared (FTIR) spectra of non-stabilised cobalt ferrite nanoparticles (CFNP) and PSSS-stabilised cobalt ferrite nanoparticles (PSSS-CFNP$_{1:1000}$ and PSSS-CFNP$_{1:100}$ plotted between 1500 and 400 cm^{-1}). Region highlighted in grey contains Metal–O stretches, blue dashed lines highlight benzene stretches of PSSS (1130 and 1010 cm^{-1}), and red dashed lines highlight sulfonate stretches of PSSS (1172 and 1040 cm^{-1}).

700 – 400 cm^{-1} which represent that metal–O (Fe–O and Co–O) stretches of the cobalt ferrite nanoparticles. The spectra for the 2 stabilised samples also contained peaks that are characteristic of PSSS. With stretch at 1130 and 1010 cm^{-1} resulting from the in plane vibration and bending respectively of the benzene ring. The bands at 1172 and 1040 cm^{-1} are due to the antisymmetric and symmetric stretches of the sulfonate group.[307]

4.3 Preparation of Cobalt Ferrite Nano-necklaces

Having demonstrated the necessary colloidal and magnetic properties, the 3 candidate CFNP composites were then investigated as potential precursors for the preparation of the 1D silica coated nanostructure, cobalt ferrite nano-necklaces (CFNNs). Building on a previously devised method, this work looks to expand upon the trans-phase methodology to produce materials with tunable and reproducible magnetic and relaxometric properties.[302] The trans-phase synthesis of the CFNN's is summarised in Figure 4.6.

In summary, the reaction contains both a dense organic layer containing an organosilica

precursor (tetraethyl orthosilicate) and a less dense aqueous layer in which the polyelectrolyte stabilised nanoparticles are suspended in the presence of the base catalyst. The entire vessel is then placed atop a strong permanent magnet. The magnetic nanoparticles subsequently align parallel to the field lines before being pulled from the aqueous layer down to the magnet and through the organic layer. As the aligned particles pass through the bottom layer, a hydrolysis and condensation reaction is initiated (electrostatically adsorbed base on particle surface from the aqueous layer acts as a catalyst) and a thin coating of silica is formed around the linear array of particles, creating the CFNN's. The resultant product can be easily extracted from the two media using a combination of centrifugation and magnetic separation.

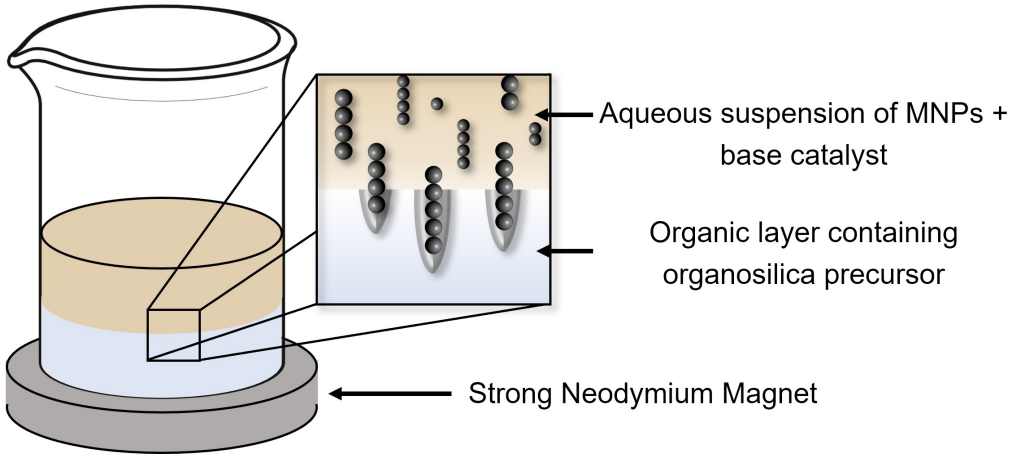

Figure 4.6: Schematic representation of the trans-phase synthesis used to produce silica coated cobalt ferrite nano-necklaces (CFNNs). The top, aqueous layer contains a suspension of PSSS-stabilised cobalt ferrite nanoparticles (PSSS-CFNPs) and base (NH_4OH) catalyst. The bottom, organic layer contains the organosilica precursor, tetraethyl orthosilicate (TEOS). Adapted from Gun'ko 2013.[302]

When considering this new approach, there are several potential factors that can impact the formation of the nano-necklaces. These include the choice of magnetic particle, the stabilising polymer (including the relative quantity of polymer), choice of base catalyst, strength of magnetic trigger, concentration of reagents, and even depth of organic layer (distance between suspended magnetic particles and permanent magnet). In this chapter, the variables that will be investigated are the relative quantity of PSSS present in the parent CFNPs, the concentration of the base catalyst, and the strength of the permanent magnet. All other variables will be fixed to reduce number of experiments. See Section 2.2.6 for the full synthetic procedure and values selected for the fixed variables. When analysing the effects of the chosen variables, the

key responses will be whether a black precipitate was observed at the bottom of the reaction vessel, presence of nano-necklaces or other silica coated nanoparticles as confirmed by TEM, and the magnetic and relaxometric properties of any observed nano-necklaces as measured by VSM and relaxometry, respectively.

4.3.1 Role of Templating Polymer in Nano-necklace Formation

The first factor to be investigated in the tuning of the trans-phase approach for the formation of the CFNN's is the importance of the stabilising and templating polymer, poly(sodium 4-styrenesulfonate) (PSSS). Its role was investigated by preparing the CFNN's using the 3 CFNP's characterised in Section 4.2. By varying the relative quantity of PSSS whilst keeping all other factors equal it will show the importance of the templating behaviour for the formation of the 1D nanostructures. The synthesis was repeated minimum of 3 times for each of the 3 different CFNP experiments.

Once the synthesis was complete, the beakers in which the PSSS-stabilised CFNPs had been used (PSSS-$CFNP_{1:100}$ and PSSS-$CFNP_{1:1000}$) could be seen with small quantities of black precipitate at the bottom. The precipitates were washed using both magnetic separation and centrifugation before imaging with TEM. Shown in Figure 4.7 are TEM images of the precipitate that formed using parent particle PSSS-$CFNP_{1:1000}$ (CFNN01). They show examples of well-formed CFNNs with a thin shell of silica maintaining their quasi-1-dimensional structures. They measure an average length of 2.15 µm ± 1.37 µm with an average diameter of 0.24 µm ± 0.18 µm (average taken across 3 replicates). In the TEM images the thin silica shell of only a few nanometres can be seen encasing the wires (4.7 ± 1.5 nm). (Figure 4.7, indicated by arrows). Also noteworthy is that CFNN's were observed in all 3 replicates, demonstrating the reproducibility of this method.

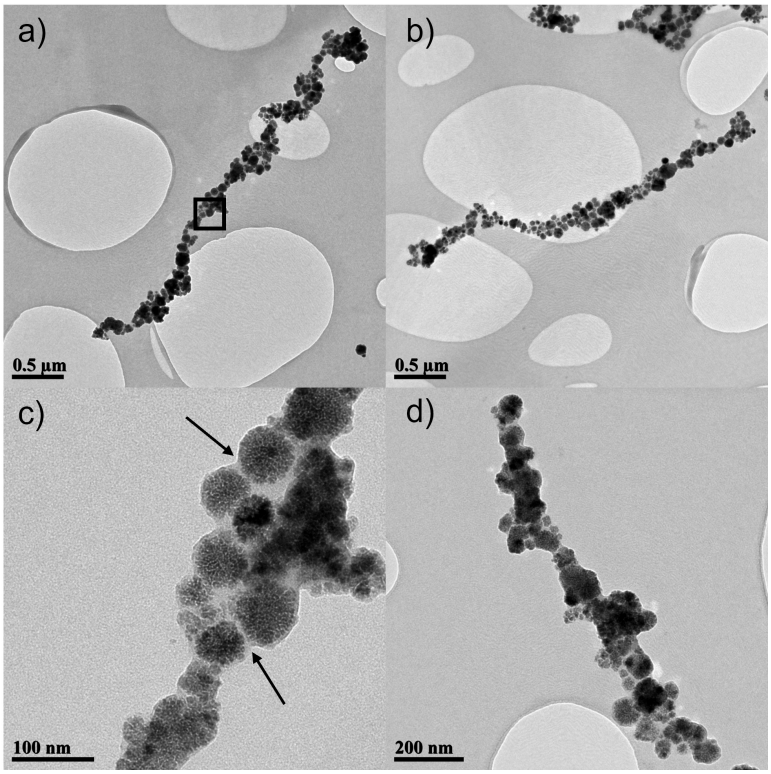

Figure 4.7: Transmission electron microscopy (TEM) images of cobalt ferrite nano-necklaces (CFNN) sample CFNN01 prepared with PSSS-CFNP$_{1:1000}$. Image c) shows the highlighted section (black box) at increased magnification. In this image the thin silica shell is highlighted with black arrows. Images sourced from each of the 3 replicated syntheses.

FTIR was used to confirm that the shell observed by TEM was formed of silica, the spectra produced is given in Figure 4.8. Shaded in grey are the two bands resulting from the ferrite nanoparticles, the first at approximately 580 cm^{-1} being attributed to the M–O stretch for the cation in the tetrahedral site and the other at approximately 450 cm^{-1} attributed to the M–O stretch with the cation in the octahedral site. The 4 peaks highlighted at 1188, 1074, 966, and 800 cm^{-1} are all characteristic of silica. The strong stretch at 1074 cm^{-1} and the shoulder centred at 1188 cm^{-1} are due to the Si–O–Si TO and LO phonon modes respectively. The peak at 966 cm^{-1} results from the silanol (Si–OH) groups at the silica surface whilst the small peak at 800 cm^{-1} is due to the siloxane (Si–O–Si) symmetric stretch vibration.[308] Due to the strength and broadness of the silica peaks it is not possible to resolve the peaks that would be expected for the stabilising PSSS as they overlap (see Figure 4.5).

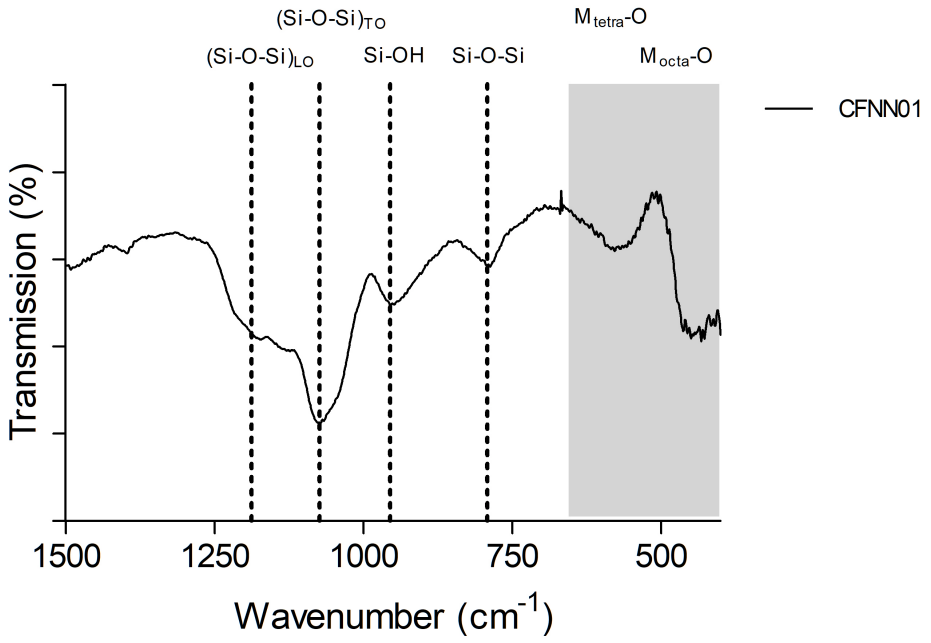

Figure 4.8: Fourier transform infrared (FTIR) spectra of silica-coated cobalt ferrite nano-necklaces (CFNN01) plotted between 1500 and 400 cm^{-1}. Region highlighted in grey (650 – 400 cm^{-1}) contains Metal–O stretches, dashed lines at 1188, 1074, 966, and 800 cm^{-1} highlight the characteristic stretches of silica.

CFNN02 was prepared using parent particle PSSS-$CFNP_{1:100}$, and therefore allows for comparison based on the increased relative quantity of PSSS. When comparing to CFNN01, one difference is instantly apparent. Rather than forming nanostructures greater than 1 µm, much smaller necklaces were produced (Figure 4.9) . These were measured to have an average length of 0.68 µm ± 0.17 µm and can be seen to consist of fewer CFNPs. The explanation for such differences in output must be attributable to the increased relative quantity of the templating polymer.

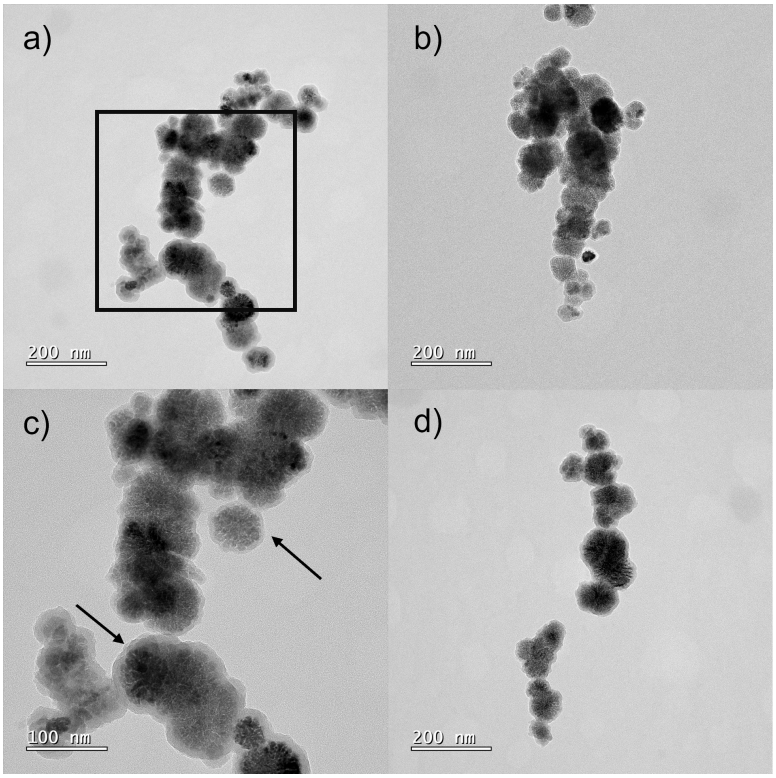

Figure 4.9: Transmission electron microscopy (TEM) images of cobalt ferrite nano-necklaces (CFNN) sample CFNN02 prepared with PSSS-CFNP$_{1:100}$. Image c) shows the highlighted section (black box) at increased magnification. In this image the thin silica shell is highlighted with black arrows. Images sourced from each of the 3 replicated syntheses.

It is not clear however the underlying cause of this difference. The colloidal properties of two PSSS-stabilised CFNPs were comparable according to DLS. The d_{hyd} for PSSS-CFNP$_{1:100}$ was marginally higher but this would not explain why the silica coated necklaces were smaller. It is therefore likely that the difference may be due to the decreased M_s of the higher PSSS particles. A reduced magnetisation may result in weaker magnetic attraction and alignment between magnetic cores and therefore result in the formation of the smaller nano-necklaces.

A control experiment was also carried out using the non-stabilised CFNPs to demonstrate the role of the PSSS in the formation of the 1D nanostructures. The presence of the hydrophilic, negatively charged PSSS on the surface of the nanoparticles may interfere with alignment and stability of the particles as they enter the organic, DCM layer. Therefore a control of non-stabilised CFNPs allow for the investigation of these possible effects. No TEM images were collected for the non-stabilised CFNP control (CFNN00) as no particles had passed through

the interface between the two layers. In Figure 4.10, a large aggregate can be observed between the two layers. The inability for the non-stabilised particles to cross the boundary between the two phases is attributed to the lack of stabiliser (PSSS) and therefore the formation of larger aggregates.

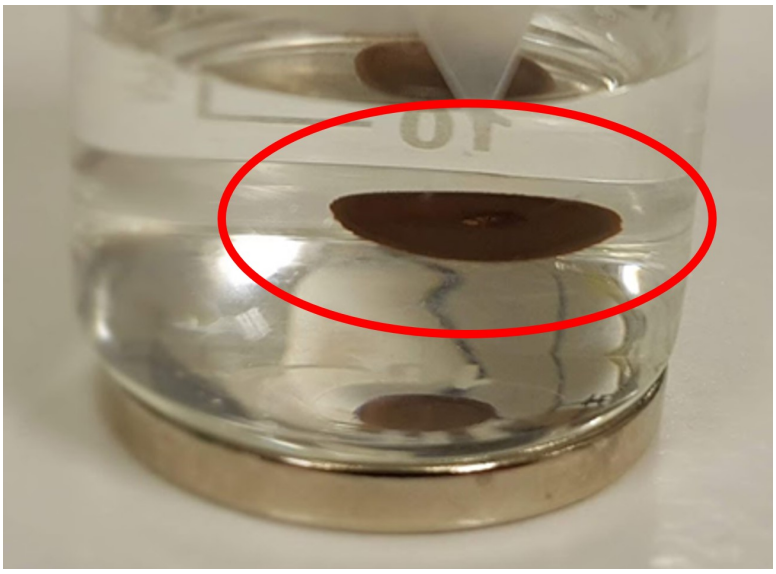

Figure 4.10: Photograph of large aggregate (circled) formed at th interface between the organic and aqueous layers of the trans-phase experiment set-up after approximately 48 hours.

This increased aggregation is exasperated by the external magnetic field. As seen in the image given in Figure 4.10, once the size of the aggregates becomes too large, they can no longer pass through into the organic layer likely due to the tension at the interface. Therefore, whilst the particles may be less hydrophilic and less negatively charged than the PSSS-CFNPs, the uncontrolled aggregation dominates the behaviour of the non-stabilised nanoparticles, preventing the formation of CFNN's. This stark contrast between what was observed for the PSSS-CFNPs and the non-stabilised particles clearly reinforces the importance of the PSSS in this synthesis.

4.3.2 Role of Base Catalyst in Nano-necklace Formation

The addition of the base catalyst to the aqueous layer is necessary for the condensation of silica onto the surface of the magnetic cores. Once adsorbed to the surface of the particle the base will trigger the formation of the silica shell, encasing the nano-necklace. The base may also act to destabilise the particles by affecting the surface charge, encouraging them to assemble into

the linear arrays before passing from one phase to the other. In this section, the concentration of base was investigated as a means of potentially tuning the physical and magnetic properties of CFNNs formed using the trans-phase method. To begin, the approach used for CFNN01 was be used as a mid-point for the concentration of ammonium hydroxide (final concentration of 0.44 M). The upper and lower bounds were therefore set at 2.5 M (CFNN03) and 0.09 M (CFNN04) respectively, the concentration was be adjusted by altering the volume of 8.8 M ammonium hydroxide that is added to the aqueous layer. As with the previous section, these experiments were carried out in triplicate.

In Figure 4.11, the TEM images collected for the high concentration sample (CFNN03) are shown. The CFNPs can be seen to be coated in a thick layer of silica (20.1 ± 3.8 nm), a thicker than what was measured for sample CFNN01 (4.7 ± 1.5 nm). The increased thickness of the coating can be attributed to the increased NH_4OH concentration in the aqueous layer. At the higher concentration, more shall be adsorbed onto the particles surface and therefore results in a greater quantity of the silica precursor condensing onto the surface of the magnetic core. A similar relationship between ammonia concentration and thickness of silica shell has been observed for the preparation of IONP@SiO_2 nanoparticles.[309–311] Interestingly, for these samples, core@shell particles appear to have been formed, but have not assembled into the 'necklace' like structure which was produced for CFNN01 and CFNN02. Image b) is the only example found where it could be described as matching the description of a nano-necklace. As so few defined necklaces were observed, size measurements were not carried out. The reason for the preferred formation of core@shells compared to nano-necklaces is not immediately evident. It is potentially a result of the increased NH_4OH adsorbed onto the surface increasing the electrostatic repulsion between core surfaces. This in turn would hinder the magnetically induced alignment of the particles and result in the core@shell particles observed herein.

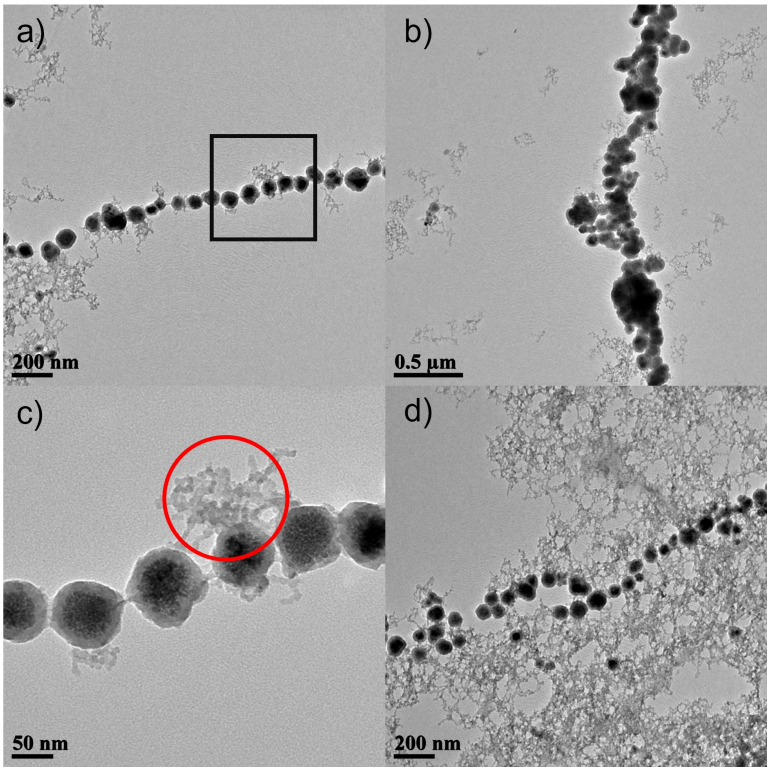

Figure 4.11: Transmission electron microscopy (TEM) images of cobalt ferrite nano-necklaces (CFNN) sample CFNN03. Images a) and b) show 1D structures with visible silica coating. Image d) shows the aggregated network of particles seen for the sample rather than the desired CFNNs.

One very apparent difference between sample CFNN01 and CFNN03 is the excess condensed silica that can be seen in great quantities within the images. Circled in red is an example of such silica by-product, with Fig 4.11 showing the scale of silica that was present throughout the sample. Note, as with previous experiments the CFNN03 sample was washed both with centrifugation and magnetic separation, however this appeared insufficient in removing the non-magnetic excess silica, which appeared to be significantly cross-linked. The cause for this excess is likely a result of the high quantity of NH_4OH, which when carried across the interface, desorbs into the organic layer. The 'free' base is then able to trigger the condensation of the TEOS forming the 'webs' of silica away from the surface of the particles. This may also have occurred for experiments CFNN01 and CFNN02, but to a much lesser degree due to the lower concentration of NH_4OH, meaning it could be more readily removed through magnetic separation.

When reducing the concentration of the NH_4OH, it would be expected that a reduced layer

of silica would form, as well as one which is potentially less uniform. This is indeed what was observed when the volume of NH_4OH was reduced (sample CFNN04) so that the concentration of base in the aqueous layer was 0.09 M. The experiment CFNN04 did result in the formation of a black precipitate at the base of the beaker which was then imaged by TEM. The images in Figure 4.12 show that the coating of the CFNPs was inconsistent, many of the particles imaged appeared to be uncoated. The black arrows on images b) and d) highlight the few examples where a thin silica shell could be seen. Without a sufficient silica shell to maintain the 1D assemblies of particles, necklace like structures were not apparent in the samples images with aggregates of particles observed instead.

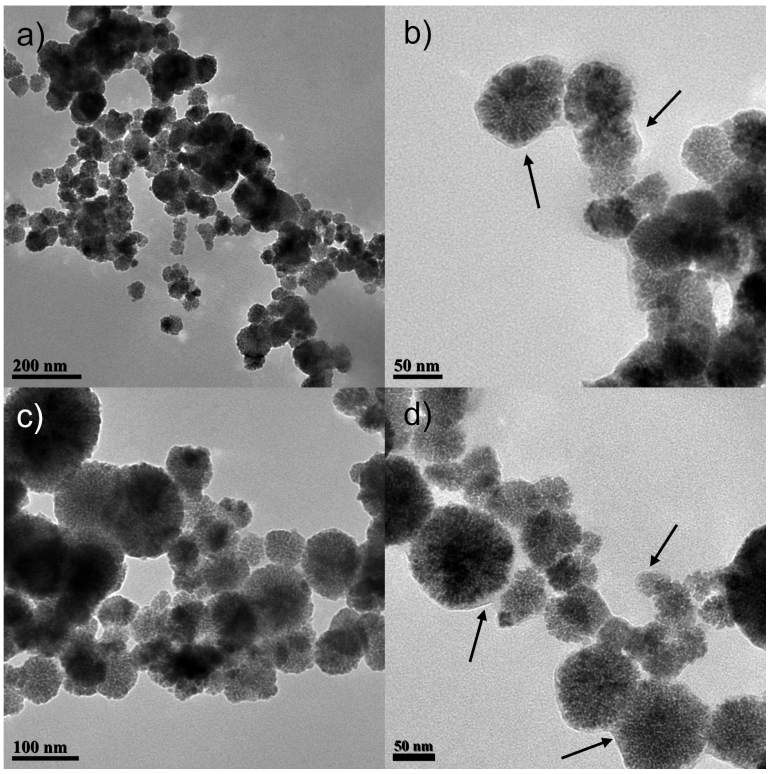

Figure 4.12: Transmission electron microscopy (TEM) images of sample CFNN04. Images a) and c) show uncoated CFNPs whereas images b) and d) show CFNPs with thin silica coating highlighted by the black arrows.

4.3.3 Role of Magnetic Trigger in Nano-necklace Formation

Finally, the strength of the magnetic trigger was investigated. A permanent magnet with a pull strength of 45.0 kg (compared to 16.3 kg for previous experiments) was chosen whilst

the remaining variables were as selected for experiment CFNN01. Therefore, this experiment (CFNN05) was designed to reveal, if any, the impact of the strength on the external magnet had on the formation and structure of possible CFNNs. The strength of the magnetic fields at the surface of the magnets is approximately 0.15 T and 0.24 T for the weak and strong magnet respectively. Using the magnetometry data collected for PSSS-CFNP$_{1:1000}$, the magnetisation of the particles at each of the fields can be estimated. Using the M vs. H plot the magnetisation of the particles increases from 45 emu/g to 51 emu/g when placed atop the stronger magnet. The effects on the nano-necklaces as a result of this increased particle magnetisation is shown in Figure 4.13.

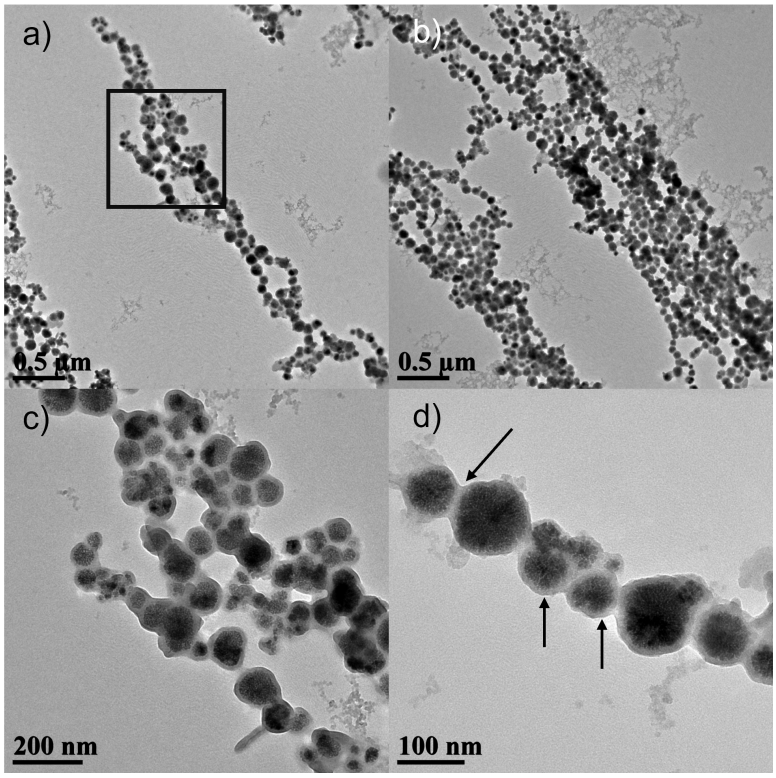

Figure 4.13: Transmission electron microscopy (TEM) images of sample CFNN05. Images b) and d) show CFNPs with thin silica coating highlighted by the black arrows. Image c) gives an increased magnification of the black box, showing the non-uniform linking of multiple chains of particles giving rise to thicker 1D structures.

Rather than forming singular strands of particles, the increased magnetic trigger strength resulted in the formation of branched chains of silica coated CFNPs. This is best seen in images

a) and b) of Figure 4.13, where the multiple chains of silica coated particles run parallel to one another with branches between them. The wires measured both an increase in length and width when compared to CFNN01 (using a weaker magnet) with a length of 4.18 ± 1.84 μm and width of 0.41 ± 0.16 μm.

The increased external magnetic field and therefore increased magnetisation of the CFNPs results in stronger magnetic attraction between cores causing them to assemble in greater numbers. Similar observations were made by Kralj *et al.,* whereby increasing the strength of the magnetic field used for the formation of nanochains instead resulted in what they referred to as nanobundles, with the nanobundles being longer and much wider than the nanochains.[266] This 'lateral' attraction for dipolar chains of particles has already been described in detail by Furst and Gast.[312]

These examples consider a uniform magnetic field, however the neodymium magnets used in this work do not produce uniform fields. Visual representations of the fields produced by the two different magnets are provided in Figure 4.14. Here we can see that the density of the field lines, particularly at the far edges of the magnet are much more compacted (increased flux density). Therefore, this may also cause chains of particles to be in closer proximity to one another before the condensation of the silica shell permanently links the chains.

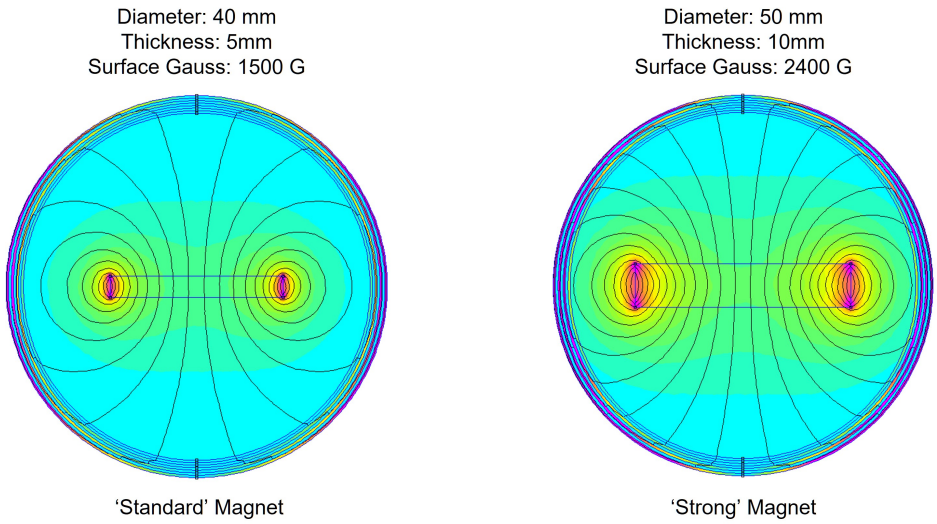

Figure 4.14: Visualisations of the non-uniform magnetic fields produced by the 'standard' strength magnet (pull strength = 16.3 kg) used for experiments CFNN00 to CFNN04, and the 'strong' magnet (pull strength = 45.0 kg) used for the experiment CFNN05. Fields modelled using FEMM software, where the blue box represents the permanent magnet and the colour is representative of flux density (B), pink equalling high flux density and blue equalling low flux density.[313]

4.4 Magnetic & Relaxometric Properties of Cobalt Ferrite Nano-necklaces

4.4.1 Magnetic Properties of Cobalt Ferrite Nano-necklaces

The magnetic properties of the cobalt ferrite nano-necklace samples, CFNN01, CFNN02, CFNN03, CFNN04, and CFNN05 were all characterised using vibrating sample magnetometry, with the magnetisation of dried powder samples measured in an external field ranging from -20 KOe to 20 KOe. Due to the very low yields from the syntheses, product from the 3 replicates were combined for the VSM measurements. The measured M_s, H_c, and M_r for the 5 samples were compared. The CFNNs are also compared to their parents particles, PSSS-CFNP$_{1:1000}$ for samples CFNN01, CFNN03, CFNN04, and CFNN05, and PSSS-CFNP$_{1:100}$ for sample CFNN02. The magnetisation vs. field plots are presented in Figure 4.15 with the M_s, H_c, and M_r value tabulated in Table 4.2.

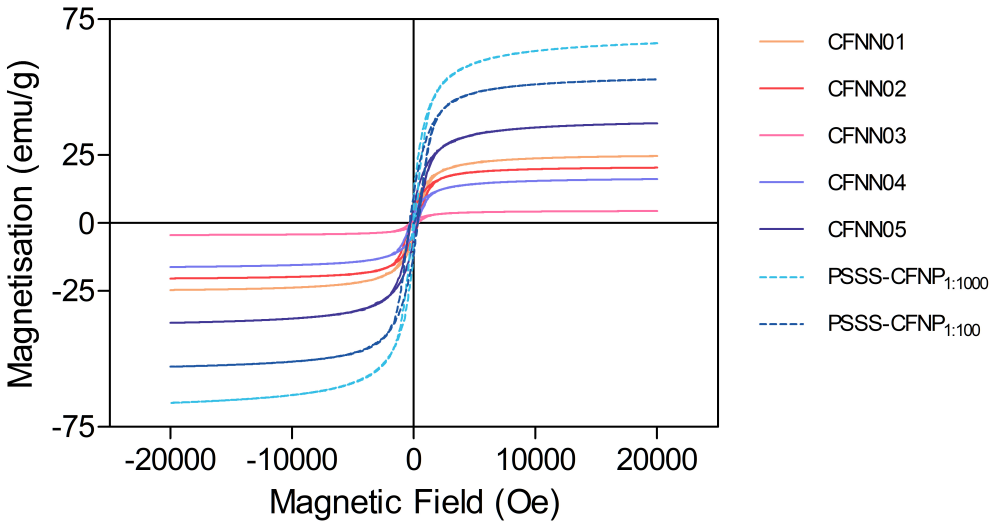

Figure 4.15: Magnetisation (mass susceptibility) of cobalt ferrite nano-necklaces (CFNN01, CFNN02, CFNN03, CFNN04, and CFNN05) and their respective parent particles (PSSS-$CFNP_{1:1000}$ and PSSS-$CFNP_{1:100}$) as measured by vibrating sample magnetometry (VSM) plotted against magnetic field strength (measured between 20 000 and – 20 000 Oe). Inset shows the presence of small hysteresis loop indicative of slight ferromagnetic behaviour.

The 5 nano-necklace samples measured M_s values in the range of 4.4 – 36.7 emu/g, all lower than the M_s values of the CFNP parents, PSSS-$CFNP_{1:1000}$ and PSSS-$CFNP_{1:100}$, which measured values of 66.2 and 52.7 emu/g respectively. The cause for this decrease is due to the measurements being normalised for total mass of sample, which includes the mass contribution of non-magnetic silica present. This is most apparent for sample CFNN03 which measured a low M_s of 4.4 emu/g, this sample also notably contained the highest relative quantity of 'free' silica as observed by TEM.

Comparisons between the nano-necklaces (omitting CFNN03 due to high silica quantity) showed that the sample that produced the highest M_s was the longest and widest sample CFNN05 (M_s = 36.7 emu/g), produced using the strong magnetic field. This was then followed by the second longest sample CFNN01 (M_s = 24.6 emu/g). These are then followed by the short CFNNs seen for CFNN02 (M_s = 20.4 emu/g). This relationship is not unexpected as the formation of linear assemblies can result in ferromagnetic coupling between particles causing an increase in the magnetic moment of chains of particles compared to single particles.[233,267,268].

With a greater number of particles in the chain forming CFNN05 there will be increased coupling and therefore increased M_s. The longer CFNN's also have an increased effective radius, that is half the length of their easy axis. Gao *et al* have demonstrated that the saturation magnetisation is proportional to the effective radius.[239] This is supported by the increasing M_s of iron oxide nanorods with increasing length.[256] What is unclear is the reason for the low M_s value measured for CFNN04 as the silica content appeared to be low (with little coating on the particles) so therefore would expect its M_s to be most similar to the parent CFNPs.

Comparing the coercivity and remanence of the CFNNs a trend is less apparent, with values measured in the range 201.1 – 345.4 Oe for H_c and 3.3 – 6.3 for M_r. When considering the magnetic properties of the CFNN's it is not sufficient to consider their dimensions alone. The thickness of a silica coating has been demonstrated to affect the magnetic properties of superparamagnetic particles, with thicker coatings distance between particles increasing are therefore reducing dipolar interactions. This in turn can lead to decreased M_s and H_c.[163,314] Repeated measurements would allow for a stronger conclusion on the magnetic behaviour of these nanostructures.

Table 4.2: The saturation magnetisation (M_s), coercivity (H_c), and remanence (M_r) of cobalt ferrite nano-necklaces as measured by vibrating sample magnetometry (VSM).

Sample Name	M_s **(emu/g)**	H_c **(Oe)**	M_r **(emu/g)**
PSSS-CFNP$_{1:1000}$	66.2	53.3	5.1
PSSS-CFNP$_{1:100}$	52.7	220.0	8.2
CFNN01	24.6	201.1	3.6
CFNN02	20.4	345.4	4.7
CFNN03	4.4	291.2	1.0
CFNN04	16.2	308.0	3.3
CFNN05	36.7	300.0	6.3

4.4.2 Transverse & Longitudinal Relaxation of Cobalt Ferrite Nano-necklaces

The longitudinal and transverse relaxivities (r_1 and r_2) of the 5 nano-necklace samples were measured at a frequency of 23 MHz. All samples were dispersed in 0.5 % Xanthan gum to prevent aggregation during measurement. Also measured were the two parent CFNP samples, PSSS-CFNP$_{1:1000}$ and PSSS-CFNP$_{1:100}$. The values collected are presented in Table 4.3.

Table 4.3: The transverse (r_1) and longitudinal (r_2) relaxivities of cobalt ferrite nano-necklaces and PSSS-stabilised cobalt ferrite nanoparticles as measured at field strength of 23 MHz.

Sample Name	r_2 **(mM^{-1}s^{-1})**	r_1**(mM^{-1}s^{-1})**	r_2/r_1
PSSS-CFNP$_{1:1000}$	118.5	6.3	18.9
PSSS-CFNP$_{1:100}$	104.9	6.5	16.1
CFNN01	141.6	5.0	28.3
CFNN02	86.2	2.2	38.7
CFNN03	73.8	0.3	226.0
CFNN04	99.9	2.4	42.1
CFNN05	52.0	1.8	29.0

Comparing the CFNNs against their respective parent particles (PSSS-CFNP$_{1:1000}$ and PSSS-CFNP$_{1:100}$) all measured a decrease in the r_1 and increase in r_2/r_1 caused by the silica coating present on the surface of the CFNNs. The silica coating reduces water access to the magnetic centres as well as potentially increasing water residence times through forming hydrogen bonds.[315,316]. This effect is particularly obvious for sample CFNN03, which as observed by TEM analysis, resulted in CF cores coated in a much thicker shell. The cross-linked silica surrounding many of the particles may also interfere with the water access and residence times and thus giving rise to the very high r_2/r_1 (226.0). Sample CFNN01 was also the only sample to measure an increase in the transverse relaxivity compared to its parent, PSSS-CFNP$_{1:1000}$. This increase is likely to be due to the strong interparticle interactions that occur between the multiple cores comprising the entire 1D structure. Similar r_2 enhancements have been observed by Sailor *et al.,* for nanoworms and Peiris *et al.,* for nanochains.[240,317]. It is also notable that CFNN01 was the sample with the highest aspect ratio and second highest M_s (24.6 emu/g) and length (2.15 $\pm$ 1.37 μm), with r_2 of MNP based contrast agents shown to be proportional to both the M_s and r_{eff} (half the easy axis).[239]

The sample measured with greatest chain length and with the highest M_s was measured to be sample CFNN05, however this sample measured the lowest r_2 of 52.0 mM^{-1}s^{-1}. This may be due to the lateral linking of chains reducing the water access to the cores that are within the centre of these wider structures. This sample also had a thicker shell in comparison to CFNN01 which may cause the reduction in r_2. Also in Table 4.3 the samples CFNN02 and CFNN04 measured r_2's of 86.2 mM^{-1}s^{-1} and 99.9 mM^{-1}s^{-1} respectively, showing that without the elongated permanent 1D structure of as observed for sample CFNN01, the enhancement in

relaxivity is not observed and may in fact have a detrimental effect on contrast performance. For future work, measurements should be repeated in triplicate in order to confirm these conclusions.

4.4.3 Low-Field Relaxation Behaviour of Cobalt Ferrite Nano-necklaces

Whilst a small amount of work has been carried out in the literature characterising the relaxometric behaviour of similar nanomaterials, such as the nanochains and nanoworms described in the introduction to this chapter, there is yet to be a detailed description of the relaxometric behaviour of 1D permanent assemblies at low fields.[240,241,269] The only example of FFC-relaxometry used for the characterisation of these materials was performed by Sailor *et al.*[269] The NMRD profiles produced by the nanoworms were typical for superparamagnetic particles, with a peak at $\sim$ 0.1 T and a plateau at lower field strengths (0.01 – 0.001 T). Using the data they were subsequently able to fit the data in good accordance with outer-sphere theory. However, when compared to a theoretical NMRD curve for isolated particles (the same size and magnetic properties as the constituent particles) the nanoworms produced a much larger peak and increased low field r_1 values. Whilst this was a comparison against a theoretical parent particle it demonstrated how the formation of permanent linear particle assemblies may enhance their low-field relaxation behaviour. In this work, the r_1 was measured between Larmor frequencies of 10 and 0.01 MHz for both the nano-necklace samples CFNN01 and its spherical counterpart PSSS-CFNP$_{1:1000}$. The resulting NMRD profiles are presented in Figure 4.16.

The low field relaxometric behaviour of PSSS-stabilised CFNPs has already been detailed in-depth with the profile given here in good agreement with past examples.[82] Neither PSSS-CFNP$_{1:1000}$'s or CFNN01's profiles share any characteristics with the model profile for a superparamagnetic behaviour (such as a low field plateau or $\nu_{\max}$). Therefore, both samples are exhibiting strong ferromagnetic behaviour (as to be expected as d_{core} is greater than the superparamagnetic limit). This is supported by the observed hysteresis in the M vs H plots as shown in Figure 4.4. For the PSSS-stabilised CFNPs this is due to both the high magnetocrystalline anisotropy of inverse spinal cobalt ferrite as well as strong interparticle interactions between particles (also observed for PAMPS-stabilised IONPs).

When comparing between the two samples (CFNN and parent CFNP) we can see that the longitudinal relaxivity of the CFNN's in the mid-region (1 – 0.1 MHz) is reduced in comparison to the parent CFNPs. However the relaxivity then rises sharply in the low field region ($<$ 0.1 MHz) resulting in an increased r_1 measured at 0.01 MHz (CFNN = 55.4 mM^{-1}s^{-1}, CFNP = 53.2 mM^{-1}s^{-1}). At the lower fields Néel relaxation dominates which itself is strongly dependent

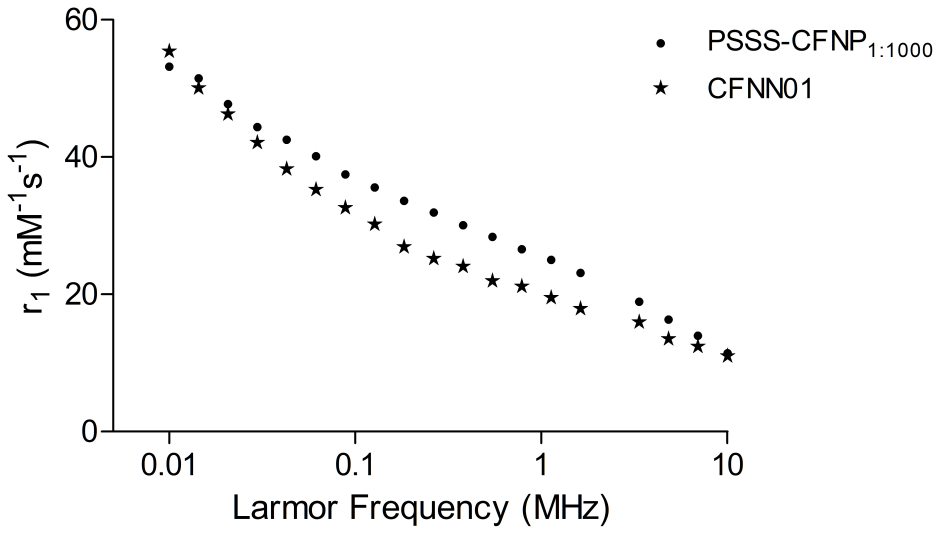

Figure 4.16: ^{1}H NMRD profiles measured at 25 °C for PSSS-stabilised cobalt ferrite nanoparticles (PSSS-CFNP$_{1:1000}$) and silica-coated cobalt ferrite nano-necklaces (CFNN01). Longitudinal relaxivities (r_1) were measured between 10 and 0.01 MHz.

on the material's anisotropy. Therefore the low field behaviour observed for the CFNNs is likely a result of increased anisotropy of the permanent 1D assembly due to strong dipolar interactions between the individual core particles. The interactions arising due to the permanent 1-dimensional structure of the CFNNs holding the magnetic cores in close proximity to one another and aligning their dipoles along the same axis. This is supported by the increased anisotropy observed for other 1D assemblies of MNPs.[233,318] The relaxation behaviour in the mid-region (0.1 – 1 MHz) has a greater Brownian component and therefore the silica shell on the surface of the CFNN results in comparative reduction in r_1, as observed for all silica coated samples in the previous section.

As FFC-relaxometry is highly sensitive to differences in molecular dynamics it makes for a powerful tool in determining the reproducibility of the trans-phase approach. Thus, plotted in Figure 4.17 are the profiles between 0.01 and 10 MHz for the 3 replicated syntheses of CFNN01. We can see from this that the profiles produced for the 2 of the samples were almost identical (r_1's at 0.01 MHz of 55.4 mM^{-1}s^{-1} and 54.0 mM^{-1}s^{-1}). However, whilst the third sample produced a similar shaped NMRD profile the longitudinal relaxivity measured was much reduced (r_1 at 0.01 MHz = 30.1 mM^{-1}s^{-1}). This sample may be an outlier or error in

concentration determination by ICP-OES. However, without an increase in sample size it is not possible to definitively confirm the reproducibility of this method.

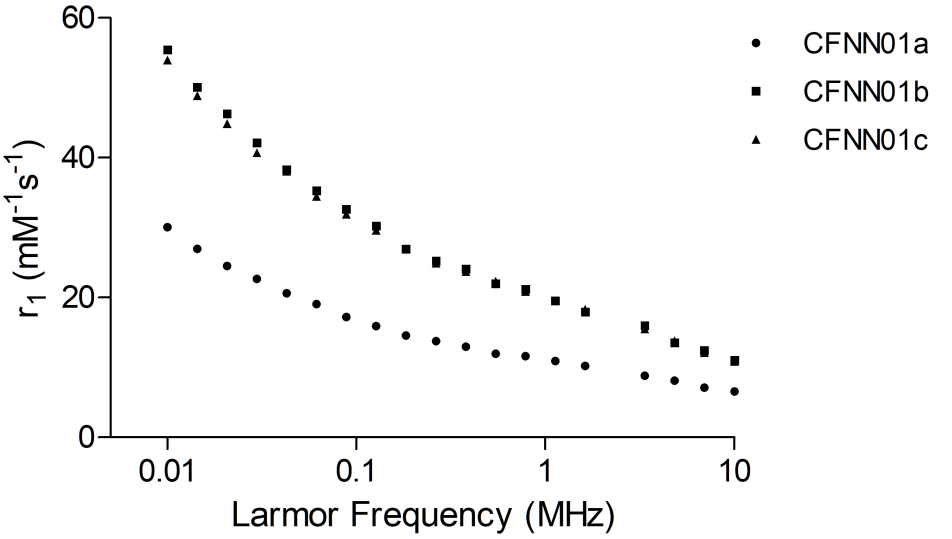

Figure 4.17: ^{1}H NMRD profiles where transverse relaxivity r_1 is plotted against frequency between 0.01 and 10 MHz for 3 replicated CFNN01 samples demonstrating the reproducibility of the trans-phase approach.

4.5 Conclusions & Future Work

4.5.1 Conclusions

1-Dimensional magnetic nanomaterials have previously exhibited unique biological and magnetic properties. The assembling of multiple magnetic particles along a single axis results in materials with strong uniaxial anisotropy and increased magnetisation, this can subsequently cause improvements in MRI contrast. Therefore, there is a genuine need for a simple and reproducible method for the preparation of these materials that still maintains the properties that make them so attractive.

For this reason, this work sought to tune a 'trans-phase' approach for the preparation of a class of 1D assemblies named 'nano-necklaces'. In this method an external magnetic field causes the migration of magnetic particles from an aqueous to an organic phase subsequently triggering a condensation reaction on the particle surfaces, resulting in silica coated linear assemblies of

magnetic nanoparticles. The key advantage to this method is that it does not require complex reagents nor expensive equipment and can be carried it in a fast and cost-effective manner. A study was carried out on how the reproducibility, magnetic, and relaxometric properties could be tuned through certain factors. A summary of these experiments is presented in Table 4.4.

First, the importance of the stabilising polymer for 'nano-necklace' formation was investigated. PSSS-stabilised CFNPs were prepared using both a high and a low quantity of PSSS, which were then compared to non-stabilised CFNPs for use as precursors for the formation of the nano-necklaces. This revealed the importance of the stabilising polymer in facilitating the trans-phase method, with the non-stabilised CFNPs unable to cross the interface between the two phases. Between the two PSSS-stabilised samples, analysis *via* TEM showed that the lower PSSS-containing sample resulted in longer nano-necklaces (2.15 ± 1.37 μm compared to 0.68 ± 0.17 μm).

Next, the quantity of base was revealed to have an important role in the formation of the silica shell. The trans-phase synthesis was carried out using 2.5 M and 0.09 M NH_4OH and then compared to samples prepared using 0.45 M. In accordance with literature the increased base concentration caused the formation of a thicker shell around the CFNPs, but also impacted the formation of the 1D assemblies likely through changes in the surface charge on the CFNP surface. Finally, the strength of the magnetic trigger was compared by using two different permanent neodymium magnets. By using a stronger magnet (pull strength of 45.0 kg vs. 16.3 kg) 'branched' chains of silica coated particles formed measuring both longer and wider (length of 4.18 ± 1.84 μM and width of 0.41 ± 0.16 μM) than the nano-necklaces formed using the weaker magnet. This was attributed to both the increased magnetisation of the CFNPs leading to increased 'lateral' attraction between the chains of particles and the more compacted magnetic field lines from the stronger magnet.[312]

Having shown how the structure of the nano-necklaces can be influenced, the magnetic and relaxometric properties were investigated. This revealed the importance of shape anisotropy for enhancing MRI contrast, with sample CFNN01 measuring the only improved r_2 when compared to its parent CFNP, with the high aspect ratio of CFNN01 likely resulting in uniaxial interactions between the magnetic cores causing the observed enhancement. To confirm this increased anisotropy of CFNN01, FFC-relaxometry was then carried out to provide greater detail on the interactions dictating the relaxometric behaviour. To date, little on the low-field behaviour of similar materials has been detailed in the literature despite a growing interest in ultra-low field MRI (ULF-MRI).[87,88] The NMRD profiles produced by the nano-necklaces

had slight difference in shape to the CFNP precursor and to even most other superparamagnetic/ferromagnetic materials. Further work is required in order to explain this behaviour, but the continued increase in r_1 with decreasing Larmor frequency appears to indicate some interactions between magnetic cores and therefore strong anisotropy.

Table 4.4: Summary of the parameters used for each cobalt ferrite nano-necklace (CFNN) preparation as well as notes on what was observed for each experiment and the length of any CFNNs produced.

Experiment Number	**CFNP Precursor**	**[NH_4OH] (M)**	**Magnetic Pull Strength (kg)**	**Observations**	**Length (μm)**
CFNN00	CFNP	0.45	16.3	CFNPs did not cross into organic layer.	N/A
CFNN01	PSSS-$CFNP_{1:1000}$	0.45	16.3	Good well-formed silica-coated CFNNs.	2.15 ± 1.37
CFNN02	PSSS-$CFNP_{1:100}$	0.45	16.3	Small silica-coated nanostructures.	0.68 ± 0.17
CFNN03	PSSS-$CFNP_{1:1000}$	2.50	16.3	Cross-linked CFNP's with thick silica shell. Excess silica by-product.	N/A
CFNN04	PSSS-$CFNP_{1:1000}$	0.09	16.3	Inconsistent silica coating. No CFNNs.	N/A
CFNN05	PSSS-$CFNP_{1:1000}$	0.45	45.0	Branched chains coated in thick shell of silica.	4.18 ± 1.84

4.5.2 Future Work

One of the main limiting factors of this approach is its ability to be scaled which depends on the size of permanent magnet available, and changes in the size and strength of the magnet can have unforeseen effects on the size and shape of the final product due to the inhomogeneous field produced by neodymium magnets. One possible solution to this is by using a Helmholtz coil which are capable of producing a uniform magnetic field, the strength of which can be tuned easily.

Also the colloidal stability of the nano-necklaces could be improved, having required suspension in 0.5 % Xanthan gum when measuring relaxation rates. This should be relatively straight-forward due to their silica coatings, with the chemistry of silica offering potential for easy surface functionalisation. Therefore, the addition of functional moieties such as polyethylene glycol (PEG) would be very achievable and improve both the colloidal stability and biocompatibility of the nano-necklaces. The silica coating offers the possibility for even further functionalisation with the addition of fluorophores and targeting ligands increasing the utility of the nano-necklaces.

Chapter 5

Layer-by-Layer Assembly of Stimuli Responsive MRI Active Polymer Microcapsules

5.1 Introduction

Whilst Chapter 4 demonstrated how polyelectrolyte stabilised MNPs can be utilised as a precursor for the formation of permanent 1D nanostructures, named 'nanonecklaces'. Though the increased anisotropy arising from the linear alignment of magnetic cores lead to improved MRI performance compared to the parent particles, this was at the cost of water access to the cores. In this chapter an alternative application for polyelectrolyte stabilised MNPs is discussed whereby magnetic cores are assembled into a more complex structure but good water access is maintained.

Discussed in Section 1.8 are hollow polymeric microcapsules (PMCs) formed by via a layer-by-layer deposition of polyelectrolytes onto a sacrificial core. Despite the straightforward preparation and mild conditions used only few examples exist where MNPs have been incorporated within these capsules. Furthermore, no work to date has investigated how changing the location of the nanoparticles within the capsule may effect these interactions or how they may be tuned in order to maximise the relaxivity of the hybrid material. In particular, what effect the location of the IONPs has upon these interactions by loading them into the hollow core or

into different layers within the capsule membrane, the latter of which is sparsely documented in literature despite the advantages of reserving the cavity for the therapeutic payload.

Another advantage of PMCs is that stimuli-responsiveness can be readily introduced through the polyelectrolytes selected to compose the capsule membrane. Interestingly, the polymer poly(sodium-4-styrenesulfonate) PSSS, used in the previous chapter to stabilised CFNPs has demonstrated pH responsiveness when combined with the positively charged polymer, poly(allylamine) hydrochloride (PAH). PMCs formed of these polymers shown to swell below pH 6.5 causing the PMCs to 'open'.[319]

The aim of the work described in this chapter was to produce pH-responsive MRI-active PMCs through the LbL deposition of PSSS-stabilised MNPs and the positively charged polymer, PAH onto a sacrificial core (calcium carbonate ($CaCO_3$) cores were selected for this purpose). In order, to tune the interparticle interactions between the MNPs in the membrane and thus the relaxometric behaviour of the results hybrids, the layer at which the MNPs was added was changed. In a further attempt to tune the interparticle interactions Sub-micron $CaCO_3$ cores are also compared to more conventionally sized particles (3 – 15 μm) as a route for the creation of smaller polymer capsules.

As well as interactions with neighbouring particles, the MRI contrast enhancement of the particle is also considerably impacted by the diffusive behaviour of surrounding water molecules, which can either increase or decrease the relaxivity of an MNP.[210] As seen with the reduction in water access to the nanonecklaces in the previous chapter. This environmental dependency can be exploited for non-invasive drug release monitoring. Such an application is particularly desirable in oncology as it would allow for reductions in side effects and increases in treatment efficacy. A number of different approaches for the MRI monitoring of drug release have been reported in literature. These typically involve MNPs encapsulated within a stimuli-responsive polymer liposome.[299,320–322] For example, Zhang *et al.* encapsulated superparamagnetic iron oxide nanoparticles and the anticancer drug, carmofur, within pH-responsive electrospun polymer fibres. When incubated at the correct pH, the measured r_2 would increase due to the release of the IONPs as the polymers swell and dissolve.[323] A linear relationship between the change in relaxivity and the cumulative release of drug was observed, demonstrating the potential of this approach for the non-invasive monitoring of drug release. However, there is yet to be work in the literature detailing how PMCs prepared using an LbL method can be applied for such an application. Therefore the final aim of this chapter was to determine the ability for IONP-PMCs to monitor the pH-triggered drug release from the capsule was investigated.

5.2 Calcium Carbonate Microparticles

5.2.1 Preparation of Vaterite Microparticles

The preparation of spherical porous $CaCO_3$ microparticles is well established in the literature.[324] The synthesis requires the rapid mixing of equal volumes of equimolar $CaCl_2$ and Na_2CO_3 solutions (summarised in Scheme 6.1). The full experimental protocol is provided in the Experimental chapter, Section 2.2.8. Doing so will result in mixtures of both the colloidal aggregation of primary particles of $CaCO_3$ into desired spherical vaterite microparticles as well as the crystallisation of $CaCO_3$ into the rhombohedral calcite phase. Changing certain experimental conditions, namely stirring time and solvent, the relative quantity of the vaterite phase can be maximised.

$$CaCl_2 + Na_2CO_3 \longrightarrow CaCO_3 + 2\,NaCl$$

Scheme 5.1: Reaction scheme for the co-precipitation preparation of calcium carbonate microparticles.

Stirring times of 15 seconds and 1 minute before filtration and washing were compared, based on examples detailed in literature (typical stirring time of 1 minute).[223,325,326] The resulting white precipitate was then characterised using IR spectroscopy and scanning electron microscopy (SEM). The size of vaterite microparticles produced by such a reaction is determined by the supersaturation level of the dissolved amorphous $CaCO_3$. The final size is typically between 3 – 15 μm, and depends on the concentration of salts, the solubility of the salts, the mixing time, and mixing speed.[327] One proven method for the formation of sub-micron vaterite particles was the addition of ethylene glycol (EG) to the reaction as described by Parakhonskiy *et al.* In doing so crystal growth was slowed due to reduced solubility and molecular diffusion.[327] In an effort to produce smaller vaterite particles, the reaction was also completed in 83 % w/w ethylene glycol. As the reaction is much slower the mixing time was varied between 15 minutes and 1 hour. The resulting precipitate was also characterised by IR and SEM.

Table 5.1: Summary of the experimental parameters for the preparation of $CaCO_3$ particles.

Sample Name	[$CaCl_2$] (M)	[Na_2CO_3] (M)	Solvent	Stirring Time (mins)	d_{core} (μm)
EG - 15 mins	0.33	0.33	83 % ethylene glycol	15	1.18 ± 0.15
EG - 1 hour	0.33	0.33	83 % ethylene glycol	60	0.91 ± 0.31
Water - 15 secs	0.33	0.33	ultrapure water	0.25	N/A
Water - 1 min	0.33	0.33	ultrapure water	1	3.27 ± 0.46

5.2.2 Characterisation of Vaterite Microparticles

The 4 $CaCO_3$ microparticle samples were first characterised with IR spectroscopy. Due to small differences in the spectra of either vaterite or calcite this can be a fast an effective method for distinguishing between the two phases. The 4 spectra that were collected are given in Figure 5.1.

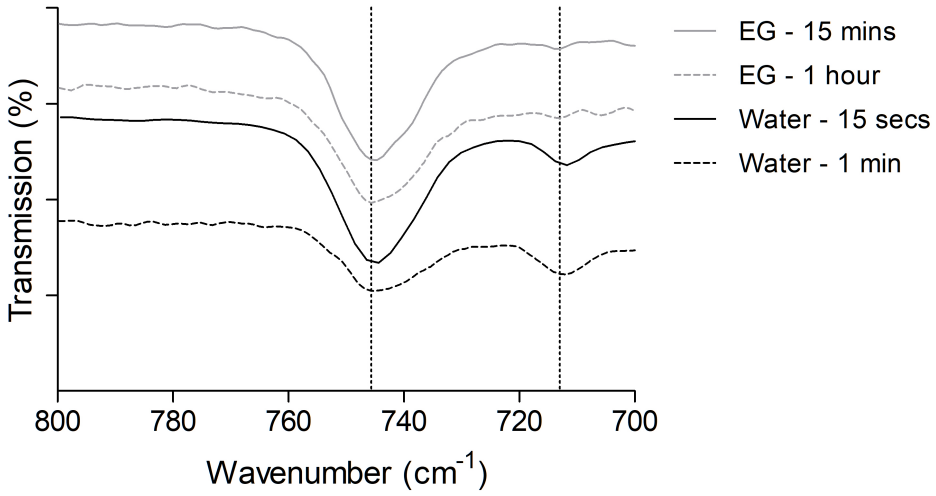

Figure 5.1: Fourier transform infrared (FTIR) spectra of $CaCO_3$ microparticles prepared in either 83 % w/w ethylene glycol (EG) or ultrapure water with different mixing times (EG: 15 minutes – 1 hour, water: 15 seconds – 1 minute). Spectra plotted between 800 and 700 cm^{-1}. Dotted lines at 745 cm^{-1} and 715 cm^{-1} are indicative of vaterite and calcite respectively.

The notable peaks for vaterite and calcite are at 745 cm^{-1} and 715 cm^{-1} respectively.[324] For this the spectra in Figure 5.1 is only given between 800 – 700 cm^{-1}. All 4 samples displayed peaks at 745 cm^{-1}, with the water samples also showing small peaks at 715 cm^{-1}. This is likely

due to the increased solubility of $CaCO_3$ in water compared to EG allowing the recrystallisation to calcite even during the very short mixing times.

The size and morphology of the vaterite particles were then analysed *via* scanning electron microscopy (SEM). The obtained images of the 4 samples are provided in Figure 5.2.

Comparing between the EG and water samples, it can be seen that the EG is indeed effective at reducing the size of the microparticles with sizes of approximately 1 micron compared to over 3 micron for the water sample (1 minute stirring). However, the morphology of the EG particles compared to the water particles differ slightly with the water sample producing spherical particles whereas the ethylene glycol resulted in elongated samples. The surfaces of the EG particles are also a different texture, in particular the EG - 15 min sample. The cause is due to differences in the growth mechanism of the particles as a result of the change in viscosity and solubility. In water the growth is spherulitic whereas in EG the growth occurs through the aggregation of nanosized amorphous precursors.[325,328] The elongation of the EG particles is then a result of the orientated attachment mechanism that has been proposed in literature.[329]

The synthesis that did not provide viable microparticles was the water with 15 seconds of stirring. In Figure 5.2, rather than well defined spherical particles a cloud of small particles is visible. This may be due to the comparatively short mixing time being insufficient for proper growth of the microparticles from the primary nanoparticles that form.

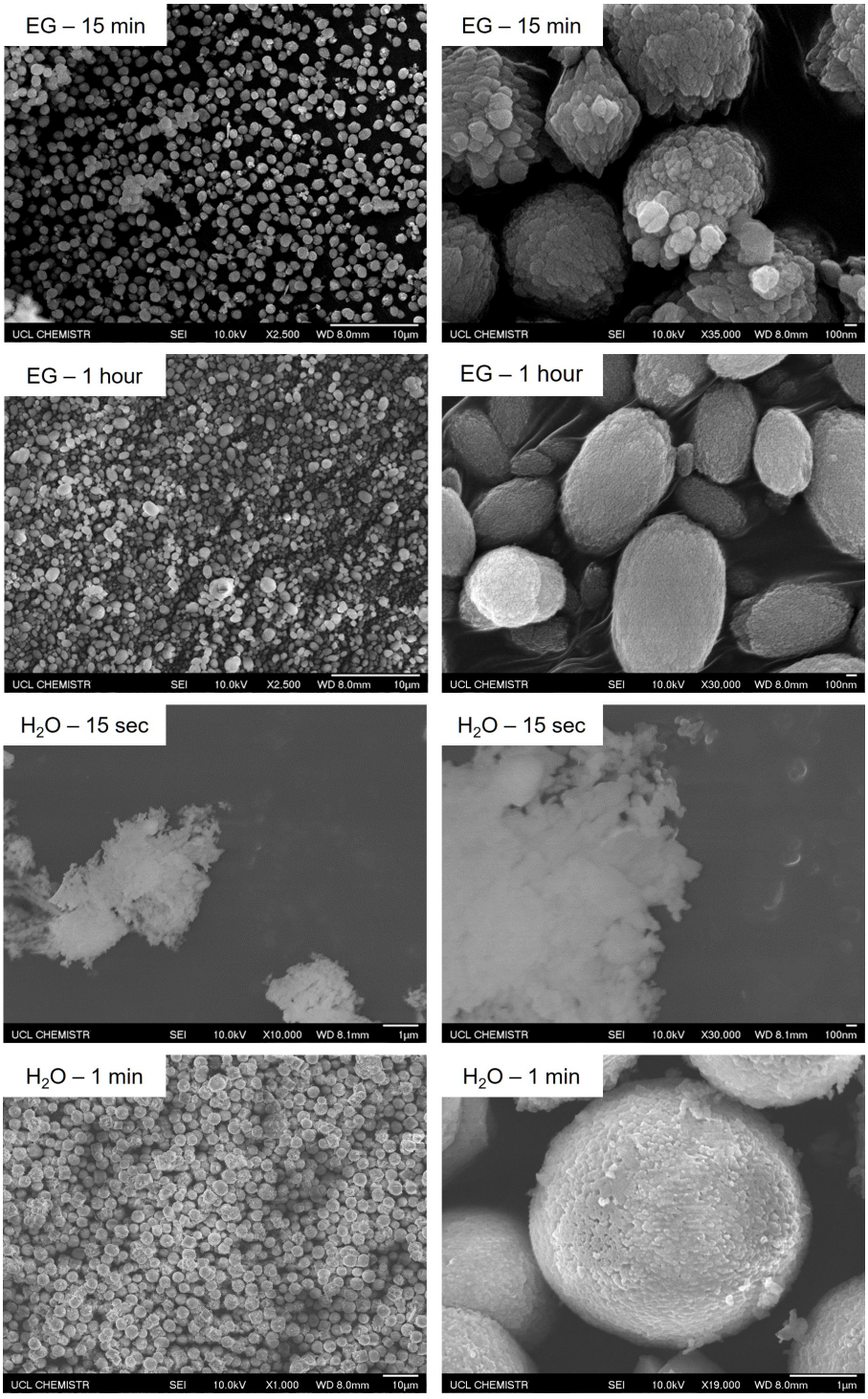

Figure 5.2: Scanning electron microscopy (SEM) images of vaterite microparticles prepared in 83 % w/w ethylene glycol (EG) or ultrapure water with different mixing times (EG: 15 minutes – 1 hour, water: 15 seconds – 1 minute). Left side are low magnification, right side are high magnification images.

5.2.3 Magnetically Doped Vaterite Microparticles

As discussed in the introduction to this chapter, $CaCO_3$ microparticles are suitable for 'pre-loading', whereby they can be formed around bioactive molecules, this is then used a means of drug loading for PMCs. However, it is also possible to trap other materials within the vaterite particles. The aim of this chapter is to produce MRI-active PMCs, through incorporating IONPs within the capsule. One possible approach is by doping the sacrificial $CaCO_3$ core with IONPs. To prepare such particles, IONPs (5 mg/ml, prepared according to protocol detailed in Experimental Section 3.2) were dispersed in equal quantities of both the $CaCl_2$ and Na_2CO_3 solutions. The reaction was then carried out with 1 minute of stirring before filtration. The black/grey precipitate was subsequently analysed by IR spectroscopy and SEM. The IR spectra for the doped particles is given in Figure 5.3.

The IR spectra exhibits characteristics of both vaterite and iron oxide. A peak can be observed at 745 cm^{-1} indicating the vaterite particles.[324] This was accompanied by the broad peak between 650 cm^{-1} and 500 cm^{-1} associated with the Fe–O stretch of iron oxide.[330] Note that the absence of a peak at 715 cm^{-1}, indicating very little recrystallisation of the calcite phase.

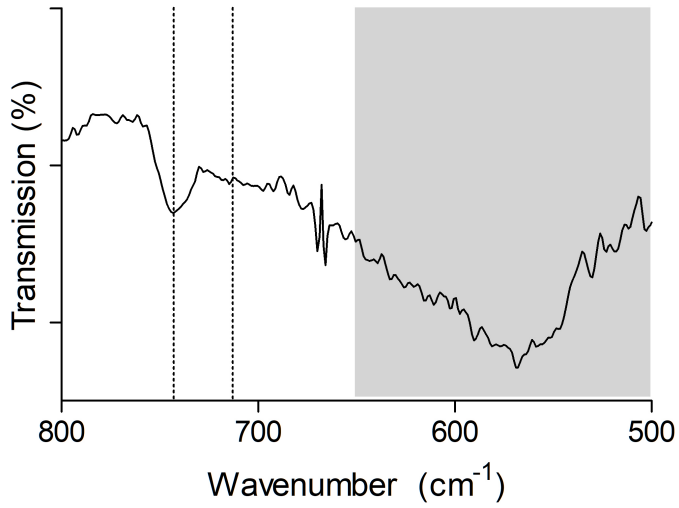

Figure 5.3: Fourier transform infrared (FTIR) spectra of $CaCO_3$ microparticles doped with iron oxide nanoparticles (IONPs). Spectra plotted between 800 and 500 cm^{-1}. Dotted lines at 745 cm^{-1} and 715 cm^{-1} are indicative of vaterite and calcite respectively. The shaded area (650 – 500 cm^{-1}) highlights the Fe–O stretch of iron oxide.

SEM in partner with energy-dispersive X-ray spectroscopy (EDS) was carried out to analyse both the size, morphology, and composition of the IONP doped vaterite particles. The images produced by SEM are given in Figure 5.4.

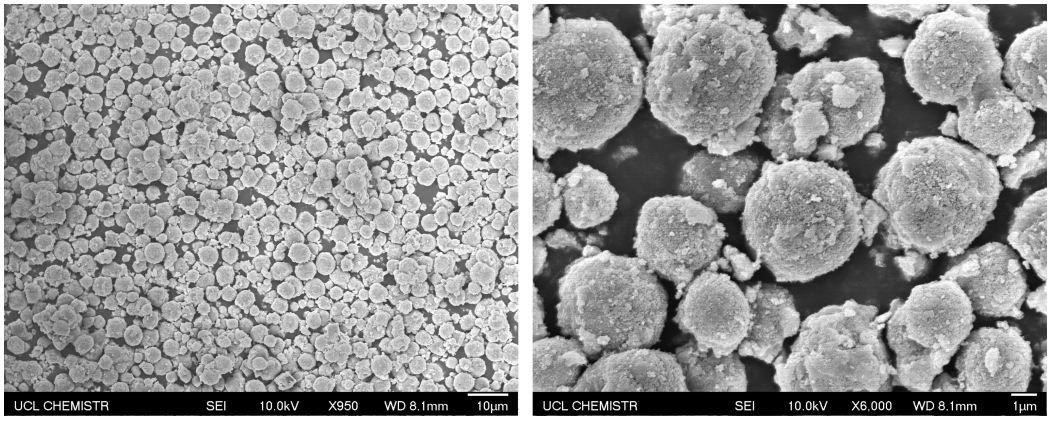

Figure 5.4: Scanning electron microscopy images of vaterite microparticles doped with iron oxide nanoparticles (IONPs) ($d_{\text{core}} = 4.01 \pm 0.95$ μm).

The spherical particles produced measured an average diameter of 4.01 ± 0.95 μm, which is similar to that observed for the non-doped particles prepared in the same manner (3.27 μm ± 0.46 μm). The surface of the particles appear to be roughened compared to the non-doped particles. This is likely the presence of clusters of IONPs on the surface of the particles. To confirm the presence of the iron oxide within the microparticles EDS analysis was carried out.

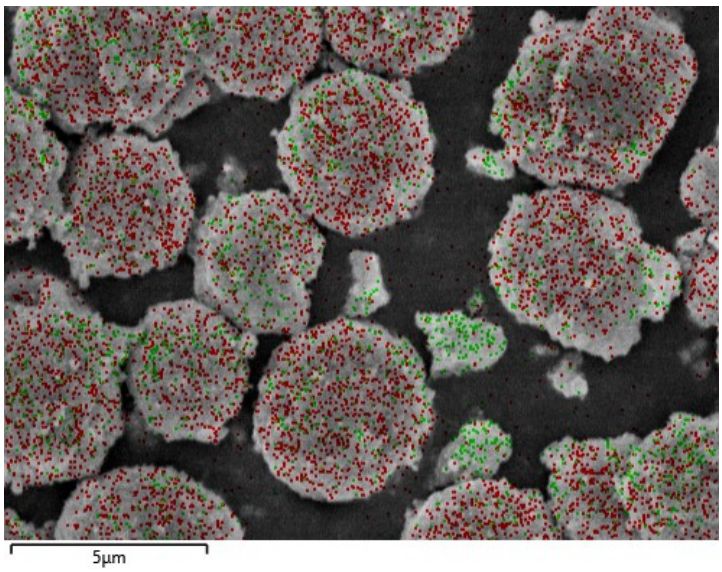

Figure 5.5: Map of calcium (red) and iron (green) measured by energy-dispersive X-ray spectroscopy (EDS) of vaterite microparticles doped with superparamagnetic iron oxide (IONPs).

In Figure 5.5 the iron within the $CaCO_3$ microparticles is visualised in green. As seen within the microparticles this confirms the successful doping the vaterite particles. Also seen by EDS are what appears to be aggregates of iron oxide particles not bound within the microparticles (presence of green colour pattern representing Fe without the presence of red representing Ca).

With the successful doping of the particles, their magnetic properties were characterised using vibrating sample magnetometry. The magnetisation was measured between 20 kOe and -20 kOe, with the resulting M vs. H curve plotted in Figure 5.6. The doped vaterite microparticles measured a M_s of 16.1 emu/g. Also plotted on the same curve is the magnetisation of the iron oxide nanoparticles used to dope the vaterite microparticles, which measured a M_s of 62.8 emu/g. The difference between the two samples is due to the normalisation with respect the total mass of sample, and therefore including the non-magnetic $CaCO_3$. Using this data however, we can estimate a mass contribution of $\sim$ 25 % IONPs within the doped vaterite microparticles.

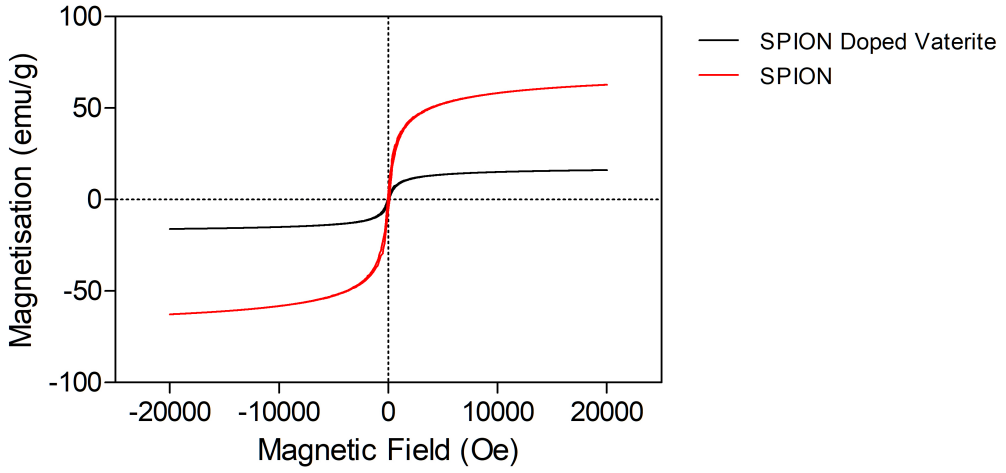

Figure 5.6: Magnetisation plotted against magnetic field for iron oxide doped vaterite microparticles. Magnetisation measured by vibrating sample magnetometry (VSM) between -20 000 Oe and 20 000 Oe.

5.3 Polymer Microcapsules

5.3.1 Preparation of Polymer Microcapsules *via* LbL Assembly

In this work polymer microcapsules were prepared using the well-established approach first devised by Sukhorukov *et al.*[211,331] A generalised scheme for the preparation is given in Figure 5.7. Briefly, the sacrificial $CaCO_3$ core is incubated with first a positively charged polyelectrolyte (PAH) followed by a washing procedure before incubating with the chosen negatively charged polyelectrolyte (PSSS) and again washing away any unbound polymer. This is then repeated until the desired number of polyelectrolyte adsorption procedures (PEAP) is achieved. The $CaCO_3$ core is finally removed by washing with 0.1 M EDTA solution (pH = 7.0) leaving behind the hollow PMC. A full description of the preparation is given in Experimental Section 5.3.1.

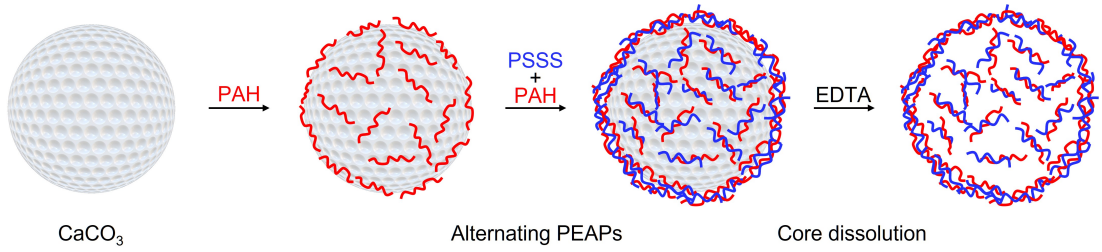

Figure 5.7: Schematic representation of the layer-by-layer (LbL) preparation of polymer microcapsules (PMCs) with a $CaCO_3$ core and poly(allylamine) hydrochloride (PAH) and poly(sodium-4-styrenesulfonate) (PSSS) as the membrane layers. Figure adapted from Sukhorukov *et al.*[331]

To produce MRI active capsules the procedure was modified so that either the core was replaced with the IONP doped vaterite microparticles, or either the first or second PSSS addition step was replaced by the incubation with PSSS-stabilised IONPs (IONPs prepared according to protocol detailed in Experimental Section 3.2). The capsules produced were characterised by measuring the ζ-potential between each PEAP to monitor change in charge (positive to negative *etc*). SEM and EDS analysis was carried out the capsules following the removal of the core.

5.3.2 Comparison of Cores for Layer-by-Layer Assembly

Prior to the incorporation of IONPs within the capsules, the different size vaterite cores were investigated for their suitability for fabricating the PMCs with only PSSS and PAH. The core produced in EG with 1 hour stirring (0.91 ± 0.31 μm) was compared to core produced in water with 1 minute stirring (3.27 ± 0.46 μm), therefore allowing a comparison between the smallest and largest cores. For each the LbL procedure was carried out in the same manner, with the progress monitored with ζ-potential (Z.P) measurements. These are shown in Figure 5.8. For both PMCs there is a change in ζ-potential after each PEAP, however as the number of steps increases the Z.P for each PAH addition (odd numbers) becomes more negative. This may be a result of stronger binding of PSSS compared to PAH causing more PAH to be removed during washing, however due the increase in Z.P after each PAH addition it can be assumed that PAH is still being bound to the core.

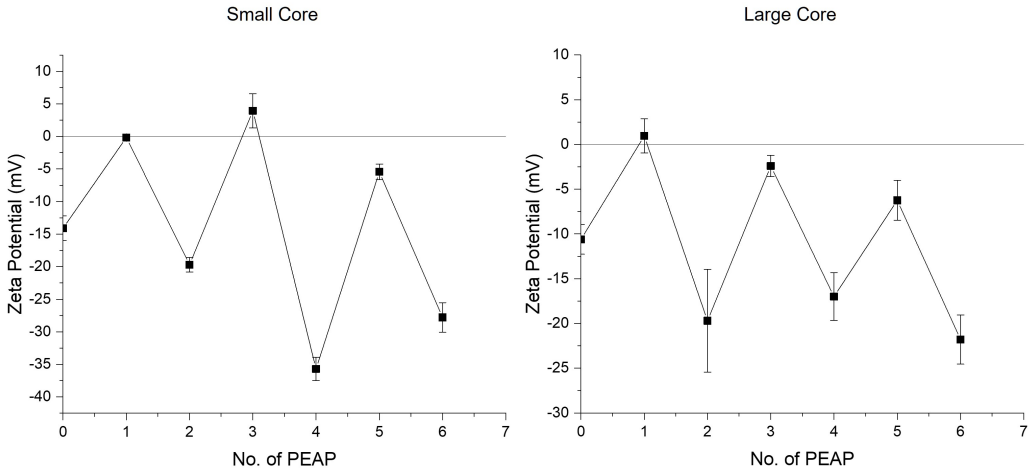

Figure 5.8: Zeta-potential plotted as a function of polyelectrolyte adsorption procedures (No. of PEAP) for polymer microcapsules deposited on both a small (left) and large (right) $CaCO_3$ core.

Given in Figure 5.9 are SEM images taken after the vaterite cores had been removed. Comparing between the two samples, there is a clear difference between PMCs produced using the large cores compared to the smaller cores. The top row depicts the 'small core' PMCs, the images show what appear to be small capsules but each capsule is poorly defined with what is likely to be excess unbound polymer joining the capsules to one another. The PMCs formed using the larger cores however appear similar to other literature examples of PMCs, with well defined spherical capsules measuring 2.44 $\pm$ 0.42 μm in diameter.[319] This diameter is smaller than the $CaCO_3$ core and is caused by the capsule contracting once the core is removed and also by the drying of the capsules when preparing for SEM analysis. This difference between the two cores can be attributed to the difference in surface area, with the larger core providing greater surface area to which the polyelectrolytes can adsorb.

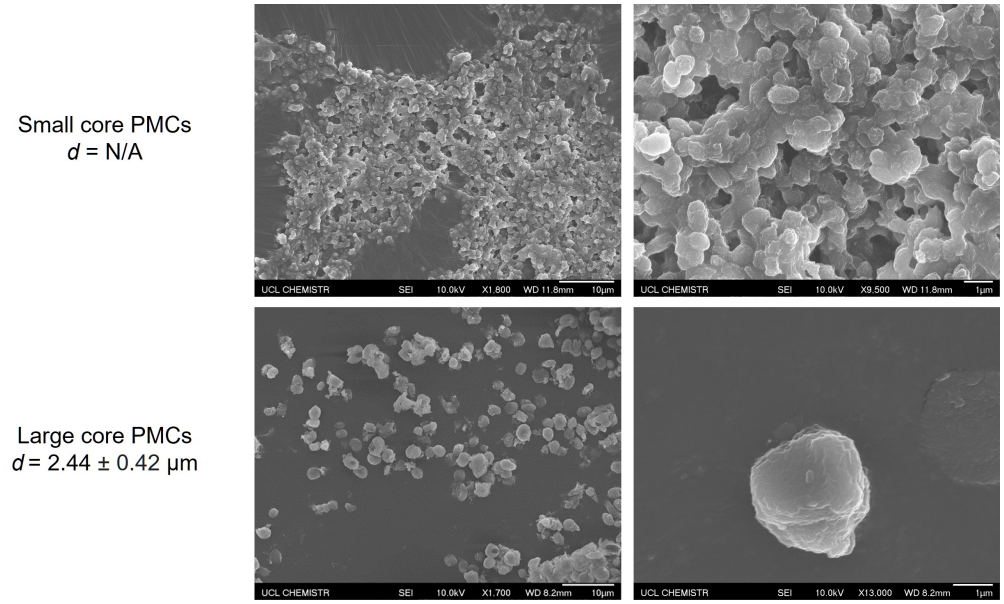

Figure 5.9: Scanning electron microscopy images (SEM) of polymer microcapsules (PMCs) fabricated using either small (top) or large (bottom) $CaCO_3$ cores.

5.3.3 Incorporation of IONPs within Polymer Microcapsules

To produce MRI-active polymer microcapsules, IONPs were incorporated *via* two different methods. The first is through the use of the IONP doped vaterite microparticles as the sacrificial core. In doing so removal of the core by washing with EDTA leaves behind IONPs within the hollow cavity of the PMC. Alternatively, one of the polyelectrolyte layers deposited onto the core during synthesis can be replaced by polyelectrolyte stabilised IONPs, in this instance PSSS-stabilised. Based on the SEM images provided in the previous section, the larger $CaCO_3$ cores were selected due to producing distinct polymer spheres. The location of the IONPs within the PMC multilayer may be adjusted through changing the step at which the IONPs are incubated with the core. Herein, PMCs were prepared by adding IONPs at the second and fourth PEAP, so that IONPs were in the inner most layer and the middle layer. All PMCs were prepared according to the protocol used for Section 5.3.1 with the discussed adjustments made. Each of the three samples (core, 2nd layer, and 4th layer) were analysed using SEM to confirm the formation of the PMC and EDS to visualise the presence of iron oxide within the capsules.

Figure 5.10 shows SEM images taken of PMCs that were produced by the alternating deposition of PAH/PSSS onto IONP-doped vaterite cores. In the images, spherical PMCs can be

observed with sizes of approx. 1 μm. EDS mapping revealed that iron was present within the capsules (green, Figure 5.11) also shown is the presence of sulfur (pink, Figure 5.11) which can be attributed to the sulfonate polymer, PSSS.

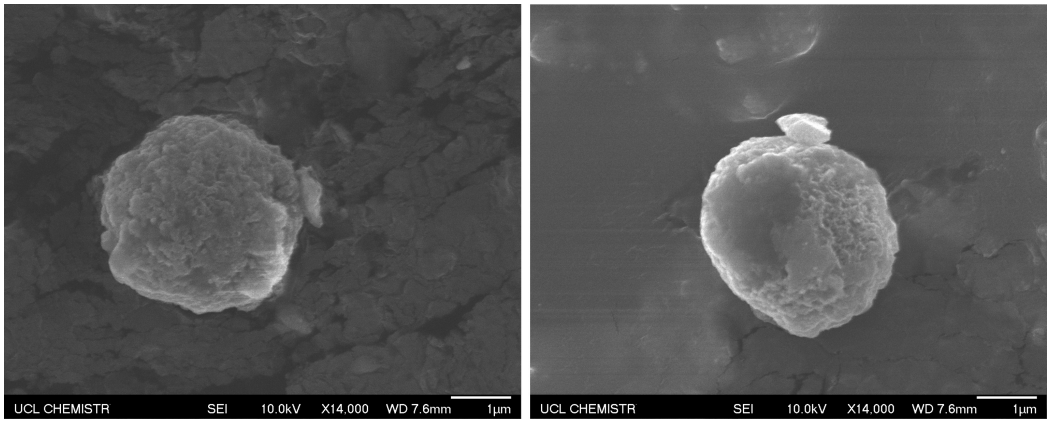

Figure 5.10: Scanning electron microscopy (SEM) images of polymer microcapsules (PMCs) fabricated using IONP-doped $CaCO_3$ cores.

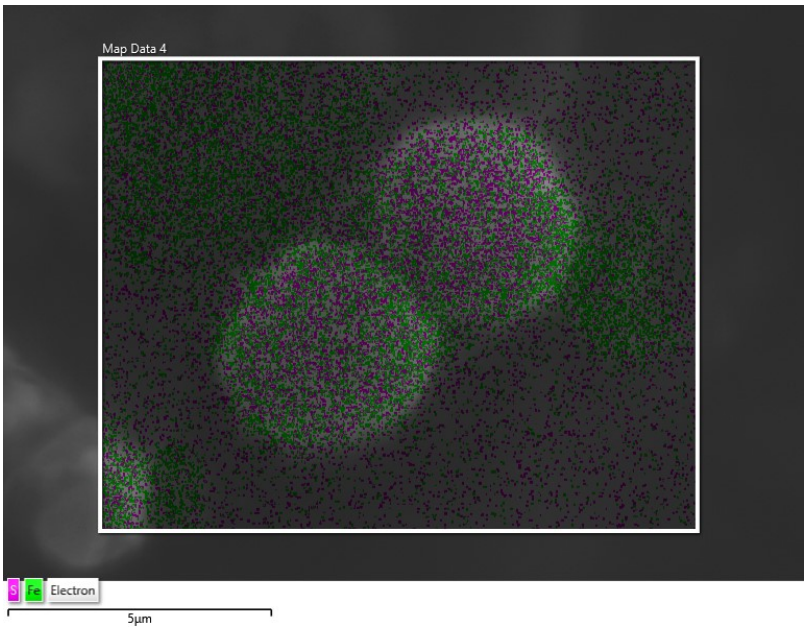

Figure 5.11: Map of iron (green) and sulfur (pink) as measured by energy-dispersive X-ray spectroscopy (EDS) of polymer microcapsules (PMCs) fabricated using IONP-doped $CaCO_3$ cores.

Whilst PMCs containing IONPs were successfully produced using a doped $CaCO_3$ core,

adding IONPs through deposition onto $CaCO_3$ core at either the second or fourth PEAP did not yield spherical capsules containing the magnetic nanoparticles. SEM analysis revealed the samples contained unstructured clusters formed of IONPs and polyelectrolyte, these can be seen in Figures 5.12 and 5.13 (addition at 2nd and 4th PEAP's respectively). The presence of iron with each samples was confirmed using ICP-OES (and EDS shown in Appendix 7.6 and 7.7).

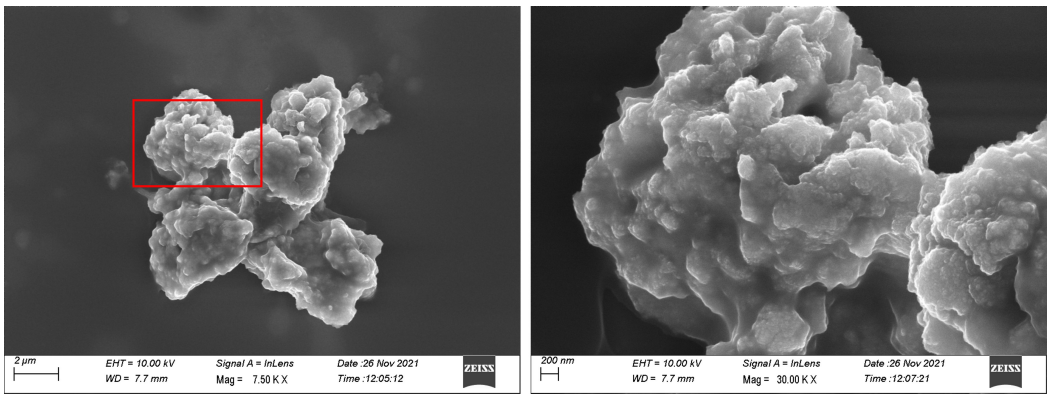

Figure 5.12: Scanning electron microscopy (SEM) images of polymer microcapsules (PMCs) with PSSS-IONPs deposited during the 2nd PEAP. Red box highlights the high magnification region shown in the right hand image. Imaging performed out by Dr Yisong Han (University of Warwick).

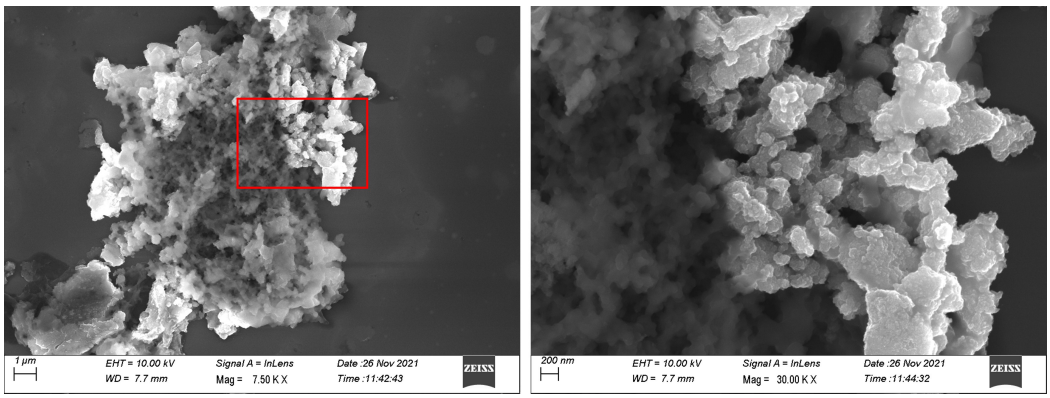

Figure 5.13: Scanning electron microscopy (SEM) images of polymer microcapsules (PMCs) with PSSS-IONPs deposited during the 4th PEAP. Red box highlights the high magnification region shown in the right hand image. Imaging performed out by Dr Yisong Han (University of Warwick).

From the images provided it is evident that the presence of the PSSS-stabilised IONPs had a dramatic effect on the layer-by-layer deposition of the two polyelectrolytes (PAH and PSSS). It

is not however apparent what caused the formation of the large nebulous clusters rather than the spherical capsules seen for previous samples, in particular as other classes of nanomaterials have been successfully incorporated within the membranes of PMCs.[223,226,332,333] One possible cause is the tendency for nanoparticles to alter the flexibility and coiling behaviour of electrostatically associated polymers.[294] The coiling behaviour of PAH (typically as a result of pH) has been shown by NMR spectroscopy to change the total quantity adsorbed onto a charged surface.[334] The stability of PMCs is also dependent on the entanglement of polymer chains which in itself is dependent on the conformation of the polymers (coils being more stable than globules).[221] Therefore the presence of the IONPs may cause the either the PAH or PSSS to adopt non-optimal conformations so that they no longer adsorb in sufficient quantities or in a manner that reduces levels of entanglement, both of which would reduced the stability of the microcapsules.

5.3.4 MRI Properties of IONP-Core PMCs

As the only successfully produced PMC, the relaxometric properties of the those containing the IONPs within the core were measured at 25 °C. The transverse and longitudinal relaxivities of this sample were calculated to be 62.6 $mM^{-1}s^{-1}$ and 6.1 $mM^{-1}s^{-1}$ respectively. This gives a high r_2/r_1 value of 10.3, showing that the magnetic PMC's are MRI active and would make for possible negative MRI contrast agents. No comparisons to non-stabilised IONPs are given as these nanoparticles aggregate very quickly when exposed to an external magnetic field, preventing good quality measurements from being taken.

To see whether it is possible to increase the relaxometry of the PMCs containing IONPs, the LbL synthesis was also carried out with a $CaCO_3$ core doped with polyvinylpyrrolidone (PVP) stabilised IONPs rather than non-stabilised. Stabilising the IONPs with PVP prevents aggregation of iron oxide cores in the capsule cavity and therefore should lead to improved relaxivity. PVP was selected for its comparatively low charge as compared to the likes of PSSS and PAH and therefore less likely to interfere with the formation of the $CaCO_3$ core and deposition of the PSSS and PAH during the LbL process. The formation of the PVP-IONP containing capsules was confirmed using SEM imaging (Figure 5.14). The r_2 and r_1 for these PMCs were calculated to be 74.0 $mM^{-1}s^{-1}$ and 9.1 $mM^{-1}s^{-1}$ respectively (r_2/r_1 = 8.1). The addition of the PVP stabiliser to the encapsulated IONPs thus resulted in an 18.2 % increase in relaxivity. This is likely due to a reduction in colloidal aggregation, which is often a cause of low r_2 values.[80,335] Whilst the transverse relaxivity has increased compared to the PMCs containing the non-stabilised IONPs, the change is marginal with repeated measurements

required to definitively conclude that this change is a direct result of the presence of the PVP-stabiliser. However, the absolute r_2 value is slightly decreased compared to the values measured for PVP-IONPs alone (r_2 = 81.1 $mM^{-1}s^{-1}$, r_1 = 5.7 $mM^{-1}s^{-1}$, r_2/r_1 = 14.1). The reason for a decreased r_2 may be due to the reduction in the water diffusion coefficient within the capsule cavity compared to the bulk water. Whilst the confinement of water molecules can have an enhancing effect, this is dependent on the ratio of the cavity diffusion coefficient to the bulk.[210] If the ratio is too small (< 0.1) there is a low probability of water molecules diffusing from the bulk to the cavity. Hence, the capsule membrane begins to act more like an exclusion layer rather than a temporary trap. The protons inside are then over-dephased meaning no enhancement in r_2 and possibly a reduction.[336,337]

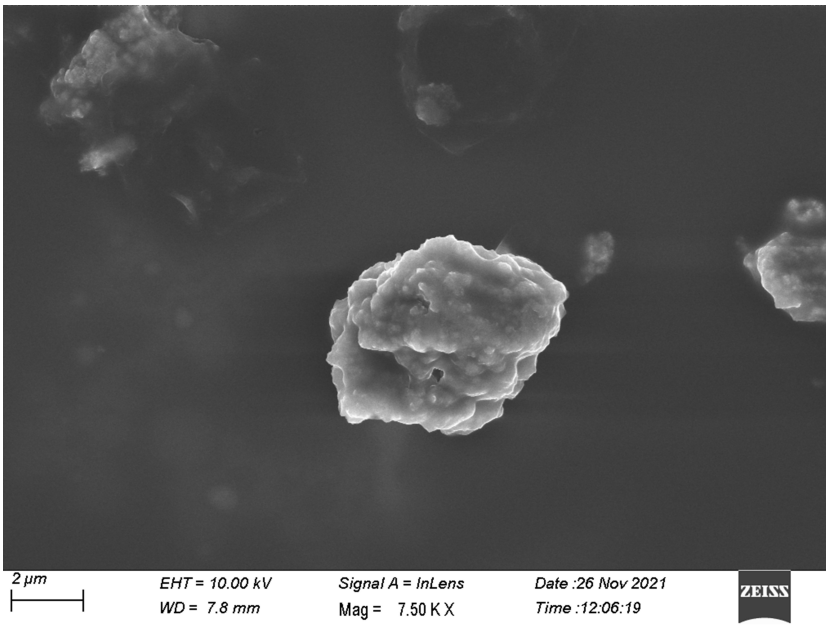

Figure 5.14: Scanning electron microscopy (SEM) image of polymer microcapsule (PMC) with core loaded with PVP-stabilised iron oxide nanoparticles (PVP-IONPs). Imaging performed out by Dr Yisong Han (University of Warwick).

5.3.5 Stimuli Response of MRI-active PMCs

As discussed in the introduction to this chapter, PMC's formed via the LbL deposition of PSSS and PAH have been demonstrated to be responsive to changes in pH.[319,338] In these works, the capsules are in their 'open' state in acidic pH's (pH 3.0) whilst being fully closed in alkali conditions (pH 10.0), this was proven using confocal microscopy which revealed the

fluorescent molecule trapped within the capsule (FITC-dextran) at was fully released at pH 3.0 but remained in the capsule cavity at pH 10.0.[338] Note that this opening and closing of the capsules is reversible and provides a method for loading the capsules with a desired cargo whilst in their 'open' state. The pH-induced swelling of the PSSS/PAH capsules are caused by changes in the electrostatic interactions between the polyelectrolytes.[217] When the environmental pH decreases, more and more of the sulfonate groups on the PSSS ($p_{ka} = 1.0$) become protonated, therefore leaving a greater number of uncompensated ammonium groups on the PAH ($p_{ka} = 10.7$).[339,340] An electrostatic repulsion between positive charges results in swelling of the whole structure. In addition, the attraction of counter-ions from the medium may increase local osmotic pressure and also contribute to the swelling effect.[341]

Whilst there have been subsequent works which also monitor the release of a fluorescent marker from PMCs formed of other polyelectrolytes, no studies to date have monitored the release of magnetic nanoparticles using MRI as a mechanism for allowing non-invasive cargo release monitoring. As the PMC swells at low pH the IONPs (and any uptaken cargo) leach from the core of the capsule into the bulk solvent. The local conditions surrounding a IONP as it travels from the core to the bulk will therefore change, with the average distance between IONPs changing as well as the diffusion coefficient of the surrounding water molecules. The transverse relaxivity (r_2) of IONPs is correlated to the diffusion coefficient and the strong interactions between the particles and will therefore change for particles depending on whether they reside in the core of the PMC or within the bulk solvent. This change in relaxivity as the PMC swells under acidic will be how the release of the particles will be monitored.

To investigate this behaviour, the relaxation rate (R_2) of the PAH/PSSS capsules containing PVP-IONPs was measured as a function of time during incubation at 3 different pH's (3.0, 7.0 and 10.0) at 25 °C. The rates were subsequently normalised with respect to concentration of Fe present in each sample (as measured by ICP-OES) and percentage change in relaxivity (Δr_2) was plotted against time (Figure 5.15).

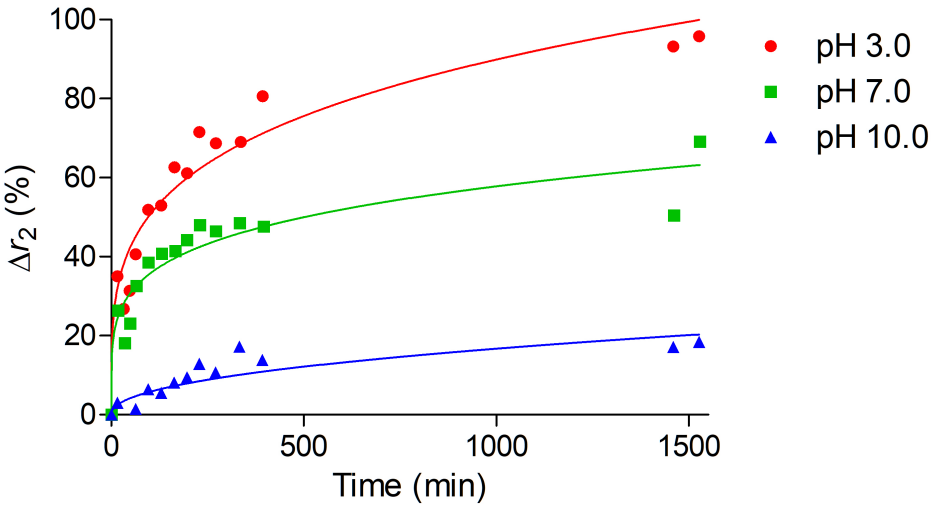

Figure 5.15: The percentage change in transverse relaxation, Δr_2, from PMCs loaded with PVP-IONPs in core as a function on incubation time in 0.25 % Xanthan Gum adjusted to pH 3.0, 7.0, and 10.0. Data fitted according to the Korsmeyer-Peppas equation.

From this profile it is evident that the more acidic the pH the greater the change in r_2 with respect to time, and therefore is indicative of pH-responsive behaviour. At pH 10 the PMCs are in the fully 'closed' state which can be evidenced by the small rise in r_2 (18 %, $\Delta r_2 = 9.4$ $mM^{-1}s^{-1}$ after 24 hours) due to low quantities of IONPs being released into the bulk solvent. As the pH is decreased to pH 7.0, a greater increase in r_2 is observed, rising by 69 % ($\Delta r_2 = 32.6$ $mM^{-1}s^{-1}$ after 24 hours). At a neutral pH the capsules are now more 'open' leading to a greater release of IONPs, when exposed to acidic conditions (pH 3.0) the capsules become fully open allowing for the release of the IONP cargo into the bulk solvent. This is then seen through a 95 % increase in r_2 ($\Delta r_2 = 44.4$ $mM^{-1}s^{-1}$ after 24 hours). To ensure that the changes observed are due to the pH-responsiveness of the PMC and not unforeseen effects on the IONPs such as degradation under acidic conditions, control experiments were carried out on PVP-IONPs dispersed in 0.25 % Xanthan gum. The relaxation rate was measured at t=0 and then again at t=1500 mins ($\sim$ 24 hours). At pH 3.0, 7.0, and 10.0 the PVP-IONPs (non-encapsulated) all measured small decreases in relaxivity of 8.4 %, 3.2 %, and 9.2 % respectively. It is likely that the decreases are a result of small amounts of aggregation over the 24 hours. This result gives clear indication of the pH-responsive nature of the PMCs as well as the ability to monitor the opening and closing of the capsules using relaxometry.

To better understand the release kinetics, the Korsmeyer-Peppas equation (Equation 5.1) was used. This equation is typically applied to release of drugs from porous hydrophilic polymers but has been adapted in an attempt to provide clarity on the release mechanism observed for the PVP-IONP loaded PMCs.

$$\frac{M_t}{M_\infty} = kt^n = \Delta r_2 \tag{5.1}$$

Where M_t/M_∞ is the fraction of drug released at time t, in this example this has been altered so that the dependent variable is instead the percentage change in measured relaxivity (Δr_2). k is the release rate constant and n is the exponent that indicates the mechanisms by which the release occurs. For a spherical sample, where n equals the value 0.43 the cargo release mechanism is described by Fickian diffusion.[342] Where $0.43 > n > 0.85$, the release is described as anomalous (non-Fickian) transport.[343] The values obtained for the release of the PVP-IONPs at the 3 different pH's are given in Table 5.2.

Table 5.2: The results of fitting the Korsmeyer-Peppas equation to PVP-IONP release from PMCs

pH	k **(min^{-1})**	n	R^2
3.0	7.35	0.25	0.94293
7.0	6.41	0.21	0.88698
10.0	0.36	0.46	0.68583

From the data produced using the Korsmeyer-Peppas model, as expected the release constant, k, decreases as the pH increases, further supporting the pH-responsiveness of the PMCs. The exponent, n, that was found by fitting the release data however was not as expected. Whilst the n value at pH 10.0 was within the range $0.43 > n > 0.85$, which would indicate a potential combination of matrix swelling and Fickian diffusion, the quality of fit ($R^2 = 0.68583$) is very low and therefore no conclusion can be drawn. Whilst the R^2 at pH 3.0 and 7.0 are improved, the n values both fall below 0.43. According to Ritger and Peppas, values below 0.43, can be caused by polydispersity within the sample with value of n being dependent on the dispersity of the sample.[343] It is also important to note that this model is designed for the release of drugs and not magnetic nanoparticles. When considering the release of the IONPs from the capsule, unlike drugs they can be can still be measured by relaxometry both inside and outside of the capsule. The measured r_2 value are therefore be comprised of two components, the contribution from IONPs within the capsules and the contribution from IONPs outside of

the capsule in the bulk solvent. As time, t, increases the relative contributions change, with a greater contribution from the IONPs outside of the capsule. It is because the environments differ inside and outside of the capsule (*i.e.* interactions with other particles and the diffusion coefficient of local water molecules) that a change in r_2 is observed over time. Whilst currently no model exists for the change in relaxivity as IONPs are released from a porous sphere, both contributions must be considered for the model to truly describe the kinetics of release.

An alternative method for determining the release mechanism is through determining a linear relationship between the % cumulative drug release and the change in r_2, as has been carried out in similar studies.[323,344] Drug loading and release were not carried out on this example (see Future Work section), thus based on similar materials in the literature, the release mechanism for the PVP-IONPs from the PSSS/PAH PMCs is likely to be a combination of matrix swelling and diffusion.[323]

5.4 Conclusions & Future Work

5.4.1 Conclusions

For the work carried out in this chapter the aim was to produce polymer microcapsules (PMCs) that would be MRI-active due to the incorporation of iron oxide nanoparticles (IONPs) *via* a layer-by-layer deposition (LbL approach). These capsules were designed to be responsive to changes in pH, utilising the polyelectrolytes PAH and PSSS, resulting in the release of any cargo contained within. This in turn would afford the ability to monitor and trace the release of any cargo contained within (e.g. therapeutic drug) using non-invasive MRI. Initial experimentation sought to optimise the co-precipitation preparation of the $CaCO_3$ core, through changing the solvent viscosity and stirring times. Those prepared using the more viscous ethylene glycol solvent were measured to be smaller (0.91 ± 0.31 μm *vs.* 3.27 ± 0.46 μm in the absence of ethylene glycol) but more elongated in comparison to those prepared using water. This was caused by differences in the growth mechanism of the particles, where in water the growth is spherulitic but in EG the growth was through the aggregation of nanosized amorphous precursors.[325,328] The utility of the small and large cores as a scaffold for the LbL preparation of PMCs was then examined, with PSSS and PAH as the negatively and positively charged polyelectrolyte layers. Using SEM analysis, PMCs produced using the smaller $CaCO_3$ cores were seen to be poorly defined compared to the well-defined spherical capsules that resulted

from the larger $CaCO_3$ cores. The difference was attributed to the difference in surface area with the larger cores providing greater surface area for the polyelectrolytes to adsorb.

To incorporate IONPs into the PMCs, $CaCO_3$ cores were doped with iron oxide nanoparticles. The presence of the particles within the core was demonstrated by elemental analysis (SEM-EDS). The IONP doped $CaCO_3$ cores were relatively large, measuring 4.01 $\pm$ 0.95 μm in diameter (within error of non-doped cores). The sequential layer-by-layer addition of the polyelectrolytes, PAH and PSSS, onto the doped core followed by the dissolution of the $CaCO_3$ resulted in PMCs with magnetic nanoparticles trapped within the hollow core, this was visualised using SEM and EDS analysis. Attempts were also made at incorporating the iron oxide nanoparticles within the PMC membrane, by adding PSSS-IONPs during different PSSS deposition PEAPs during the LbL process. However, this only resulted in the formation of unstructured clusters containing both iron oxide nanoparticles and the two polyelectrolytes. It was theorised that the cause was interactions between the polymers and the nanoparticles resulting in sub-optimal polymer conformations preventing sufficient adsorption and capsule stability.

The relaxometric properties of the IONP containing PMC were measured using single field relaxometry (24 MHz), the transverse relaxivity (r_2) was measured to be 62.6 $mM^{-1}s^{-1}$ with a high r_2/r_1 value of 10.3. This high ratio shows the PMCs to be potential negative MRI contrast agents, though the absolute r_2 was modest compared to other materials described in previous chapters and also to clinical examples such as Feridex (120 $mM^{-1}s^{-1}$). Therefore, to prevent aggregation of IONPs within the capsule cavity, the capsules were prepared as before but with PVP-stabilised IONPs rather than non-stabilised. This saw an 18.2 % increase in r_2 (74.0 $mM^{-1}s^{-1}$), likely due to the presence of the stabiliser preventing aggregation which is commonly attributed to decreased r_2 values. Finally in order to demonstrate the possible utility of these PMCs to act as non-invasive tracers to monitor the release of cargo, the response of the PVP-IONP PMCs to different pH's was investigated by incubating the capsules at pH 3, 7, and 10 and measuring how the relaxation rate changed with respect to time. When comparing the changes at the different pH's, the r_2 increased by a greater percentage at the acidic pH (95 % increase), with the smallest change being when incubated at pH 10. The pH range of sensitivity was as expected according to literature descriptions of PAH/PSSS PMCs in literature.[338] This shows the stimuli responsiveness of the PVP-IONP PMCs, with the capsules swelling in acidic conditions which in turn allows the IONP cargo to diffuse into the bulk solvent. Whilst examples in the literature have detailed MRI monitored drug release from the

likes of liposomes or polymer matrices, this is the first instance where the pH-triggered release of magnetic particles from a PMC has been monitored by relaxometry and provides a foundation for the monitoring of drug release from the capsules.[322,323,344]

5.4.2 Future Work

The work detailed within this chapter acts as a proof of concept for the potential of IONP loaded PMCs as stimuli responsive drug carriers, in future these would allow for the release of their cargo to be monitored by MRI. These early experiments provide an excellent platform for on which future experiments can be designed. The first of which are drug release studies, whereby the PVP-IONP loaded capsules are loaded with a fluorescent drug model such as doxorubicin (DOX). The drug loading and drug encapsulation efficiencies will be calculated before drug release experiments are carried out. The release of DOX into the bulk solvent will be monitored by UV/vis spectroscopy, whilst simultaneously monitoring the release of the encapsulated IONPs by measuring the transverse relaxation rate. The responsiveness of the capsule will be investigated by incubating capsules at pH 3, 7, and 10, allowing the release profiles to be compared and relationships to be derived to permit accurate assessment of the use of the MRI signal changes in mapping the drug release.

Also still to be investigated is how the relaxivity of the PMCs can be tuned depending on the location of the IONPs within the capsules, either within the core as shown here or within the membrane. Attempts at loading IONPs within the membrane were attempted in this chapter but were unsuccessful, so further optimisation of the LbL protocol is required through investigating the effects of the concentration of IONPs has on a polymer's propensity to deposit onto the scaffold. Alternatively, the the use of a stabiliser other than PSSS for the IONPs can be tested, with examples such as citric acid having been used in the literature.[223] Once successful, comparisons of the absolute relaxometric properties and the relative change in relaxation as a result of a pH-trigger will be made between the core-loaded capsules and membrane-loaded capsules. The deposition of IONPs within the PMC membrane would also allow comparisons of the difference in water diffusion between the different layers of the membrane as well as the the water pool within the cavity of the capsule.

Finally, the stimuli-responsive properties of the capsules may be tuned to more biologically relevant pH's through the use of different polyelectrolytes, as in this work the capsules were only 'closed' at a pH of 10, whereas for clinical application a pH of 7.4 would be more suitable. Examples included chitosan, polyacrylic acid (PAA), poly(N-vinylpyrrolidone) (PVP).[214,345]

Chapter 6

Utilising Design of Experiments for Synthesis of Bi-magnetic Core-shell Nanoparticles

6.1 Introduction

To this point the work detailed within this thesis has focussed on how strong dipolar interactions between assembled MNPs can result in enhancement of measured MRI contrast. The focus of this chapter however is to investigate an alternative interaction which also has the potential to boost MRI performance of negative contrast agents. Introduced in Section 1.7.3, are bi-magnetic core-shell nanoparticles. In such particles there is a strong exchange coupling interaction which subsequently results in increased r_2 values, as shown for Fe@$MnFe_{204}$ core-shell particles which measured an r_2 of 430 $s^{-1}mM^{-1}$ (measured at 0.47 T).[191] The increased relaxivity was attributed to the measured increase in M_s for the bi-magnetic samples. One noted obstacle for these materials however is the formation of magnetic 'dead' layers, which may result in reduction of M_s and r_2.

This shows the importance of the synthetic approach used when preparing bi-magnetic core-shell particles, which is typically done through a seeded growth method. This is a two step process where pre-made MNPs are used for the subsequent deposition of the magnetic shell.[182,184–186] Most commonly a thermal decomposition or solvothermal procedure is used,

which as with the preparation of MNPs affords high crystallinity and control over morphology but does require high temperatures, organic solvents, and post-processing steps for water solubility. Interestingly, high temperatures used can have a detrimental effect on the core particles such as reduced saturation magnetisation (M_s).[181] As nanosized materials are dynamic entities when in solution, the high temperatures can result in dissolution and recrystallisation by the Otswald ripening process.[187] This dissolution phenomena has been reported for ferrite cores composed of $MnFe_2O_4$ and $ZnFe_2O_4$.[181]

Considering these obstacles in reproducibility and reliability and the complex mechanisms of shell growth, this work seeks to apply a systematic design of experiments (DoE) methodology to find the optimal co-precipitation conditions. Use of DoE (also called multivariate analysis) provides an efficient means for the optimisation of this synthesis by adjusting values for specific variables systematically, reveals the complex relationships between factors that determine an outcome.[346,347] Compared to the more common approach of 'one factor at a time' (OFAT) for optimisation, DoE allows for the full experimental domain to be investigated whilst completing fewer experiments. Use of DoE has already been demonstrated an effective tool for the optimisation of MNPs. For example, Roth *et al.,* successfully applied the DoE method to create a model for the co-precipitation preparation of iron oxide nanoparticles, finding that it could subsequently be used for the tuning of M_s.[348] Similarly, Forge *et al.* used this methodology to optimise the MRI response of superparamagnetic nanoparticles.[75]

The aim of this chapter was to use a systematic approach for the optimisation of the co-precipitation preparation of bi-magnetic core-shells. Due to the array of 'hard' and 'soft' behaviours exhibited by ferrites whilst having consistent crystalline phases and similar cell parameters, they are the best candidates for growing core-shell particles. $CoFe_2O_4$ was selected as the 'hard' core due to its high magnetocrystalline anisotropy (beneficial for strong MRI contrast), whilst iron oxide (γ-Fe_2O_3/Fe_3O_4) is the chosen 'shell' due to high M_s and low cytotoxicity.[349,350] An initial study was performed before a fractional factorial experiment was carried out for the optimisation of key synthetic parameters.

6.2 Initial Experiments

6.2.1 Preparation Cobalt Ferrite Nanoparticles

As mentioned in the introduction to this chapter cobalt ferrite, $CoFe_2O_4$, was selected as the 'hard' core of the bi-magnetic core-shell nanoparticles. The CFNPs were prepared using the same co-precipitation route as used in Chapter 4. Briefly, Co^{2+} and Fe^{2+} salts were precipitated in a 1:2 molar ratio using a base catalyst before heating at 90 °C for 2 hours (full protocol given in the Experimental chapter, Section 2.2.4).[82] In this chapter however, the focus is solely on non-stabilised CFNPs with no additional surface functionalisation. The cores were characterised by dynamic light scattering (DLS), X-ray diffraction (XRD), and transmission electron microscopy (TEM).

6.2.2 Preparation & Characterisation of Bi-magnetic Core-shells

To produce the core-shell particles the $Fe^{2+/3+}$ salts (0.012 mmol per mg of CFNP) were dissolved in an aqueous suspension of the non-stabilised CFNPs (2.5 mg/ml) and after 10 minutes of stirring the base catalyst was added. The black precipitate was washed *via* magnetic separation and centrifugation before drying. The product was characterised using DLS, XRD and TEM. The reaction is summarised in Figure 6.1.

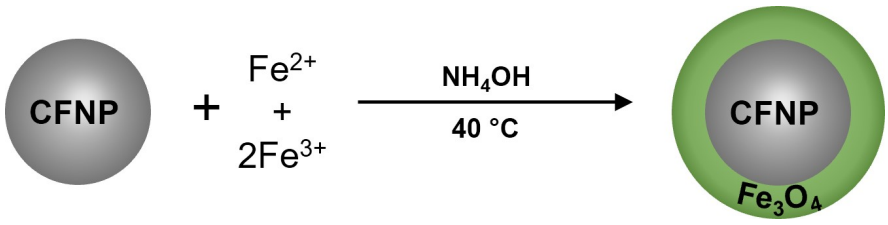

Figure 6.1: Schematic representation of the formation of bi-magnetic core-shell nanoparticles by coating of $CoFe_2O_4$ nanoparticles (CFNPs) with Fe_3O_4 *via* a co-precipitation method.

The product was first characterised using DLS to compare the hydrodynamic diameters against the CFNPs before coating with iron oxide. They are compared in Table 6.1. The formation of a shell around a magnetic core has been shown to increase the d_{hyd}.[188,189] However, this is not observed for the samples herein. After the co-precipitation of iron oxide in the presence of the CFNPs, the hydrodynamic diameter decreases from 283.1 ± 11.3 nm to 211.0 ± 3.4 nm. A comparison between the dispersity of the samples, shows an increase in the PDI from

0.324 ± 0.016 to 0.374 ± 0.016. The two results suggest that rather than core-shell particles forming, a second population of smaller iron oxide nanoparticles has formed causing the average hydrodynamic diameter to decrease whilst increasing the polydispersity.

Table 6.1: Comparison of the colloidal properties, the average crystallite size, and average core size of $CoFe_2O_4$ nanoparticles before and after iron oxide shell formation.

Sample Name	$d_{\mathbf{hyd}}$ **(nm)**[a]	**PDI**[a]	$d_{\mathbf{core}}$ **(nm)**[b]
CFNP	283.1 ± 11.3	0.324 ± 0.016	44.4 ± 22.8
Core-shell	211.0 ± 3.4	0.374 ± 0.016	20.1 ± 13.0

[a]Hydrodynamic diameter d_{hyd} and polydispersity index (PDI) measured by dynamic light scattering (DLS); [b] Average core diameter (d_{core}) as measured by transmission electron microscopy (TEM) ($n > 100$).

Transmission electron microscopy (TEM) was then used to identify potential core-shell particles and to measure changes in core size. Images are given in Figure 6.2. Presented in the top row are the parent cobalt ferrite nanoparticles (CFNPs), the images show quasi-spherical particles with a mean diameter (d_{core}) of 44.4 ± 22.8 nm. Images of the CFNPs after the attempted shell formation are then given in the bottom row of the figure. What was instantly recognisable upon analysis of the images was the presence of a large quantity of small (7 – 15 nm) particles. These particles can be assumed to be iron oxide as the size matches that of IONPs prepared *via* co-precipitation in literature as well as those prepared in Chapter 3.[71,98,351] The large quantities of IONPs made it difficult to distinguish possible core-shell particles, a few examples of iron oxide particles deposited onto the surface of the CFNP were observed (circled in red, Figure 6.2) though this may have been merely aggregation whilst preparing the TEM grid. As with the DLS, the average core sizes measured by TEM (d_{core}) decreased with respect to the parent CFNPs (parent = 44.4 ± 22.8 nm and core-shell = 20.1 ± 13.0 nm). This decrease in d_{core} is caused by the population of small iron oxide particles biasing the average diameter. Due to this second population being overwhelmingly dominant in comparison to the larger CFNPs, the deviation from the mean is lower for the core-shells than the CFNPs. This is portrayed within the histograms presented in Figure 6.2, where the peak is narrower but tail is longer. The TEM analysis confirmed that the observations by DLS were indeed a result of the formation of a second population of smaller particles. The cause for this second population of iron oxide nanoparticles, which from TEM imaging appeared to be greater in number than the parent CFNPs, is likely a result of an excess of Fe salts used in the core-shell preparation. Therefore, if bi-magnetic core-shells are to be successfully prepared further optimisation of the

protocol is required.

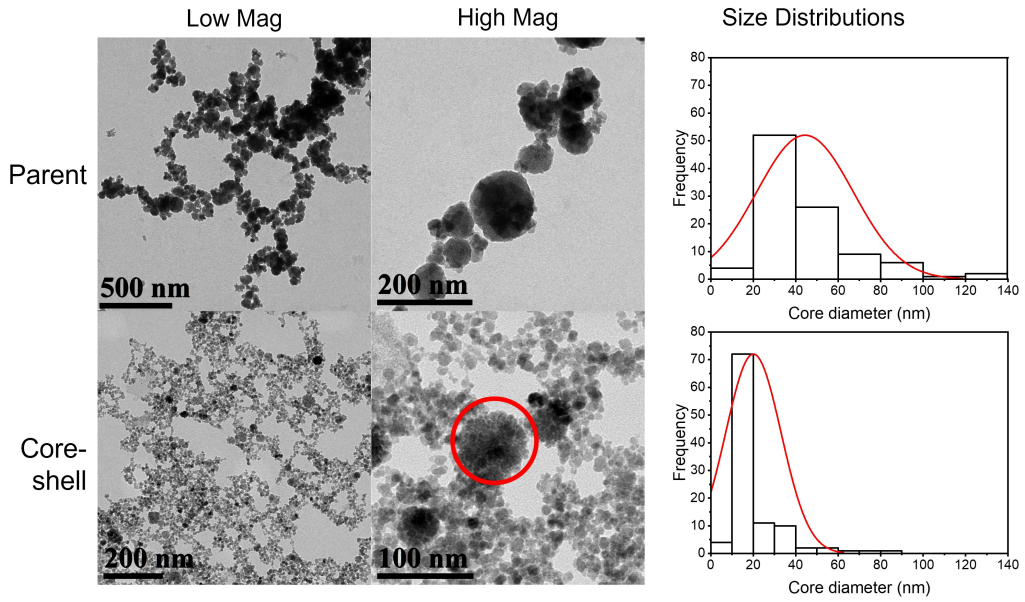

Figure 6.2: Transmission electron microscopy (TEM) images showing cobalt ferrite nanoparticles (CFNPs) before (top row) and after (bottom row) iron oxide shell formation. Images show the formation of a second population of iron oxide nanoparticles (IONPs). Red circle highlights a lone CFNP surrounded by IONPs. Also given are the size distributions as histograms (red line is the Gaussian distribution fitted to core size data).

To confirm that the particles imaged by TEM were ferrites (either maghemite/magnetite or cobalt ferrite), X-ray diffraction (XRD) analysis was performed on both the parent and core-shell sample. The produced pattern is given in Figure 6.3, with peaks observed at 13.7 °, 16.1 °, 16.8 °, 19.5 °, 25.4 °, and 27.7 ° which represent the (220), (311), (222), (400), (422), (511), and (440) planes of the cubic inverse spinel crystal structure. Due to both materials present adopting the same crystal structure with very similar lattice parameters ($CoFe_2O_4$ $a = 8.3919$ Å, γ-Fe_2O_3 $a = 8.3464$ Å, and $Fe_3O_4 = 8.3952$ Å) it is not possible to distinguish between the 3 ferrites.[290,352]

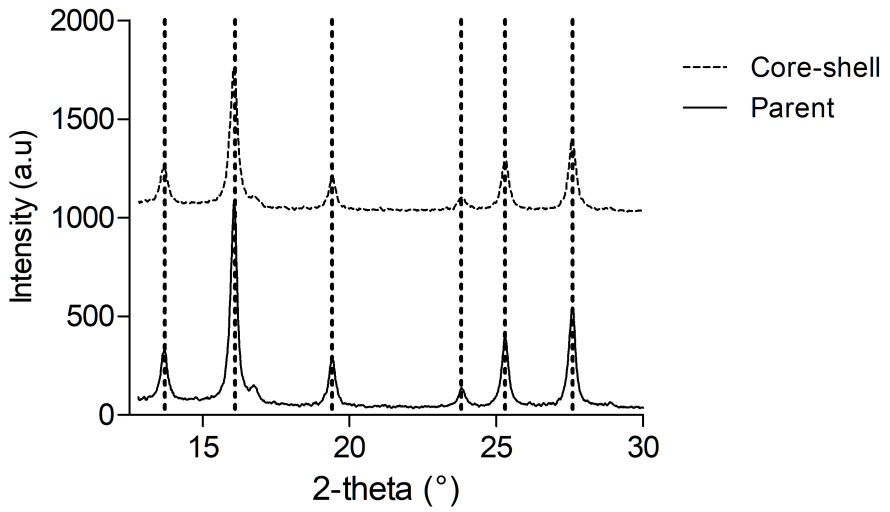

Figure 6.3: X-ray Diffraction patterns of CFNPs before (parent, solid line) and after (core-shell, dashed line) plotted between $2\theta = 12.5°$ and 30.0°. Pattern shows very small differences after iron oxide shell formation. Dashed lines at 13.7 °, 16.1 °, 16.8 °, 19.5 °, 25.4 °, and 27.7 ° represent the (220), (311), (222), (400), (422), (511), and (440) planes respectively.

6.3 Design of Experiments Approach

As discussed in the introduction to this chapter multivariate analysis or design of experiments (DoE) is an efficient method for devising experiments that include a large number of variables. As seen in the work detailed to this point, the ratio of reagents is an important variable for the co-precipitation preparation of bi-magnetic core-shell nanoparticles. However, what is unclear are what other experimental factors may be significant for this preparation. Therefore, in this section a screening experiment built using the principles of DoE was carried out to identify other key variables, as well as possible interactions between factors.

Using JMP software, a 2^4 fractional factorial experiment was designed.[272] A 2^4 full factorial is would be 4 factors at 2 levels (minimum and maximum) and therefore would require 16 treatments, and would be able to model the main linear effects and 2-, 3- and 4-way interactions. However, for a screening experiment, only the linear effects and 2-way interactions are necessary. Therefore, a fractional factorial experiment was completed so that 2^{4-1} experimental runs are required. Two mid-points were included in the experimental design as they can be used to

test adequacy of model (identify presence of curvature in model). Based on the findings from the preliminary experiments, two of the factors investigated were the quantity of CFNPs (mg) and the quantity of Fe salts (mmol). The other two factors, reaction time and method of iron salt solution addition, were selected based on other works detailed in literature, in particular, the co-precipitation preparation of $Zn_{0.5}Mn_{0.5}Fe_2O_4$@Fe_3O_4 core-shell particles performed by Cardona *et al.*[188] For each factor an upper and lower boundary must be set, the range must be sufficient that the optimum level falls within the experimental domain. Therefore, 0.3 mmol and 3.0 mmol were set as the boundaries for total Fe salt quantity, whilst 40 mg and 200 mg where set as the boundaries for quantity of CFNPs. The combination of these upper and lower limits gives mg of CFNPs to mmol of Fe salts ratios between 13 : 1 and 666 : 1, which should allow for a large enough domain to find the optimum (Cardona *et al* used a 33 : 1 ratio for the co-precipitation preparation of the $Zn_{0.5}Mn_{0.5}Fe_2O_4$@Fe_3O_4 core-shells). The time boundaries selected were 30 to 120 minutes based on co-precipitation of ferrites detailed in literature.[348,353,354]

As for the addition of Fe salts, this is a categorical not continuous factor, that is the salts were added either instantaneously or drop-wise with no in-between. By adding the Fe salt solution drop-wise, this may prevent the concentration from reaching the critical point where LaMer burst nucleation would take place, forming a second population of iron oxide nanoparticles rather than a iron oxide shell on the surface of the CFNPs.[355]

With the boundaries set for the 4 varied factors, the other possible variables the temperature (40 °C), total volume (33 ml), and the quantity and choice of base catalyst (6 ml of 8.8 M NH4OH) were fixed. For these DoE experiments non-stabilised CFNPs were used as a non-stabilised core had been used in other literature examples.[180] Using this information the JMP software produced the 10 total experimental runs (including 2 mid-points) for these screening experiments. The details of all 10 are given in Table 6.2.

Table 6.2: Breakdown of each of the experimental factors for the 10 runs as determined by 2^4 fractional factorial experimental design

Sample Code	Pattern[a]	CFNP (mg)[b]	Fe (mmol)[c]	Time (min)[d]	Addition Sequence[e]
DoE01	+ + + +	200	3.00	120	Slow
DoE02	- - - +	40	0.30	30	Slow
DoE03	+ - - +	200	0.30	30	Slow
DoE04	+ + - -	200	3.00	30	Fast
DoE05	- - - -	40	0.30	30	Fast
DoE06	0 0 0 -	120	1.65	75	Fast
DoE07	+ - + -	200	0.30	120	Fast
DoE08	- + + -	40	3.00	120	Fast
DoE09	- - + +	40	0.30	120	Slow
DoE10	0 0 0 +	120	1.65	75	Slow

[a] + and - equal the upper and lower boundaries. 0 represents the mid-point with the pattern matching the factor order: CFNP mass, total Fe mmol, reaction time and addition sequence. [b] The mass of non-stabilised CFNPs; [c] The total molar quantity of Fe salts added; [d] Total stirring time at 40 °C; [e] Fast is the instantaneous addition of Fe salts and slow is the drop-wise addition at a rate of 0.15 mL min^{-1}.

A DoE approach requires measurable responses to identify the effects of and interactions between the different experimental factors. These can be either quantitative or qualitative and can be either a single response or several. Initially, the aim was for the responses to be whether core-shells were formed (a qualitative yes or no), a measured percentage core-shells to non-core shells, and shell thickness. Saturation magnetisation and transverse relaxivity would also be measured. However, due to unforeseen circumstances TEM analysis wasn't a viable means of characterisation. As an alternative a combination of analytical techniques were investigated as potential methods of identifying the presence of core-shell particles. The techniques chosen were dynamic light scattering (DLS), X-ray fluorescence (XRF), X-ray diffraction (XRD), and vibrating sample magnetometry (VSM).

6.3.1 Dynamic Light Scattering

Dynamic light scattering has been used a means of characterising bi-magnetic core-shell particles, with examples demonstrating an increase in d_{hyd}.[188,189] Therefore, in order to identify the possible formation of core-shell structures, dynamic light scattering was used for the characterisation of the 10 DoE samples. The results are given in Table 6.3, with the parent CFNP d_{hyd}

and PDI also included for comparison. It is predicted that if core-shells structures had formed the measured d_{hyd} of the DoE samples would increase relative to the parent CFNP. However, if a second population of iron oxide nanoparticles had formed as seen for the initial coating attempt the average diameter would decrease with an accompanying increase in the PDI as had been observed for the initial attempted synthesis.

Table 6.3: The colloidal properties of the 10 DoE core-shell samples as measured by dynamic light scattering compared to parent cobalt ferrite nanoparticles.

Sample Name	$d_{\mathbf{hyd}}$ **(nm)**[a]	**PDI**[a]	**Stabilised** $d_{\mathbf{hyd}}$ **(nm)**[b]	**Stabilised PDI**[b]
CFNP	394.1 ± 15.6	0.388 ± 0.023	279.5 ± 7.0	0.376 ± 0.023
DoE01	490.9 ± 54.6	0.502 ± 0.097	233.7 ± 0.5	0.304 ± 0.033
DoE02	442.9 ± 20.1	0.509 ± 0.052	232.8 ± 4.2	0.414 ± 0.027
DoE03	953.1 ± 152.0	0.321 ± 0.367	282.3 ± 7.7	0.445 ± 0.030
DoE04	5452.3 ± 7945.5	1.000	262.9 ± 6.6	0.405 ± 0.048
DoE05	711.8 ± 68.5	0.392 ± 0.011	236.8 ± 2.9	0.455 ± 0.023
DoE06	758.1 ± 49.7	0.388 ± 0.024	237.6 ± 1.8	0.386 ± 0.029
DoE07	1111.1 ± 86.6	0.432 ± 0.028	231.6 ± 1.2	0.464 ± 0.026
DoE08	623.2 ± 17.1	0.521 ± 0.012	221.8 ± 0.9	0.321 ± 0.015
DoE09	625.8 ± 43.4	0.456 ± 0.033	245.3 ± 3.2	0.346 ± 0.09
DoE10	413.7 ± 16.7	0.393 ± 0.024	186.8 ± 1.2	0.360 ± 0.012

[a]Colloidal properties of the 10 non-stabilised DoE core-shell samples measured by dynamic light scattering (DLS) ; [b]Colloidal properties of 10 DoE core-shell samples after stabilisation with citric acid, measured by DLS.

Initial analysis was carried out on the particles with no post-processing, however as the surfaces of the core-shell samples had not been functionalised with a stabiliser the DLS data collected was unreliable. This is due to the low colloidal stability of the particles, and the rapid formation of large aggregates, as evidenced by trending observed in the d_{hyd} measured by DLS and the presence of peaks at > 1000 nm. The trending was particularly apparent for samples DoE01, DoE02, and DoE09, where the mean value decreased by 10 - 15 % between each measurement, likely a result of aggregates in sample sedimenting. (See Appendix 7.3, 7.4, and 7.5 for DLS curves). To remedy this, a post-stabilisation process was carried out on samples using citric acid. The functionalisation with the small negatively charged stabiliser should improve the colloidal stability of the samples and allow for improved data collection of the formed composites. The d_{hyd} and PDI of these samples are denoted by the 'stabilised'

columns in Table 6.3. After citrate stabilisation the d_{hyd} for the 10 samples were measured to be between 186.8 and 282.3 nm and PDI's measured between 0.304 and 0.464. Comparing the hydrodynamic diameters against the parent CFNPs (with citrate stabilisation) all samples but DoE03 measured a decrease in d_{hyd} ($<$ 279.5 nm). The samples also did not suffer from the same trending in mean diameter as observed for the non-stabilised samples. For DoE03 the diameter was within error of the parent CFNP sample. For the measured PDI values, samples DoE02 – 05 and DoE07 measured an increase in PDI, samples DoE01 and DoE08 measured a decrease, with the remaining 3 samples (DoE06, DoE09, and DoE10) measuring PDI's within error of the parent CFNP (0.376 ± 0.023).

A decrease in d_{hyd} and increase in PDI is strong evidence for the formation of a second population of iron oxide particles, as observed in the initial experiment. Both are observed for samples DoE02, DoE04, DoE05, DoE06, and DoE07. No sample measured an increase in d_{hyd}, which according to literature can be seen upon the formation of bi-magnetic core-shells. This data alone however is insufficient in confirming or refuting the formation of core-shells.[188,189] This is due to the limitations of the technique itself; DLS calculates the diameter according to the Stokes-Einstein equation, which does not account for the likes of concentration which may also offer an explanation for any observations presented.

6.3.2 Elemental Analysis

Typically elemental analysis of bi-magnetic core-shells would be carried out using energy-dispersive X-ray spectroscopy (EDS), which in combination with TEM can provide insight into the composition of individual core-shell particles. Without this option, X-ray fluorescence (XRF) was investigated as a possible alternative. Whilst not offering the same detail in composition as EDS, XRF provides information for the entire samples, rather than the 'snapshot' given by EDS. Therefore it provides a more statistically significant representation of the relative cobalt and iron quantities in each of the samples. Using this data, it is possible to calculate an estimated quantity of iron present from $CoFe_2O_4$, %Fe(CF), with the remaining assumed to be from either an iron oxide shell or second population of iron oxide nanoparticles, %Fe(IO). The calculation of % Fe attributed to iron oxide particles/shell is summarised below.

$$\begin{aligned} \%\mathrm{Fe(CF)} &= \frac{\%\mathrm{Co} \times 2}{\%\mathrm{Fe(Total)}} \times 100 \\ \%\mathrm{Fe(IO)} &= 100 - \%\mathrm{Fe(CF)} \end{aligned} \tag{6.1}$$

%Fe(Total) and %Co are the atom percentages as measured by XRF for iron and cobalt respectively. All Fe present in the sample is from contained within the cobalt ferrite core or iron oxide shell, the relative proportion of Fe that is contained within the cores can therefore be calculated (%Fe(CF)) as a percentage of the total Fe (%Fe(Total)), assuming CF stoichiometry of $CoFe_2O_4$ for every 1 Co atom there will be 2 Fe atoms within the core. All remaining iron present therefore must be a result of the newly formed iron oxide within the sample. The %Fe(IO) can be calculated by subtracting %Fe(CF) from 100. The results are summarised in Table 6.4. Also included are the calculated values from the initial experiment, from TEM analysis it was deemed that the quantity of Fe present in this sample was too high due to the presence of excess small iron oxide particles. Therefore, the calculated %Fe(IONP) from this sample can be set as the upper limit, above which the formation of a second population of iron oxide nanoparticles can be assumed.

Table 6.4: The calculated percentage contribution of elemental Fe in DoE samples due to cobalt ferrite nanoparticles and iron oxide shell/nanoparticles using XRF.

Sample Code	**% Fe(Total)**[a]	**% Co** [a]	**%Fe(CF)**[b]	**%Fe(IO)**[c]
Initial EXP	83.8	15.8	37.9	62.1
DoE01	84.3	10.6	25.2	74.8
DoE02	85.6	13.3	31.1	68.9
DoE03	81.6	17.7	43.4	56.6
DoE04	89.2	10.2	22.9	77.1
DoE05	79.6	19.7	49.5	50.5
DoE06	89.0	10.3	23.2	76.8
DoE07	81.4	17.9	44.1	55.9
DoE08	99.5	0.0	0.0	100.0
DoE09	86.0	12.7	29.5	70.5
DoE10	89.0	10.4	23.3	76.7

[a]Atom percentages of iron and cobalt as measured by X-ray fluorescence (XRF); [b]Calculated quantity of iron within a sample attributed to cobalt ferrite nanoparticles (CFNPs) relative to total iron measured (calculated according to Equation 6.1); [c] Calculated quantity of iron within a sample attributed to iron oxide (IO) relative to total iron measured (calculated according to Equation 6.1).

Comparing the calculated values we see that samples DoE03, DoE05, and DoE07 are the

only samples that fall below the upper limit of 61.9 % (56.6 %, 50.5 %, and 55.9 % respectively). Both samples DoE03 and DoE07 were produced using the maximum CFNP quantity (200 mg) and minimum Fe salt quantity (0.3 mmol), so a reduced relative quantity of iron oxide to cobalt ferrite would be expected. Experiment DoE05, however used the minimum of both CFNPs and Fe salts (40 mg and 0.3 mmol) and was calculated to have the lowest %Fe(IONP). All other DoE samples were calculated to have an %Fe(IONP) greater than the 61.9 % limit, implying the production of a significant quantity of iron oxide separate to the cobalt ferrite particles and hence presumed to be excess iron oxide particles existing as a second population, rather than a core-shell particle. This result was unexpected as all DoE experiments were carried out with a greater CFNP to Fe salt ratio compared to the initial experiment detailed in Section 6.2.2 (8.3 mg CFNP per 1 mmol of Fe for initial experiment compared to 13.3 to 666 mg per 1 mmol). Among these samples, DoE08 stands out having measured 0 % cobalt by XRF. Whilst this experimental run did use the minimum CFNP mass (40 mg) and maximum Fe quantity (3.0 mmol) it should be expected that a percentage of cobalt should be measured within the sample.

Therefore to test the validity of these results, mixtures of independently prepared CFNPs and IONPs were prepared at 75:25, 50:50, and 25:75 (CFNP:IONP) ratios and the % Fe and % Co were measured by XRF. The data is given in Table 6.5.

Table 6.5: The calculated percentage contribution of elemental Fe in pre-made mixtures of cobalt ferrite nanoparticles and iron oxide nanoparticles.

CFNP:IONP[a]	**%Fe(Total)**[b]	**%Co**[b]	**%Fe(CF)**[c]	**%Fe(IO)**[d]
0:100	99.3	0	0	100
25:75	99.4	0	0	100
50:50	89.0	10.4	23.4	76.6
75:25	84.3	15.1	35.8	64.2
100:0	76.7	19.7	51.2	48.8

[a]Relative quantities of cobalt ferrite nanoparticles (CFNP) to iron oxide particles (IONP) given as a ratio [b]Atom percentages of iron and cobalt as measured by X-ray fluorescence (XRF); [c]Calculated quantity of iron within a sample attributed to cobalt ferrite nanoparticles (CFNPs) relative to total iron measured (calculated according to Equation 6.1); [d] Calculated quantity of iron within a sample attributed to iron oxide (IO) relative to total iron measured (calculated according to Equation 6.1).

These results show a clear trend in under-valuing the quantity of Co within a sample, so much so that a sample entirely of CFNPs is calculated to be almost 50 % iron oxide. Upon closer inspection of the XRF spectra, over-estimation of Fe within a sample is due to the overlap of

the Co K_α peak (6.926 KeV) with the Fe K_β peak (7.058 KeV). Being unable to resolve the two peaks means that XRF is not a suitable technique for the characterisation of future samples. As an alternative, inductively coupled plasma optical emission spectrometry (ICP-OES) was carried out on the 10 samples. The percentages of Fe and Co were calculated using the raw ICP data, which were transformed to give the relative iron oxide to cobalt ferrite percentages using Equation 6.1, the results are given in Table 6.6.

Table 6.6: The calculated percentage contribution of elemental Fe in DoE samples due to cobalt ferrite nanoparticles and iron oxide shell/nanoparticles using ICP-OES

Sample Code	**% Fe(Total)**[a]	**%Co**[a]	**%Fe(CF)**[b]	**%Fe(IO)**[c]	**XRF-ICP**[d]
CFNP	66.2	33.8	100.0	0.0	48.8
Initial EXP	85.4	14.6	34.2	65.8	3.7
DoE01	91.2	8.8	19.3	80.7	5.9
DoE02	87.4	12.6	28.9	71.1	2.2
DoE03	90.0	10.0	22.1	77.9	21.3
DoE04	84.8	15.2	36.0	64.0	-13.1
DoE05	94.0	6.0	12.7	87.3	36.8
DoE06	90.4	9.6	21.2	78.8	2.0
DoE07	89.0	11.0	24.8	75.2	19.3
DoE08	95.3	4.7	9.8	90.2	-9.8
DoE09	90.9	9.1	20.0	80.0	9.5
DoE10	87.6	12.4	28.3	71.7	-5.0

[a] Atom percentages of iron and cobalt as measured by inductively coupled plasma optical emission spectroscopy (ICP-OES); [b] Calculated quantity of iron within a sample attributed to cobalt ferrite nanoparticles (CFNPs) relative to total iron measured (calculated according to Equation 6.1); [c] Calculated quantity of iron within a sample attributed to iron oxide (IO) relative to total iron measured (calculated according to Equation 6.1). [d] Difference between %Fe (CFNP) as calculated by XRF and ICP-OES.

The ICP analysis provided a new upper limit for %Fe(IO), calculated to be 65.8 % (see Table 6.6). Therefore, based on the TEM observations of the initial attempt values above this limit likely contains a too great proportion of iron oxide and therefore a second population of IONPs. Interestingly, only 1 sample, DoE04, met this criteria and fell below the new limit. This data appears more reliable than the XRF having correctly identified a sample as containing only CFNPs (Sample CFNP; the measured values %Fe(Total) and %Co gave %Fe(CFNP) = 102.3

% which is not possible so value of 100 is given). As 9 of the 10 samples measured high relative quantities of iron oxide (%Fe(IO)), including high CFNP to Fe salt samples DoE03 and DoE07, no conclusions can be drawn without complete TEM and EDS analysis of the samples.

6.3.3 X-ray Diffraction

For other examples of bi-magnetic core-shells detailed in the literature, Debye-Scherrer analysis has been demonstrated to show that upon formation of a crystalline shell the calculated crystallite size will increase.[177,180,181,356]. The calculation was carried out using the XRD patterns for the parent and core-shell samples, with the average crystallite size calculated from the peak width at half maximum of the 5 strongest peaks at 13.7 °, 16.1 °, 19.5 °, 25.4 °, and 27.7 ° 2-theta using the Debye-Scherrer equation (see Equation 2.8). The 5 calculated diameters were then averaged for the DoE 10 samples are compared to the parent CFNP (non-stabilised non core-shell). The data is represented in Figure 6.4.

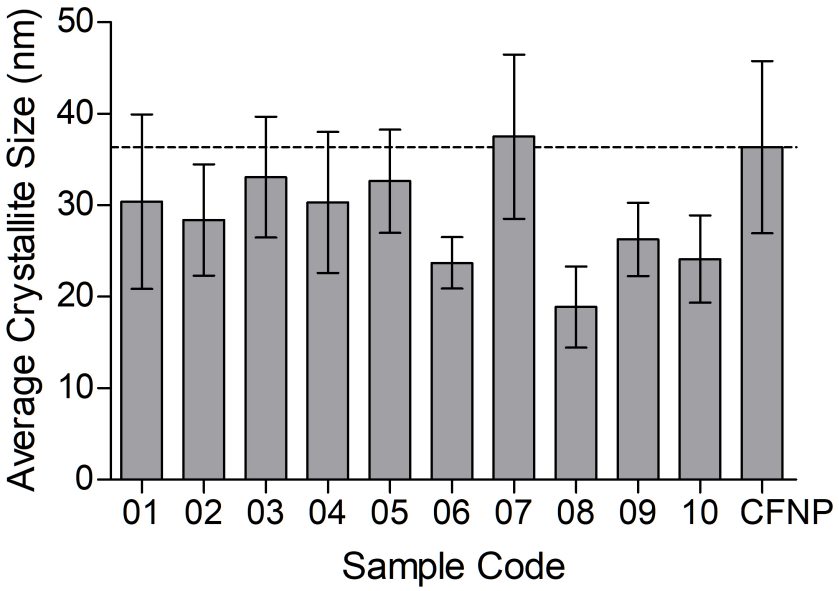

Figure 6.4: Average crystallite size (nm) as calculated by Debye-Scherrer analysis from corresponding XRD patterns of 10 DoE samples. Error bars represent the standard deviation from the mean for diameters calculated from 5 strongest peaks by XRD analysis. Dashed line represents the mean value for parent cobalt ferrite nanoparticles (CFNP).

Whilst 9 out of 10 samples measured a reduced mean size in comparison to the parent nanoparticles, which would indicate the presence of second population of smaller iron oxide nanoparticles (rather than core-shells), the errors associated with the calculation for each are too great to make a definitive conclusion. This may be due to the limitations of Debye-Scherrer analysis. This method of size analysis only provides a lower limit for the size of a coherently scattering domain, therefore crystal lattice imperfections, particles formed of aggregated crystallites, as well as instrumental and sample preparation effects can all influence the calculated crystallite size. Furthermore, whilst the literature shows the formation of a ferrite shell around a ferrite core results in an increased crystallite size, for this to be true there must be no imperfections. The shell and core must form a single uniform domain, which is almost certainly not the case, based on the TEM images obtained herein, where the shell is formed *via* a co-precipitation route which can lead to reduced crystallinity compared to thermal routes.

6.3.4 Vibrating Sample Magnetometry

The exchange coupling between the shell of 'hard-soft' bi-magnetic core-shell particles results in magnetic behaviour that can be considered as a combination of the intrinsic parameters of each ferrite phase. As detailed in the introduction to this chapter, the coating of a CF core in a soft magnetic shell results in a comparative increase in magnetisation and decrease in coercivity.[178] The reduction in coercivity is attributed to the shell 'leading' the magnetisation at lower field strengths.[357] The increase in M_s results from the higher magnetisation of iron oxide (M_s of bulk magnetite = 92 emu/g) as well as the increase in particle diameter.[358] The magnetic behaviour of the 10 DoE samples was measured using vibrating sample magnetometry (VSM) with the magnetisation, and coercivity obtained from the resulting $M-H$ plot. Magnetometry was also carried out on the parent CFNPs, the results are summarised in Table 6.7.

Table 6.7: Saturation magnetisation (M_s) and coercivity (H_c) of 10 DoE samples and parent CFNP as measured by vibrating sample magnetometry.

Sample Name	M_s **(emu/g)**	H_c **(Oe)**
CFNP	74.6	370.5
DoE01	66.6	127.1
DoE02	76.6	162.8
DoE03	74.0	430.4
DoE04	75.5	237.4
DoE05	84.3	354.0
DoE06	77.4	220.9
DoE07	77.1	483.9
DoE08	71.9	40.0
DoE09	70.5	158.9
DoE10	77.8	88.1

As a control measure to identify sample containing a second IONP population rather than core-shell particles, the magnetisation was also measured for the pre-made mixtures of CFNPs and IONPs at ratios of 75:25, 50:50, and 25:75 (CFNP:IONP). The magnetisation was also measured for iron oxide NPs synthesised *via* co-precipitation (ratio therefore 0:100). This data is provided in Table 6.8.

Table 6.8: Saturation magnetisation and Coercivity of pre-made mixtures of cobalt ferrite and iron oxide nanoparticles as measured by vibrating sample magnetometry.

CFNP:IONP	M_s **(emu/g)**	H_c **(Oe)**
0:100	60.7	20.3
25:75	62.8	72.1
50:50	65.8	97.3
75:25	70.8	231.0
100:0	74.6	370.5

The M_s's for bulk cobalt ferrite and magnetite is 81 and 92 emu/g respectively, however due to size effects such as spin canting CFNPs and IONPs will often measure a reduced value as

observed for the parent CFNP ($M_s = 74.6$ emu/g) and the IONP control ($M_s = 60.7$ emu/g)[359]. Despite magnetite having the higher bulk M_s, from the control measurements we see that the IONPs measure a lower M_s. This is caused by differences in size, with the smaller IONPs experiencing greater size effects in comparison to the larger CFNPs. From Table 6.8, by mixing the two samples together the M_s and H_c decrease with increasing IONP (compared to the parent $CoFe_2O_4$ nanoparticles). This provides a possible means of differentiating between core-shell containing samples and mixed population containing samples, as in literature core-shells have exhibited increased M_s due to increased size and decreased H_c, whereas a mixed population shows a decrease in both M_s and H_c due to the smaller IONPs.

For the 10 DoE samples, 6 samples (DoE02, DoE04–07, and DoE10) measured an increase in M_s ranging between 75.5 and 84.3 emu/g. All but one of the 6 samples (DoE02, DoE04–07) also measured a decrease in coercivity. These samples are therefore the strongest candidates for containing possible bi-magnetic core-shell nanoparticles. Samples DoE01, DoE08, and DoE09 measured decreases in both M_s and H_c strongly indicating the presence of a second population of small iron oxide nanoparticles.

6.3.5 Transmission Electron Microscopy

Due to lack of access to imaging facilities, only samples DoE03, DoE06, and DoE07 were imaged *via* TEM. To identify to possible iron oxide coating on the CFNPs, energy-dispersive X-ray spectroscopy (EDS) was used to map the distribution of cobalt and iron. The images as well as the Co and Fe maps produced by EDS analysis are presented in Figures 6.5, 6.6 and 6.7. All images were collected prior to citrate-stabilisation, therefore no coatings should be present on the particle surface.

Figure 6.5 shows sample DoE03, which measured an decrease in M_s, d_{hyd}, and d_{XRD}, all indicators of a second population of smaller iron oxide nanoparticles. TEM analysis revealed particles that appear to have a coating, most notable in the top image of Figure 6.5 (highlighted by black arrows). Also highlighted within this figure (red circle) is what appears to be evidence of a second population of iron oxide nanoparticles, due to being much smaller in size compared to the parent CFNPs (6.2). However, the EDS maps do not support the presence of either the shell or second population of IONPs. An iron oxide shell or IONPs would not show the presence of cobalt, however it can be observed at both the 'shell' and in the region highlighted by the red circle. Though this is not necessarily definitive, EDS operates according to the same principles as XRF, with XRF having shown to incorrectly identify the elements due to overlapping of the

Co K_α and Fe K_β peaks, it is possible that this may also be the case for the EDS mapping.

With this in mind, images of sample DoE06 (Figure 6.6) appear to show cobalt ferrite nanoparticles again surrounded by a second population of smaller iron oxide particles (circled in red). Again EDS detected the presence of cobalt but to a much lesser degree, therefore more likely that these small particles are indeed iron oxide. This is supported by the decrease in both the d_{hyd} and d_{XRD} that was seen for sample DoE06. Sample DoE07 did not appear to contain a separate population of iron oxide nanoparticles, but there is a possible iron oxide shell visible in the bottom image (Figure 6.7, highlighted by black arrows). Sample DoE07 measured a small increase in the mean d_{XRD} compared to the parent CFNPs as well as increased M_s which would support the formation of the iron oxide shell. However, DoE07 also measured a decrease in d_{hyd} and an increase in H_c which does not concur with literature observations.

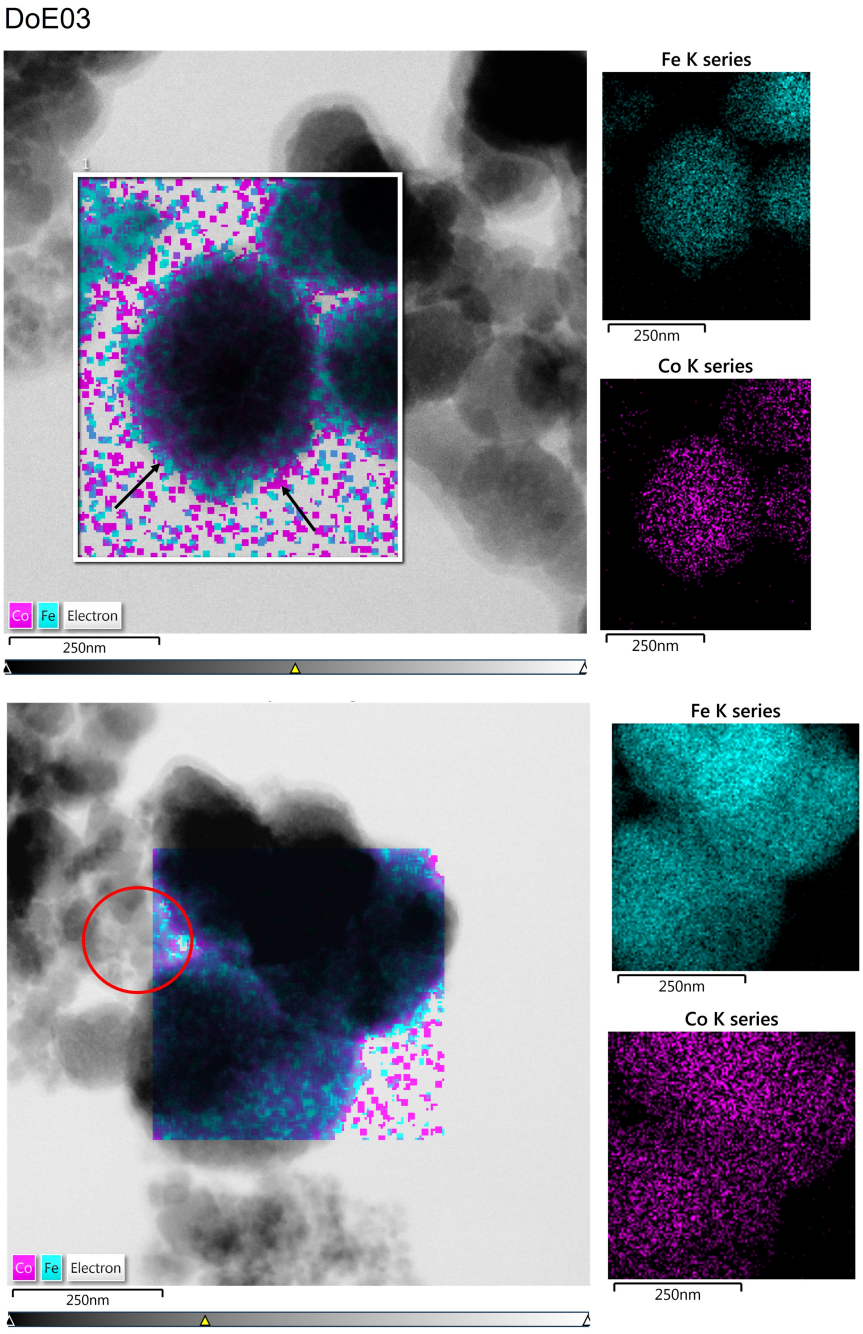

Figure 6.5: Transmission electron microscopy (TEM) images of sample DoE03 with maps showing distribution of cobalt (purple) and iron (blue) as measured by energy-dispersive X-ray spectroscopy (EDS) The black arrows highlight possible iron oxide shell and red circle highlights possible iron oxide nanoparticles. Images and EDS performed by Dr Yisong Han (University of Warwick).

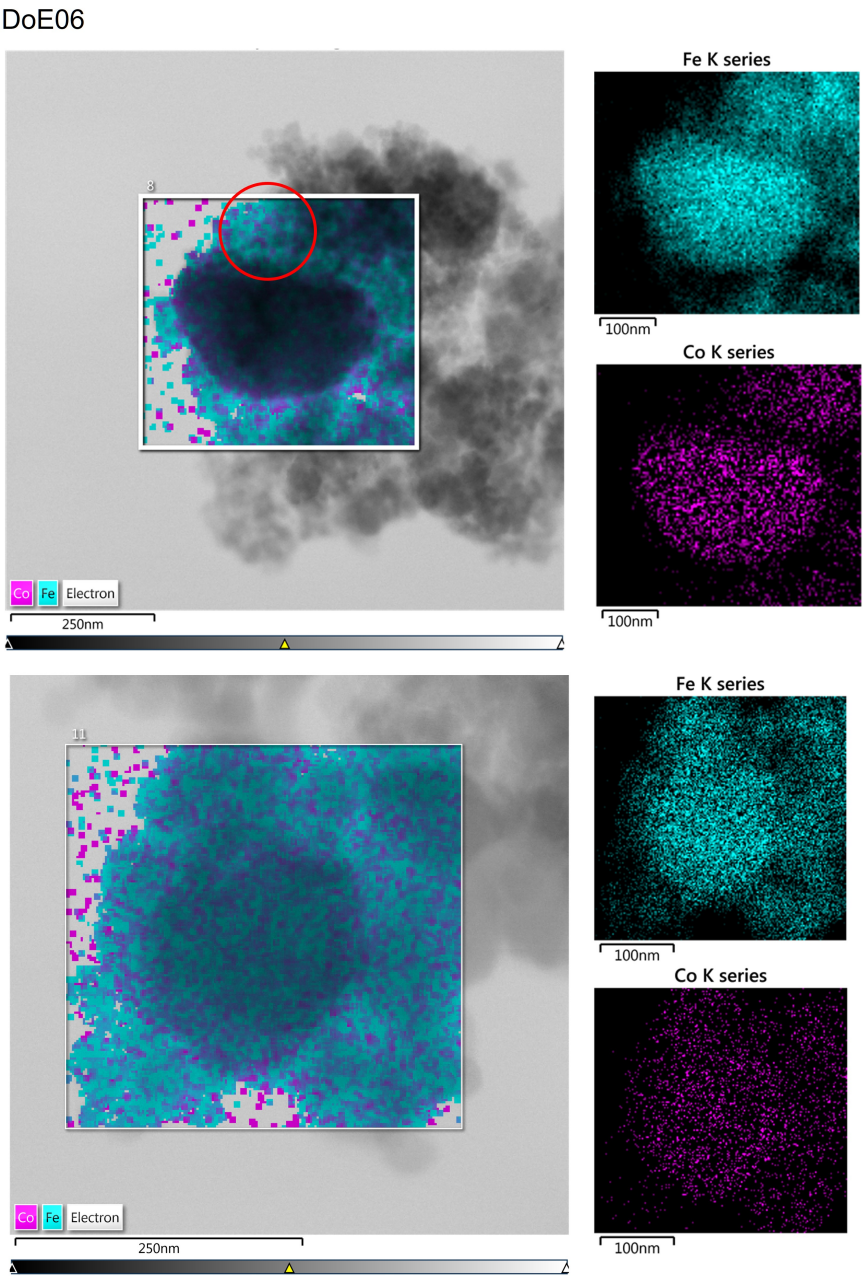

Figure 6.6: Transmission electron microscopy (TEM) images of sample DoE06 with maps showing distribution of cobalt (purple) and iron (blue) as measured by energy-dispersive X-ray spectroscopy (EDS). Secondary population of iron oxide nanoparticles highlighted by red circle. Images and EDS performed by Dr Yisong Han (University of Warwick).

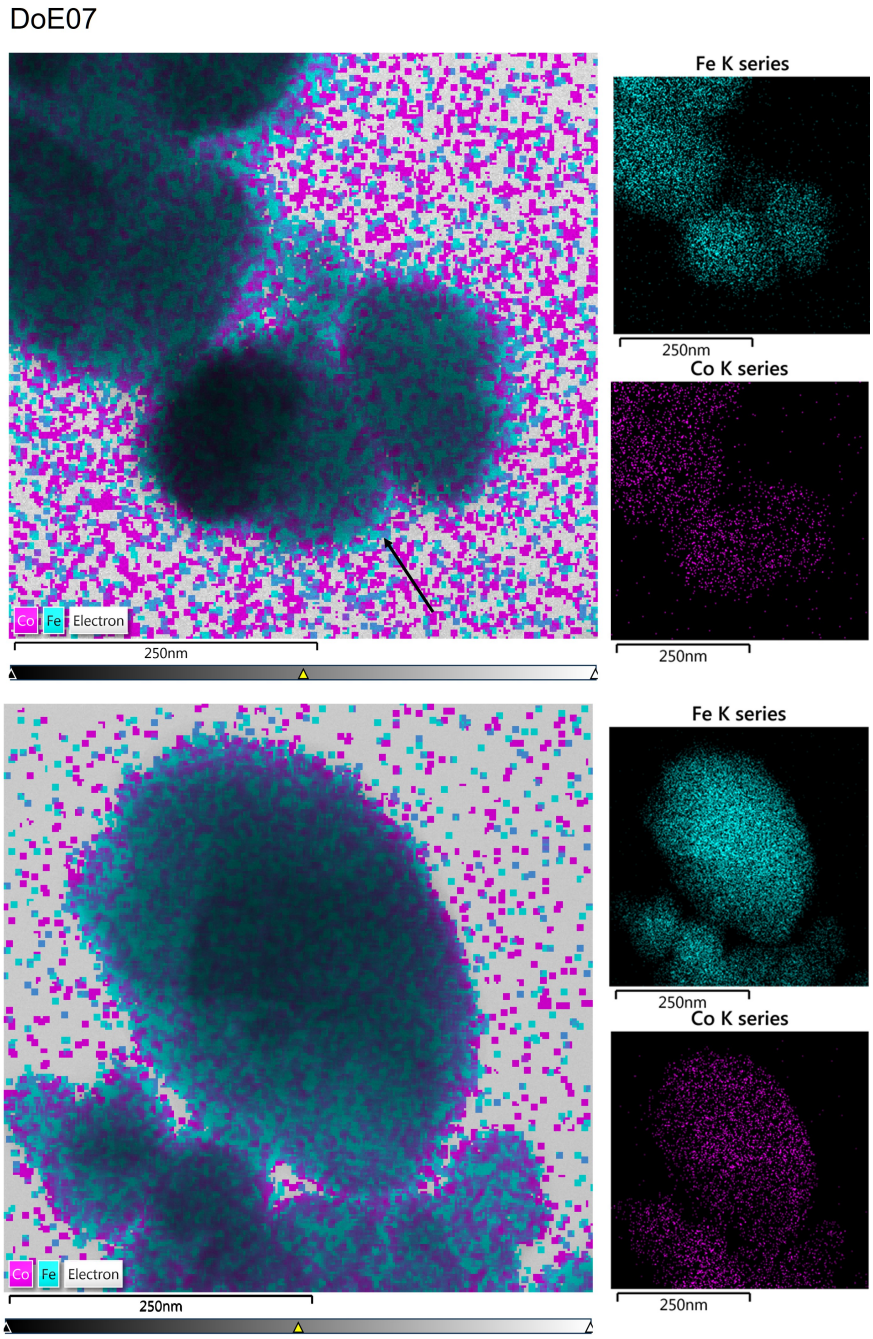

Figure 6.7: Transmission electron microscopy (TEM) images of sample DoE07 with maps showing distribution of cobalt (purple) and iron (blue) as measured by energy-dispersive X-ray spectroscopy (EDS). Images and EDS performed by Dr Yisong Han (University of Warwick).

6.4 Conclusions & Future Work

6.4.1 Conclusion

The aim of this work was to produce a bi-magnetic core-shell nanoparticle through the coating of a 'hard' cobalt ferrite nanoparticle core with a 'soft' iron oxide shell. Such materials have been shown to demonstrate unique magnetic properties due to exchange coupling between the two ferrite phases.[177,189,356,360] The coupling would result in magnetic properties that combine both the high crystalline anisotropy of the $CoFe_2O_4$ core with the strong magnetisation and low coercivity of γ-Fe_2O_3/Fe_3O_4. Such a combination would make the core-shell particles appealing for application as negative MRI contrast agents. Predominately, bi-magnetic materials have been produced using solvothermal and thermal decomposition methods, though these routes require harsh conditions, organic solvents, and can even damage the core reducing the magnetic potency of the final product. With far fewer examples in the literature of a co-precipitation synthesis, this work originally sought to find an optimal approach by utilising design of experiments (DoE). Doing so would investigate the entire experimental domain in a minimum number of experimental runs whilst also revealing possible secondary interactions between factors. The 4 factors chosen were the mass of CFNPs, the quantity of Fe salts, the reaction time and the method of base addition. Due to the lack of access to TEM, a combination of techniques were used to identify possible core-shell particles to be submitted for imaging; these were DLS, XRF, ICP-OES, XRD, and VSM. Collected data was compared against results reported for similar materials as well as mixtures of pre-made CFNPs and IONPs.

XRF was deemed an unsuitable technique due to overlap of the Co K_α and Fe K_β peak. Of the remaining techniques, the decrease in the d_{hyd} as measured by DLS, and the decrease in the average crystallite size calculated by Debye-Scherrer analysis of XRD patterns indicated the presence of a second population of small iron oxide particles. However the effectiveness of Debye-Scherrer analysis for characterising core-shell samples is disputable, as the equation only gives a lower bound estimation for coherent uniform domain crystallites. ICP-OES was used a means of quantifying relative quantities of CFNPs to iron oxide present in each sample. It found that despite the broad range of CFNP: Fe salt ratios investigated, all but one sample (DoE04) measured an increase in relative iron oxide content compared to the initial study carried out, therefore implying the formation of a secondary population of IONPs. Magnetometry measurements however, revealed 6 samples to measure an increase in M_s, with 5 samples also measuring a decrease in H_c, indicative of bi-magnetic core-shell particles.[361] TEM and EDS

analysis was carried out on 3 of the DoE samples, with TEM images of sample DoE03 in particular showing signs of shell formation. However, EDS maps were elusive in confirming the iron oxide shells.

6.4.2 Future Work

Due to limitations in being able to characterise the samples fully the DoE in this chapter was unable to determine which of the 4 experimental factors were significant for the formation of bi-magnetic core-shell particles. Therefore, for future research full TEM analysis would afford a complete initial screening experiment which would then guide the design of an optimisation experiment with fewer factors. Within this optimisation experiment it would also be possible to not only optimise with respect to core-shell formation but also optimise for MRI properties such as transverse relaxivity. As discussed in the introduction, very little work has been carried out on defining the relaxometric properties of these materials; an optimisation experiment would provide the most in-depth study to date and could guide design of high-performance negative MRI contrast agents. Likewise, such an approach could be applied to the optimisation of the MRI behaviour of bi-magnetic core-shell nanoparticles prepared *via* solvothermal/thermal decomposition methods.

Chapter 7

Conclusions & Future Work

7.1 Conclusions

This work sought to carefully design negative MRI contrast agents with enhanced relaxo-metric properties by exploiting their complex magnetic and colloidal properties. These materials were prepared through various methods, including *in situ* co-precipitation reactions layer-by-layer assembly, and trans-phase condensation reactions. Their structural, colloidal, magnetic, and relaxometric properties were characterised, revealing how careful consideration during the design of ferrite-based nanocomposites can result in contrast agents capable of strong MRI enhancement.

The *in situ* co-precipitation preparation of iron oxide nanoparticles (IONPs) in the presence of a negatively charged polyelectrolyte has previously been shown to encourage strong dipolar interparticle interactions between the magnetic cores resulting in increased transverse relaxivities. However, the use of biopolymers such as heparin or commercially available polymers such as poly(sodium-4-styrene) sulfonate (PSSS) suffer from broad molecular weights and therefore the potential for fine-tuning of behaviour is limited.[71,98] Alternatively, in Chapter 1 the synthetic polymer, poly(2-acrylamido-2-methylpropane sodium sulfonate) (P(AMPS)) was utilised for its much narrower size distribution ($Đ$ = 1.10 – 1.51) and enabled probing the complex inter-particle interactions with much finer control than previously possible. Fast field cycling (FFC) relaxometry carried out on the P(AMPS)-IONP composites produced nuclear magnetic relaxation dispersion (NMRD) profiles with with strong low field longitudinal relaxivities, due to the strong interparticle interactions, with the low field behaviour observed to be dependent

upon the molecular weight of the stabilising polymer. The cause was revealed by small-angle X-ray scattering (SAXS) analysis, showing that the molecular weight of the polymer chain dictated the size of the resulting "multi-core" clusters and therefore the strength of the interactions between cores. Similarly, due to the differences in the degree of clustering the transverse relaxivity of the nanocomposites were also dependent on the molecular weight of the stabiliser with one example measure an r_2 of more than 400 $mM^{-1}s^{-1}$. This exceptionally high r_2 value, (an over 3-fold increase compared to Feridex) is also evidence that due to the hydrophilicity of the stabilising polymer water access to internal particles is not inhibited.

The importance of strong inter-particle dipolar interactions on the MRI properties of ferrite based contrast agent also lead to the investigation of permanent 1-dimensional magnetic nanostructures. Formation of such materials would give another means for encouraging these interactions between neighbouring cores. A 'trans-phase' approach using polyelectrolyte stabilised cobalt ferrite nanoparticles as a precursor was used for synthesising the 1D magnetic nanomaterials. Cobalt ferrite nanoparticles (CFNPs) were selected due to their large core-size, high magnetocrystalline anisotropy, and strong magnetic saturation. This method used a magnetic trigger for the formation of a silica shell encasing the particles into an elongated structure named a 'nano-necklace'. This process was optimised by examining the role the stabiliser, the strength of base catalyst, and strength of magnetic trigger with conditions shown to affect size, shape, and thickness of coating of the formed 1D nanostructures. The shape anisotropy of the nano-necklaces resulted in elevated low field longitudinal relaxivity compared to the spherical counterparts as measured by FFC-relaxometry. As the behaviour within the low field range is strongly correlated to the anisotropy of the sample, this increase in r_1 was attributed to the increased anisotropy due to the 1D structure of the nano-necklaces.

Another material investigated in this work due to its high potential as a negative MRI contrast agent, was bi-magnetic core-shell nanoparticles. In particular, developing and optimising a novel synthetic protocol for the co-precipitation coating of 'hard' cobalt ferrite cores with 'soft' iron oxide. Similar materials have exhibited unique magnetic properties due to the exchange coupling between the core and shell making them appealing as MRI contrast agents. In order to efficiently optimise the preparation, the statistical approach 'design of experiments' was used to design an initial 2^4 screening experiment to reveal important factors and interactions. A range of analytical techniques including, dynamic light scattering (DLS), X-ray fluorescence (XRF), inductively coupled plasma optical emission spectrometry (ICP-OES), X-ray diffraction (XRD), and vibrating sample magnetometry (VSM), were used in the absence of TEM analysis for the

identification of potential bi-magnetic core-shell nanoparticles. However, the characterisation completed was too limited to allow for statistical analysis with further work needed before the co-precipitation formation of core-shell nanoparticles may be optimised.

Layer-by-layer deposition of polyelectrolytes onto a sacrificial core has been long established as a method for preparing functional polymer microcapsules (PMCs). By selecting stimuli-responsive polymers for the capsule membrane, the resulting capsules may be used for selectively triggered drug release. In Chapter 6, pH-responsive MRI-active PMCs were formed *via* the LbL deposition of poly(allylamine) (PAH) and poly(sodium-4-styrenesulfonate) (PSSS) onto a $CaCO_3$ core doped with iron oxide nanoparticles. After incubation the resulting PMCs in acidic conditions (pH 3.0), the release of the IONPs from the capsules could be monitored by measuring the change in relaxation rate over time. This is the first instance in which release of IONPs from a PMC was monitored by relaxometry, and is the first step towards monitoring pH-triggered drug release from a capsule using MRI. Attempts were also made at depositing IONPs within the capsule membrane during the LbL process, however this did not yield satisfactory capsules.

7.2 Future Work

With regards to the silica coated cobalt ferrite nano-necklaces, further experiments will look to functionalise the 1D nanostructures to improve colloidal stability, and therefore MRI capabilities. One of the primary motivations for using silica as the coating was the relative ease at which it may be functionalised. Therefore, polyethylene glycol, a popular coating agent which can reduce opsonisation an enhance blood circulation half-life, can be readily attached to the surface of the nano-necklaces, improving the colloidal stability and bio-compatibility of the nano-necklaces. Further functionalisation experiments could also be carried out with the addition of fluorescent or targeting moieties onto the silica surface, resulting in a multi-modal targeted bio-imaging contrast agent.

As discussed in Chapter 5, limitations in access to TEM analysis prevented a full screening experiment to be completed. Therefore, full TEM analysis would be completed to determine which of the experimental factors were significant for the formation of the core-shell particles. This would then be followed by an optimisation experiment in which fewer factors would be investigated through a response surface design such as a central composite design (CCD), such an experimental design would reveal higher order interactions between the experimental fac-

tors. Once the optimal reaction conditions had been found a final confirmation experiment would be designed as a means of testing the robustness of the model produced via the optimisation experiments. The relaxometric properties of the core-shell particles formed during the optimisation experiments would be measured, and a response surface analysis could be carried out with respect to different experimental factors and their effects on relaxivity of the resulting core-shell particles examined. The response surface would ultimately allow for experimental parameters to be selected in order to optimise for different chosen characteristics such as strong saturation magnetisation or high transverse relaxivity.

Finally, the capacity of the MRI-active polymer microcapsules to act as pH-responsive drug delivery systems will be investigated. To do so the capsules will be loaded with a fluorescent drug model such as doxorubicin (DOX), the drug loading and drug encapsulation efficiency will be calculated before drug release experiments are undertaken. The release of DOX will be monitored by UV/vis spectroscopy, whilst simultaneously measuring the change in transverse relaxation rate, in order to develop a MRI-trackable release system. As with the pH-response experiment carried out in Chapter 6, the drug release profile will be measured at different pH's (3.0, 7.0, and 10.0) to demonstrate the pH responsiveness of the microcapsules.

Appendix

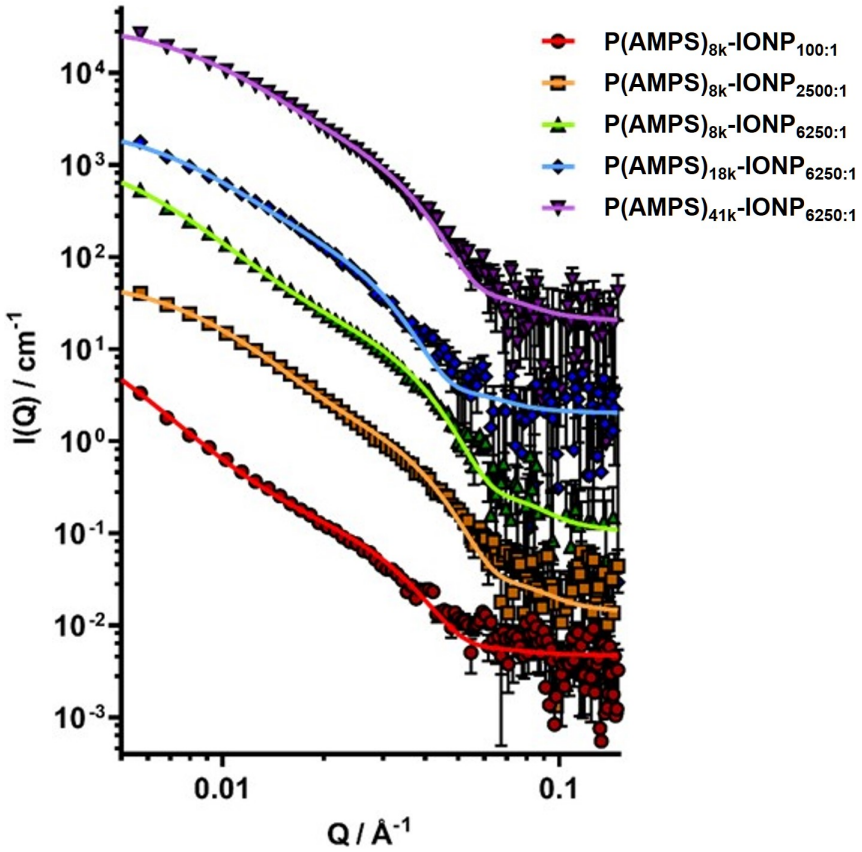

Figure 7.1: Small-angle X-ray scattering (SAXS) data (points) for aqueous suspensions of P(AMPS) stabilised aggregates iron oxide nanoparticles with corresponding fits (lines) to models describing fractal-like clusters of spherical particles.

Table 7.1: Summary of colloidal and magnetic properties of P(AMPS) stabilised cobalt ferrite nanoparticles (P(AMPS)-CFNPs) as measured by DLS and VSM.

Sample	$d_{\mathbf{hyd}}$ **(nm)**	**PDI**	M_s **(emu g^{-1})**
$P(AMPS)_{8k}$-$CFNP_{1:100}$	114.3 ± 2.1	0.363	52.3
$P(AMPS)_{8k}$-$CFNP_{1:2500}$	281.9 ± 4.0	0.280	82.3
$P(AMPS)_{18k}$-$CFNP_{1:100}$	–	–	72.2
$P(AMPS)_{18k}$-$CFNP_{1:2500}$	215.0 ± 4.9	0.301	79.5
$P(AMPS)_{41k}$-$CFNP_{1:100}$	–	–	62.4
$P(AMPS)_{41k}$-$CFNP_{1:2500}$	–	–	63.8

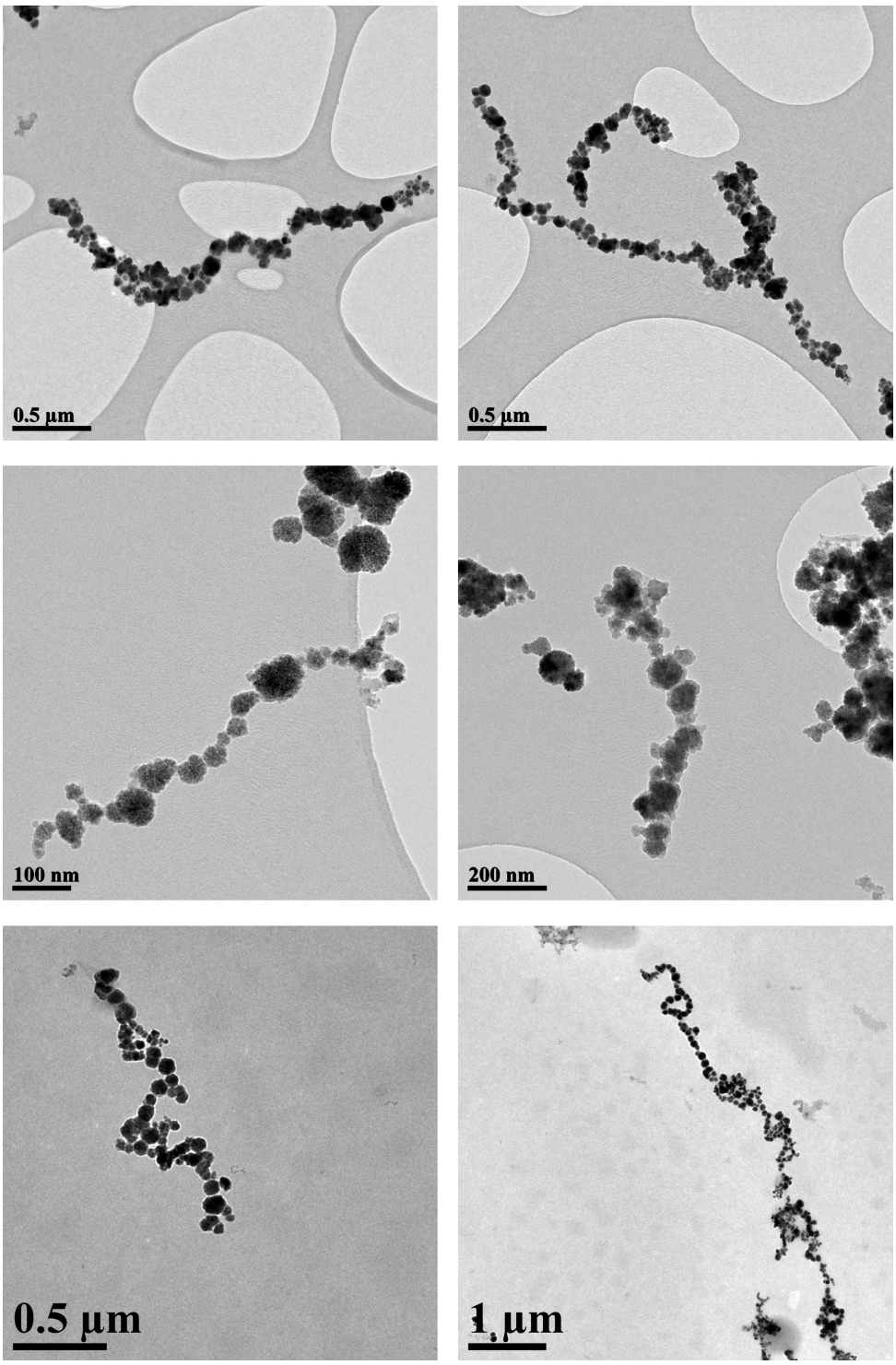

Figure 7.2: Additional transmission electron microscopy (TEM) images of silica coated cobalt ferrite nano-necklaces produced according to experiment CFNN01.

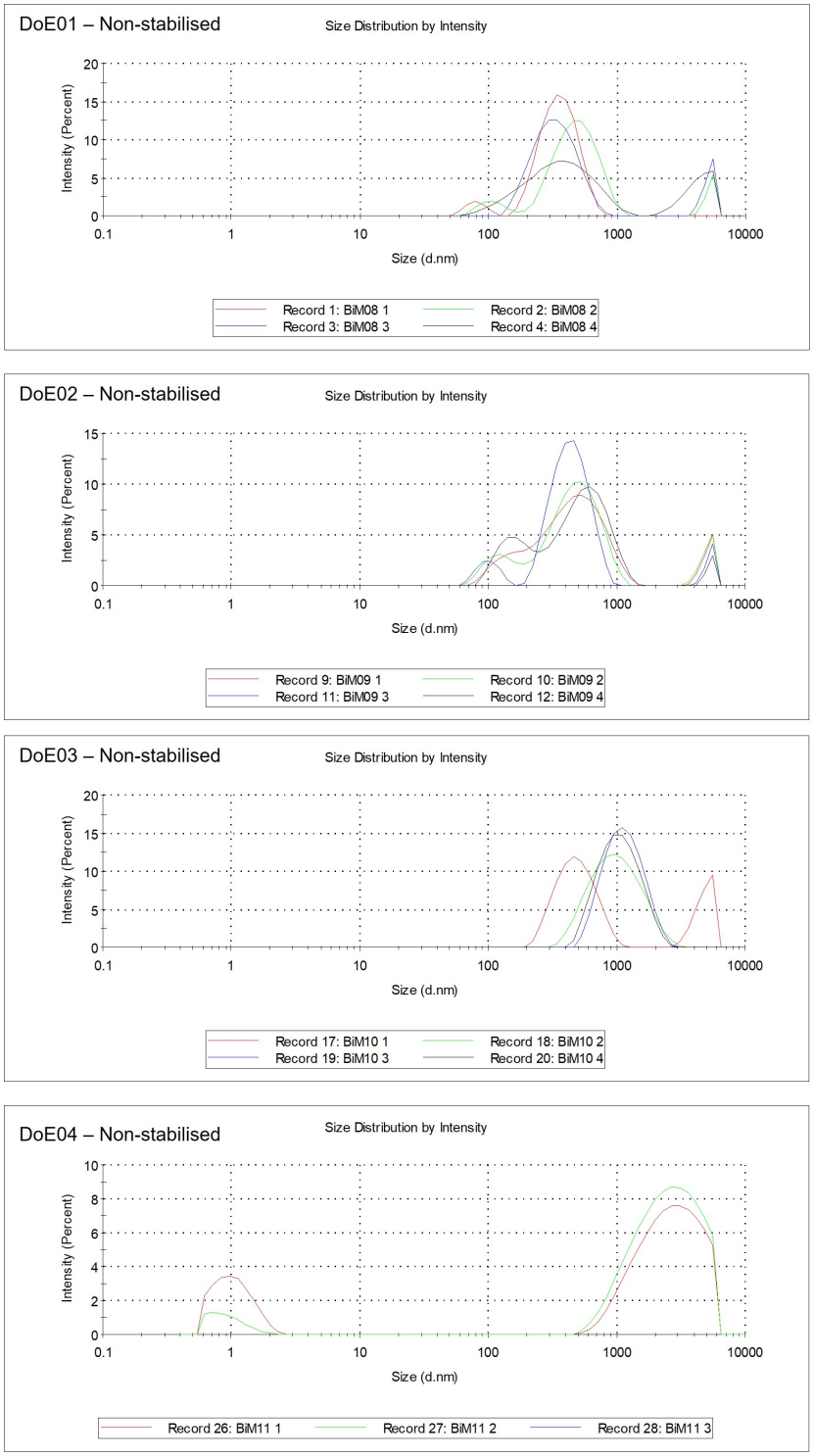

Figure 7.3: Size distribution by intensity curves for bi-magnetic core-shell nanoparticle samples DoE01, 02, 03 and 04, as measured by dynamic light scattering (DLS).

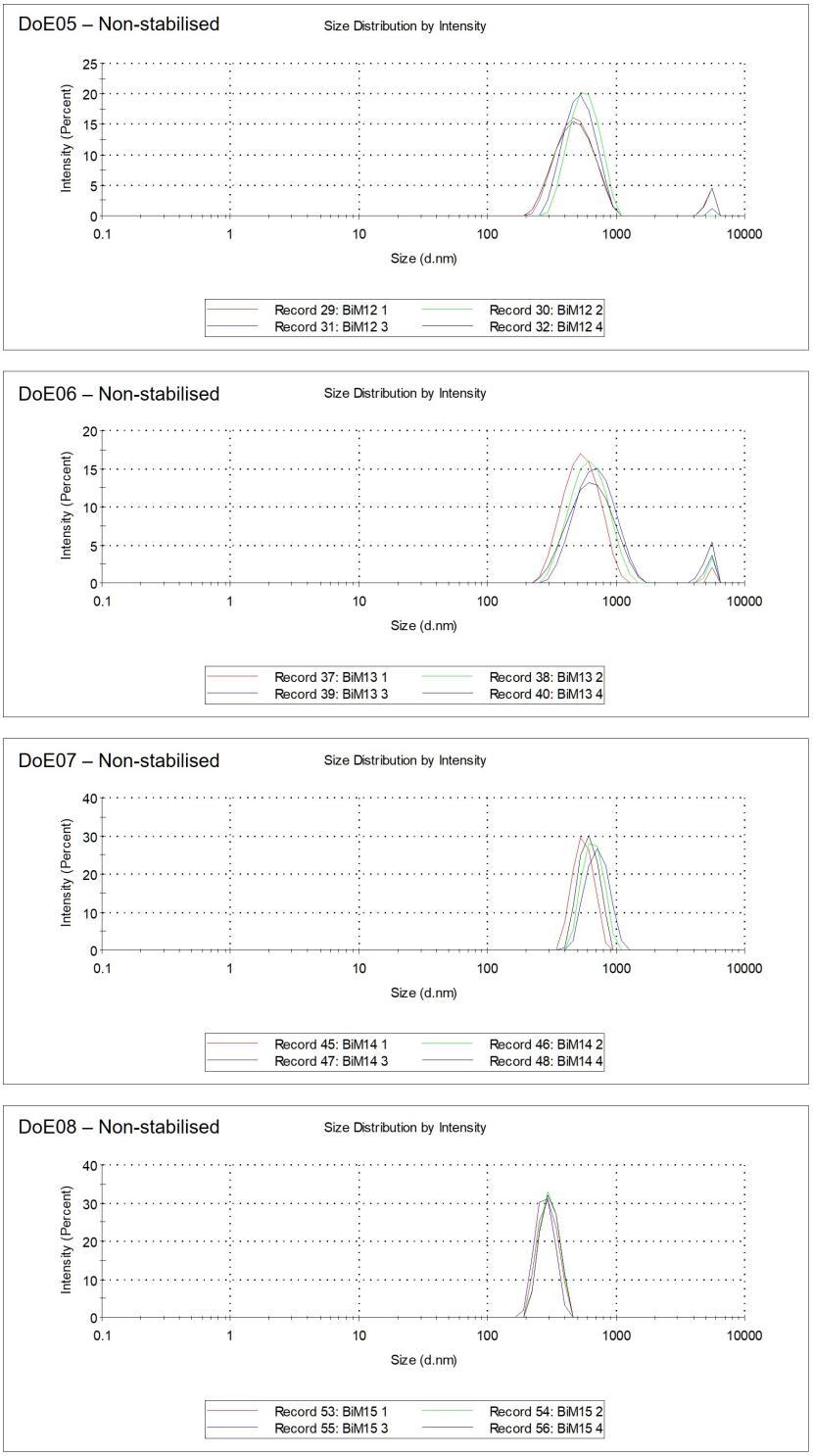

Figure 7.4: Size distribution by intensity curves for bi-magnetic core-shell nanoparticle samples DoE04, 05, and 06, as measured by dynamic light scattering (DLS).

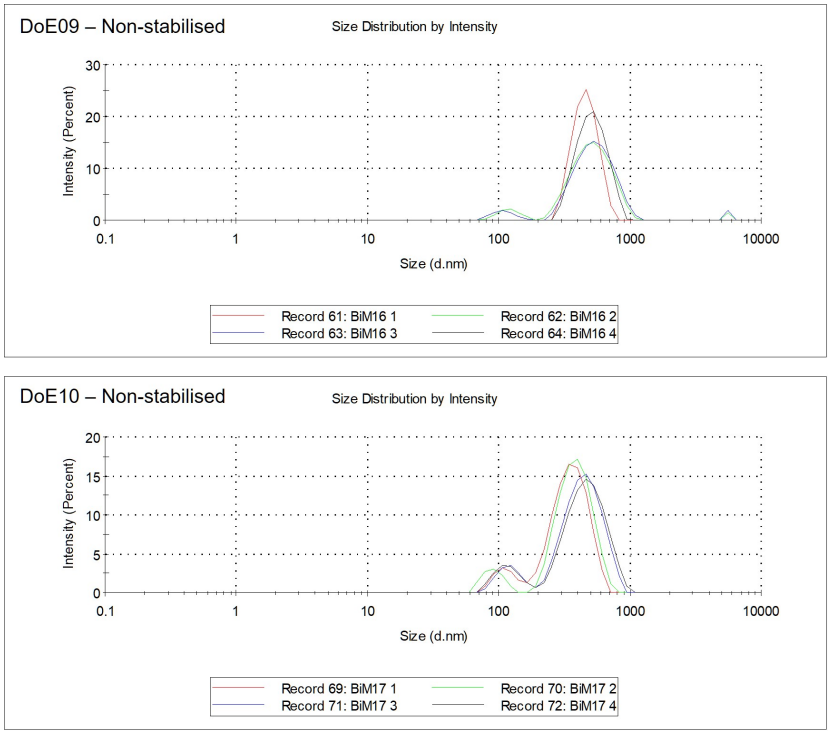

Figure 7.5: Size distribution by intensity curves for bi-magnetic core-shell nanoparticle samples DoE09 and 10, as measured by dynamic light scattering (DLS).

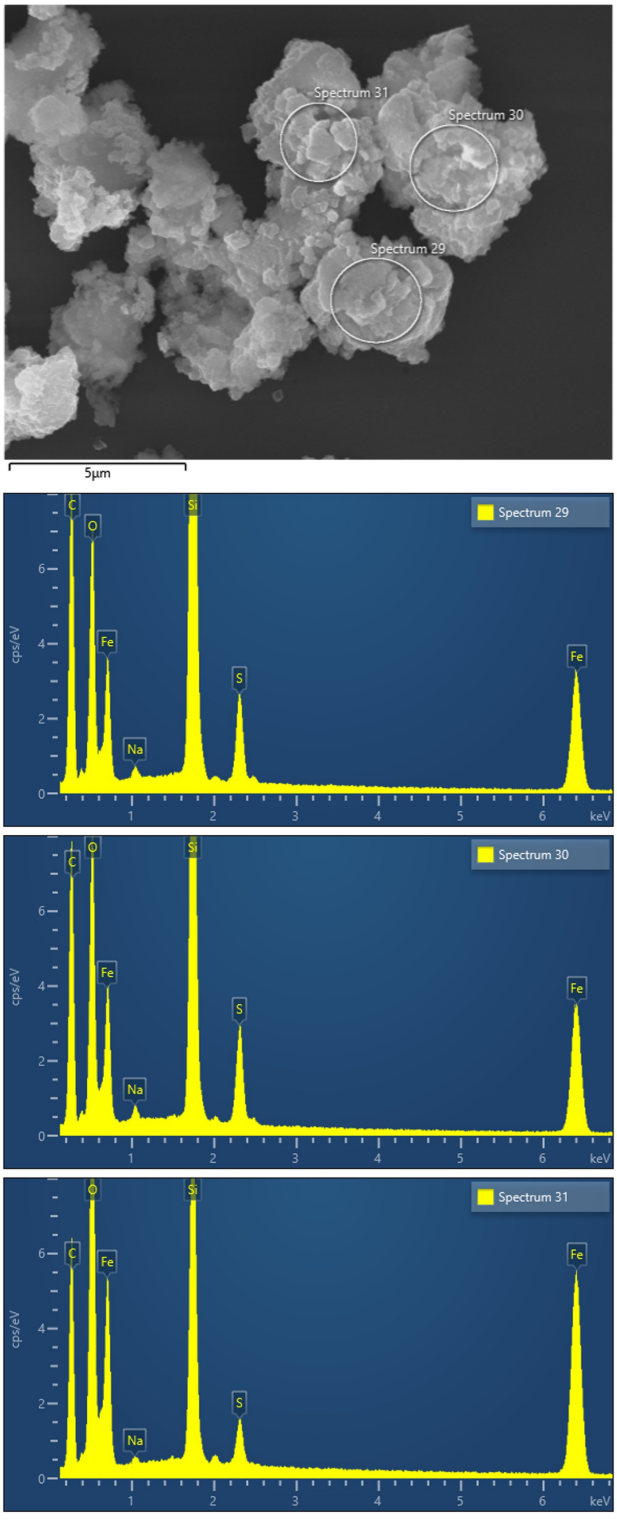

Figure 7.6: EDS spot analysis performed on polymer microcapsules (PMCs) with PSSS-IONPs deposited during the 2nd PEAP confirming the presence of iron in sample. Analysis carried out by Dr Yisong Han of the University of Warwick.

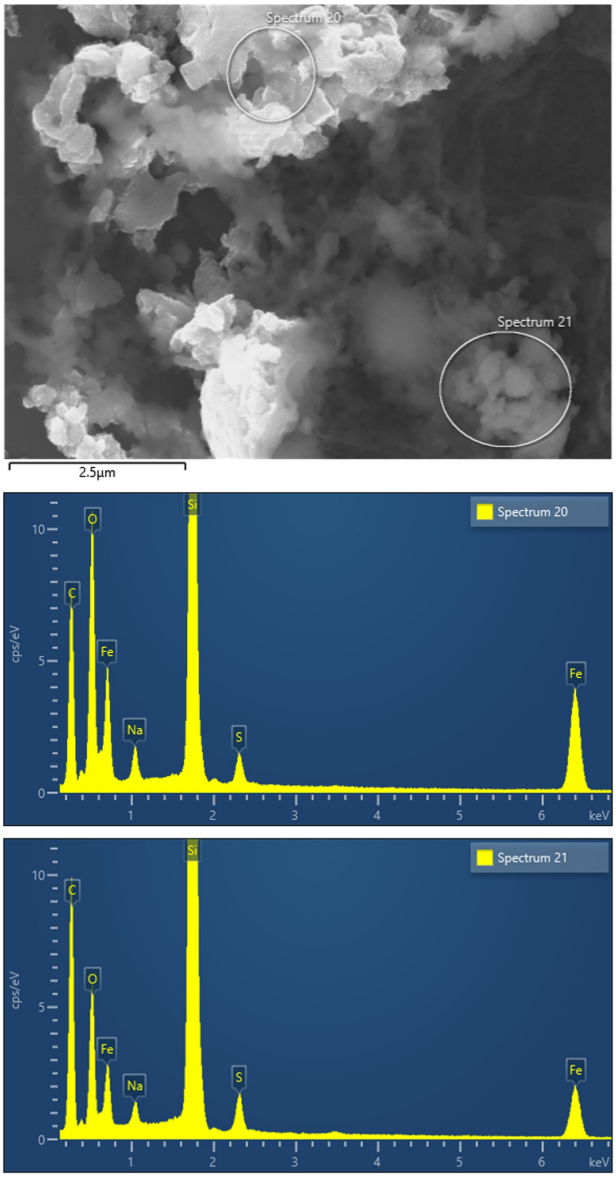

Figure 7.7: EDS spot analysis performed on polymer microcapsules (PMCs) with PSSS-IONPs deposited during the 4th PEAP confirming the presence of iron in sample. Analysis carried out by Dr Yisong Han of the University of Warwick.

Publications & Presentations

Publications

1. **Exploring Precision Polymers to Fine-Tune Magnetic Resonance Imaging Properties of Iron Oxide Nanoparticles**
   A.M. King, C. Bray, L. Bogart, S. Hall, J.C. Bear, S. Perrier, G.-L. Davies*
   Journal of Colloid and Interface Science, **2020**, 579, 401-411.

2. **pH-Responsive Nanocomposite Fibres Allowing MRI Monitoring of Drug Release**
   Z. Zhang, C.J.R. Wells, A.M. King, J.C. Bear, G.-L. Davies*, G.R. Williams*
   Journal of Materials Chemistry B, **2020**, 8, 7264-7274.

3. **Environmentally Relevant Concentrations of Titanium Dioxide Nanoparticles Pose Negligible Risk to Marine Microbes**
   C.J. Dedman, A.M. King, J. Christie-Oleza, G.-L. Davies*
   Environmental Science – Nano, **2021**, 8, 1236-1255.

4. **Controlling the Growth of SPION@SiO2 Nanoparticles Using Design of Experiments**
   C.L.G. Harman, N. Mac Fhionnlaoich, A.M. King, C.J.R. Wells, J.R.H. Manning, P. Scholes, G.-L. Davies,* S. Guldin*
   Pending Submission

5. **Magnetically Driven Preparation of 1D Nano-Necklaces**
   A.M. King, T. Insinna, C.J.R. Wells, Y.K. Gun'ko, G.-L. Davies*
   Pending Submission

Presentations

Presentations

1. **Exploiting Precision Designed Polymers to Control Imaging Behaviour in MRI Contrast Agents**
   14th International Conference on Materials Chemistry. *Birmingham, UK.*
   8^{th} – 11^{th} July 2019

2. **High-performance Biocompatible MRI Contrast Agents: Exploiting Inter-particle Interactions with Permanent and Dynamic Nanoparticle Arrays**
   2020 Materials Research Society (MRS) Virtual Spring/Fall Meeting & Exhibit.
   27^{th} November – 4^{th} December 2020

Posters

1. **Using Heparin-mimics to Produce High Performance Stabilised Negative MRI Contrast Agents**
   12^{th} International Conference on the Scientific and Clinical Applications of Magnetic Carriers. *Copenhagen, Denmark.*
   22^{nd} – 26^{th} May 2018

2. **High-performance Biocompatible MRI Contrast Agents: Tuning Nanoparticle Interactions Through Precision-Engineered Bio-polymer Mimics**
   RSC Materials Chemistry Division Poster Symposium. *London, UK.*
   22^{nd} November 2018

Bibliography

1. Grand View Research, *Nanomaterials Market Size & Share Report, 2021-2028*, 2021, https://www.grandviewresearch.com/industry-analysis/nanotechnology-and-nanomaterials-market.

2. K. ISO, *ISO/TS 80004-2: 2015. Nanotechnologies-Vocabulary-Part 2: Nano-objects*, 2015.

3. J. G. Croissant, K. S. Butler, J. I. Zink and C. J. Brinker, *Nature Reviews Materials*, 2020, **5**, 886–909.

4. E. C. Dreaden, A. M. Alkilany, X. Huang, C. J. Murphy and M. A. El-Sayed, *Chemical Society Reviews*, 2012, **41**, 2740–2779.

5. P. Xu, G. M. Zeng, D. L. Huang, C. L. Feng, S. Hu, M. H. Zhao, C. Lai, Z. Wei, C. Huang, G. X. Xie and Z. F. Liu, *Use of iron oxide nanomaterials in wastewater treatment: A review*, 2012.

6. R. Tenne, *Nature Nanotechnology*, 2006, **1**, 103–111.

7. K. A. S. Usman, J. W. Maina, S. Seyedin, M. T. Conato, L. M. Payawan, L. F. Dumée and J. M. Razal, *NPG Asia Materials*, 2020, **12**, 58.

8. M. Yuan, M. Liu and E. H. Sargent, *Nature Energy*, 2016, **1**, 16016.

9. J. Nicolas, S. Mura, D. Brambilla, N. Mackiewicz and P. Couvreur, *Chemical Society Reviews*, 2013, **42**, 1147–1235.

10. S. Mura, J. Nicolas and P. Couvreur, *Nature Materials*, 2013, **12**, 991–1003.

11. I. Lostalé-Seijo and J. Montenegro, *Nature Reviews Chemistry*, 2018, **2**, 258–277.

12. J. N. Anker, W. P. Hall, O. Lyandres, N. C. Shah, J. Zhao and R. P. Van Duyne, *Nature Materials*, 2008, **7**, 442–453.

13. A. M. Shrivastav, U. Cvelbar and I. Abdulhalim, *A comprehensive review on plasmonic-based biosensors used in viral diagnostics*, 2021.

14. M. Colombo, S. Carregal-Romero, M. F. Casula, L. Gutiérrez, M. P. Morales, I. B. Böhm, J. T. Heverhagen, D. Prosperi and W. J. Parak, *Chemical Society Reviews*, 2012, **41**, 4306–4334.

15. K. Li and B. Liu, *Chem. Soc. Rev.*, 2014, **43**, 6570–6597.

16. M. J. Mitchell, M. M. Billingsley, R. M. Haley, M. E. Wechsler, N. A. Peppas and R. Langer, *Nature Reviews Drug Discovery*, 2021, **20**, 101–124.

17. N. Erathodiyil and J. Y. Ying, *Accounts of Chemical Research*, 2011, **44**, 925–935.

18. J. M. Schnorr and T. M. Swager, *Chemistry of Materials*, 2010, **23**, 646–657.

19. S. Barui and V. Cauda, *Multimodal decorations of mesoporous silica nanoparticles for improved cancer therapy*, 2020.

20. W. Y. Huang, G. L. Davies and J. J. Davis, *Chemical Communications*, 2013, **49**, 60–62.

21. S. Jafari, H. Derakhshankhah, L. Alaei, A. Fattahi, B. S. Varnamkhasti and A. A. Saboury, *Biomedicine & Pharmacotherapy*, 2019, **109**, 1100–1111.

22. S. Unser, I. Bruzas, J. He and L. Sagle, *Sensors*, 2015, **15**, 15684–15716.

23. E. Petryayeva and U. J. Krull, *Analytica Chimica Acta*, 2011, **706**, 8–24.

24. D.-E. Lee, H. Koo, I.-C. Sun, J. H. Ryu, K. Kim and I. C. Kwon, *Chem. Soc. Rev.*, 2012, **41**, 2656–2672.

25. L. Dykman and N. Khlebtsov, *Chem. Soc. Rev.*, 2012, **41**, 2256–2282.

26. J. Li and J. J. Zhu, *Analyst*, 2013, **138**, 2506–2515.

27. K. D. Wegner and N. Hildebrandt, *Chemical Society Reviews*, 2015, **44**, 4792–4834.

28. J.-S. Ni, Y. Li, W. Yue, B. Liu and K. Li, *Theranostics*, 2020, **10**, 1923–1947.

29. M. Shokouhimehr, Y. Piao, J. Kim, Y. Jang and T. Hyeon, *Angewandte Chemie*, 2007, **119**, 7169–7173.

30. A. Moser, K. Takano, D. T. Margulies, M. Albrecht, Y. Sonobe, Y. Ikeda, S. Sun and E. E. Fullerton, *Journal of Physics D: Applied Physics*, 2002, **35**, R157.

31. B. Jiang, L. Lian, Y. Xing, N. Zhang, Y. Chen, P. Lu and D. Zhang, *Environmental Science and Pollution Research 2018 25:31*, 2018, **25**, 30863–30879.

32. A. Hervault, A. E. Dunn, M. Lim, C. Boyer, D. Mott, S. Maenosono and N. T. K. Thanh, *Nanoscale*, 2016, **8**, 12152–12161.

33. B. Thiesen and A. Jordan, *International Journal of Hyperthermia*, 2008, **24**, 467–474.

34. W.-F. Ma, K.-Y. Wu, J. Tang, D. Li, C. Wei, J. Guo, S.-L. Wang and C.-C. Wang, *Journal of Materials Chemistry*, 2012, **22**, 15206.

35. M. Arruebo, R. Fernández-Pacheco, M. R. Ibarra and J. Santamaría, *Nano Today*, 2007, **2**, 22–32.

36. K. Hayashi, M. Nakamura, H. Miki, S. Ozaki, M. Abe, T. Matsumoto, W. Sakamoto, T. Yogo and K. Ishimura, *Theranostics*, 2014, **4**, 834–844.

37. S. Louguet, B. Rousseau, R. Epherre, N. Guidolin, G. Goglio, S. Mornet, E. Duguet, S. Lecommandoux and C. Schatz, *Polymer Chemistry*, 2012, **3**, 1408.

38. W. Liu, L. Nie, F. Li, Z. P. Aguilar, H. Xu, Y. Xiong, F. Fu and H. Xu, *Biomaterials Science*, 2016, **4**, 159–166.

39. C. Wang, S. Ravi, G. V. Martinez, V. Chinnasamy, P. Raulji, M. Howell, Y. Davis, J. Mallela, M. S. Seehra and S. Mohapatra, Journal of Controlled Release, 2012, pp. 82–92.

40. M. Dowaidar, H. N. Abdelhamid, M. Hällbrink, K. Freimann, K. Kurrikoff, X. Zou and Ü. Langel, *Scientific Reports*, 2017, **7**, 9159.

41. C. E. Diebel, R. Proksch, C. R. Green, P. Neilson and M. M. Walker, *Nature*, 2000, **406**, 299–302.

42. G. Falkenberg, G. Fleissner, K. Schuchardt, M. Kuehbacher, P. Thalau, H. Mouritsen, D. Heyers, G. Wellenreuther and G. Fleissner, *PLOS ONE*, 2010, **5**, e9231.

43. K. Momma and F. Izumi, *Journal of Applied Crystallography*, 2011, **44**, 1272–1276.

44. C. N. Chinnasamy, A. Yang, S. D. Yoon, K. Hsu, M. D. Shultz, E. E. Carpenter, S. Mukerjee, C. Vittoria and V. G. Harris, *Journal of Applied Physics*, 2007, **101**, 09M509.

45. Y. W. Jun, J. W. Seo and J. Cheon, *Accounts of Chemical Research*, 2008, **41**, 179–189.

46. D. Levy, R. Giustetto and A. Hoser, *Physics and Chemistry of Minerals*, 2012, **39**, 169–176.

47. N. Lee and T. Hyeon, *Chem. Soc. Rev.*, 2012, **41**, 2575–2589.

48. A.-H. Lu, E. L. Salabas and F. Schüth, *Angewandte Chemie International Edition*, 2007, **46**, 1222–1244.

49. S. Currie, N. Hoggard, I. J. Craven, M. Hadjivassiliou and I. D. Wilkinson, *Understanding MRI: Basic MR physics for physicians*, 2013.

50. T.-H. Shin, Y. Choi, S. Kim and J. Cheon, *Chem. Soc. Rev.*, 2015, **44**, 4501–4516.

51. J. Estelrich, M. J. Sánchez-Martín and M. A. Busquets, *International Journal of Nanomedicine*, 2015, **10**, 1727–1741.

52. G.-L. Davies, I. Kramberger and J. J. Davis, *Chemical Communications*, 2013, **49**, 9704.

53. A. N. Oksendal and P.-A. Hals, *Journal of Magnetic Resonance Imaging*, 1993, **3**, 157–165.

54. P. Caravan, *Strategies for increasing the sensitivity of gadolinium based MRI contrast agents*, 2006.

55. P. Caravan, J. J. Ellison, T. J. McMurry and R. B. Lauffer, *Chemical Reviews*, 1999, **99**, 2293–2352.

56. E. J. Werner, A. Datta, C. J. Jocher and K. N. Raymond, *Angewandte Chemie International Edition*, 2008, **47**, 8568–8580.

57. J. Kurtkoti, T. Snow and B. Hiremagalur, *Gadolinium and nephrogenic systemic fibrosis: Association or causation*, 2008.

58. A. Kribben, O. Witzke, U. Hillen, J. Barkhausen, A. E. Daul and R. Erbel, *Journal of the American College of Cardiology*, 2009, **53**, 1621–1628.

59. M. A. Perazella, *Clinical Journal of the American Society of Nephrology*, 2007, **2**, 200–202.

60. A. Myrissa, S. Braeuer, E. Martinelli, R. Willumeit-Römer, W. Goessler and A. M. Weinberg, *Acta Biomaterialia*, 2017, **48**, 521–529.

61. R. J. McDonald, J. S. McDonald, D. F. Kallmes, M. E. Jentoft, D. L. Murray, K. R. Thielen, E. E. Williamson and L. J. Eckel, *Radiology*, 2015, **275**, 772–782.

62. M. Rogosnitzky and S. Branch, *BioMetals*, 2016, **29**, 365–376.

63. R. Jin, B. Lin, D. Li and H. Ai, *Current Opinion in Pharmacology*, 2014, **18**, 18–27.

64. Q. A. Pankhurst, N. T. K. Thanh, S. K. Jones and J. Dobson, *Journal of Physics D: Applied Physics*, 2009, **42**, 224001.

65. R. A. Brooks, F. Moiny and P. Gillis, *Magnetic Resonance in Medicine*, 2001, **45**, 1014–1020.

66. R. A. Brooks, F. Moiny and P. Gillis, *Magnetic Resonance in Medicine*, 2002, **47**, 257–263.

67. Y. W. Jun, Y. M. Huh, J. S. Choi, J. H. Lee, H. T. Song, S. Kim, S. Yoon, K. S. Kim, J. S. Shin, J. S. Suh and J. Cheon, *Journal of the American Chemical Society*, 2005, **127**, 5732–5733.

68. H. B. Na, I. C. Song and T. Hyeon, *Advanced Materials*, 2009, **21**, 2133–2148.

69. S. Laurent, D. Forge, M. Port, A. Roch, C. Robic, L. Vander Elst and R. N. Muller, *Chemical Reviews*, 2008, **108**, 2064–2110.

70. J. S. Ananta, B. Godin, R. Sethi, L. Moriggi, X. Liu, R. E. Serda, R. Krishnamurthy, R. Muthupillai, R. D. Bolskar, L. Helm, M. Ferrari, L. J. Wilson and P. Decuzzi, *Nature Nanotechnology*, 2010, **5**, 815–821.

71. S. A. Corr, Y. K. Gun'ko, R. Tekoriute, C. J. Meledandri and D. F. Brougham, *Journal of Physical Chemistry C*, 2008, **112**, 13324–13327.

72. C. J. Meledandri and D. F. Brougham, *Low field magnetic resonance techniques in the development of nanomaterials for biomedical applications*, 2012.

73. A. Ouakssim, A. Roch, C. Pierart and R. N. Muller, *Journal of Magnetism and Magnetic Materials*, 2002, **252**, 49–52.

74. A. Roch, R. N. Muller and P. Gillis, *The Journal of Chemical Physics*, 1999, **110**, 5403–5411.

75. D. Forge, A. Roch, S. Laurent, H. Tellez, Y. Gossuin, F. Renaux, L. V. Elst and R. N. Muller, *Journal of Physical Chemistry C*, 2008, **112**, 19178–19185.

76. P. Mathieu, Y. Coppel, M. Respaud, Q. T. Nguyen, S. Boutry, S. Laurent, D. Stanicki, C. Henoumont, F. Novio, J. Lorenzo, D. Montpeyó and C. Amiens, *Molecules*, 2019, **24**, 4629.

77. C. J. Meledandri, J. K. Stolarczyk, S. Ghosh and D. F. Brougham, *Langmuir*, 2008, **24**, 14159–14165.

78. E. Taboada, E. Rodríguez, A. Roig, J. Oró, A. Roch and R. N. Muller, *Langmuir*, 2007, **23**, 4583–4588.

79. Q. L. Vuong, P. Gillis, A. Roch and Y. Gossuin, *Wiley Interdisciplinary Reviews: Nanomedicine and Nanobiotechnology*, 2017, **9**, 1–22.

80. A. Roch, Y. Gossuin, R. N. Muller and P. Gillis, *Journal of Magnetism and Magnetic Materials*, 2005, **293**, 532–539.

81. O. B. Miguel, Y. Gossuin, M. Morales, P. Gillis, R. Muller and S. Veintemillas-Verdaguer, *Magnetic Resonance Imaging*, 2007, **25**, 1437–1441.

82. G.-L. Davies, S. A. Corr, C. J. Meledandri, L. Briode, D. F. Brougham and Y. K. Gun'ko, *ChemPhysChem*, 2011, **12**, 772–776.

83. S. J. Byrne, S. A. Corr, Y. K. Gun'ko, J. M. Kelly, D. F. Brougham and S. Ghosh, *Chemical Communications*, 2004, **10**, 2560–2561.

84. S. Ghosh, D. Carty, S. P. Clarke, S. A. Corr, R. Tekoriute, Y. K. Gun'Ko and D. F. Brougham, *Physical Chemistry Chemical Physics*, 2010, **12**, 14009–14016.

85. M. Lévy, F. Gazeau, C. Wilhelm, S. Neveu, M. Devaud and P. Levitz, *The Journal of Physical Chemistry C*, 2013, **117**, 15369–15374.

86. L. Lartigue, P. Hugounenq, D. Alloyeau, S. P. Clarke, M. Lévy, J.-C. Bacri, R. Bazzi, D. F. Brougham, C. Wilhelm and F. Gazeau, *ACS Nano*, 2012, **6**, 10935–10949.

87. M. A. Espy, A. N. Matlachov, P. L. Volegov, J. C. Mosher and R. H. Kraus, IEEE Transactions on Applied Superconductivity, 2005, pp. 635–639.

88. M. Espy, A. Matlashov and P. Volegov, *Journal of Magnetic Resonance*, 2013, **229**, 127–141.

89. R. Kodama, *Journal of Magnetism and Magnetic Materials*, 1999, **200**, 359–372.

90. R. H. Kodama, A. E. Berkowitz, E. J. McNiff, Jr. and S. Foner, *Physical Review Letters*, 1996, **77**, 394–397.

91. S. Kubickova, D. Niznansky, M. P. Morales Herrero, G. Salas and J. Vejpravova, *Applied Physics Letters*, 2014, **104**, 223105.

92. B. Martínez, X. Obradors, L. Balcells, A. Rouanet and C. Monty, *Physical Review Letters*, 1998, **80**, 181–184.

93. N. Moumen and M. P. Pileni, *The Journal of Physical Chemistry*, 1996, **100**, 1867–1873.

94. V. K. LaMer and R. H. Dinegar, *Journal of the American Chemical Society*, 1950, **72**, 4847–4854.

95. R. Massart, *IEEE Transactions on Magnetics*, 1981, **17**, 1247–1248.

96. L. Vayssières, C. Chanéac, E. Tronc and J. P. Jolivet, *Journal of Colloid and Interface Science*, 1998, **205**, 205–212.

97. J. Santoyo Salazar, L. Perez, O. De Abril, L. Truong Phuoc, D. Ihiawakrim, M. Vazquez, J. M. Greneche, S. Begin-Colin and G. Pourroy, *Chemistry of Materials*, 2011, **23**, 1379–1386.

98. L. Ternent, D. A. Mayoh, M. R. Lees and G.-L. Davies, *Journal of Materials Chemistry B*, 2016, **4**, 3065–3074.

99. Y. Piao, J. Kim, H. B. Na, D. Kim, J. S. Baek, M. K. Ko, J. H. Lee, M. Shokouhimehr and T. Hyeon, *Nature Materials*, 2008, **7**, 242–247.

100. A. F. Rebolledo, O. Bomatí-Miguel, J. F. Marco and P. Tartaj, *Advanced Materials*, 2008, **20**, 1760–1765.

101. T. Hyeon, S. S. Lee, J. Park, Y. Chung and H. B. Na, *Journal of the American Chemical Society*, 2001, **123**, 12798–12801.

102. S. Sun and H. Zeng, *Journal of the American Chemical Society*, 2002, **124**, 8204–8205.

103. G. Gao, R. Shi, W. Qin, Y. Shi, G. Xu, G. Qiu and X. Liu, *Journal of Materials Science*, 2010, **45**, 3483–3489.

104. X. Sun, C. Zheng, F. Zhang, Y. Yang, G. Wu, A. Yu and N. Guan, *Journal of Physical Chemistry C*, 2009, **113**, 16002–16008.

105. J. Wan, W. Cai, X. Meng and E. Liu, *Chemical Communications*, 2007, **0**, 5004.

106. C. Cheng, F. Xu and H. Gu, *New Journal of Chemistry*, 2011, **35**, 1072.

107. M. Sanchez-Dominguez, K. Pemartin and M. Boutonnet, *Current Opinion in Colloid & Interface Science*, 2012, **17**, 297–305.

108. J. Wang, Z. H. Shah, S. Zhang and R. Lu, *Nanoscale*, 2014, **6**, 4418–4437.

109. M. Darbandi, F. Stromberg, J. Landers, N. Reckers, B. Sanyal, W. Keune and H. Wende, *J. Phys. D. Appl. Phys.*, 2012, **45**, 195001.

110. C. Okoli, M. Sanchez-Dominguez, M. Boutonnet, S. Järås, C. Civera, C. Solans and G. R. Kuttuva, *Langmuir*, 2012, **28**, 8479–8485.

111. O. Lemine, K. Omri, B. Zhang, L. El Mir, M. Sajieddine, A. Alyamani and M. Bououdina, *Superlattices and Microstructures*, 2012, **52**, 793–799.

112. J.-H. Lee, Y.-M. Huh, Y.-w. Jun, J.-w. Seo, J.-t. Jang, H.-T. Song, S. Kim, E.-J. Cho, H.-G. Yoon, J.-S. Suh and J. Cheon, *Nature Medicine*, 2007, **13**, 95–99.

113. H. Yang, C. Zhang, X. Shi, H. Hu, X. Du, Y. Fang, Y. Ma, H. Wu and S. Yang, *Biomaterials*, 2010, **31**, 3667–3673.

114. A. Ereath Beeran, S. S. Nazeer, F. B. Fernandez, K. S. Muvvala, W. Wunderlich, S. Anil, S. Vellappally, M. S. Ramachandra Rao, A. John, R. S. Jayasree and P. R. Harikrishna Varma, *Physical Chemistry Chemical Physics*, 2015, **17**, 4609–4619.

115. L. Yang, L. Ma, J. Xin, A. Li, C. Sun, R. Wei, B. W. Ren, Z. Chen, H. Lin and J. Gao, *Chemistry of Materials*, 2017, **29**, 3038–3047.

116. L. O. Simonsen, H. Harbak and P. Bennekou, *Science of the Total Environment*, 2012, **432**, 210–215.

117. H. M. Joshi, Y. P. Lin, M. Aslam, P. V. Prasad, E. A. Schultz-Sikma, R. Edelman, T. Meade and V. P. Dravid, *Journal of Physical Chemistry C*, 2009, **113**, 17761–17767.

118. M. C. Franchini, G. Baldi, D. Bonacchi, D. Gentili, G. Giudetti, A. Lascialfari, M. Corti, P. Marmorato, J. Ponti, E. Micotti, U. Guerrini, L. Sironi, P. Gelosa, C. Ravagli and A. Ricci, *Small*, 2010, **6**, 366–370.

119. A. Sathya, P. Guardia, R. Brescia, N. Silvestri, G. Pugliese, S. Nitti, L. Manna and T. Pellegrino, *Chemistry of Materials*, 2016, **28**, 1769–1780.

120. H. Yang, T. Ogawa, D. Hasegawa and M. Takahashi, *Journal of Applied Physics*, 2008, **103**, 07D526.

121. M. Nidhin, S. S. Nazeer, R. S. Jayasree, M. S. Kiran, B. U. Nair and K. J. Sreeram, *RSC Advances*, 2013, **3**, 6906.

122. P. P. Wyss, S. Lamichhane, M. Rauber, R. Thomann, K. W. Krämer and V. P. Shastri, *Nanomedicine*, 2016, **11**, 1017–1030.

123. Z. Zhou, Z. Zhao, H. Zhang, Z. Wang, X. Chen, R. Wang, Z. Chen and J. Gao, *ACS Nano*, 2014, **8**, 7976–7985.

124. Z. Zhao, Z. Zhou, J. Bao, Z. Wang, J. Hu, X. Chi, K. Ni, R. Wang, X. Chen, Z. Chen and J. Gao, *Nature Communications*, 2013, **4**, 2266.

125. Z. Zhou, X. Zhu, D. Wu, Q. Chen, D. Huang, C. Sun, J. Xin, K. Ni and J. Gao, *Chemistry of Materials*, 2015, **27**, 3505–3515.

126. O. Veiseh, J. W. Gunn and M. Zhang, *Advanced Drug Delivery Reviews*, 2010, **62**, 284–304.

127. A. Ruiz, Y. Hernández, C. Cabal, E. González, S. Veintemillas-Verdaguer, E. Martínez and M. P. Morales, *Nanoscale*, 2013, **5**, 11400.

128. G. Storm, S. O. Belliot, T. Daemen and D. D. Lasic, *Advanced Drug Delivery Reviews*, 1995, **17**, 31–48.

129. M. Yu, S. Huang, K. J. Yu and A. M. Clyne, *International Journal of Molecular Sciences 2012, Vol. 13, Pages 5554-5570*, 2012, **13**, 5554–5570.

130. Z. Wang, R. Qiao, N. Tang, Z. Lu, H. Wang, Z. Zhang, X. Xue, Z. Huang, S. Zhang, G. Zhang and Y. Li, *Biomaterials*, 2017, **127**, 25–35.

131. K. Hayashi, K. Ono, H. Suzuki, M. Sawada, M. Moriya, W. Sakamoto and T. Yogo, *ACS Applied Materials and Interfaces*, 2010, **2**, 1903–1911.

132. M. K. Yu, D. Kim, I. H. Lee, J. S. So, Y. Y. Jeong and S. Jon, *Small*, 2011, **7**, 2241–2249.

133. S. I. Jenkins, M. R. Pickard, N. Granger and D. M. Chari, *ACS Nano*, 2011, **5**, 6527–6538.

134. H. Li, K. Yan, Y. Shang, L. Shrestha, R. Liao, F. Liu, P. Li, H. Xu, Z. Xu and P. K. Chu, *Acta Biomaterialia*, 2015, **15**, 117–126.

135. C. L. Yang, J. P. Chen, K. C. Wei, J. Y. Chen, C. W. Huang and Z. X. Liao, *Nanomaterials*, 2017, **7**, 85.

136. S. Santra, C. Kaittanis, J. Grimm and J. M. Perez, *Small*, 2009, **5**, 1862–1868.

137. K. Mandal, D. Jana, B. K. Ghorai and N. R. Jana, *ACS Applied Nano Materials*, 2019, **2**, 3292–3299.

138. J. Liu, Z. Sun, Y. Deng, Y. Zou, C. Li, X. Guo, L. Xiong, Y. Gao, F. Li and D. Zhao, *Angewandte Chemie International Edition*, 2009, **48**, 5875–5879.

139. A. Villanueva, M. Cañete, A. G. Roca, M. Calero, S. Veintemillas-Verdaguer, C. J. Serna, M. del Puerto Morales and R. Miranda, *Nanotechnology*, 2009, **20**, 115103.

140. A. G. Roca, R. Costo, A. F. Rebolledo, S. Veintemillas-Verdaguer, P. Tartaj, T. González-Carreño, M. P. Morales and C. J. Serna, *Journal of Physics D: Applied Physics*, 2009, **42**, 224002.

141. L. H. Reddy, J. L. Arias, J. Nicolas and P. Couvreur, *Chemical Reviews*, 2012, **112**, 5818–5878.

142. C. Sun, K. Du, C. Fang, N. Bhattarai, O. Veiseh, F. Kievit, Z. Stephen, D. Lee, R. G. Ellenbogen, B. Ratner and M. Zhang, *ACS Nano*, 2010, **4**, 2402–2410.

143. T. Y. Liu, S. H. Hu, K. H. Liu, D. M. Liu and S. Y. Chen, *Journal of Controlled Release*, 2008, **126**, 228–236.

144. Z. R. Stephen, F. M. Kievit and M. Zhang, *Materials Today*, 2011, **14**, 330–338.

145. S. Tong, S. Hou, Z. Zheng, J. Zhou and G. Bao, *Nano Letters*, 2010, **10**, 4607–4613.

146. A. S. Karakoti, S. Das, S. Thevuthasan and S. Seal, *Angewandte Chemie International Edition*, 2011, **50**, 1980–1994.

147. M. Pernia Leal, S. Rivera-Fernández, J. M. Franco, D. Pozo, J. M. de la Fuente and M. L. García-Martín, *Nanoscale*, 2015, **7**, 2050–2059.

148. J. F. Lutz, S. Stiller, A. Hoth, L. Kaufner, U. Pison and R. Cartier, *Biomacromolecules*, 2006, **7**, 3132–3138.

149. E. K. Larsen, T. Nielsen, T. Wittenborn, H. Birkedal, T. Vorup-Jensen, M. H. Jakobsen, L. Ostergaard, M. R. Horsman, F. Besenbacher, K. A. Howard and J. Kjems, *ACS Nano*, 2009, **3**, 1947–1951.

150. A. K. Gupta, R. R. Naregalkar, V. D. Vaidya and M. Gupta, *Recent advances on surface engineering of magnetic iron oxide nanoparticles and their biomedical applications*, 2007.

151. K. L. Ang, S. Venkatraman and R. V. Ramanujan, *Materials Science and Engineering C*, 2007, **27**, 347–351.

152. K. G. Paul, T. B. Frigo, J. Y. Groman and E. V. Groman, *Bioconjugate Chemistry*, 2004, **15**, 394–401.

153. D. Bonvin, J. A. M. Bastiaansen, M. Stuber, H. Hofmann and M. Mionić Ebersold, *Dalton Trans.*, 2017, **46**, 12692–12704.

154. T. J. Chen, T. H. Cheng, C. Y. Chen, S. C. N. Hsu, T. L. Cheng, G. C. Liu and Y. M. Wang, *Journal of Biological Inorganic Chemistry*, 2009, **14**, 253–260.

155. O. L. Gobbo, K. Sjaastad, M. W. Radomski, Y. Volkov and A. Prina-Mello, *Magnetic nanoparticles in cancer theranostics*, 2015.

156. N. Lee, D. Yoo, D. Ling, M. H. Cho, T. Hyeon and J. Cheon, *Chemical Reviews*, 2015, **115**, 10637–10689.

157. T. J. Daou, J. M. Grenèche, G. Pourroy, S. Buathong, A. Derory, C. Ulhaq-Bouillet, B. Donnio, D. Guillon and S. Begin-Colin, *Chemistry of Materials*, 2008, **20**, 5869–5875.

158. B. Basly, D. Felder-Flesch, P. Perriat, C. Billotey, J. Taleb, G. Pourroy and S. Begin-Colin, *Chem. Commun.*, 2010, **46**, 985–987.

159. C. Boyer, V. Bulmus, P. Priyanto, W. Y. Teoh, R. Amal and T. P. Davis, *J. Mater. Chem.*, 2009, **19**, 111–123.

160. B. Basly, G. Popa, S. Fleutot, B. P. Pichon, A. Garofalo, C. Ghobril, C. Billotey, A. Berniard, P. Bonazza, H. Martinez, D. Felder-Flesch and S. Begin-Colin, *Dalton Trans.*, 2013, **42**, 2146–2157.

161. H. Duan, M. Kuang, X. Wang, Y. A. Wang, H. Mao and S. Nie, *Journal of Physical Chemistry C*, 2008, **112**, 8127–8131.

162. A. L. Morel, S. I. Nikitenko, K. Gionnet, A. Wattiaux, J. Lai-Kee-Him, C. Labrugere, B. Chevalier, G. Deleris, C. Petibois, A. Brisson and M. Simonoff, *ACS Nano*, 2008, **2**, 847–856.

163. H. L. Ding, Y. X. Zhang, S. Wang, J. M. Xu, S. C. Xu and G. H. Li, *Chemistry of Materials*, 2012, **24**, 4572–4580.

164. Y. Lu, Y. Yin, B. T. Mayers and Y. Xia, *Nano Letters*, 2002, **2**, 183–186.

165. L. Zhang, W. F. Dong and H. B. Sun, *Multifunctional superparamagnetic iron oxide nanoparticles: Design, synthesis and biomedical photonic applications*, 2013.

166. B. Shen, Y. Ma, S. Yu and C. Ji, *ACS Applied Materials and Interfaces*, 2016, **8**, 24502–24508.

167. A. Kertmen, P. Torruella, E. Coy, L. Yate, G. Nowaczyk, J. Gapiński, C. Vogt, M. Toprak, S. Estradé, F. Peiró, S. Milewski, S. Jurga and R. Andruszkiewicz, *Langmuir*, 2017, **33**, 10351–10365.

168. Y. A. Barnakov, M. H. Yu and Z. Rosenzweig, *Langmuir*, 2005, **21**, 7524–7527.

169. D. K. Yi, S. T. Selvan, S. S. Lee, G. C. Papaefthymiou, D. Kundaliya and J. Y. Ying, *Journal of the American Chemical Society*, 2005, **127**, 4990–4991.

170. M. Chen, S. Yamamuro, D. Farrell and S. A. Majetich, Journal of Applied Physics, 2003, pp. 7551–7553.

171. Y. Okada, T. Y. Takano, N. Kobayashi, A. Hayashi, M. Yonekura, Y. Nishiyama, T. Abe, T. Yoshida, T. A. Yamamoto, S. Seino and T. Doi, *Bioconjugate Chemistry*, 2011, **22**, 887–893.

172. Y. Lu, C. Shi, M. J. Hu, Y. J. Xu, L. Yu, L. P. Wen, Y. Zhao, W. P. Xu and S. H. Yu, Advanced Functional Materials, 2010, pp. 3701–3706.

173. H. Yu, M. Chen, P. M. Rice, S. X. Wang, R. L. White and S. Sun, *Nano Letters*, 2005, **5**, 379–382.

174. X. Zhao, Y. Cai, T. Wang, Y. Shi and G. Jiang, *Analytical Chemistry*, 2008, **80**, 9091–9096.

175. F. Frederix, K. Bonroy, W. Laureyn, G. Reekmans, A. Campitelli, W. Dehaen and G. Maes, *Langmuir*, 2003, **19**, 4351–4357.

176. J. Li, Y. Hu, J. Yang, P. Wei, W. Sun, M. Shen, G. Zhang and X. Shi, *Biomaterials*, 2015, **38**, 10–21.

177. F. Fabris, E. Lima, E. De Biasi, H. E. Troiani, M. Vásquez Mansilla, T. E. Torres, R. Fernández Pacheco, M. R. Ibarra, G. F. Goya, R. D. Zysler and E. L. Winkler, *Nanoscale*, 2019, **11**, 3164–3172.

178. M. S. Angotzi, A. Musinu, V. Mameli, A. Ardu, C. Cara, D. Niznansky, H. L. Xin and C. Cannas, *ACS Nano*, 2017, **11**, 7889–7900.

179. A. López-Ortega, M. Estrader, G. Salazar-Alvarez, A. G. Roca and J. Nogués, *Physics Reports*, 2015, **553**, 1–32.

180. M. Sanna Angotzi, V. Mameli, C. Cara, A. Musinu, C. Sangregorio, D. Niznansky, H. L. Xin, J. Vejpravova and C. Cannas, *Nanoscale Advances*, 2020, **2**, 3191–3201.

181. M. Angotzi, Valentina Mameli, Claudio Cara, Davide Peddis, H. L. Xin, Claudio Sangregorio, M. Laura Mercuri and Carla Cannas, *Nanoscale Advances*, 2021, **3**, 1612–1623.

182. J. H. Lee, J. T. Jang, J. S. Choi, S. H. Moon, S. H. Noh, J. W. Kim, J. G. Kim, I. S. Kim, K. I. Park and J. Cheon, *Nature Nanotechnology*, 2011, **6**, 418–422.

183. K. Vamvakidis, S. Mourdikoudis, A. Makridis, E. Paulidou, M. Angelakeris and C. Dendrinou-Samara, *Journal of Colloid and Interface Science*, 2018, **511**, 101–109.

184. H. Zeng, J. Li, Z. L. Wang, J. P. Liu and S. Sun, *Nano Letters*, 2004, **4**, 187–190.

185. J. Li, H. Zeng, S. Sun, J. P. Liu and Z. L. Wang, *Journal of Physical Chemistry B*, 2004, **108**, 14005–14008.

186. O. Masala and R. Seshadri, *Journal of the American Chemical Society*, 2005, **127**, 9354–9355.

187. S. G. Kwon and T. Hyeon, *Small*, 2011, **7**, 2685–2702.

188. F. A. Cardona, E. S. Urquiza, P. De La Presa, S. H. Tobón, U. Pal, P. H. Fraijo, M. J. Yacaman, J. D. L. Ramírez, R. Ivkov, A. Angulo-Molina and M. Á. Méndez-Rojas, *RSC Advances*, 2016, **6**, 77558–77568.

189. F. Arteaga-Cardona, E. Santillán-Urquiza, U. Pal, M. E. Méndoza-Álvarez, C. Torres-Duarte, G. N. Cherr, P. de la Presa and M. Méndez-Rojas, *Journal of Magnetism and Magnetic Materials*, 2017, **441**, 417–423.

190. J. D. A. Gomes, M. H. Sousa, F. A. Tourinho, R. Aquino, G. J. Da Silva, J. Depeyrot, E. Dubois and R. Perzynski, *Journal of Physical Chemistry C*, 2008, **112**, 6220–6227.

191. T. J. Yoon, H. Lee, H. Shao and R. Weissleder, *Angewandte Chemie - International Edition*, 2011, **50**, 4663–4666.

192. H.-M. Song, J. I. Zink and N. M. Khashab, *Physical Chemistry Chemical Physics*, 2015, **17**, 18825–18833.

193. M. Chastellain, A. Petri, A. Gupta, K. V. Rao and H. Hofmann, *Advanced Engineering Materials*, 2004, **6**, 235–241.

194. C. C. Huang, C. Y. Tsai, H. S. Sheu, K. Y. Chuang, C. H. Su, U. S. Jeng, F. Y. Cheng, C. H. Su, H. Y. Lei and C. S. Yeh, *ACS Nano*, 2011, **5**, 3905–3916.

195. H. Yang, Y. Zhuang, Y. Sun, A. Dai, X. Shi Xiangyang, D. Wu, F. Li, H. Hu and S. Yang, *Biomaterials*, 2011, **32**, 4584–4593.

196. L. Gutiérrez, L. de la Cueva, M. Moros, E. Mazarío, S. de Bernardo, J. M. de la Fuente, M. P. Morales and G. Salas, *Nanotechnology*, 2019, **30**, 112001.

197. Y. Javed, L. Lartigue, P. Hugounenq, Q. L. Vuong, Y. Gossuin, R. Bazzi, C. Wilhelm, C. Ricolleau, F. Gazeau and D. Alloyeau, *Small*, 2014, **10**, 3325–3337.

198. D. V. Berkov and N. L. Gorn, *Journal of Physics Condensed Matter*, 2001, **13**, 9369–9381.

199. S. Mørup, M. F. Hansen and C. Frandsen, *Beilstein Journal of Nanotechnology*, 2010, **1**, 182–190.

200. Y. Lalatonne, J. Richardi and M. P. Pileni, *Nature Materials*, 2004, **3**, 121–125.

201. Z. Zhou, R. Tian, Z. Wang, Z. Yang, Y. Liu, G. Liu, R. Wang, J. Gao, J. Song, L. Nie and X. Chen, *Nature Communications*, 2017, **8**, 15468.

202. E. M. Claesson and A. P. Philipse, *Langmuir*, 2005, **21**, 9412–9419.

203. J.-H. Lee, Y.-w. Jun, S.-I. Yeon, J.-S. Shin and J. Cheon, *Angewandte Chemie International Edition*, 2006, **45**, 8160–8162.

204. L. E. Euliss, S. G. Grancharov, S. O'Brien, T. J. Deming, G. D. Stucky, C. B. Murray and G. A. Held, *Nano Letters*, 2003, **3**, 1489–1493.

205. B. S. Kim, J. M. Qiu, J. P. Wang and T. A. Taton, *Nano Letters*, 2005, **5**, 1987–1991.

206. H. Yang, N. Wang, L. Mo, M. Wu, R. Yang, X. Xu, Y. Huang, J. Lin, L. M. Zhang and X. Jiang, *Materials Science and Engineering C*, 2019, **98**, 9–18.

207. X. Yang, Y. Chen, R. Yuan, G. Chen, E. Blanco, J. Gao and X. Shuai, *Polymer*, 2008, **49**, 3477–3485.

208. Y. Zhong, S. Huang, C. Zheng, J. Huang, B. Li, S. Han, H. Xiao, Y. Wang and X. Shuai, *Biomaterials Science*, 2021, **9**, 5218–5226.

209. S. Balasubramaniam, S. Kayandan, Y.-N. Lin, D. F. Kelly, M. J. House, R. C. Woodward, T. G. S. Pierre, J. S. Riffle and R. M. Davis, *Langmuir*, 2014, **30**, 1580–1587.

210. T. D. T. Nguyen, A. Pitchaimani, C. Ferrel, R. Thakkar and S. Aryal, *Nanoscale*, 2018, **10**, 284–294.

211. G. B. Sukhorukov, E. Donath, S. Davis, H. Lichtenfeld, F. Caruso, V. I. Popov and H. Möhwald, *Polymers for Advanced Technologies*, 1998, **9**, 759–767.

212. J. Campbell, J. Abnett, G. Kastania, D. Volodkin and A. S. Vikulina, *ACS Applied Materials & Interfaces*, 2021, **13**, 3259–3269.

213. C. Ribeiro, J. Borges, A. Costa, V. Gaspar, V. Bermudez and J. Mano, *Molecules*, 2018, **23**, 625.

214. R. Kurapati, T. W. Groth and A. M. Raichur, *ACS Applied Bio Materials*, 2019, **2**, 5512–5527.

215. C. E. Stavarache and L. Paniwnyk, *Journal of Drug Delivery Science and Technology*, 2018, **45**, 60–69.

216. W. Tong, C. Gao and H. Möhwald, *Macromolecules*, 2006, **39**, 335–340.

217. B. G. De Geest, R. E. Vandenbroucke, A. M. Guenther, G. B. Sukhorukov, W. E. Hennink, N. N. Sanders, J. Demeester and S. C. De Smedt, *Advanced Materials*, 2006, **18**, 1005–1009.

218. G. Schneider and G. Decher, *Nano Letters*, 2004, **4**, 1833–1839.

219. Q. Wei, H. Ai and Z. Gu, *Colloids and Surfaces B: Biointerfaces*, 2011, **85**, 63–72.

220. C. Schüler and F. Caruso, *Biomacromolecules*, 2001, **2**, 921–926.

221. T. Mauser, C. Déjugnat, H. Möhwald and G. B. Sukhorukov, *Langmuir*, 2006, **22**, 5888–5893.

222. S. De Koker, R. Hoogenboom and B. G. De Geest, *Chemical Society Reviews*, 2012, **41**, 2867–2884.

223. J. E. Read, D. Luo, T. T. Chowdhury, R. J. Flower, R. N. Poston, G. B. Sukhorukov and D. J. Gould, *Nanoscale*, 2020, **12**, 7735–7748.

224. M. Szcz ch, D. Orsi, N. Łopuszyńska, L. Cristofolini, K. Jasiński, W. P. W glarz, F. Albertini, S. Kereïche and K. Szczepanowicz, *RSC Advances*, 2020, **10**, 43607–43618.

225. K. Szczepanowicz, P. Piechota, W. P. Weglarz and P. Warszyński, *Colloids and Surfaces A: Physicochemical and Engineering Aspects*, 2017, **532**, 351–356.

226. M.-L. De Temmerman, S. J. Soenen, N. Symens, B. Lucas, R. E. Vandenbroucke, C. Libert, J. Demeester, S. C. De Smedt, U. Himmelreich, J. Rejman, U. Leuven and C. Gasthuisberg, *Nanomedicine*, 2014, **9**, 1363–1376.

227. S. Carregal-Romero, P. Guardia, X. Yu, R. Hartmann, T. Pellegrino and W. J. Parak, *Nanoscale*, 2015, **7**, 570–576.

228. H. Ai, *Advanced Drug Delivery Reviews*, 2011, **63**, 772–788.

229. R. Singh, D. Pantarotto, L. Lacerda, G. Pastorin, C. Klumpp, M. Prato, A. Bianco and K. Kostarelos, *Proceedings of the National Academy of Sciences of the United States of America*, 2006, **103**, 3357–3362.

230. Z. Liu, W. Cai, L. He, N. Nakayama, K. Chen, X. Sun, X. Chen and H. Dai, *Nature Nanotechnology*, 2007, **2**, 47–52.

231. Y. Geng, P. Dalhaimer, S. Cai, R. Tsai, M. Tewari, T. Minko and D. E. Discher, *Nature Nanotechnology*, 2007, **2**, 249–255.

232. L. A. Bauer, N. S. Birenbaum and G. J. Meyer, *Journal of Materials Chemistry*, 2004, **14**, 517–526.

233. K. Nakata, Y. Hu, O. Uzun, O. Bakr and F. Stellacci, *Advanced Materials*, 2008, **20**, 4294–4299.

234. C. Martinez-Boubeta, K. Simeonidis, A. Makridis, M. Angelakeris, O. Iglesias, P. Guardia, A. Cabot, L. Yedra, S. Estradé, F. Peiró, Z. Saghi, P. A. Midgley, I. Conde-Leborán, D. Serantes and D. Baldomir, *Scientific Reports*, 2013, **3**, 1–8.

235. B. Mehdaoui, R. P. Tan, A. Meffre, J. Carrey, S. Lachaize, B. Chaudret and M. Respaud, *Physical Review B - Condensed Matter and Materials Physics*, 2013, **87**, 174419.

236. N. Guskos, S. Glenis, V. Likodimos, J. Typek, M. Maryniak, Z. Roslaniec, M. Kwiatkowska, M. Baran, R. Szymczak and D. Petridis, *Journal of Applied Physics*, 2006, **99**, 084307.

237. J. Dai, J.-Q. Wang, C. Sangregorio, J. Fang, E. Carpenter and J. Tang, *Journal of Applied Physics*, 2000, **87**, 7397.

238. A. F. Gross, M. R. Diehl, K. C. Beverly, E. K. Richman and S. H. Tolbert, *The Journal of Physical Chemistry B*, 2003, **107**, 5475–5482.

239. L. Yang, Z. Wang, L. Ma, A. Li, J. Xin, R. Wei, H. Lin, R. Wang, Z. Chen and J. Gao, *ACS Nano*, 2018, **12**, 4605–4614.

240. P. M. Peiris, E. Schmidt, M. Calabrese and E. Karathanasis, *PLoS ONE*, 2011, **6**, e15927.

241. Y. Sun, C. Yan, J. Xie, D. Yan, K. Hu, S. Huang, J. Liu, Y. Zhang, N. Gu and F. Xiong, *ACS Applied Materials and Interfaces*, 2019, **11**, 29536–29548.

242. J.-H. H. Park, G. Von Maltzahn, L. Zhang, A. M. Derfus, D. Simberg, T. J. Harris, E. Ruoslahti, S. N. Bhatia and M. J. Sailor, *Small*, 2009, **5**, 694–700.

243. M. Mammen, S. K. Choi and G. M. Whitesides, *Angewandte Chemie - International Edition*, 1998, **37**, 2754–2794.

244. C. E. Smith, J. Lee, Y. Seo, N. Clay, J. Park, A. Shkumatov, D. Ernenwein, M.-H. Lai, S. Misra, C. E. Sing, B. Andrade, S. C. Zimmerman and H. Kong, *ACS Applied Materials & Interfaces*, 2017, **9**, 1219–1225.

245. J. Juárez, A. Cambón, A. Topete, P. Taboada and V. Mosquera, *Chemistry - A European Journal*, 2011, **17**, 7366–7373.

246. H. Wu, G. Liu, Y. Zhuang, D. Wu, H. Zhang, H. Yang, H. Hu and S. Yang, *Biomaterials*, 2011, **32**, 4867–4876.

247. D. Li, Z. Tang, Y. Gao, H. Sun and S. Zhou, *Advanced Functional Materials*, 2016, **26**, 66–79.

248. Fei Xiong, Jilai Tian, Ke Hu, Xiawen Zheng, Jianfei Sun, Caiyun Yan, Juan Yao, Lina Song, Yu Zhang and Ning Gu, *Nanoscale*, 2016, **8**, 17085–17089.

249. J. Yuan, Y. Xu and A. H. Müller, *Chemical Society Reviews*, 2011, **40**, 640–655.

250. S. J. Hurst, E. K. Payne, L. Qin and C. A. Mirkin, *Multisegmented one-dimensional nanorods prepared by hard-template synthetic methods*, 2006.

251. J. E. McCarthy, A. Prina-Mello, T. Rakovich, Y. Volkov and Y. K. Gun'Ko, *Journal of Materials Chemistry*, 2011, **21**, 14219–14225.

252. S. Mann, I. Manners, A. J. Patil, M. A. Winnik, I. Manners, H. Wang, K. Liu and S. Petrov, *Advanced Materials*, 2009, **21**, 1805–1808.

253. S. Nath, C. Kaittanis, V. Ramachandran, N. S. Dalal and J. M. Perez, *Chemistry of Materials*, 2009, **21**, 1761–1767.

254. W. Wu, X. Xiao, S. Zhang, J. Zhou, L. Fan, F. Ren and C. Jiang, *Journal of Physical Chemistry C*, 2010, **114**, 16092–16103.

255. I. Milosevic, H. Jouni, C. David, F. Warmont, D. Bonnin and L. Motte, *Journal of Physical Chemistry C*, 2011, **115**, 18999–19004.

256. J. Mohapatra, A. Mitra, H. Tyagi, D. Bahadur and M. Aslam, *Nanoscale*, 2015, **7**, 9174–9184.

257. X. Zhu, J. Fan, Y. Zhang, H. Zhu, B. Dai, M. Yan and Y. Ren, *Journal of Materials Science*, 2017, **52**, year.

258. G. A. DeVries, M. Brunnbauer, Y. Hu, A. M. Jackson, B. Long, B. T. Neltner, O. Uzun, B. H. Wunsch and F. Stellacci, *Science*, 2007, **315**, 358–361.

259. H. Y. Lee, S. H. R. Shin, A. M. Drews, A. M. Chirsan, S. A. Lewis and K. J. Bishop, *ACS Nano*, 2014, **8**, 9979–9987.

260. Q. Liu, S. Shen, Z. Zhou and L. Tian, *Materials Letters*, 2009, **63**, 2625–2627.

261. M. Klokkenburg, C. Vonk, E. M. Claesson, J. D. Meeldijk, B. H. Erné and A. P. Philipse, *Journal of the American Chemical Society*, 2004, **126**, 16706–16707.

262. Q. He, T. Yuan, X. Yan, Z. Luo, N. Haldolaarachchige, D. P. Young, S. Wei and Z. Guo, *Chemical Communications*, 2014, **50**, 201–203.

263. R. Sheparovych, Y. Sahoo, M. Motornov, S. Wang, H. Luo, P. N. Prasad, I. Sokolov and S. Minko, *Chemistry of Materials*, 2006, **18**, 591–593.

264. J. Fresnais, J. F. Berret, B. Frka-Petesic, O. Sandre and R. Perzynski, *Advanced Materials*, 2008, **20**, 3877–3881.

265. F. Hu, Q. Jia, Y. Li and M. Gao, *Nanotechnology*, 2011, **22**, 245604.

266. S. Kralj and D. Makovec, *ACS Nano*, 2015, **9**, 9700–9707.

267. M. Tadic, S. Kralj, Y. Lalatonne and L. Motte, *Applied Surface Science*, 2019, **476**, 641–646.

268. M. Tadic, S. Kralj and L. Kopanja, *Materials Characterization*, 2019, **148**, 123–133.

269. Y. Gossuin, S. Disch, Q. L. Vuong, P. Gillis, R. P. Hermann, J.-H. Park and M. J. Sailor, *Contrast Media & Molecular Imaging*, 2010, **5**, 318–322.

270. S. A. Corr, S. J. Byrne, R. Tekoriute, C. J. Meledandri, D. F. Brougham, M. Lynch, C. Kerskens, L. O'Dwyer and Y. K. Gun'ko, *Journal of the American Chemical Society*, 2008, **130**, 4214–4215.

271. C. Bray, R. Peltier, H. Kim, A. Mastrangelo and S. Perrier, *Polymer Chemistry*, 2017, **8**, 5513–5524.

272. *JMP® Version 15.0.0*, 2021.

273. C. A. Schneider, W. S. Rasband and K. W. Eliceiri, *NIH Image to ImageJ: 25 years of image analysis*, 2012.

274. G. David and J. Pérez, *Journal of Applied Crystallography*, 2009, **42**, 892–900.

275. F. Zhang, J. Ilavsky, G. G. Long, J. P. Quintana, A. J. Allen and P. R. Jemian, Metallurgical and Materials Transactions A: Physical Metallurgy and Materials Science, 2010, pp. 1151–1158.

276. M. Doucet, J. H. Cho, A. Gervaise, J. Bakker, W. Bouwman, P. Butler and A. Washington, *SasView version 4.1.2*, 2017.

277. J. Teixeira, *Journal of Applied Crystallography*, 1988, **21**, 781–785.

278. K. Lagarec and D. G. Rancourt, *Recoil-Mössbauer spectral analysis software for Windows*, 1998.

279. J. Fock, L. K. Bogart, D. González-Alonso, J. I. Espeso, M. F. Hansen, M. Varón, C. Frandsen and Q. A. Pankhurst, *Journal of Physics D: Applied Physics*, 2017, **50**, 265005.

280. P. Gurnani, C. P. Bray, R. A. E. Richardson, R. Peltier and S. Perrier, *Macromolecular Rapid Communications*, 2019, **40**, 1800314.

281. M. Doi and S. F. Edwards, *Journal of the Chemical Society, Faraday Transactions 2: Molecular and Chemical Physics*, 1978, **74**, 1789–1801.

282. A. Van Veluwen, H. N. W. Lekkerkerker, C. G. De Kruif and A. Vrij, *Faraday Discussions of the Chemical Society*, 1987, **83**, 59–67.

283. M. Baalousha, *Science of The Total Environment*, 2009, **407**, 2093–2101.

284. N. Maximova and O. Dahl, *Environmental implications of aggregation phenomena: Current understanding*, 2006.

285. M. I. Dar and S. A. Shivashankar, *RSC Adv.*, 2014, **4**, 4105–4113.

286. A. M. Jubb and H. C. Allen, *ACS Applied Materials & Interfaces*, 2010, **2**, 2804–2812.

287. D. Cao, H. Li, L. Pan, J. Li, X. Wang, P. Jing, X. Cheng, W. Wang, J. Wang and Q. Liu, *Scientific Reports*, 2016, **6**, 32360.

288. J. Y. Park, P. Daksha, G. H. Lee, S. Woo and Y. Chang, *Nanotechnology*, 2008, **19**, 365603.

289. T. Kawaguchi, A. Yoshino, M. Hasegawa, T. Hanaichi, S. Maruno and N. Adachi, *Journal of Materials Science: Materials in Medicine*, 2002, **13**, 113–117.

290. J. Fock, L. K. Bogart, O. Posth, M. F. Hansen, Q. A. Pankhurst and C. Frandsen, *Hyperfine Interactions*, 2016, **237**, 1–11.

291. W. Szczerba, R. Costo, S. Veintemillas-Verdaguer, M. d. P. Morales and A. F. Thünemann, *Journal of Applied Crystallography*, 2017, **50**, 481–488.

292. A. Boni, A. M. Basini, L. Capolupo, C. Innocenti, M. Corti, M. Cobianchi, F. Orsini, A. Guerrini, C. Sangregorio and A. Lascialfari, *RSC Advances*, 2017, **7**, 44104–44111.

293. D. Sarkar and P. Somasundaran, *Langmuir*, 2004, **20**, 4657–4664.

294. E. P. Currie, W. Norde and M. A. Cohen Stuart, *Advances in Colloid and Interface Science*, 2003, **100-102**, 205–265.

295. R. Mangal, S. Srivastava and L. A. Archer, *Nature Communications*, 2015, **6**, 7198.

296. A. Tuteja, P. M. Duxbury and M. E. Mackay, *Macromolecules*, 2007, **40**, 9427–9434.

297. L. E. Wilkins, D. J. Phillips, R. C. Deller, G.-L. Davies and M. I. Gibson, *Carbohydrate Research*, 2015, **405**, 47–54.

298. T. Liu, R. Bai, H. Zhou, R. Wang, J. Liu, Y. Zhao and C. Chen, *RSC Advances*, 2020, **10**, 7559–7569.

299. L. Q. Chen, L. Fang, J. Ling, C. Z. Ding, B. Kang and C. Z. Huang, *Chemical Research in Toxicology*, 2015, **28**, 501–509.

300. Q. Ran, Y. Xiang, Y. Liu, L. Xiang, F. Li, X. Deng, Y. Xiao, L. Chen, L. Chen and Z. Li, *Scientific Reports*, 2015, **5**, 1–15.

301. Q. Feng, Y. Liu, J. Huang, K. Chen, J. Huang and K. Xiao, *Scientific Reports*, 2018, **8**, 1–13.

302. I. Gounko, G.-L. Davies and S. Byrne, *Phase Transfer Reactions*, 2013.

303. Z. Zhang, A. J. Rondinone, J. X. Ma, J. Shen and S. Dai, *Advanced Materials*, 2005, **17**, 1415–1419.

304. B. Babić-Stojić, V. Jokanović, D. Milivojević, Z. Jagličić, D. Makovec, N. Jović and M. Marinović-Cincović, *Journal of Nanomaterials*, 2013, **2013**, 1–9.

305. K. M. Krishnan, A. B. Pakhomov, Y. Bao, P. Blomqvist, Y. Chun, M. Gonzales, K. Griffin, X. Ji and B. K. Roberts, *Journal of Materials Science 2006 41:3*, 2006, **41**, 793–815.

306. S. Singamaneni, V. N. Bliznyuk, C. Binek and E. Y. Tsymbal, *Journal of Materials Chemistry*, 2011, **21**, 16819.

307. J. C. Yang, M. J. Jablonsky and J. W. Mays, *Polymer*, 2002, **43**, 5125–5132.

308. S. L. Warring, D. A. Beattie and A. J. McQuillan, *Langmuir*, 2016, **32**, 1568–1576.

309. F. Jiang, Y. Fu, Y. Zhu, Z. Tang and P. Sheng, *Journal of Alloys and Compounds*, 2012, **543**, 43–48.

310. M. Stjerndahl, M. Andersson, H. E. Hall, D. M. Pajerowski, M. W. Meisel and R. S. Duran, *Langmuir*, 2008, **24**, 3532–3536.

311. A. Lapresta-Fernández, T. Doussineau and S. Dutz, *Nanotechnology*, 2008, **19**, 85601.

312. E. M. Furst and A. P. Gast, *Physical Review E*, 2000, **62**, 6916–6925.

313. D. Meeker, *Finite Element Method Magnetics Version 4.2*, 2015.

314. K. Mohan Kant, K. Sethupathi and M. S. Ramachandra Rao, Journal of Applied Physics, 2008, p. 07D501.

315. Y. K. Peng, C. W. Lai, C. L. Liu, H. C. Chen, Y. H. Hsiao, W. L. Liu, K. C. Tang, Y. Chi, J. K. Hsiao, K. E. Lim, H. E. Liao, J. J. Shyue and P. T. Chou, *ACS Nano*, 2011, **5**, 4177–4187.

316. M. Jeon, M. V. Halbert, Z. R. Stephen and M. Zhang, *Iron Oxide Nanoparticles as T1 Contrast Agents for Magnetic Resonance Imaging: Fundamentals, Challenges, Applications, and Prospectives*, 2021.

317. J. H. Park, G. Von Maltzahn, L. Zhang, M. P. Schwartz, E. Ruoslahti, S. N. Bhatia and M. J. Sailor, *Advanced Materials*, 2008, **20**, 1630–1635.

318. D. Toulemon, M. V. Rastei, D. Schmool, J. S. Garitaonandia, L. Lezama, X. Cattoën, S. Bégin-Colin and B. P. Pichon, *Advanced Functional Materials*, 2016, **26**, 2454–2462.

319. G. B. Sukhorukov, A. A. Antipov, A. Voigt, E. Donath and H. Mhwald, *Macromolecular Rapid Communications*, 2001, **22**, 44–46.

320. W. Park, J. Chen, S. Cho, S. J. Park, A. C. Larson, K. Na and D. H. Kim, *ACS Applied Materials and Interfaces*, 2016, **8**, 12711–12719.

321. C. Lorenzato, A. Cernicanu, M. E. Meyre, M. Germain, A. Pottier, L. Levy, B. D. de Senneville, C. Bos, C. Moonen and P. Smirnov, *Contrast Media and Molecular Imaging*, 2013, **8**, 185–192.

322. A. Salunkhe, V. Khot, S. I. Patil, S. A. Tofail, J. Bauer and N. D. Thorat, *ACS Applied Bio Materials*, 2020, **3**, 2305–2313.

323. Z. Zhang, C. J. Wells, A. M. King, J. C. Bear, G. L. Davies and G. R. Williams, *Journal of Materials Chemistry B*, 2020, **8**, 7264–7274.

324. Q. Shen, H. Wei, Y. Zhou, Y. Huang, H. Yang, D. Wang and D. Xu, *Journal of Physical Chemistry B*, 2006, **110**, 2994–3000.

325. D. B. Trushina, T. V. Bukreeva and M. N. Antipina, *Crystal Growth and Design*, 2016, **16**, 1311–1319.

326. D. V. Volodkin, A. I. Petrov, M. Prevot and G. B. Sukhorukov, *Langmuir*, 2004, **20**, 3398–3406.

327. B. V. Parakhonskiy, A. Haase and R. Antolini, *Angewandte Chemie - International Edition*, 2012, **51**, 1195–1197.

328. R. Beck and J. P. Andreassen, *Crystal Growth and Design*, 2010, **10**, 2934–2947.

329. N. Gehrke, H. Cölfen, N. Pinna, M. Antonietti and N. Nassif, *Crystal Growth and Design*, 2005, **5**, 1317–1319.

330. B. Lesiak, N. Rangam, P. Jiricek, I. Gordeev, J. Tóth, L. Kövér, M. Mohai and P. Borowicz, *Frontiers in Chemistry*, 2019, **0**, 642.

331. G. B. Sukhorukov and H. Möhwald, *Trends in Biotechnology*, 2007, **25**, 93–98.

332. A. G. Skirtach, A. A. Antipov, D. G. Shchukin and G. B. Sukhorukov, *Langmuir*, 2004, **20**, 6988–6992.

333. A. G. Skirtach, C. Dejugnat, D. Braun, A. S. Susha, A. L. Rogach, W. J. Parak, H. Möhwald and G. B. Sukhorukov, *Nano Letters*, 2005, **5**, 1371–1377.

334. R. N. Smith, M. McCormick, C. J. Barrett, L. Reven and H. W. Spiess, *Macromolecules*, 2004, **37**, 4830–4838.

335. J. M. Perez, L. Josephson, T. O'Loughlin, D. Högemann and R. Weissleder, *Nature Biotechnology*, 2002, **20**, 816–820.

336. C. Paquet, H. W. de Haan, D. M. Leek, H.-Y. Lin, B. Xiang, G. Tian, A. Kell and B. Simard, *ACS Nano*, 2011, **5**, 3104–3112.

337. H. W. De Haan and C. Paquet, *Magnetic Resonance in Medicine*, 2011, **66**, 1759–1766.

338. A. A. Antipov, G. B. Sukhorukov, E. Donath and H. Möhwald, *Journal of Physical Chemistry B*, 2001, **105**, 2281–2284.

339. A. I. Petrov, A. A. Antipov and G. B. Sukhorukov, *Macromolecules*, 2003, **36**, 10079–10086.

340. L. Li, L. Ferng, Y. Wei, C. Yang and H. F. Ji, *Journal of Colloid and Interface Science*, 2012, **381**, 11–16.

341. T. Mauser, C. Déjugnat and G. B. Sukhorukov, *Macromolecular Rapid Communications*, 2004, **25**, 1781–1785.

342. R. W. Korsmeyer, R. Gurny, E. Doelker, P. Buri and N. A. Peppas, *International Journal of Pharmaceutics*, 1983, **15**, 25–35.

343. P. L. Ritger and N. A. Peppas, *Journal of Controlled Release*, 1987, **5**, 23–36.

344. X. Zhu, J. Li, P. Peng, N. Hosseini Nassab and B. R. Smith, *Nano Letters*, 2019, **19**, 6725–6733.

345. M. Delcea, H. Möhwald and A. G. Skirtach, *Advanced Drug Delivery Reviews*, 2011, **63**, 730–747.

346. V. Czitrom, *American Statistician*, 1999, **53**, 126–131.

347. N. D. Burrows, S. Harvey, F. A. Idesis and C. J. Murphy, *Langmuir*, 2017, **33**, 1891–1907.

348. H. C. Roth, S. P. Schwaminger, M. Schindler, F. E. Wagner and S. Berensmeier, *Journal of Magnetism and Magnetic Materials*, 2015, **377**, 81–89.

349. S. Moise, E. Céspedes, D. Soukup, J. M. Byrne, A. J. El Haj and N. D. Telling, *Scientific Reports*, 2017, **7**, 1–11.

350. D. H. Kim, S. H. Lee, K. N. Kim, K. M. Kim, I. B. Shim and Y. K. Lee, Journal of Magnetism and Magnetic Materials, 2005, pp. 287–292.

351. L. A. Thomas, L. Dekker, M. Kallumadil, P. Southern, M. Wilson, S. P. Nair, Q. A. Pankhurst and I. P. Parkin, *Journal of Materials Chemistry*, 2009, **19**, 6529–6535.

352. C. R. Stein, M. T. Bezerra, G. H. Holanda, J. André-Filho and P. C. Morais, *AIP Advances*, 2018, **8**, 056303.

353. O. Karaagac, B. B. Yildiz and H. Köçkar, *Journal of Magnetism and Magnetic Materials*, 2019, **473**, 262–267.

354. A. M. King, C. Bray, S. C. Hall, J. C. Bear, L. K. Bogart, S. Perrier and G. L. Davies, *Journal of Colloid and Interface Science*, 2020, **579**, 401–411.

355. N. T. Thanh, N. Maclean and S. Mahiddine, *Mechanisms of nucleation and growth of nanoparticles in solution*, 2014.

356. V. Nica, C. Caro, J. M. Páez-Muñoz, M. P. Leal and M. L. Garcia-Martin, *Nanomaterials*, 2020, **10**, 907.

357. T.-J. Yoon, H. Lee, H. Shao, S. A. Hilderbrand and R. Weissleder, *Advanced Materials*, 2011, **23**, 4793–4797.

358. H. Zeng, J. Li, Z. L. Wang, J. P. Liu and S. Sun, *Nano Letters*, 2004, **4**, 187–190.

359. Z. Wang, X. Liu, M. Lv, P. Chai, Y. Liu, X. Zhou and J. Meng, *Journal of Physical Chemistry C*, 2008, **112**, 15171–15175.

360. F. Liu, J. Zhu, W. Yang, Y. Dong, Y. Hou, C. Zhang, H. Yin and S. Sun, *Angewandte Chemie International Edition*, 2014, **53**, 2176–2180.

361. T.-J. Yoon, H. Lee, H. Shao and R. Weissleder, *Angewandte Chemie International Edition*, 2011, **50**, 4663–4666.